l'université nantes angers le mans
PÔLE DE RECHERCHE ET D'ENSEIGNEMENT SUPÉRIEUR

UNIVERSITÉ DE NANTES

Thèse de Doctorat

Hao CHEN

Mémoire présenté en vue de l'obtention du
grade de Docteur de l'Université de Nantes
sous le label de L'Université Nantes Angers Le Mans

École doctorale : STIM

Discipline : Electronique et Génie Electrique
Spécialité : Génie Electrique
Unité de recherche : *IREENA*

Soutenue le 11 Juillet 2014

Modeling and Control of a Marine Current Energy Conversion System using a Doubly Salient Permanent Magnet Generator

JURY

Président :	**Abdelmounaïm TOUNZI**	Professeur, Université de Lille I
Rapporteurs :	**Mohamed El Hachemi BENBOUZID**	Professeur, Université de Bretagne Occidentale
	Tianhao TANG	Professeur, Shangai Maritime University, Chine
Directeur de Thèse :	**Mohamed MACHMOUM**	Professeur, Polytech'Nantes
Co-directeur de Thèse :	**Mohammed El Hadi ZAÏM**	Professeur, Polytech'Nantes
Encadrante :	**Nadia AÏT AHMED**	Maître de Conférences, Polytech'Nantes

l'université nantes angers le mans
PÔLE DE RECHERCHE ET D'ENSEIGNEMENT SUPÉRIEUR

UNIVERSITÉ DE NANTES

Thèse de Doctorat

Hao CHEN

Mémoire présenté en vue de l'obtention du
grade de Docteur de l'Université de Nantes
sous le label de L'Université Nantes Angers Le Mans

École doctorale : STIM

Discipline : Electronique et Génie Electrique
Spécialité : Génie Electrique
Unité de recherche : *IREENA*

Soutenue le 11 Juillet 2014

Modeling and Control of a Marine Current Energy Conversion System using a Doubly Salient Permanent Magnet Generator

JURY

Président :	**Abdelmounaïm TOUNZI**	Professeur, Université de Lille I
Rapporteurs :	**Mohamed El Hachemi BENBOUZID**	Professeur, Université de Bretagne Occidentale
	Tianhao TANG	Professeur, Shangai Maritime University, Chine
Directeur de Thèse :	**Mohamed MACHMOUM**	Professeur, Polytech'Nantes
Co-directeur de Thèse :	**Mohammed El Hadi ZAÏM**	Professeur, Polytech'Nantes
Encadrante :	**Nadia AÏT AHMED**	Maître de Conférences, Polytech'Nantes

ACKNOWLEDGEMENT

The work presented in this thesis has been implemented in the laboratory IREENA (Institut de Recherche en Energie Electrique de Nantes Atlantique, Saint-Nazaire, France) which is under the direction of Professor **Mohamed MACHMOUM**.

Firstly of all, I would like to express my sincere thanks to each member of the PhD thesis defense committee members who have agreed to evaluate this work and this thesis:

I wish to thank Prof. **Mohamed El Hachemi BENBOUZID** from Université de Bretagne Occidentale (France) and Prof. **Tianhao TANG** from Shangai Maritime University (China) to be the reviewers of my PhD thesis.

I am also grateful to Prof. **Abdelmounaïm TOUNZI** from Université de Lille I to be the president of my PhD defense.

I would also like to express my heartfelt appreciation to my supervisors: Mr. **Mohamed Machmoum** Mr. **Mohammed El Hadi ZAÏM** and Mrs. **Nadia AÏT-AHMED**.

Mr. **Mohamed MACHMOUM**, professor of electrical engineering department in Polytech'Nantes, thanks very much for his guidance which lead me complete my work.

Mr. **Mohammed El Hadi ZAÏM**, professor of electrical engineering department in Polytech'Nantes, thanks very much for teaching me so much knowledge about the electrical machine as well as your support and encouragement at my difficult moments

Mrs. **Nadia AÏT-AHMED**, associate Professor of electrical engineering department in Polytech'Nantes, thanks very much for your supervision in this thesis and all of your supports in every aspects for these years.

In these years, I met many nice people in our laboratory. I especially thanks: Yue AMELON, Zhihao SHI, Jian ZHANG, Ahmed BOUABDALLAH, Luc MOREAU, Ouahid DAHMANI, Nacereddine HARKATI, Nassim BEKKA, Fiacre djonkone SENGHOR, Duc-Quan NGUYEN, Didier TRICHET, Abdoulaye DIENG, Christine BROHAN, Franck JUDIC as well as the others for their support and assistance.

Finally, I wish to state my gratitude to my family; they always believe in and encourage me not only during this thesis study but also during my whole life.

Avant-propos

Les travaux présentés dans ce mémoire ont été effectués au sein de l'Institut de Recherche en Energie Electrique de Nantes Atlantique (IREENA, Saint Nazaire, France) sous la direction du professeur **Mohamed MACHMOUM**.

Je souhaite tout d'abord exprimer mes plus sincères remerciements aux membres du jury qui ont accepté d'évaluer ces travaux et ce document:

Messieurs **Mohamed El Hachemi BENBOUZID**, professeur à l'Université de Bretagne Occidentale (France), et **Tianhao TANG**, professeur à Shangai Maritime University (Chine), pour avoir accepté d'être les rapporteurs de ce mémoire.

Monsieur **Abdelmounaïm TOUNZI**, professeur à l'Université de Lille I, pour avoir présidé ce jury.

Monsieur **Mohamed MACHMOUM**, professeur au département génie électrique de polytech'Nantes, pour avoir dirigé et orienté mes travaux.

Monsieur **Mohammed El Hadi ZAÏM**, professeur au département génie électrique de polytech'Nantes, pour m'avoir fait bénéficier de ses connaissances sur les machines électriques, pour m'avoir soutenu et encouragé dans les moments les plus difficiles,

Madame **Nadia AÏT-AHMED**, maître de conférences au département génie électrique de Polytech'Nantes, pour avoir encadré cette thèse et m'avoir supporté (dans tous les sens du terme) pendant toute la durée des travaux.

Les années passées au Laboratoire m'ont amenées à côtoyer des personnes que je tiens à remercier particulièrement : Yue AMELON, Zhihao SHI, Jian ZHANG, Ahmed BOUABDALLAH, Luc MOREAU, Ouahid DAHMANI, Nacereddine HARKATI, Nassim BEKKA, Fiacre djonkone SENGHOR, Duc-Quan NGUYEN, Didier TRICHET, Abdoulaye DIENG, Christine BROHAN, Franck JUDIC ainsi que tous les autres pour leur soutien et leur aide.

Enfin, un grand merci à ma famille qui m'a toujours soutenue et encouragée dans mes études et ma vie.

Contents

List of Figures

List of Tables

General Introduction

Today's global energy production is highly dependent on fossil fuel resources such as oil, gas and coal. These resources are limited and their use results in emission of greenhouse gases which has a profound, devastating impact on the environment. According to the Kyoto protocol, there is a worldwide agreement to reduce the emission of greenhouse gases. To provide a sustainable power production in the future and respecting the Kyoto protocol at the same time, there is a growing demand for energy from renewable sources such as wind, geothermal, solar and ocean. The current European target is to have 20% of the European's energy from renewable sources by 2020.

Therefore, the efficiency and reliability of renewable technologies has been continuously improved and an important technological advance has been noted. Many new renewable energy sectors are emerging and interesting developments are taking place in the last few years. The most motivating sector is the ocean renewable energy. Indeed, the oceans cover more than 70% of the earth's surface and are an abundant source of renewable energy which is much huger than others sources. In fact, the oceans represent an energy resource which is theoretically far larger than the entire human race could possibly use.

Several techniques of exploiting and extracting ocean energy have been suggested. The most studied ones are classified as follows: wave energy, marine current energy, ocean thermal energy, energy from salinity gradients, cultivation of the marine biomass. However, due to technology limitations and economic considerations, the most attractive choice is marine current energy. According to "The Exploitation of Tidal Marine Currents" project which has analyzed 106 locations in European territorial waters, the installed rated capacity can reach 12000MW, able of yielding 48 TWh of electrical energy per annum. Ocean renewable energy resources are generally more costly and difficult to exploit reliably than the land-based options, less than 3% is located in areas suitable for power generation. However, marine current energy has the remarkable advantage of highly prediction which makes it more attractive than the other renewable energy.

France has a huge potential for exploiting marine current renewable energy, coupled with strong R&D and industrial capabilities to develop these technologies for the market. To achieve the goal, French government sectors, laboratories and companies collaborate to build a complete research and development system including funding, source modeling, experiment, generator design, converters, transmission, and integration to the grid and so on.

IREENA laboratory is currently carrying an interregional project called Hydrol 44 involving academic partners (LHEEA, LBMS, IRENAV, LASQUO and IREENA) and industrials partners

(Alstom Hydro, Jeumont and Eca-EN) whose purpose is to organize a “task force” in the West region dedicated to the study of marine current energy conversion chains.

This Ph.D. thesis fits in this context and its main objective is to contribute on modeling and control of a Marine Current Energy Conversion System (MCECS) based on a low speed generator. This will require multiphysics modelings from the hydrokinetic resource to the electricity grid, design and control of an innovative generator and the associated power electronic interfaces.

This thesis is organized in four chapters:

Chapter I mainly presents the characteristics of the marine current energy, their advantages, drawbacks and technological challenges. The principle energy extraction concepts and the relative projects in the world are presented. Moreover, it classifies the geared and direct drive train systems and summarizes the electrical generators associated to the marine current system. The existed power converters for permanent magnet generators are also addressed in the end of this chapter.

Chapter II deals with the modeling of the Marine Current Energy Conversion System. First, two methods to model the predictable marine current speed are detailed. The practical model based on SHOM data is chosen for the system. Then the blade element theory is introduced to determine the suitable marine current turbine geometry parameters. At last, the doubly salient permanent magnet generator model is developed and compared with the conventional permanent magnet generator.

Chapter III analyzes the generator performances supplied by classic current: square and sinusoidal current waveforms firstly. Then, the current analysis to get less torque ripple is presented. Considering the torque ripple and THD of the voltage criteria, a specific waveform for stator currents is searched. The current containing fundamental and 2^{nd} harmonic current component allows to the best performances. The impact of the mutual inductance between stator phases on the generator performances for each kind of current waveforms is detailed.

Chapter IV proposes a robust controller for the non-linear time variant machine system. Moreover, the control strategies for the marine current energy conversion system at both low and high marine current speeds are analyzed, assessed and compared. The MPPT strategy (for low marine current speed) and constant electromagnetic power control strategy (for high marine current speed) are proposed for the machine side system. The grid side system is controlled to maintain the DC-bus voltage constant and keep a unity power factor on the grid. The main results, based on the developed marine current turbine multiphysics simulation tool including realistic resource, the low speed generator (DSPMG), power electronics and appropriate control algorithms, are presented and discussed.

Chapter I

Literature Review

GLOSSARY

ADEME	Agence de l'Environnement et de la Maîtrise de l'Energie
BEC	Blue Energy Canada Inc
CCPS	Clean Current Power Systems
CFD	Computational Fluid Dynamics
CRADA	Cooperative Research And Development Agreement
DDPMG	Direct Drive Permanent Magnet Generator
DFIG	Doubly-Fed Induction Generator
DPA	Department of Aeronautical Engineering
EC	European Commission
EIA	Environmental Impact Assessment
EMEC	European Marine Energy Centre
EMP	Environmental Monitoring Program
ESG	Excited Synchronous Generator
GDFIG	Gearbox Doubly-Fed Induction Generator
HV	High Voltage
IFREMER	Institut Français de Recherche pour l'Exploitation de la Mer
INSEAN	Italian National Institute for Naval Architecture Studies and Testing
IG	Induction Generator
MCECS	Marine Current Energy Conversion System
MCT	Marine Current Turbine
MPPT	Maximum Power Point Tracking
NRC	National Research Council of Canada
NPS	Nova Scotia Power Inc
ORPC	Ocean Renewable Power Company
OTEC	Ocean Thermal Energy Conversion
PMSG	Permanent Magnet Synchronous Generator
PWM	Pulse Width Modulation
SRG	Switched Reluctance Generator
UNESCO	United Nations Educational, Scientific and Cultural Organization

UNIDO	United Nations Industrial Development Organization
WECS	Wind Energy Conversion System

I.1 *Introduction*

Reducing greenhouse gas emissions becomes a top priority in the world with the emergence of global warming and environmental problems. Thus, one worldwide agreement aimed at reducing greenhouse gas-Kyoto Protocol emerges as the times require. Countries in the world respect the agreement and simultaneously, vigorously seek to develop a variety of renewable energy (Wind, Geothermal, Solar and Ocean Energy). It becomes imperative to meet the human growing demand for the energy.

At present, more than 60 countries and regions have passed relevant laws, regulations or plan to strengthen the realization of the strategic target of renewable energy. For example, the European Union has passed resolutions in March 2006: renewable energy will reach at least 20% of the proportion in the energy demand in Europe by 2020. Although America hasn't signed the Kyoto Protocol, it has also proposed in 2011: by 2030, 20% of the national electric power will be provided by wind power and biofuels will take up over 30% of the vehicle fuel consumption. So, more and more researchers take attention in renewable energy. According to these, by the end of 2009, renewable energy is responsible for 12.415% of global final energy consumption (see Fig.I.1), while accounts for 3.02% of global electricity production (see Fig.I.2) [1].

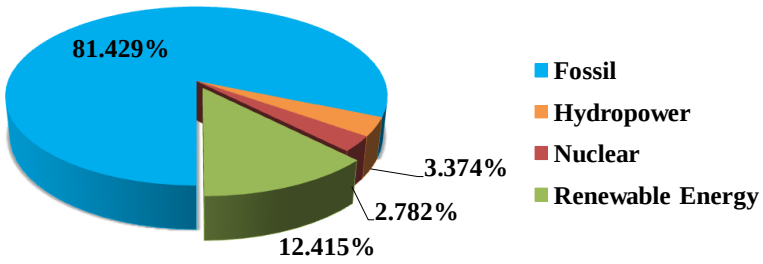

Fig.I.1 Energy share of global final energy consumption, 2009

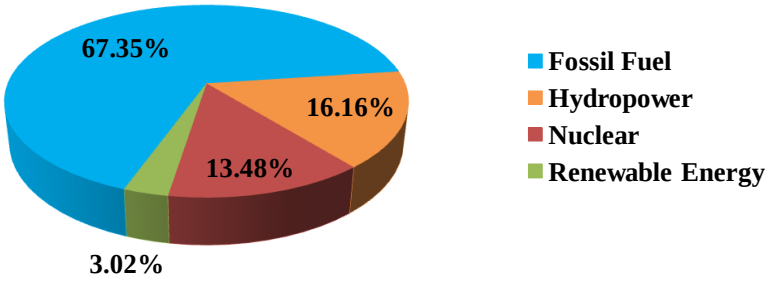

Fig.I.2 Energy share of global electricity production, 2009

I.2 *Ocean Energy Resource*

With the increasing requirement of the energy and the novel problems for the classical renewable energies such as cost and availability when needed appeared, in recent years, researchers have begun to address other alternatives. As we know, the oceans cover more than 70%

of the earth's surface and can produce much greater energy than other sources every year. According to authority, global ocean resource is estimated at between 2,000 and 4,000 TWh per year. Less than 0.1% of the ocean power could satisfy 5 times of world energy demand! However, ocean renewable energy resources are generally more costly and difficult to exploit reliably than the land-based options. Consequently, we cannot use much of the ocean energy (see Fig.I.3 and Fig.I.4) [1].

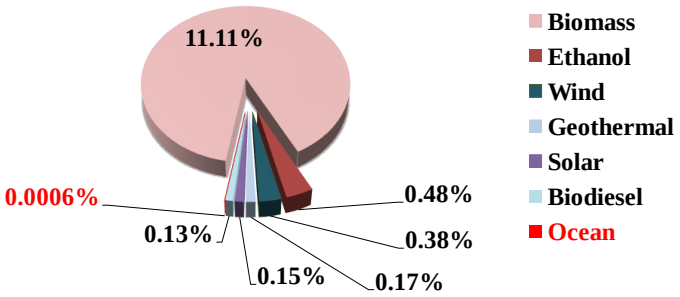

Fig.I.3 Renewable energy share of global final energy consumption, 2009

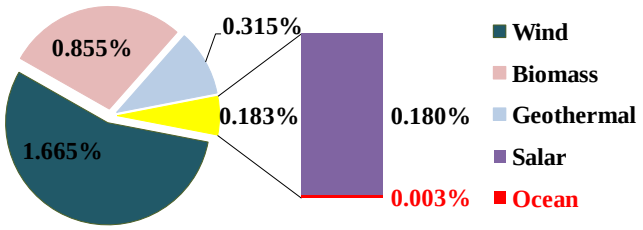

Fig.I.4 Renewable energy share of global electricity production, 2009

I.3 *Forms of Ocean Energy*

Ocean energy is available in different forms. Therefore, numerous techniques of exploiting and extracting ocean energy have been suggested. The most prominent ones can be classified as follows: wave energy, tidal energy, osmotic energy (energy from salinity gradients), ocean thermal energy, and cultivation of the marine biomass [2].

a) Wave energy

Wave energy is the kinetic and potential energy of the ocean surface wave. The energy is directly proportional to the wave height square, the wave period and the wave width surface. This energy is transmitted from the wind energy to ocean. Wind energy is imparted to the sea surface through friction and pressure, causing waves. The world's first commercial wave energy project named Pelamis (750 kW), is presented in Fig.I.5.

(a) Pelamis

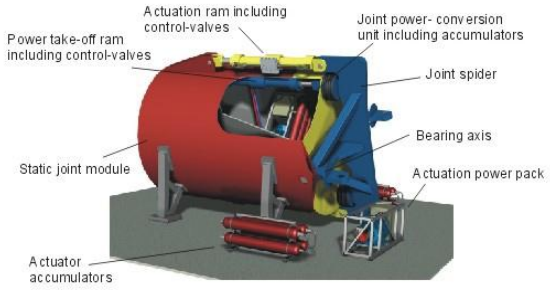

(b) Technology of Pelamis

Fig.I.5 Pelamis, world's first commercial wave energy project, Agucadoura, Portugal [3]

b) Tidal energy

There are two forms of energy caused by the tide: the tidal current energy and the tide energy. Although the tide and the tidal current don't have much impact in the open oceans, it can create a rapid current up to 7 m/s when the current flow in and out of narrower areas like bays, estuaries and harbors. According to law of conservation of mechanical energy, the tides with big difference between high tide and low tide bring always huge energy of tidal currents.

A tidal current, a major part of marine current, is a regular horizontal movement based on the rising and falling of the tide. It has a principle of 12 hours period that depends on the relative positions of the earth, lunar and sun. The minor part of marine current is called ocean current. It is the stable flow between sea bottom and channels which is mainly caused by prevailing winds, earth's rotation and the difference of temperature and salinity density. It has a long-time period. All the marine current can be magnified by underwater topography especially in the vicinity of land or in straits between islands and the mainland [2] [4].

Tide energy is also very interesting, which is caused by the vertical sea water movement. Usually, it needs one big dam near the seacoast, and extract the tide potential energy via the big difference height of the flood and ebb tides. This energy is proportional to the square of tidal range and the reservoir area.

Fig.I.6 Seaflow, world's first MCECS pilot project at a commercial scale [5]

Fig.I.6 gives the world first commercial scale marine current system Seaflow, which is installed on the north coast of Devon on 30 May, 2003. It has a 300 kW two blades, horizontal axis turbine with 11 m rotor diameter and 2.1 m pile diameter.

Fig.I.7 presents the world's biggest tidal power station-Sihwa Lake, which is located in South Korea, 2011. According to some statistics, it is able of generating about 254,000 kW daily which is a little bigger than the Rance tidal power station (240,000 kW per day) in France.

Fig.I.7 Sihwa Lake, South Korea [6]

Fig.I.8 La Rance,France [7]

c) Osmotic energy (or osmosis power)

Osmotic energy is one chemical form for the ocean energy. The freshwater and saltwater always have pressure difference. Theoretically, the freshwater from water to sea can bring 0.65 kWh/ft^3. One river with 1 m^3/s speed can produce 2,340 kW electricity [2].

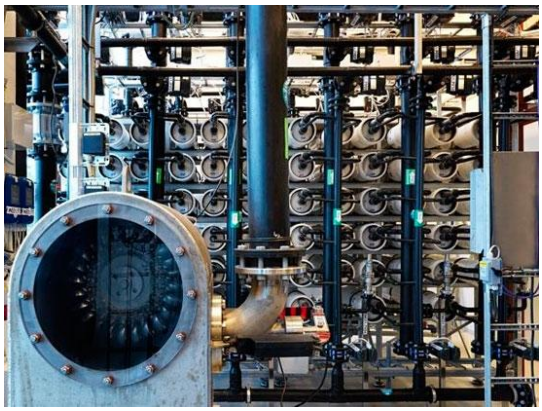

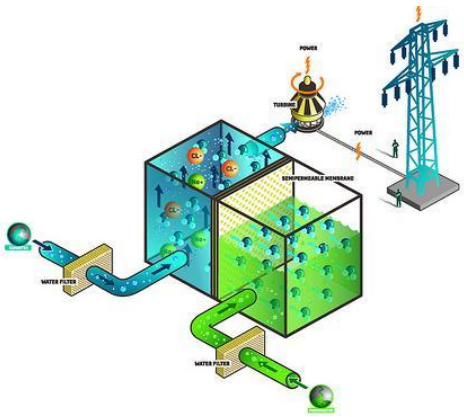

Fig.I.9 World's first osmosis plant, Norway [8] [9]

Fig.I.9 introduces the world's first prototype osmosis power plant by Statkraft, on the Oslo fjord, southern Norway. It uses a special membrane and can produce 2 to 4 kW electricity to run a coffee machine.

d) Ocean thermal energy

Ocean thermal energy refers to the energy due to the temperature difference between the ocean surface and abysmal sea. The ocean is a huge solar thermal energy collector and its storage. It can absorb most of the solar energy which is projected onto the earth, and heat the ocean

surface. While the abysmal sea is still with a very low temperature, so the vertical temperature difference can bring a huge energy. The minimum required difference is 20 ℃ between the surface and abysmal sea with 1,000 m for the recent technique. It is estimated that the generation power can reach 2 TW if we can well use temperature difference.

Although attempts to develop and refine Ocean Thermal Energy Conversion (OTEC) technology have been started in the 1880s, the first OTEC plant was built in Matanzas, Cuba until 1930. Fig.I.10 shows the world's only operating OTEC in Japan, by Saga University.

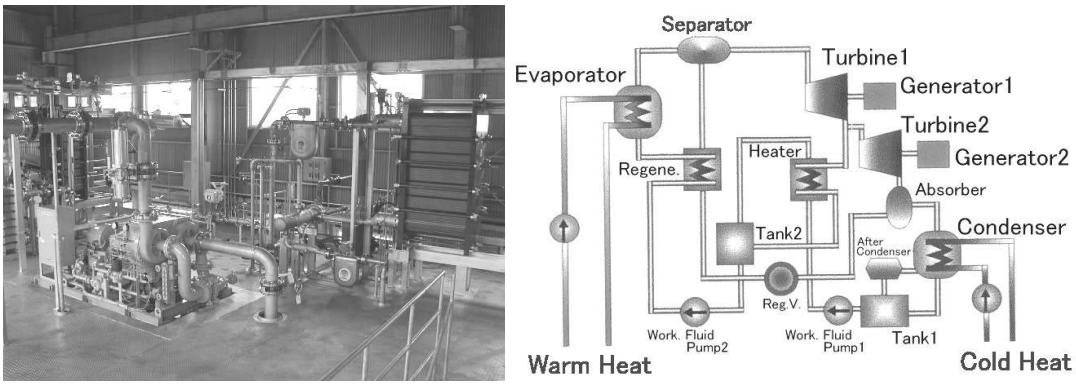

a) OTEC of Saga University b) Block Diagram of Uehara Cycle

Fig.I.10 The world's only operating OTEC, Japan [10]

e) Conclusion

Theoretically, these ocean-based renewable resources could meet the world's energy requirements over. Unfortunately, harnessing the kinetic energy in waves presents a different set of technical challenges which have pushed engineers to suggest a wide variety of designs. Tide energy always needs the construction of tidal barrages near the seacoast. Ocean thermal energy conversion is possible in certain locations with large temperature differences, by extracting energy with a heat engine. However, due to technology limitations and economic considerations, osmotic and thermal energy developments also are very limited in these years.

Nowadays, the attraction of marine currents for renewable energy developers is more and more obvious.

I.4 *Marine Current Energy*

I.4.1 The Physics of Tide and Tidal Current

As presented in section I.3, marine current energy is a horizontal movement based on tide rising and falling. The tide is essentially a long, slow wave which is generated by the interaction of the gravitational fields caused by of the moon and the sun with the Earth's ocean (see Fig.I.11). The gravitational force is given by:

$$f = K\frac{mM}{d^2} \tag{I.1}$$

Where: m is the mass of the water (kg); M is the mass of the sun or the lunar (kg); d is the distance between the ocean and the lunar or sun (m); K is the universal constant of gravitation (6.67×10^{-11} $m^3kg^{-1}s^{-2}$).

From formula (I.1), we can deduce that the attractive force highly depends on the masses and distance respectively. Although the sun has large mass, as the lunar is so much closer to the earth, the force produced by the lunar is 2.17 times larger than that of sun (68% from lunar, 32% from sun) [11].

Since the earth rotates, the distance among the earth oceans, the lunar and the sun will vary. When the ocean is on aligned position relative to the sun or the lunar, the distance between the ocean and the attracting body is less or greater than when the ocean is on the opposition positions. The ocean will have a tendency to escape from the earth. This force appears twice every day due to the relative position of each attracting body.

It is necessary to take into account the beating effect caused firstly by different relative positions of the earth, the lunar and the sun, which can create the spring and neap tides, and secondly the different types of oscillatory effects. If there is no oscillatory effect in the ocean, lunar force, which is the stronger for tide generation, will produce approximately only 5.34 cm high tidal range [11].

The tides are generated by the moon and the sun. The actions of these two bodies can therefore, according to their relative positions, be added, creating higher tides, or be opposed thus creating lower tides. Changes in water level are conditioned primarily by the phases of the Moon. The Sun, Moon and Earth are aligned; the forces add up, the tides are important. The Sun, Moon and Earth form a right angle, the forces thwart the tides are low.

When the tidal reaches a maximum, the tide is called spring tide. It corresponds to the phases of new and full moon called. It is explained by the combined effects of the Moon and Sun effects. Conversely, when the tidal range is at a minimum, the tide is called neap tide. The moon is still in its first and last quarters, called quadrature.

In summary, every full moon and every new moon, about fortnightly, tidal amplitudes pass through a maximum. Each first and last quarter, the amplitudes of wave pass through a minimum (see Fig.I.11).

The rise and the fall of tide in water level, which are caused by gravitation is always accompanied by a horizontal movement of water. This is called the **tidal current**. The strongest tidal currents occur at or around the peak of high and low tides. When the tide is rising and the current is directed towards the shore, the tidal current is called the **flood current**, and when the tide is receding and the current is directed back out to sea, it is called the **ebb current** [12]. This means that tide and tidal current have nearly the same period.

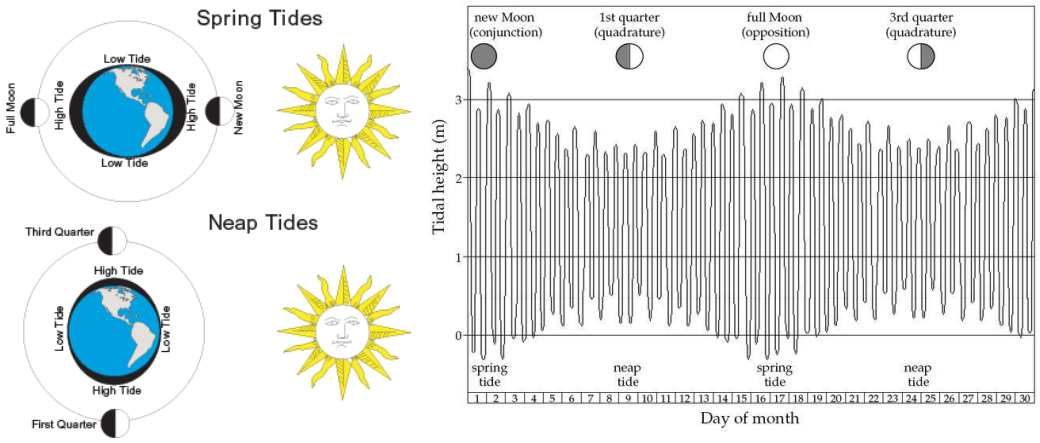

a) Relative positions of sun, moon and earth b) Relative height

Fig.I.11 Spring and neap tides [13]

I.4.2 Type of Tide

The lunar does not rotate around the earth's equator, but follows an orbit that is inclined to the earth's axis with a 19 years period. The angle between the orbit of the lunar revolution and the earth equator can mainly determine the type of tides in any particular location. There are three mainly types of tide at different locations in the world, called **semidiurnal, diurnal, and mixed** [11] [14]. Fig.I.12 can briefly explain the effect of the lunar declination to the type of tide.

Semi-diurnal tide, which has a period of approximately half tidal day (12 h 25 min), is the predominant type all over the world. It has two high and two low waters each tidal day with relatively similar ranges. This type is more likely to find any locations when the lunar is over the equator or at the equator all the time.

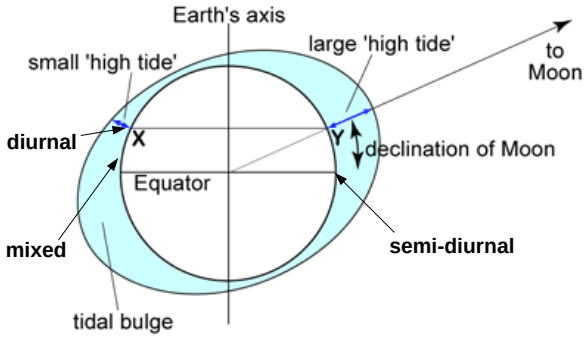

Fig.I.12 The Moon's Declination Effect [14]

When the lunar and its associated tidal bulges are either north or south of the equator (the furthest from the equator), most locations at high latitudes in theory would be impacted by tidal bulge and would experience one single high tide and one single low tide per tidal day. This is called **diurnal tide** with one tidal day period (24 h 50 min).

Mixed tide combines the characteristics of semi-diurnal and diurnal tides. This tide also tends to occur as the moon moves furthest north or south of the equator. They are characterized by

conspicuous two unequal high tides and two unequal low tides (higher high and lower high waters and/or higher low and lower low waters) per tidal day.

Fig.I.13 shows the principle waveform of three mainly types tides. As the relative positions of the moon, sun and earth change at a known rate, tidal currents are predictable.

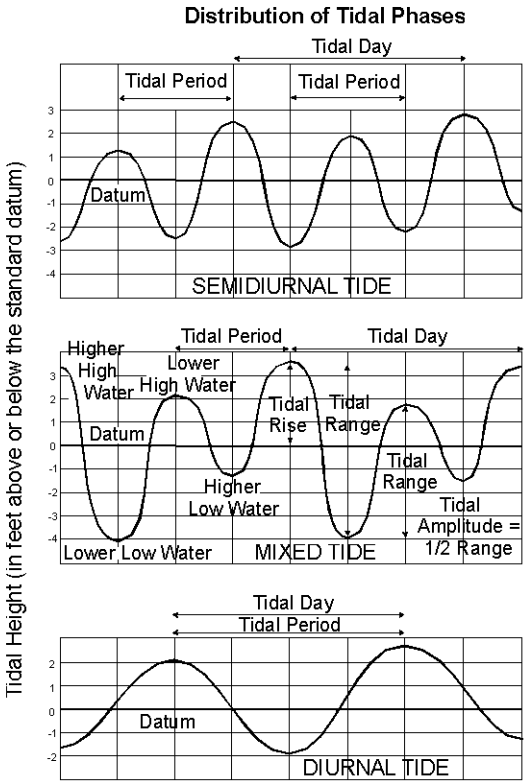

Fig.I.13 Principal Types of Tides [15]

I.4.3 Marine Current Energy Assessment

According to the data provided by United Nations Educational, Scientific and Cultural Organization (UNESCO) in 1981, the total of the theoretical ocean energy capacity is about 76.6 TW. Table I.1 shows the potential for the first four kinds of the ocean energy. Principal sites for tidal power development worldwide are illustrated in Fig.I.14 [16].

Table I.1 Ocean energy capacity [1]

	Ocean Energy Capacity
Ocean Thermal Energy	40 TW
Osmosis Energy	30 TW
Wave Energy	3 TW
Tidal Energy (+ocean current)	3.6 TW
Total	76.6 TW

The global ocean resource is estimated between 2,000 and 4,000 TWh per year, and the total tidal energy potential is estimated to be 500~1000 TWh per year. While for the marine current energy, due to the too low velocity and energy density in some areas for economic exploitation, there is an estimated 50,000 MW or approximately 180 TWh per year of economically

exploitable resource available worldwide, with energy density up to 15 kW/m^2 (see Table I.2) [11] [17].

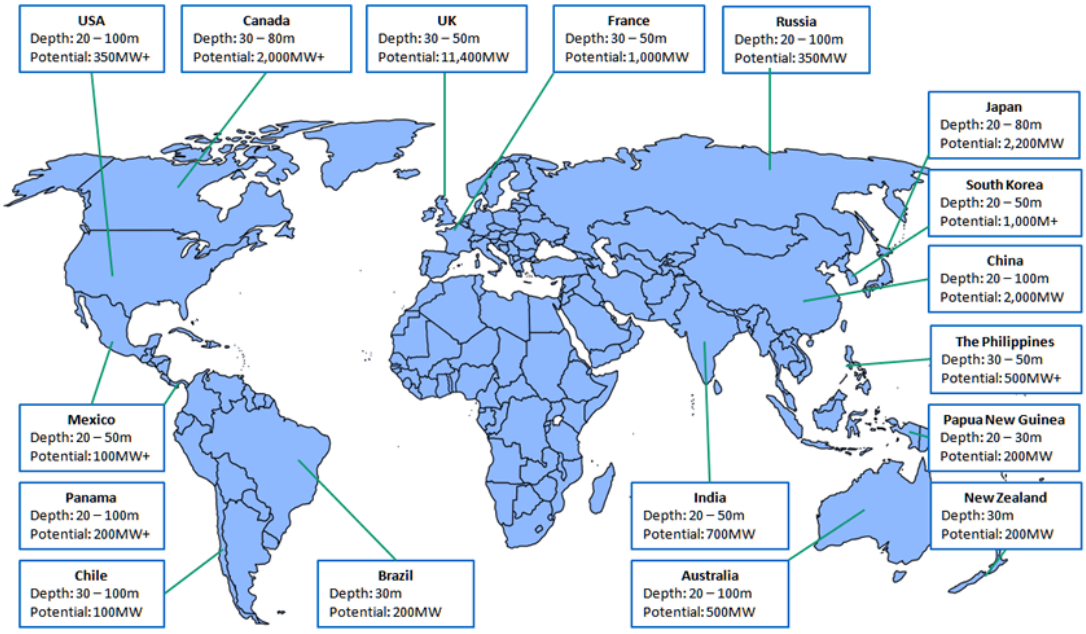

Fig.I.14 High potential areas for tidal resources worldwide [18]

Table I.2 Ocean Energy Potential [17]

	Estimated Resource
Global Ocean Resources	2,000~4,000TWh /year
Tidal Energy	500~1000 TWh/year
Marine Current Energy	50 GW or ~180 TWh/year (Economically Exploitable)

The EC (European Commission) also sponsored project "*The Exploitation of Tidal Marine Currents*" in 1996. The Resource Assessment identified 106 possible sites along the European

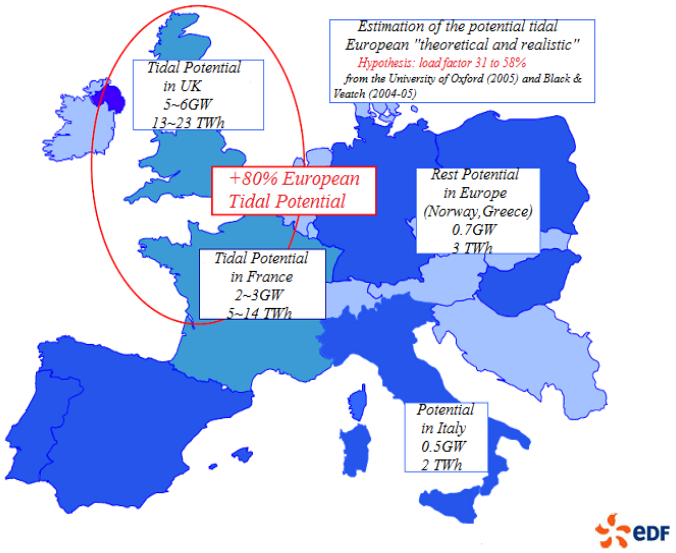

Fig.I.15 Marine current potential in European [19]

coastline with certain predefined characteristics which are suitable for marine current energy exploitation. 29 of these sites have an enormous energy capacity exceeding 10,000 kWh per square meter of cross-section per annum. According to the analysis with assumption, the annual electricity supplied to the European grid will be around 48 TWh/year with an installed capacity of 12,500 MW. The marine current resource is of special interest for Great Britain, France, Greece and Italy (see Fig.I.15): 15 sites may have installed MCECS (Marine Current Energy Conversion System) in farms with rated power exceeding 10 MW/km^2 of sea-bed [1] [4].

I.4.4 Advantages of Marine Current Energy

Marine current energy is an inexhaustible green energy resource. It is a non-harmful disturbance, with a low visual exposure. It does not require barrages across the water ways.

Besides, another important characteristic is the high power density caused by sea density (800 times larger than air density), as the kinetic power varies depending on the density and the cube of velocity of the marine current, the marine current speeds are almost one-tenth the speed of wind for the same power (see Table I.3). At the sites where the marine currents move at higher speeds, between 2 and 3 m/s, a MCT can produce four times as much energy per the rotor swept area, compared to a similarly rated power of Wind Turbine. In other words, MCT can provide significant power at relatively low marine current velocities; the size and the weight of a marine current turbine can be much smaller than the similar rated power of wind turbine (one-tenth, one twentieth respectively).

As a renewable resource, marine current energy has the distinct advantage of being predictable compared with other forms of renewable energy, up to 98% accuracy for decades, which make the marine current energy development an attractive resource option. The marine current charts are accurate for years ahead. It is mainly independent of prevailing weather conditions that can highly impact other renewable generation forecasts.

Table I.3 Power density of marine currents compared with wind and solar resources [20]

	Energy resource						
	Marine Current					Wind	Solar
Velocity (m/s)	1	1.5	2	2.5	3	13	Peak at noon
Velocity (knots)	1.9	2.9	3.9	4.9	5.8	25.9	
Power density(kW/m^2)	0.52	1.74	4.12	8.05	13.91	1.37	~1.0

The MCECS technology is similar to WECS (Wind Energy Conversion System) technology, especially offshore WECS. The configurations of a rotor rotating by a moving fluid connected to a drive train, a gearbox and a generator with associated power electronics are all common features of these two technologies. Thus, existing expertise in offshore WECS can be considered at least partially transferable to marine current energy [21]. Some pilot projects and the first commercial project have successfully harnessed power from marine current using the offshore WECS technologies. Compared with Offshore WECS, they have almost the same system structure such as: offshore transformer platform, submarine cables, directional drilling and cable vault, the only difference is the turbines and foundations [17].

Finally, another distinct characteristic must be mentioned is the relatively high utilization factor. This factor is defined as the actual annual energy output divided by the installed device theoretical maximum. Marine current is likely to have a factor up to 40~50%; while the corresponding utilization factor of wind energy is usually between 25~30%. A high utilization factor is important to achieve an economically viable power production [22].

I.4.5 Drawbacks of Marine Current Energy

The marine currents always have a very low velocity that rarely exceed 5 m/s. Normally, the limitation for the interesting sites is that the marine current moves at least 1 m/s which is close to neap tides. The target marine current velocity is an average of 2.5 m/s with a maximum of 4 m/s. The good tidal sites should have capacity factors bigger than 35% [17]. This means there are only a few locations in the world where the marine currents are economical exploited compared with winds.

Once the power is extracted from marine currents, delivering it to the customer must be a very costly and complex process due the long distances and subsea cabling issues. This will be an economic problem.

The other drawback is the technology. Although some expertise and energy conversion technique achieved in the wind turbines can be considered partially transferable to the marine current technology. However, the technology especially for this new renewable energy is still in its infancy, and has high capital cost compared with classic fuel resource (some more details are given in section I.4.7 and Table I.4).

I.4.6 Environmental Impacts

The environmental impacts of marine current energy have been considered as benign; however, there are lots of unknowns regarding potential environmental impacts from these exciting new technologies.

It is well known that any system which produces electricity must be assessed in its entirety to pinpoint any energy, environmental, social or economic implications. Until now, there are no many details on the exact environmental impacts of MCECS carried out by EIA (Environmental Impact Assessment). As a result, it is also impossible to quantify the exact impact of an array of turbines may have on the ecology, environment and existing users. However, it must be admitted that an MCECS with 18 m diameter and operating in the sea up to 50 m deep, must inevitably have some negative or positive impact on the surrounding environment. The level of impact would be determined by the quantity of units installed and the MCECS density [23] [24].

As MCECS have a very similar system with offshore WECS, they own many analogous environmental impacts. Some studies have listed the possible and likely impacts of these systems and they were classified into two main categories: one is common to offshore WECS, and the other is unique for MCECS [25].

a) Common environmental impacts

Table I.4 Energy comparison [17] [23]

		Renewable resource	Low capital cost	Minimal environmental impact	Predictable	Modular	Scalable	Load factor (%)	Capital cost per MW (£MM)	Influenced by
fossil		NO	YES	NO	YES	NO	YES	80~90	0.9	Fossil oil
Nuclear		NO	YES	NO	YES	NO	YES	90	1.2	Nuclear fuel
Wind	onshore	YES	NO	YES	NO	YES	YES	20~30	1.1	Climate, Wind, Pressure
	offshore						YES	35	2.5	
Solar	PV	YES	NO	YES	NO	YES	NO	16	4.5	Solar intensity/Exposure
	Thermal						YES	-	3.6	
Hydro		YES	YES	NO	YES	NO	NO	30	1.0	Dam, River
Wave		YES	NO	YES	NO	YES	YES	35	4.0~5.9	Wind Seafloor topography
Marine current		YES	NO	YES	YES	YES	YES	30~50	2.1	Moon, Gravity, Seafloor topography

- Visual impact: The principle visual impact would be the electrical substations (offshore transformer platform & cable vault) and over lines near the cable vault.
- Construction & Installation: the construction and installation may disturb the seabed and cause sediment displacement, which lead to destruction of habitat and marine benthos, and even contaminate the local environment.

b) Unique to MCECS

- Physical Impacts: The influence of tidal energy extraction on coastal processes, tidal flows, seabed scouring (seabed morphology) and sediment transport.
- Ecological Impacts: Possible interaction between moving submerged rotor blades and marine creatures which means the rotating blades can occasionally kill swimming sea life and some fish may no longer live in these areas.
- Pollution: the mechanical fluids, such as lubricants or the anti-fouling paint, can leak out, which may be harmful to the marine life nearby.

I.4.7 Technology Challenges

Based on the experience of tested prototypes and commercial projects, some common technologies challenges become more and more thorny. This section will focus on the most pressing problems on which all researchers must confront at present [5] [25] - [27].

a) ***Installation***

Normally, most MCECS devices will have a similar installation, foundation and mooring processes. Constructing foundations and installation during water movement will be a very challenging problem. So there is generic research in this area.

b) ***Maintenance***

Maintenance in the complex marine environment is quite important. Normally, for maintenance of MCECS it would be necessary to use a platform or ocean-going vessel, and could be difficult and hazardous. For economic reasons, some methods are taken at the design stage (such as reduce the moving parts), as well as tenacious lubricants, good quality seals and bearings and strong blades are used in the MCECS, to reduce the frequency and difficulty of maintenance procedures. The system only requires the minimum level maintenance.

c) ***Cavitation***

As the size of MCECS devices increase, the velocities at the tips of the rotor blades are relatively high. Certain operational difficulties will be encountered. One of the problems is called cavitation which may be difficult to avoid at all the points along the blades. It always occurs when the partial pressure locally falls below the vapor pressure of water and its potential damage effect usually appears at low velocity in pumps and propellers. The research in this part need propose the choices of blade profiles and materials to resist or reduce the cavitation effects which can bring about the efficiency loss, functional constraints and damage problem.

In order to avoid cavitation, it means limiting the rotor tip ratio and hence turbine speed. It follows that as the turbine radius increasing, the turbine speed has to decrease to maintain the same maximum tip ratio. For the purpose of keep the blade tip velocity below the cavitation velocity of around 7 m/s for near surface turbines in high marine current velocities, low tip ratios are needed badly (see Table I.5) [4].

Table I.5 Maximum tip ratio for avoiding cavitation [4]

Marine Current velocity (m/s)	Max. tip ratio to avoid cavitation
2.0	3.5
2.5	2.8
3.0	2.3

d) ***Packing Density***

It needs to response that how many and what size MCECS devices can cause a significant effect on the marine environment and flow pattern. Many factors considered include seabed structure and depth, flow pattern and available area. All the research will help developers find the most suitable sites, and understand the implications of MCECS farms. Based on [21], some results for the packing density are showed as:

- For water depth 20~25m, 5m turbine diameter used, giving 1800 units/km^2;
- For water depth 25~40m, 10m turbine diameter used, giving 82 units/km^2;
- For water depth >40, 20m turbine diameter used, giving 38 units/km^2;

e) ***Turbulence***

The turbulent structure of the flow field is another important design driver which affects the components design to resist fatigue. Understanding the turbulence levels is important not only to the sitting of individual units but can also inform the realistic limits to device design.

f) ***Fouling***

Fouling by unwanted marine growth and bio-fouling, will extremely increase the dag and lower the efficiency of the turbine. There are four main physical characteristics (salinity, temperature, sediment transport and turbidity) which are very important to the devices in the sea. Many devices installed in the sea became artificial reefs which attract a various marine organisms; meanwhile, the metal parts are much easier corroded (see Fig.I.16). All these problems can affect the performance and cause significant fouling what leads to a necessity of regular maintenance. Regretfully, due to the MCECS size and depth in the water, it is not easy to meet this requirement. As a result, several methods such antifouling paints and sonic and ultra-sonic systems have been proposed for preventing bio-fouling .Unfortunately, each method has its own challenges and drawbacks. For the corrosion, the use of corrosion-resistant materials like stainless steels, high-nickel alloys, copper-nickel alloys, nickel-copper alloys and titanium which can greatly reduce, or even eliminate, corrosion damage becomes more and more interesting.

g) ***Stress***

There are also some challenges associated with higher density (1,025 kg/m^3) which gives high strain on the turbine. The turbine can extract the energy which is considered as the velocity reduction on the either side of the turbine blades. Essentially, it is the change in momentum of the marine current. A turbine and its anchoring structure must resist this force in order not to fail.

Fig.I.16 Biofouling & Erosion for MCECS [24]

I.5 *Turbine Concept, Installation & Relative Projects*

One of the main issues of MCECS is to design the MCT to harness the kinetic energy of marine current energy into mechanical energy which can drive a generator. As the basic physical principles for extracting energy from marine currents are virtually identical to those of wind, many researchers suggest using the similar techniques which has been successfully developed for WECS. However, there are a number of differences and difficulties in the design of MCT, including stall characteristics and the possible occurrence of cavitation in the blades. A special attention is that the MCT has shorter and thicker blades than Wind Turbine in order to withstand the larger stresses due to the higher density of the water.

Similar to Wind Turbine, the efficiency of MCT depends on the marine current rate. A plot of MCT output as a function of marine current speed typically consists of four regions (see Fig.I.17) [12] [26] [28] [29].

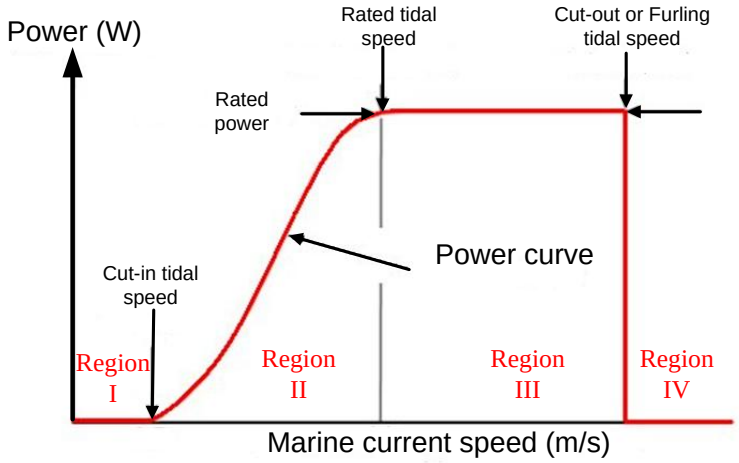

Fig.I.17 Typical power curve

Region I: Zero to cut-in tidal speed

Region II: Cut-in tidal speed to rated tidal speed

Region III: Rated tidal speed to cut-out tidal speed

Region IV: Greater than cut-out tidal speed

- **Cut-in tidal speed**: Low-speed tidal may not have enough power to overcome friction in the turbine drive train and electrical losses in the system. The cut-in tidal speed is the minimum needed to generate net power. So, MCT will not rotate and there is no generated power when marine current speed is below cut-in tidal speed, just as in Region I.
- **Rated tidal speed**: In Region II, as velocity increases above the cut-in tidal speed, the electrical power delivered by the generator tends to increase proportionally to the cubed marine current speed. When marine current speed reaches the rated tidal speed, the generator will deliver as much power as it is designed for. Above the rated tidal speed (in Region III), there must be some way to shed some of the tidal power otherwise the generator may be damaged. Three approaches widely used in WT, which maybe apply to MCT, to limit the power on the turbine are: an active pitch-control system, a passive stall-control design, and a combination of the two. There are also some generator control strategies such as flux weakening control which can decrease the electrical power with high rotating speed. In this region, the power output will be constant, equates to rated power, regardless of velocity.
- **Cut-out** or **furling tidal speed**: In Region IV, the marine current speed is so strong that there is real dangerous for MCECS. Beyond this cut-out tidal speed (furling tidal speed), the system must be shut down and the output power obviously goes to zero. Maybe there is no necessary for MCECS, as the highest spring tides are not much greater than monthly maximum spring tidal currents.

MCT devices can be classified in a number of different ways with overlap between categories. In this thesis, these devices will be classified depending on the way they interact with the water in terms of motion. So, the whole of the different models available could be mainly classified as follows:

• Horizontal Axis Turbines

• Vertical Axis Turbines

• Oscillating Hydroplane Systems

For the sake of increase the marine current velocity passing through the turbine and the capture of effective power, ducted structure (Venturi Effect) may be used around the blades for streamline and concentrate the flow towards the rotors for both horizontal and vertical turbines [1] [30].

Currently some concepts are undergoing prototype testing and refinement prior to commercialization. Other interesting variants of the concepts are also emerging. A review of

some well-known projects and concepts are briefly presented according to the turbine classification.

At present, only two systems are being investigated for commercial development: the oscillating aerofoil driving hydraulic accumulators; and horizontal axis turbines evolved from wind power technology, with two prototypes installed off the coasts of Norway and England [31].

I.5.1 Horizontal Axis Turbine

Horizontal axis turbine (axial flow turbine) which is the most common turbine concept is very similar to the wind turbines usually seen in wind farms. It extracts energy from moving water in much the same way as wind turbine extract energy from moving air (see Fig.I.18). The marine current causes the rotors to rotate around the horizontal axis which is parallel to the water flow and generate power. The amount of power that can be harvested from the water current also depends on the rotor diameter.

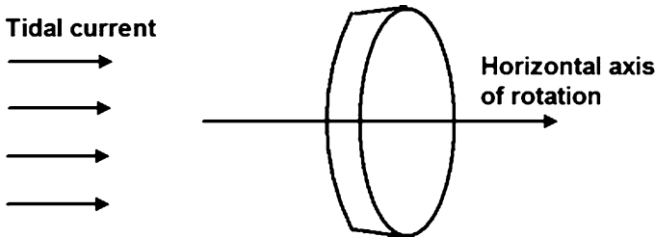

Fig.I.18 Horizontal axis turbine [32]

Nowadays, the majority of the marine current devices are the horizontal axis turbines. This type of turbine can also be classified depending on the number of blades. Multi-bladed devices are favourable as they can generate greater starting torque and reduce balancing problems compared with single-blade devices. However, it will bring much more hydrodynamic losses. Depending on turbine design, the blades can either have a fixed pitch or variable pitch to enable the turbine to operate during flow in both directions [12] [30] [32] - [35].

There are many projects and concepts proposed and tested for horizontal axis system. This section just presents some of them.

I.5.1.1 SeaGen (UK)

SeaGen (1.2 MW at 2.4 m/s), the world's first grid connected commercial marine current energy turbine, was installed in Strangford in May 2008 (see Fig.I.19).

This device comprises twin axial flow rotors of 16m diameter, each driving a generator through a gearbox like a hydro-electric or wind turbine. These twin turbines can be operated independently. The generator output is rectified, inverted and exported to the 11 kV grid via a step-up transformer. Until 2011, it has successfully operated for in excess of 4,000 operating hours and generated in excess of 2.5 GWh of electricity on to the grid [33]. The rotors have a patented full span pitch control which allows them to operate on both flood and ebb tides. These

two rotors can be raised above the surface for safe and easy maintenance access. This is so called surface piercing structure.

Fig.I.19 Seagen, the first grid connected commercial project in the world [5]

MCT is currently developing a 5 MW array in Kyle Rhea, Skye, a 10 MW array near Skerries, Anglesey. They have a 100 MW project approved at Brough Ness in the Pentland Firth [33] (see Fig.I.20).

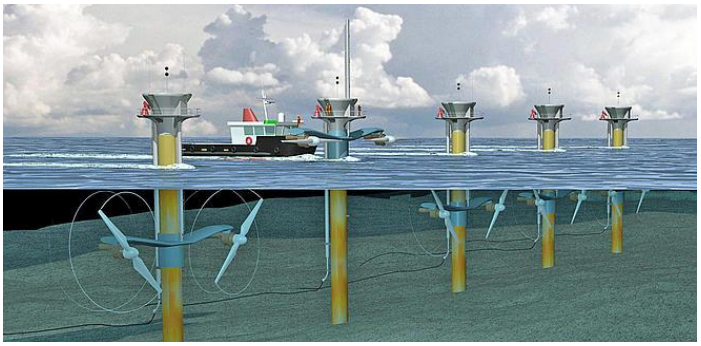

Fig.I.20 Seagen farm [36]

I.5.1.2 Sabella (France)

The first France submarine marine current turbine “Sabella D03”, 3 m in rotor diameter, 10 kW in power, which was successfully immersed in April 2008 next to Bénodet, in Odet’s estuary in South Brittany for a fully year, has a pioneering achievement in France (see Fig.I.21).

It was an experimental project, which owned only 1/3 scale tidal turbine prototype, lead by the consortium SABELLA with the support of public territorial authorities and Agence de l’Environnement et de la Maîtrise de l’Energie (ADEME), and technical support from Institut Français de Recherche pour l'Exploitation de la Mer (IFREMER). A lot of experiments and measures have been carried out, demonstrating among other things its innocuousness towards

wildlife and low acoustic impact. This turbine it now exposed at the forecourt of the Ocean Discovery Park Océanopolis in Brest, for educational purposes [37].

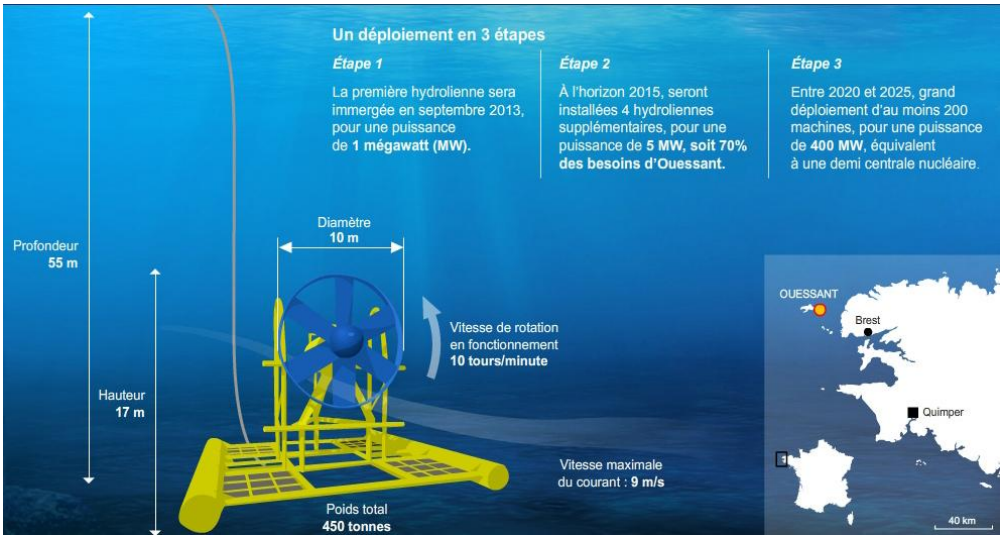

Fig.I.21 Sabella D10 [38]

Following the previous prototype "Sabella D03", SABELLA continues to strengthen its industrial credibility by producing a full-scale demonstrator: "Sabella D10"(see Fig.I.21). This full-scale turbine will be installed in Fromveur Passage near to South Ushant (Brittany) in winter 2013/2014.

As a tidal turbine's production capacity mainly depends on the hydrokinetic variable and the future marine current turbine farm requirement of a wide range of capacities turbine (0.3 to 2 MW), SABELLA offers the range "D10", "D12" and "D15" to meet market demands (see Table I.6).

Table I.6 Sabella type [37]

Speed	"D10" Diameter:10 m	"D12" Diameter:12 m	"D15" Diameter:15 m
2.5 m/s	0.3 MW	0.4 MW	0.6 MW
3.0 m/s	0.5 MW	0.7 MW	1 MW
3.5 m/s	0.75 MW	1 MW	1.6 MW
4.0 m/s	1.1 MW	1.5 MW	2.5 MW

Compared with Seaflow and SeaGen, there are some differences. All the types of Sabella has more blades but fixed pitch angle; the direct drive permanent magnets generators will be used to avoid any complex mechanical element and minimum maintenance; the system is invisible from the sea surface which does not disturb the ships; the turbine can be separated from the foundation support which means the turbine can be easily replaced for maintenance.

I.5.1.3 Clean Current Tidal Turbine (Canada) & TGL Turbine (UK)

Clean Current Power Systems (CCPS) is a pioneer in the development of hydrokinetic turbines with twelve years of experience in this field. From 2001, it has begun the research and development of an underwater ducted turbine. During 12 years of researches, it has built and

tested four prototypes. Between 2003~2004, two of them were deployed and operated safely at a 200 m reserve at the Institute for Ocean Technology in St. John's, Newfoundland. One third scale Clean Current machine with 6 meters in diameter, 65 kW rated power was the first tidal turbine installed in Canada, on the Race Rocks Ecological Reserve in September 2006 (see Fig.I.22). It still focuses the tidal turbines for water depth of 25 m or less. Until now, it continues its leading ship in the development of technologies for in-stream turbine electricity generation devices and other applications.

The Clean Current Turbine contains a bi-directional ducted horizontal axis turbine with a variable speed Direct Drive Permanent Magnet Generator (DDPMG). The duct design increases power output by up to 40% as compared to unducted turbines. The only moving part-turbine blades would enhance the stability. Moreover, the rotor disks and generator are adapted to be removed as a modular unit such that maintenance and replacement is easily facilitated. As a result, the bearing seals will be replaced every 5 years and the generator will be overhauled every 10 years. The service life of turbine generator is 25~30 years [12] [39].

In 2009, Alstom had signed a licensing agreement with CCPS, with the goal of bringing its first commercial tidal power products to market by 2012. But, effective 15th November, 2012, both companies have decided by mutual agreement to terminate their agreement. Then, in 2013, Alstom completed the acquisition of Bristol-based Tidal Generation Ltd (TGL), which was established in 2005. In September 2010, TGL developed a 500 kW tidal stream turbine – Deepgen – which was successfully deployed and connected to the grid at EMEC's tidal test site at the Fall of Warness in Eday Fig.I.23. In March 2012, TGL announced that the device had generated over 200 MWh into the national grid since installing their device on site [30].

Fig.I.22 Clean Current Turbine [40]

Fig.I.23 Deepgen turbine [30]

I.5.1.4 Open-Centre Turbine (Ireland)

Established in 2005, Dublin-based OpenHydro Group Ltd is an energy technology company which designs and manufactures marine turbines to generate renewable energy from tidal streams. OpenHydro has signed an agreement (CRADA: Cooperative Research And Development Agreement) with the U.S. Navy which gives the company access to Carderock's world-class design and engineering facilities plus highly experienced personnel to design the

turbine. Until now, there are 4 prototypes having been developed and tested in Palatka, Florida. In 2007, they have deployed the first turbine (6 m in diameter), rated at 250 kW, firstly using the tidal test site at the Fall of Warness off the island of Eday, at EMEC (European Marine Energy Centre) in Orkney, Scotland (see Fig.I.24.a). It is also the first successful system to generate electricity from the marine current and to connect to the UK National Grid. Moreover, it has successfully demonstrated a method of safely and economically deploying and recovering turbines directly on the seabed.

All the OpenHydro turbines have a high solidity horizontal axis rotor with symmetric, fixed pitch blades. The rim driven structure which has been already studied for ship propulsion is used. It has only one slow-moving rotor and lubricant-free construction which permits the minimization of maintenance requirements. The alignment of the rotor to the flow is fixed (no yaw control). Power generation is accomplished by a variable speed, DDPMG incorporated into the enclosing shroud. The center section of the rotor is open. The turbine is secured to the seabed by a tripod gravity base [12] [41] [42].

In 2007, agreements for tidal farm deployments were announced which aims to deploy four 16 meters in diameter, 2 MW rated power tidal turbines in Paimpol-Bréhat (Côtes-d'Armor), Brittany-the first marine current park in France (Cooperation between EDF and OpenHydro). The first turbine of this project has been tested in the Bay of Douarnenez on August 31, 2011(see Fig.I.24.b).

a) 25 kW prototype turbine b) 2MW tidal turbines with EDF

Fig.I.24 Open-Centre Turbine [43]

I.5.2 Vertical Axis Turbine

For vertical axis turbines (cross flow turbine), water stream flow is perpendicular to the rotational axis of the turbine as shown in Fig.I.25.

One of the most interesting characteristics for the vertical axis turbine is the independence of the direction of the flow, which is an advantage in extracting marine current energy from any direction. Furthermore, it can be much more easily applied at any specific site than horizontal axis turbine, since vertical axis turbine has more freedom to change its height and the radius. However, there is one need of a larger area for installation, and if cavitation occurs the whole

blade will be affected instead of just the tip for horizontal axis turbine. The major problems associated with the vertical axis turbine are high torque fluctuations with each revolution and no self-starting capabilities [12] [30] [32] - [35].

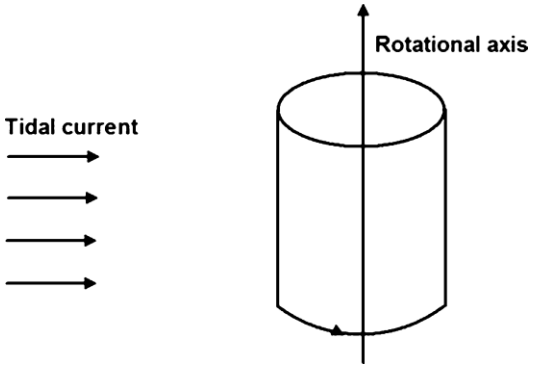

Fig.I.25 Vertical axis turbine [32]

The design of vertical axis turbine varies more than the horizontal axis turbine, including Savonius, Darrieus and H-rotor models (see Fig.I.26). Most of these designs have been successfully applied to the wind power industry. They extract energy from the tides in a similar manner to the horizontal axis turbine; however, the turbine is mounted on a vertical axis. It can transfer the mechanical torque to the water surface directly without the complex transmission systems or an underwater nacelle.

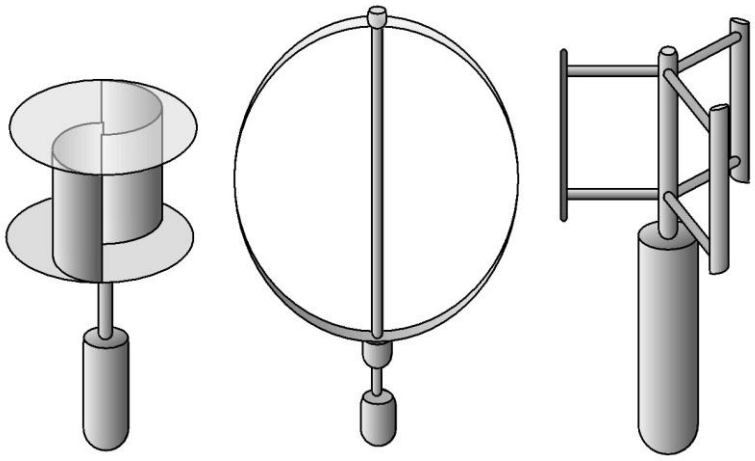

a) Savonius-Rotor b) Darrieurs-Rotor c) H-Rotor

Fig.I.26 Three different types of vertical axis turbines [44]

Several vertical axis turbines have been designed and tested for their feasibility in commercial applications. Some projects based on these three types will be showed in the following sections.

I.5.2.1 Savonius-Rotorv (Malaysia)

Fig.I.27 Savonius-Rotor model [45]

According to our literature, there are not many organizations who research the Savonius-type turbine for marine current energy except the Department of Marine Technology, Universiti Teknologi Malaysia. In section I.4.5, the target marine current velocity is an average of 2.5 m/s with a maximum of 4 m/s, however, Malaysia's ocean has a low current velocity averaging 0.56 m/s, which is much below this working velocity which is available for current energy devices presently. In [45], in order to overcome this velocity limitation and design a suitable device, Savonius-Rotor turbine, which has been already used for wind energy application, was proposed and researched. The laboratory experiment was carried out in the towing tank facility in Marine Technology Laboratory at Universiti Teknologi Malaysia (see Fig.I.27).

I.5.2.2 Gorlov Helical Turbine (USA)

Darrieus rotor in marine currents, named after the French engineer Georges Darrieus who patented the design in 1931, has the same principles as the land devices. Some researches have been done in [46]; up to 56% high efficiency has been found for this kind of turbine, although it is not clear how such efficiency was reached. The Darrieus turbine also offers the advantage of a higher operating tip speed ratio compared to a drag device such as a Savonius rotor. This makes it easier to integrate with a generator and a lower gear ratio is possible. However the conventional Darrieus turbine suffers from self-start problems at lower flow speeds (such as marine current speed) due its discrete blade angles and low starting torque.

Among all the vertical axis turbines, Gorlov Helical Turbines, based on the Darrieus rotor concept, have the best performance which was invented by Alexander Gorlov in 1995. Regardless of the marine current direction, the Gorlov Helical Turbine always rotates in the same direction which simplifies design and allows exploitation of any direction tidal power to provide a higher energy conversion, with approximately maximum 35% of the energy extraction efficient. There are two mainly advantages of the helical blade: it improves the self-start of the turbine

compared to Darrieus turbine; it reduces the torque oscillation during rotation [23] [32] [47]. A diagram of a four-bladed turbine is shown in Fig.I.28.

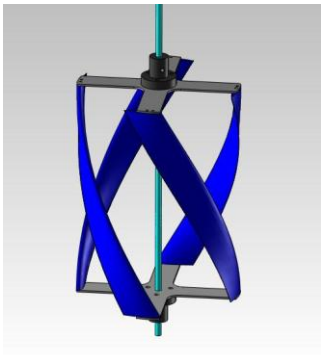

Fig.I.28 Helical Gorlov Turbine [47]

Fig.I.29 Helical Gorlov Turbine projects[48]

The test of the prototype Gorlov Helical Turbine using three twisted blades developed by GCK Technology Inc which is based in the USA, was performed in Amesbury, Massachusetts, in 2004. This was in partnership with Verdant Power. During the test, a small turbine generated up to 0.8kW in currents of 1.5 m/s. On July 10, 2002, a 10 KW 1 m in diameter turbine was also tested in Uldolmok Strait, South Korea (see Fig.I.29). With the successful tests, the Korean Ocean R&D Institute began work on a 1 MW plant based on the larger turbine. Gorlov Helical Turbines have been also deployed in Maine, New York, and Brazil. The turbine in Maine, developed by ORPC (Ocean Renewable Power Company), USA, in September, 2012, is so called OCGen Turbine Generator Unit. It has a rated capacity of 150 kW [49] - [52].

I.5.2.3 Enermar Project (Italy)

H-Rotor is very similar to Darrieus-Rotor. The only difference is that the long blades of the common Darrieus design are replaced by straight vertical blade sections attached to the central tower with horizontal supports. The project which uses the H-Rotor turbine technology - Kobold Turbine is called Enermar Project. It was launched in 2001 in the Strait of Messina, financed by Ponte di Archimede S.p.A., the Sicilian Government and the European Union. In 2006, with the help of INSEAN (Italian National Institute for Naval Architecture Studies and Testing), this system became the first turbine to be connected to the Italian national grid.

This system which consists of a support platform and the Kobold Turbine has been moored by four anchoring blocks where the water depth is 18~25 m (see Fig.I.30). It is located in the Strait of Messina where is along the Sicilian coast with an average marine current of about 2 m/s. The platform, designed by the Ponte di Archimede S.p.A, houses gearbox, a 160 kW Permanent Magnet Synchronous Generator (PMSG). The Kobold turbine (6 m in diameter, equipped with three blades with a span of 5 m) is placed under the platform. The turbine has been developed by Department of Aeronautical Engineering (DPA) at the University of Naples. This system has a rated power of 160 kW at 3.5 m/s current speed implying 25% efficiency [27] [49]. In [53] and

[54], 18 kW induction generators (by University of Messina) and 160 kW direct-drive permanent magnet generators (by Uppsala University) are also proposed for this project.

Starting from 2004, United Nations Industrial Development Organization (UNIDO) finalized a project aiming at promoting and disseminating in selected developing countries the use and application of the Kobold turbine. Subsequently 3 Asian countries (Republic of China, Indonesia and Philippines) became involved in the Kobold project. Right now, the optimal site analysis for these three countries carried out by UNIDO has been finished. Later, three new prototypes would be installed in these countries.

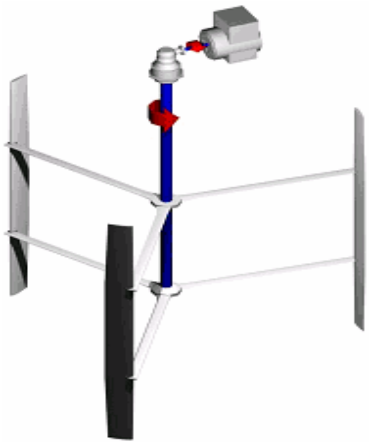

Fig.I.30 Enermar Project [12]

I.5.2.4 Blue energy project (Canada)

The Blue Energy Project, by Blue Energy Canada Inc. (BEC), has 4-blade H-rotor turbine mounted in a duct structure marine caisson which connected variable speed direct drive permanent electrical generator to convert the kinetic energy (see Fig.I.31). This duct structure is very different from that of Enermar Project in Italy and can increase the marine current speed for the turbine. The foundation of this system will vary depending on the site selection: gravity mounted on a crushed rock substrate or mooring in the sea by anchoring to the ocean floor.

From 1982 to 1987, the company's predecessor Nova Energy has developed 4 prototypes (20 kW Free Stream Turbine B1, 100 kW Hydro Dam turbine B2, 4 kW VEGA 1 in the Gulf Stream, 5kW Tor 5). Most of this work was carried out by the research grants from the National Research Council of Canada (NRC). In March 2006, BEC has signed a collaborative research with University of British Columbia to develop computer simulations of the previous turbine tests with the NRC. This collaboration also needs develop an experimental tank in order to provide data from a physical model to validate the numerical simulations.

BEC is currently designing a 1 MW turbine to be installed in Scotland. This will be expanded to a 10 MW capacity with the addition of three 3 MW turbines. These systems are considered to operate with marine current speed up to 5 m/s. Moreover, it is also designing a Midrange Power System for remote communities, such as in the Philippines, using two 250 kW turbines which

might be deployed in three to four years. For large scale power production, BEC has a concept design that multiple turbines are linked in series to create a tidal fence across an ocean passage or inlet [12] [23] [49] [51] [52] [55] - [57].

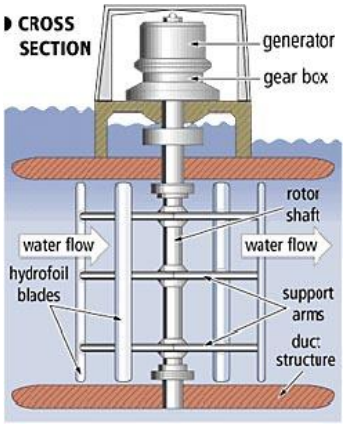

Fig.I.31 Blue energy project [57]

I.5.3 Oscillating Hydrofoil

The oscillating hydrofoil induces hydrodynamic lift and drag forces due to a pressure difference on the either side of hydrofoil section which is caused by the relative motion of the tidal current over the section. These forces induce tangential force to the fixing arm to make a large wing hydroplane moves up and down or a whale's tail hydroplane moves left and right. These motions can drive reciprocating hydraulic rams pump, high pressure hydraulic fluid to run a hydraulic motor and electrical generator. There are not many existed system using this technology in marine current energy. Normally, it is used for wave energy extraction [12] [30] [32] - [34]. In this section, two projects with different movements will be presented.

I.5.3.1 Stingray turbine (UK)

The Engineering Business Ltd, a Newcastle (UK) based company, with funding from the DTI, developed the "Stingray" concept oscillating hydrofoil as a prototype marine current turbine in Fig.I.32. The Stingray concept is an unusual design compared to the conventional technologies, with the similar principles of operation of "Stingray" moving up and down. It consists of variable-pitch oscillating hydrofoil, similar to an aeroplane wing, to transform kinetic energy from the marine current into hydraulic power and generate electrical power. The hydrofoil is attached by an arm to the fixed seabed-anchored base, which allows the hydrofoil to move vertically. This makes it to be suitable typically in any water depth up to 100 meters where avoid most damaging effects of waves.

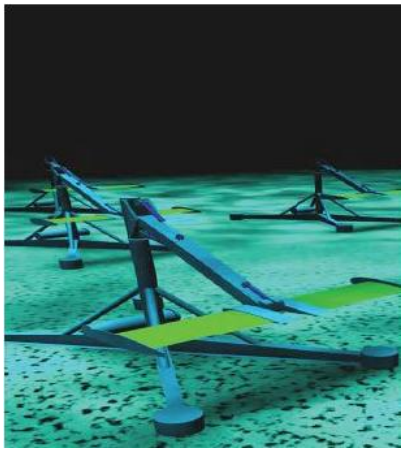

a) Design of Stingray turbine [23]

b) 150 kW prototype Stingray [12]

Fig.I.32 Stingray turbine

The first phase of this project started in 2001, involving mathematical and physical modeling and the design of a 150 kW prototype for sea trials. This demonstrator is predicted to produce the equivalent of between 300 MWh and 500 MWh over one full year. This would be sufficient for about 80 to 130 homes and is equivalent to about 0.2% of electricity consumption on Shetland. In August 2002 the prototype was completed and was installed in September 2002, in Yell Sound, off the Shetland Islands in UK. However it remained submerged for only 12 days. Investigation and analysis of data led to some device refinements and the reinstallation of the device in 2003, in Yell Sound, operating for 53 days. During these tests, it proved to achieve a mean hydraulic power of 85.4 kW in an average current speed of 2 m/s over a 30 minute period and produce 250 kW at peak capacity with averaged 90 kW in a 1.5 m/s measured marine current speed during its initial power cycles. This unit did not seem to have any significant environmental impact and the projected future cost of electricity by a commercial 100 MW farm is 0.1 €/kWh.

Engineering Business Ltd then planned the construction of tidal farms formed by machines of 500 kW rating. However, in the absence of appropriate further funding and the inflated development costs of this device (total costs expended to be £1.87 million.), Engineering Business Ltd has declared to suspend this project and no longer developing this technology [12] [23] [27] [49] [52].

I.5.3.2 BioSTREAMTM system (Australia)

BioPOWER systems, located in Australia, created one new design of marine current power generation which is somewhat like vertical-hydrofoil version of the Stingray in UK. This concept is based on the movement of the shark tail which has managed to become 90% efficient in transferring power to energy. Due to the single point of rotation, BioSTREAM^{TM} can align with the flow in any direction, and change the pitch slowly when the marine current past the caudal

fin device to make arm sway back and forth to drive a generator in the base of the system (see Fig.I.33). Power is accomplished using a system of gears and a flywheel connected to generator.

Right now, a 250 kW BioSTREAM^{TM} scale project is still in development. The system will be used to deliver from 50 kW up to 250 kW, depending on the demand required and location conditions [12] [49] [51] [58].

Fig.I.33 Prototype device of bioSTREAM^{TM} system [58]

I.5.4 Other Designs

Some special projects and concepts will be presented in this section.

- Flumill Power Tower (Norway)

Flumill AS, a Norwegian renewable energy company, has developed a special system Flumill Power Tower based on Archimedes Screw for marine current energy. It is described as fully patented, robust, environmentally friendly and economically viable, and can harvest electrical power from the natural flow of water. This system can be also used without buoyancy chambers and mounted horizontally (see Fig.I.34).

This system has gone through a multitude of CFD (Computational Fluid Dynamics) simulations as well as extensive tank, tow and pilot tests. Flumill AS has also successful carried out tow testing performed over two weeks in 2011, and EMEC testing in Orkney, Island, from September 2011 to January 2012 (see Fig.I.34). Thanks to the NOK 57.5 million partial funding from Enova in the autumn of 2012, Flumill's next step is to deploy a fullscale pilot in Rystraumen, near Tromsoe in northern Norway. Moreover, a fully commercial tide park is planned for the UK in 2014-15 [59].

Fig.I.34 The Flumill tidal system (2 MW) [59]

- Tidal Kite (Swedish)

A tidal kite is tethered to the sea bed and carries a turbine below the wing. The first tidal kite was developed by Swedish company Minesto. They have constructed the first 1.4 m wingspan sea trial prototype in Strangford Lough in Northern Ireland in the summer of 2011. The kite is tethered by a cable to the sea floor and then "flies" in the sea water. It swoops round in an 8-shaped trajectory by a rudder to reach a speed ten times the marine current speed. In 2013 the Deep Green pilot plant began operation off North Ireland. The plant uses carbon fiber kites with a wingspan of 8~14 m (26~46 ft). The 8 m carbon fiber kite has a rated power of 120 kW at 1.3 m/s. The 14 m wingspan has a rated power of 850 kW at 1.7 m/s. The company wishes to develop a 3 MW array in 2015.

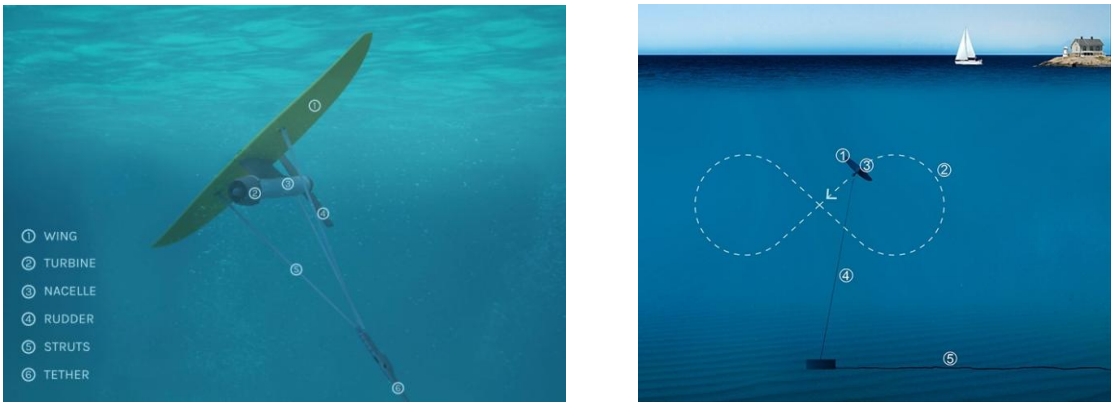

a) Tidal Kite structure b) Movement of Tidal Kite

Fig.I.35 Tidal Kite [60]

The kite doesn’t sink in the water as the neutral buoyancy. Each device is equipped with a gearless turbine to generate electricity which is transmitted by the attachment sub-sea cable to a transformer and then to the electricity grid (see Fig.I.35) [60].

I.5.5 Support Structure

The support structure of MCECS is considered as one crucial component when designing the overall system. It must bear its own weight but also withstand the harsh operating conditions. All the systems presented to date can be either seabed-mounted (fixed to the seabed) or moored (hanged from floating platform or seabed) structures (see Fig.I.36). The choice of suitable

support structure highly depends on depth, unit size, the seabed material and the economic considerations. The principle variations are shown in Fig.I.37 [4] [23] [25] [30] [33] [61].

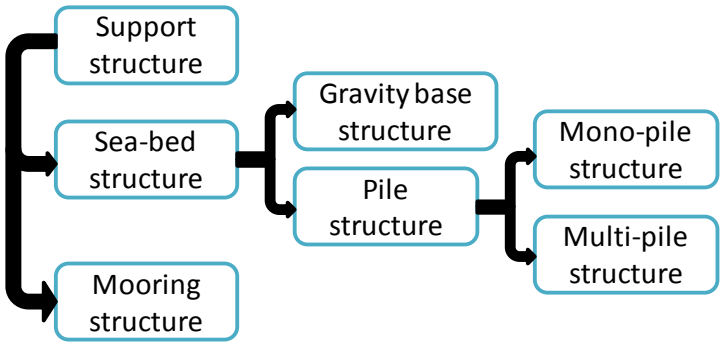

Fig.I.36 Classification of support structure

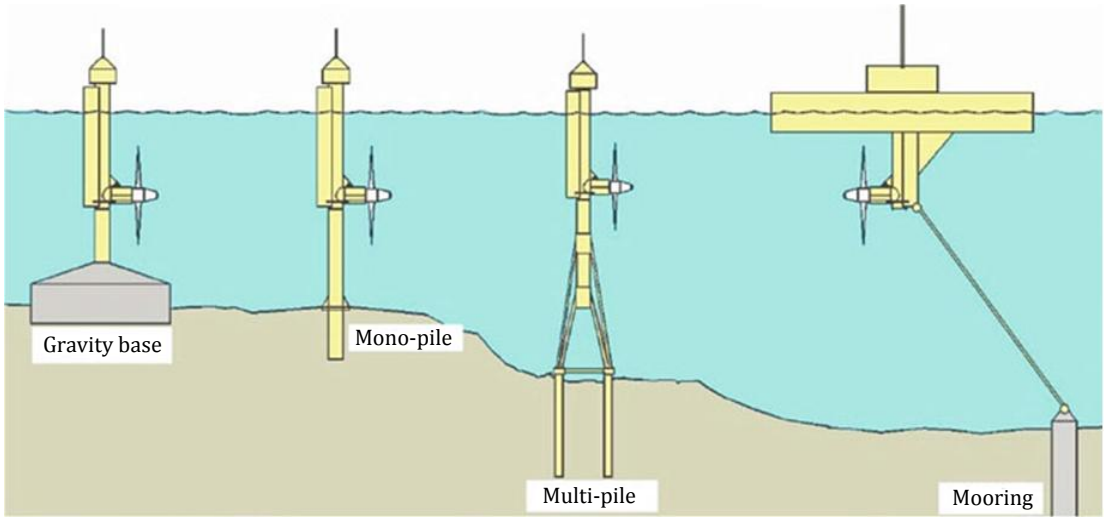

Fig.I.37 Structure concepts for marine current turbine [32]

I.5.5.1 Gravity Structure

A gravity structure primarily consists of a large steel or concrete base and column attached to the seabed. The seabed needs to be prepared for installation. The gravity structure composed of steel has the advantage of ease of production, transportation and installation, but is susceptible to scouring. As this structure may be made of either steel or concrete and achieve stability by its own weight, it must be more massive than the other options. According to the literature, Lunar Energy Ltd has used this structure with one three-leg gravity foundation for rotech tidal turbine (see Fig.I.38) [62] [63].

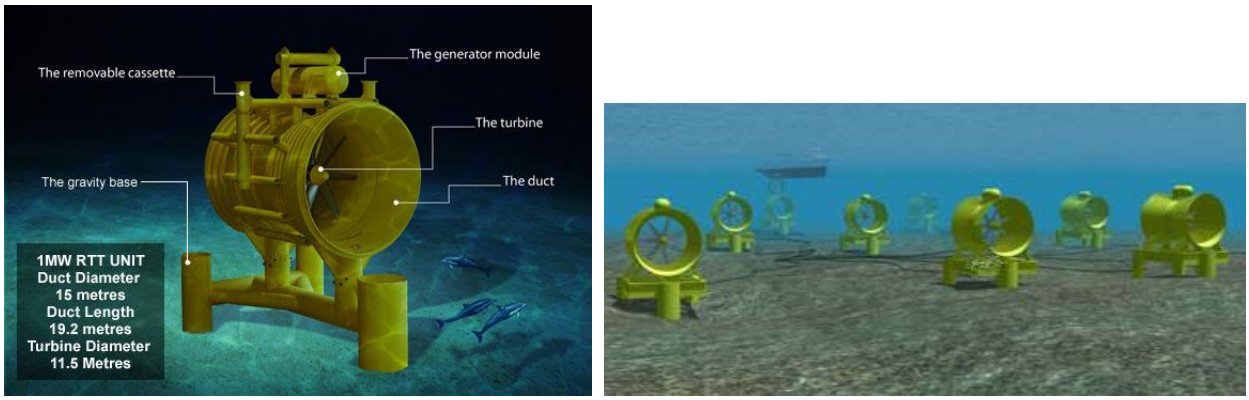

Fig.I.38 Rotech tidal turbine (Lunar Energy Ltd, 2011) [62]

I.5.5.2 Pile Structure

The principle of this structure is very similar to that used to most large WECS, whereas the device will be attached to one or more steel or concrete piles penetrating the seabed. The piles are fixed to the seabed by hammering if the ground conditions are sufficiently soft or by pre-drilling, positioning and grouting if the rock is harder. The simplest form of this structure is a single pile penetrating the seabed with the turbine fixed to the pile at the desired depth of deployment. The pile may stick out on the water surface or below. Horizontal axis turbine will often be suitable to use this structure.

Essentially, there are two variations for pile structure: mono- and multi- pile structure.

Mono-pile structure (20~30 m depth) is the most interesting choice right now. It consists of a large diameter hollow-steel beam driven 20~30 m into the seabed for the water depth less than approximately 30m if surface piercing structure is considered. The major advantage of this structure is that no preparation of the seabed is needed. The first pilot project, Seaflow, has just used this structure (see Fig.I.6).

In deeper waters, the systems have more interesting in a multi-pile structure rather than a mono-pile, which increases the costs but allows the use of a larger and more powerful turbine giving a greater energy capture capability. Multi-pile structure (30~60 m depth) is anchored to the seabed using steel piles driven approximately 10~20 m into the seabed according to the seabed condition at each corner. This structure would be applicable for surface piercing designs in greater water depths (perhaps 50 m), but it will be considerably much more expensive. The major advantages of multi-pile structure are the reduction in structural loadings by comparison with other structures and the possible corrosion reduction due to a reduction in leg diameter. Seagen, the first commercial project, has adopted this scheme (see Fig.I.19).

I.5.5.3 Mooring Structure

This structure provides a more reliable solution for the deep water condition. It is clearly much more easily towed to site or removed for maintenance or repair; what's more, it is also not so sensitive to variations in the depth of water at different locations which is an excessively big problem for the build and install of the seabed mounted structure in deeper water.

There are three options for it. Firstly, a conventional chains or wires or synthetic ropes system fixes at the seabed by drag, pile or gravity anchors. The second option is a taut line mooring using light weight fibre ropes attaching to the barge hull. In each of these two cases, 4 to 6 lines should be considered. The last option is one or more turbines mounted to a single platform, which can move in relation to changes in sea level.

I.5.5.4 Conclusion

Normally, the seabed mounted structure is preferred for shallow water as it will be relatively simple and cheap to install, and this structure is generally more solid than mooring structure due to the dynamic wave problem. Since piercing structure can solve a number of problems, in particular enabling deployment and maintenance of the turbine form the surface, the seabed mounted structure located in shallow water is also considered to adopt this structure. The expected depth limit for this system will be between 30m and 50 m, depending on many factors such as seabed material and surface, current speed, wave climate, etc. However, If all the systems in the marine current farm are using this structure, this area will be designated an exclusion zone for all shipping.

For the water deeper than 50 m, either totally submerged seabed mounted, or mooring structure, are the interesting selections. Generally, a turbine even in deep water still needs its relative high rotor as 75% of the marine current energy is typically to be found in the top 50% of the flow. Some researchers have proposed some special design for some specific site with deep water: there is first MCECS for the depths of 20~40 m, and between 40 m and 80 m for second device (see Fig.I.39).

However, increased depth does not only mean higher installation costs, but also leads to significantly higher forces on the structure. Experience has showed the difficulties of deploying an MCECS in intense currents and great depths. The ideally depth of water needs to be in excess of about 15 m at low tide and probably no more than 40 or 50 m at high tide. The minimum level will accommodate a rotor of about 10m diameter. The seabed mounted structure technology using mono or multi-piles is more mature, and carries fewer uncertainties than using floating moored devices [20] [26] [35].

Fig.I.39 Artists impression of the 4 MW Pentland Firth design at a depth of 60 m and a 20 m rotor for power generation [7]

I.6 *Electric Generator in MCECS*

As presented in section I.4.5, normally, the speed of the marine current can rarely exceed 5 m/s and the target marine current velocity is an average of 2.5 m/s with a maximum of 4 m/s. As a result, lower current velocity leads to lower turbine speeds. Therefore, if conventional generators such as Induction Generator (IG), Doubly-Fed Induction Generator (DFIG) and PMSG are used to produce electricity, a use of a gearbox is necessary to achieve relative higher rotor speed, and this can cause a maintenance problem in the future. However, if special low speed generators are used, generators can be directly connected to the turbine. This means that the generator and the turbine have the same axis rotation speeds.

Right now, much of the technology which has been suggested for the extraction of marine current energy is the same that used for wind applications. It is then obvious that some wind electrical generator topologies could be used for marine turbines.

The existing marine current systems can also be divided into two kinds: Geared Drive Train System including IG and PMSG, and Direct Drive Train System based principally on synchronous generators.

I.6.1 Geared Drive Train System

It consists of a low speed shaft which is connected to the turbine, a gearbox and a high speed shaft to transfer the mechanical torque to the classical generator. As discussed in section I.4.7, the MCECS will operate submerged in water and is not easily accessible. The maintenance for the system will be a big technology challenge. Thus the remote operation, fault diagnosis and condition monitoring will be essential for the system.

At present, there are no enough related documents of the experiment for the MCECS maintenance, but some references for the wind turbine can be used. The use of gearbox: will add to the volume of MCECS, generate additional noise which may affect the marine benthos nearby, increase mechanical power losses and bring regularly maintenance to avoid MCECS failures. For a typical wind turbine, 20% of the downtime is due to gearbox failures, and an average gearbox

failure takes about 256 h to repair [1]. And furthermore, the price of the gearbox will take up to 30% of the total price (see Table I.7).

Table I.7 Items covered in the rotor/nacelle costing exercise [4]

Assembly	Item	Qty	% Of Total Cost	Assembly Sub-Total
Rotor	Rotor blades	4	24%	
	Blade roots	4	4%	
	Rotor hub	1	6%	
	Rotor faring	1	1%	
	Sub-total:			35%
Drive train	Main shaft	1	3%	
	Seal assembly	1	1%	
	Main bearings	2	1%	
	Gearbox	1	30%	
	Generator	1	5%	
	Sundries (Couplings, cooling system...		3%	
	Sub-total:			42%
Nacelle	Nacelle body and fittings	1	8%	
	Sub-total:			8%
Electrical & control	Turbine controls/safety system	1	6%	
	Switchgear	1	9%	
	Sub-total:		15%	
TOTAL:			100%	100%

Although gearbox brings some price and maintenance problems, many companies prefer the mature technique used in wind system presently. So many manufacturers use the PMSG, IG, DFIG connected to multi-stage gearbox. In [64], a single-stage Gearbox Doubly-Fed Induction Generator (GDFIG) is presented.

I.6.2 Direct Drive Train System

In a direct drive train system, the generators are directly driven by the turbine hub or the turbine blades. It means the generator will rotate at a very low nominal speed in the range of 5~50 rpm (tr/min) depending on the turbine size, the current velocity and the site condition [65]. In order to compensate for the low rotation speed, generators with several poles are necessary to maintain the desired frequency. However, this will result in a large generator diameter [65].

The direct drive system will be more reliable, as it could reduce: overall system size and weight, the installation and maintenance cost, driven train, the mechanical components, eliminate the noise from the gearbox and minimize regularly maintenance requirements by avoiding mechanically complex systems with many moving parts, besides a flexible control method and quick response to marine current fluctuations and load variation. What's more, it will improve the overall efficiency due to the low cut-in speed and reliability [22] [65] [66].

Theoretically, the direct drive marine current generators are a low speed machines which do not differ much from the conventional generators types. In comparison with conventional high

speed generators, they have a much larger diameter, almost about the same efficiency and about the same total weight and, at present, a slightly higher price. The most important difference is that the low speed direct-driven generator makes a very high rated torque. This is an important difference, since the size and the losses of a low-speed generator depend on the rated torque rather than on the rated power [67].

Different low speed direct-drive generators have been proposed in the literature as: IG, Excited Synchronous Generator (ESG), Switched Reluctance Generator (SRG) and PMSG. While, based on the discussion in [67], SRG and IG have a low power factor leading to a large stator, and ESG is larger and less efficient than PMSG. Consequently, the PMSG is proved to be the most attractive choice for a direct driven system as its highest yield energy although more expensive price [1]. Basically, DDPMG can be divided into radial-flux, axial-flux machines and transverse flux machines, according to the flux direction in the air gap [1].

Several studies have been made about low speed electrical machines for the marine current generators. Some special DDPMG based on ducted structure are proposed by researchers. The Clean Current Tidal Turbine proposes one bi-directional ducted horizontal axis turbine with a DDPMG. Fig.I.40.a shows the 1 MW (3m/s) Clean Current turbine and Fig.I.40.b shows an axial segmented stator providing fault tolerance. Open-Centre Turbine which also called rim driven generator system support by Open Hydro Group Ltd has a circumferential generator with rotor attached to the blades and stator in the surrounding duct. Fig.I.41 shows the Open-Centre Turbine 250 kW prototype and the direct drive generator with an active part surround the blades [1] [68] [69].

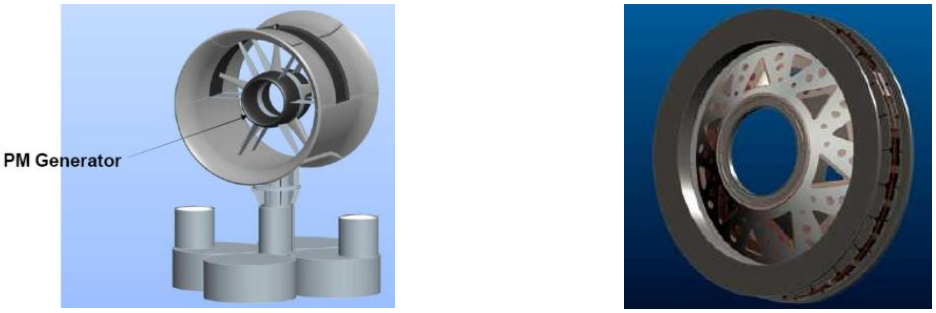

a) Clean Current turbine b) Clean Current generator

Fig.I.40 Clean Current Tidal Turbine

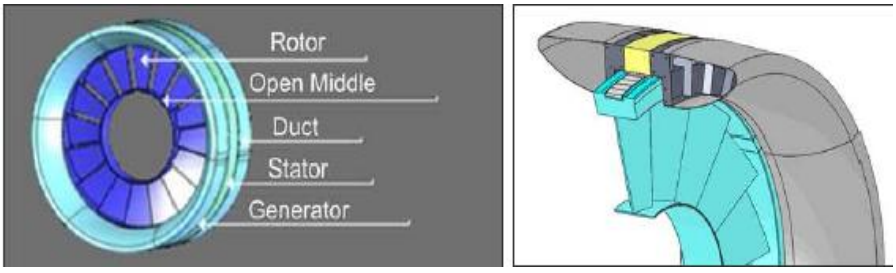

a) Open Hydro turbine b) Open Hydro generator

Fig.I.41 Open-Centre Turbine

Table I.8 briefly summarizes the advantages and disadvantages of the DDPM generators.

Table I.8 Advantages and disadvantages of DDPMG generator [1]

Advantages	Disadvantages
-Full speed range; -Complete control of reactive and active power; -Higher reliability & lower maintenance (Absence of gearbox and mechanical components); -No power converter for field; -Higher efficiency & energy yield; -Good thermal characteristics; -Simple and robust.	-Full scale power Converter; -Permanent magnets needed (expensive); -Multipole generator (big and heavy); -Larger diameter for more poles; -Demagnetisation at high temperature or due to high opposing magnetic field from armature winding

I.6.3 Conclusion

Table I.9 summarized the existing marine current systems: the generators divided into IG, PMSG and DDPMG [1] [70].

Table I.9 Marine current generators

Plan name/ Technology	Company/Organization	Generator Type	Rated Power	Status	Year	Turbine Type
SeaGen	Marine Current Turbines (UK)	IG	2*600 kW	O	2008	HV
SeaFlow	Marine Current Turbines (UK)	IG	300 kW	O	2003	HV
HS1000	Hammerfest Strøm (Norway & UK)	IG	1 MW	O	2011	HV
Enermar Project	Kobold Turbine INSEAN (Italy), Ponte di Archimede S.p.A. (Italy), Sicilian Government, European Union & UNIDO	IG	18 kW			VF
		PMSM	160 kW	O	2011	
EnCurrent Turbine	New Energy Corporation Inc (Canada)	PMSG	5 kW		2009-2010	VF
			10 kW			
			25 kW		2010	
			125 kW		2009	
			250 kW		2010	
CoRMaT	Energy Systems Research Unit at the University of Strathclyde (UK)	DDPMG	20 kW	O	2011	HF
Clean Current Tidal Turbine	Clean Current (Canada) & Alstom (France)	DDPMG	1 MW			HF
TGL	Tidal Generation Ltd (UK)	IG	500 kW	R	2010	HV
	Tidal Generation Ltd (UK) & Alstom (France)		1 MW	O	2013	
Open-Centre Turbine	OpenHydro Group Ltd (Ireland)	DDPMG	250 kW		2008	HF
	Nova Scotia Power (Ireland) & OpenHydro Group Ltd (Ireland)		1 MW		2009	
	EDF (France) & OpenHydro Group Ltd (Ireland)		2 MW	O	2011	
Tocardo	Teamwork Technology BV (Netherlands)	DDPMG	45 kW	O	2008	HF
			200 kW	O	2013	
C-GEN	University of Edinburgh & Scotrenewables Tidal Power Ltd (UK)	DDPMG	20 kW		undergo	HF
			600 kW			
Sabella D10	Sabella (France)	DDPMG	200 kW		undergo	HF
Gorlov Helical Turbine	Korean Ocean R&D Institute (South Korea)	IG	500 kW		undergo	VF
		PMSG				
	ORPC (US)	DDPMG	140 kW	O	2008	VF

Gorlov Helical Turbine	Korean Ocean R&D Institute (South Korea)	IG	500 kW			VF
		PMSG				
	ORPC (US)	DDPMG	150 kW	O	2012	
Blue energy	Blue Energy Canada Inc (Canada)	DDPMG	250 kW			VF
			1 MW			
RTT	Lunar energy (UK)	IG	1 MW		2009	HV
			1/20th scale		2004	
RTT 2000			2 MW			
SMD TidEl	SMD Hydrovision (UK)	PMSG	1 MW		undergo	HF
Ak1000	Atlantis Resources Corporation (Canada)	DDPMG	1 MW	O	2011	HF
HyTide 1000	Voith Hydro Ocean Current Technologies (German)	DDPMG	1 MW	O	2013	HF
HyTide 110-5.3			110 kW		2011	

IG: Induction Generator; PMSG: Permanent-Magnet Synchronous Generator. DDPMG: Direct-Drive Permanent-Magnet Generator; Speed: generator speed in rpm.
Status: O-Operation, R- Retrieve; Year: the year of installation; RTT: Rotech Tidal Turbine;
for turbine type: XY: X = (H: Horizontal V: Vertical), Y= (V: Variable pitch angle, F: Fixed pitch angle);

I.7 *Converter Topologies*

PMSG seems the most attractive choice for a direct-driven system; as a result, this section will present only the converter topologies for PMSG. The converter topologies for WECS and MCECS have almost exactly the same essence. A review of converter topologies used to PMSG in WECS is detailed in [23] [71] [72]. There are four mainly structures: thyristor supply-side inverter, hard-switching supply-side inverter, intermediate DC/DC (Direct Current) converter or Back-to-Back PWM (Pulse Width Modulation) converter. For these different structures, there are some different converter options and control schemes like shown in Table I.10. More details can be seen in [71].

a) Thyristor supply-side inverter (Fig.I.42.a)

This inverter has the advantage of low cost and maximises the output power of the converter by the continuous control of the inverter firing angle. However, an active compensator or a smoothing system is needed for the reactive power and harmonic distortion.

b) Hard-switching supply-side inverter (Fig.I.42.b)

In order to maximize the system's output power, a power mapping technique including the maximum power versus DC voltage characteristic is used. Furthermore, the control system is improved by using a derivative control on the stator frequency as it also changes with change in DC-link voltage. The control system is like the MPPT (Maximum Power Point Tracking) which maps the power generated to a reference power so as to set the operating DC voltage.

c) Intermediate DC/DC converter (Fig.I.42.c)

This structure is another design. Compared to the hard-switch topology, this structure is more flexible to both strong and weak AC systems. The inverter power control can be achieved by regulating the magnitude of the fundamental line current and the phase angle between line current and line voltage. The VSI is also switched at the frequency of the carrier signal to enable proper output harmonic definition. Also the shaft speed is matched to optimal values of the DC

Voltage and current according to the maximum power from the generator. The VSI controller can set the DC-link constant and vary the reactive power so as to maximise real power.

d) Back-to-Back PWM converters (Fig.I.42.d)

This structure is implemented with two 6-switch, hard switched converters and a DC-link capacitor. The generator side rectifier works as a driver controlling the generator torque, using a vector control strategy. In order to maximize the torque and minimize the Joule losses simultaneously, the direct-axis current will be held to zero. The MPPT provides the optimum rotor speed as a result of the marine current speed to the output power. The supply side converter controls the line current to the grid and the DC bus voltage.

Table I.10 Converter options for PMSG [71]

Structures	Converter Options	Control Schemes
Thyristor supply - side inverter	Diode bridge/SCR inverter / compensator	Simple firing angle control of one converter
	SCR rectifier/SCR inverter	Simple firing angle control of both converters
Hard-switching supply-side inverter	Diode bridge/Hard-switching inverter	Power mapping technique including stator frequency derivative control MPPT, marine current speed prediction control
Intermediate DC/DC converter stage	Diode bridge/DC boost/Hard-switching inverter	Vector control of supply side inverter DC Voltage control via chopper duty ratio
Back-to-back PWM converters	Back-to-back hard-switching inverters	MPPT, vector control of both converters
	Back-to-back hard-switching inverters (reduced switch)	Generator controlled through MPPT inverter current controlled through PI controllers

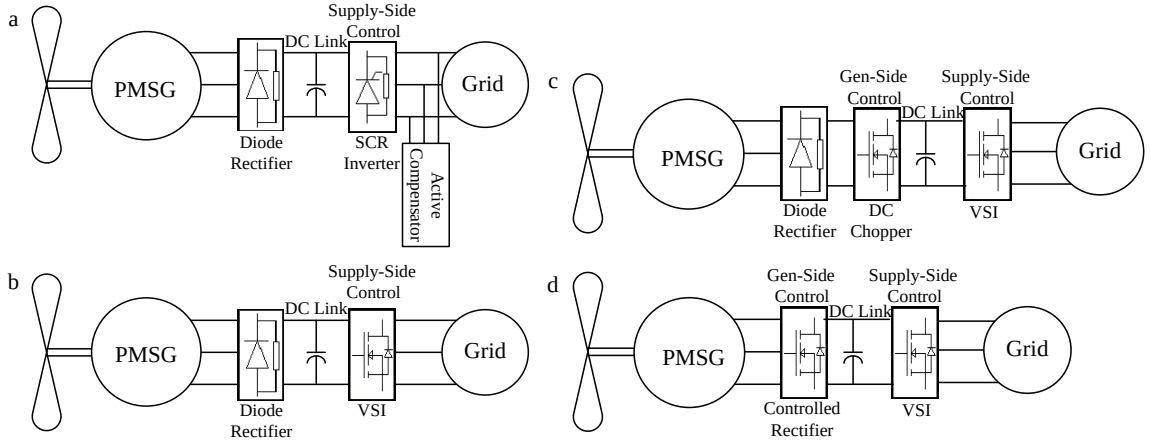

Fig.I.42 PMSG converter schemes

I.8 *Conclusion*

This chapter has summarized the state of art for marine current energy systems. It begins with the introduction of the energy situation right now for both conventional and renewable energies. Then, Ocean energy forms and especially marine current energy are presented, as well as their major advantages and disadvantages. The emphasis has been put on marine current turbine

concepts and some well-known projects divided by the turbine concept. Finally, the electrical generators used in the mainly existed projects are listed and classified according to that there is the gearbox or not.

Next chapter concerns the modeling of the marine current system based on a low speed generator.

Chapter II

Modeling of the Marine Current Energy Conversion System

NOMENCLATURE

V_{tide} Tidal current velocity (m/s);

ρ Density of the ocean (1024 kg/m^3);

A Cross section of the MCT (m^2);

P_{hyd} Hydrodynamic power from marine current (W);

C_p power coefficient Betz's coefficient/Power coefficient

P_{mec} extractable mechanical power (W);

λ Tip Speed Ratio;

β pitch angle (rad);

R Radius of the turbine (m);

Ω Turbine rotational speed (rad/s).

a axial induction factor;

Ω Machine mechanical speed, it is equal to turbine speed (rad/s);

ω_e Electrical speed (rad/s);

f electrical frequency (Hz);

N_r Number of teeth in the rotor.

L_j Self-inductances in phase *j*, *j=a, b, c* or *o, d, q* (mH);

M_{ij} Mutual-inductances between two phases, *i* & *j=a, b, c* or *o, d, q, i≠j* (mH);

φ_{mj} PM flux-linkage components, *j=a, b, c* or *o, d, q* (Wb);

θ_e Electrical position (rad);

θ_m Mechanical position (rad);

Γ_{em} Electromagnetic Torque (Nm);

p Number of pole pairs;

$[L_s]$ Stator inductance matrix;

$[i_s]$ Current vector;

$[\varphi_m]$ PM flux-linkage vector;

Γ_r Reluctant torque or salient torque (Nm);

Γ_{pm}. Permanent magnet torque or "hybrid" torque (Nm);

P Active power (W);

Q Reactive power (VAR);

P_{em} Electromagnet power for DSPMG, PMSSG or PSPMG in abc or o-d-q frame (W);

T_3 Concordia and Park matrix;

$R(\theta_e)$ Park matrix;

R_s Resistance of each phase (Ω)

v_j Phase voltage (V);

i_j Phase current (A);

e_{mj} EMF induced on stator windings of each phase due to the magnet (V) without load.

P_{cu} Joule losses (W);

w_f Energy stored in the armature windings of DSPMG (J).

GLOSSARY

BEM	Blade Element Momentum;
BET	Blade Element Theory;
DDPMG	Direct Drive Permanent Magnet Generator;
DSPMG	Doubly Salient Permanent Magnet Generator;
FEM	Finite Element Method;
EMF	ElectroMotive Force;
FFT	Fast Fourier Transform
HAM	Harmonic Analysis Method;
MCECS	Marine Current Energy Conversion System;
MCT	Marine Current Turbine;
MPPT	Maximum Power Point Tracking
MT	Momentum Theory;
NACA	National Advisory Committee for Aeronautics;
PM	Permanent Magnet;
PMSG	Permanent Magnet Synchronous Generator
PMSSG	Permanent Magnet Smooth Synchronous Generator
PSPMG	Pole Salient Permanent Magnet Generator
SHOM	Service Hydrographique et Océanographique de la Marine;
TSR	Tip Speed Ratio;
VRM	Variable Reluctance Machine
WECS	Wind Energy Conversion System;

II.1 *Introduction*

As already presented above, Marine Current Energy Conversion System (MCECS) is very similar with Wind Energy Conversion System (WECS). The system extracts only one friction of the hydrodynamic energy by MCT and transforms it into mechanical energy. The rotating turbine drives the Direct Drive Permanent Magnet Generator (DDPMG) via the shaft to generate electrical energy. The energy will be finally injected to the grid through power electronic devices. The global system can be simply presented in Fig.II.1.

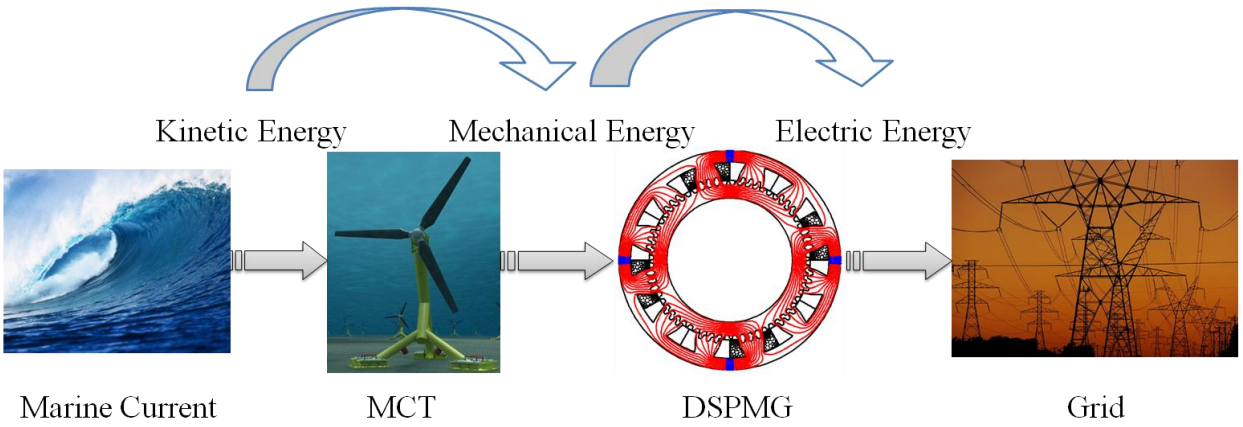

Fig.II.1 Global MCECS scheme

This chapter focuses on the modeling of a marine current energy extracting system. Firstly, some methods for modeling the marine resource (tidal current) will be briefly introduced. Secondly, an algorithm based on Blade Element Momentum (BEM) theory is used to approach a hydrodynamic turbine model which is suitable to design requirements. Thirdly, a model of a non-conventional low speed Doubly Salient Permanent Magnet Generator (DSPMG) will be developed. Matlab/Simulink® has been chosen to model and simulate the MCECS for our work.

II.2 *Marine Current Modeling*

Tide and marine current (tidal current) are periodically in motion. In fact, it is not easy to get the exact movement. In any hydrodynamic model for tidal current flow in a channel, there is a requirement for accurate water height data. For any subsequent resource evaluation and site capacity estimation there must be a large amount of data available (usually of at least 1 year). There are several methods to model the marine current such as Harmonic Analysis Method (HAM), practical model, Double Cosine Method, Tidesim, Tide 2D. The first two popular methods will be detailed in this section. More information for the other methods can be found in [20] [21] [23] [61] [73].

II.2.1 Harmonic Analysis Method

In the theory of the HAM method, the tide at any location can be divided into several tidal harmonic components (partial tides) and the tidal amplitudes and phases of each partial tide can be calculated according to the tidal observations.

Each single simple tide corresponds to an object called imaginary celestial body. So the whole tide caused by the tidal force due to the imaginary celestial bodies can be written as:

$$\xi = K \sum_j C_j \phi_j \cos(\sigma_j t + V_j) \quad \text{(II.1)}$$

Where: ξ is the height of the tide (m); σ_j is the Circular frequency (rad/s); t is time (s); V_j is the initial phase when t=0 (rad); K is a Common factor; C_j is the amplitude factor and ϕ_j is the latitude factor.

In [21] and [74], authors calculated elements of some primary harmonic tides, and then defined the names and the symbols of the 11 very important harmonic components to consider in the modeling of the resource:

4 semidiurnal partial tides: M_2 (Principal Lunar Semidiurnal Constituent), S_2 (Principal Solar Semidiurnal Constituent), N_2 (Large Lunar Elliptic Semidiurnal Constituent), K_2 (Lunisolar Semidiurnal Constituent);

4 diurnal partial tides: K_1 (Lunisolar Diurnal Constituent), O_1 (Principal Lunar Diurnal Constituent), P_1 (Principal Solar Diurnal Constituent), Q_1 (Large Lunar Elliptic Diurnal Constituent);

3 Shallow water constituents (due to the topography and effect of interference): M_4 (Lunar 1/4 Diurnal Shallow Water Constituent), MS_4 (Lunisolar 1/4 Diurnal Shallow Water Constituent), M_6 (Lunar 1/4 Diurnal Shallow Water).

Based on the ratio (F) of the sum of the amplitudes of the two main diurnal components (K_1 and O_1) to the sum of the amplitudes of the main semi-diurnal components (M_2 and S_2), the tides can easily be divided into three types, just as presented in section I.4.2: diurnal tide for F>3; semi-diurnal tide for F<0.25; mixed tide for 0.25<F<3 [21].

Based on equation (II.1), the tidal height can be also written in a short form as follows:

$$H(t) = H_0 + \sum_{i=1}^{m} A_i cos\,(\omega_i t + \varphi_i) \quad \text{(II.2)}$$

Where: $H(t)$ is the tidal height, H_0 is the mean sea level; A_i, ω_i and φ_i, are respectively the amplitude, the angular speed and the phase angle of every harmonic constituent. The amplitude and phase angle which are known as harmonic constants are unique for every location. While the angular speed (in degrees per solar hour) for each harmonic constituent is known from astronomical knowledge of the motion of the earth sun and moon. It is constant for all the sites.

Although this method always needs a large amount of data to determine the phase and amplitude of the most influential tidal constituents, one option which employs harmonic analysis of a 30-day tidal record is used to confirm the harmonic constants. Once these harmonic constants have been determined for each site of interest, a very accurate prediction of the tide at any time could be made by taking into account to the sum of the water height contributions from each constituent to the mean water level (see formula (II.2)).

For the angular speed, different harmonic constituents have their own speed, which are sums and differences of small integral multiples of 5 basic astronomical speeds which are known very accurately [21] [72] [75]. They are:

- T Rotation of the Earth on its axis, with respect to the Sun, 15 degrees/solar hour;
- H Rotation of the Earth about the sun, 0.04106864 degrees/solar hour;
- s Rotation of the Moon about the Earth, 0.54901653 degrees/solar hour;
- p Precession of the Moon's perigee, 0.00464183 degrees/solar hour;
- N Precession of the plane of the Moon's orbit, -0.00220641 degrees/solar hour.

This section will present the position of interest: Aberdeen, British site. The harmonic constituents, which are highly dependent on astronomy and geography, affected to harmonic tides for this site are presented in [21] [72] [76].

According to the parameters provided above, the equation to predict the tidal height can be summarized in equation (II.3).

$$\begin{aligned} H(t) = H_0 &+ A_{M_2}\cos\left(\omega_{M_2}t + \varphi_{M_2}\right) + A_{S_2}\cos\left(\omega_{S_2}t + \varphi_{S_2}\right) \\ &+ A_{N_2}\cos\left(\omega_{N_2}t + \varphi_{N_2}\right) + A_{K_1}\cos\left(\omega_{K_1}t + \varphi_{K_1}\right) \\ &+ A_{O_1}\cos\left(\omega_{O_1}t + \varphi_{O_1}\right) + A_{M_4}\cos\left(\omega_{M_4}t + \varphi_{M_4}\right) + A_{M_6}\cos\left(\omega_{M_6}t + \varphi_{M_6}\right) \end{aligned} \tag{II.3}$$

Based on the harmonic constant values, the tidal height prediction can be determined simply. The tidal height as a function of tidal hour in one year, 2011, was shown in Fig.II.2, in which it is easy to zoom in one moth prediction and several days.

Spring tides occur when M_2 and S_2 are in phase so that both height peak at the same time to cause greater tidal height range. If M_2 and S_2 are out of phase and tend to reduce tidal range, neap tides appear. The maximum tidal height range will happen when M_2, S_2 and N_2 are all peak at about the same time which is called perigean-spring tides. It will occur several times in one year [72].

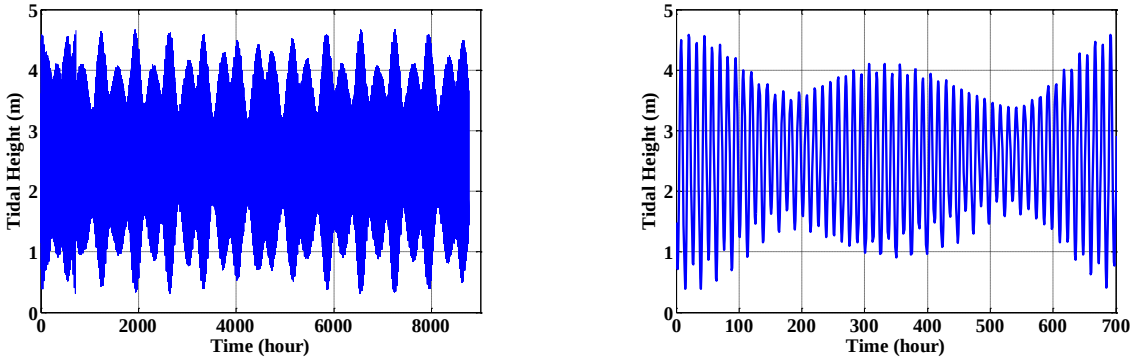

a) Tidal Height in one year

b) Tidal Height in one month

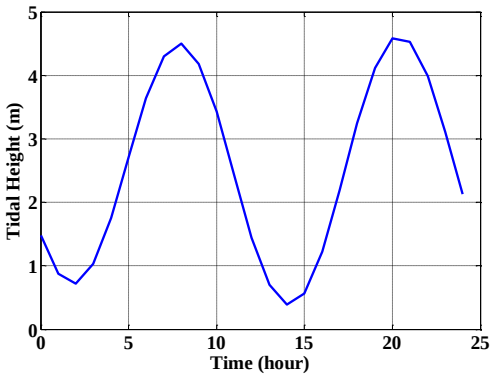

c) Tidal Height on one day

Fig.II.2 Tidal Height at Aberdeen, British, 2011

As the tidal height is predicted by the harmonic analysis mentioned above, it leads to develop the marine current (tidal current) velocity. Normally, tidal currents are reinforced in channels between land masses. Each channel is unique in terms of the width, depth and roughness etc. The basic premise of this channel model method is to take a real channel and idealize it into a simple mathematical model.

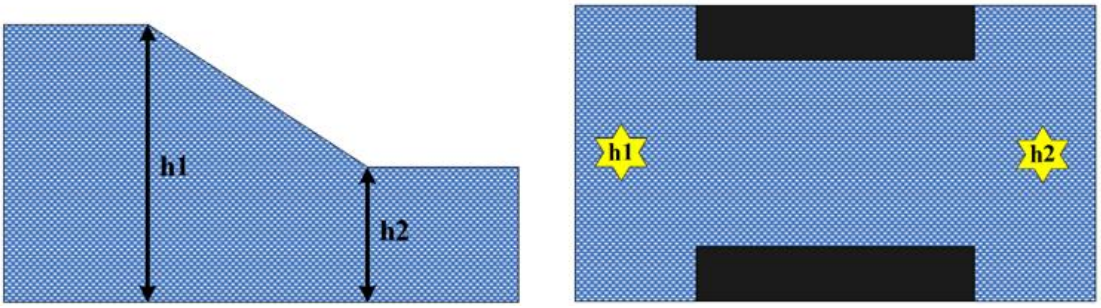

Side view Top view

Fig.II.3 Side view and top view of channel model [72]

According to Fig.II.3, the theoretical flow velocity V_{th} which would result from the pressure gradient caused by the head difference existing between two separate water heights is estimated in (II.4):

$$V_{th} = \sqrt{2g|h_1 - h_2|} \quad \text{(II.4)}$$

Where: g is the gravitational constant (9.8 N/kg), h_1 is the water height of 1st site (m), h_2 is the water height of 2nd site (m).

But, due to the Law of Conservation of Mechanical energy and taken into account the effect of material in the seabed as well as effect of channel blockage, the tidal current velocity equation can be written as [21] [23]:

$$V_{tide} = \cos\theta_f \, K_f K_Z \sqrt{\frac{2g|h_1 - h_2|}{1 + K_L + K_T}} \quad \text{(II.5)}$$

With

If h_1 >h_2, it is flood tide;

If h_1 <h_2, it is ebb tide;

K_L Effective loss coefficient due to the depth, width and roughness of the channel;

K_T Turbine coefficient which represented the number of turbines, swept area and channel cross-sectional area;

K_Z As presented in section I.5.5.4, 75% of the marine current energy is typically found in the top 50% of the flow. So marine current velocity will be a function of depth in the water:

$K_Z = (\frac{Z}{0.32h})^{1/7}$ for the bottom, 0<Z<0.5H; $K_Z = 1.07$ for the top, 0.5H<Z<H;

K_f Correction factor for ebb and flood, in this section, ebb correction factor is 1, and flood correction factor is 0.8;

θ_f Flow angle in flood and ebb tide face to MCT as the variation in the angles of the mean flow direction in ebb and flood.

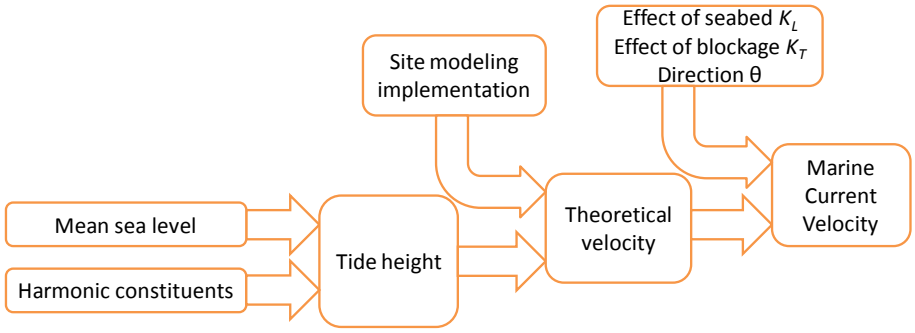

Fig.II.4 Marine current velocity calculation based on HAM

Fig.II.4 gives the process of calculating the tidal height and marine current velocity based on HAM. Fig.II.5shows the simulation results of the final marine current velocity for British site Aberdeen in September, 2011, based on HAM. The marine current velocity of certain month and certain day are presented in Fig.II.5.b and c.

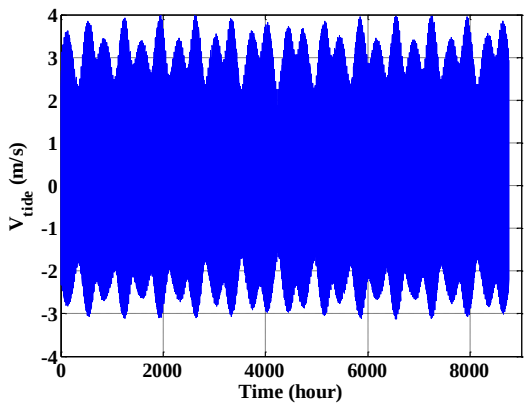

a) Marine current velocity in one year

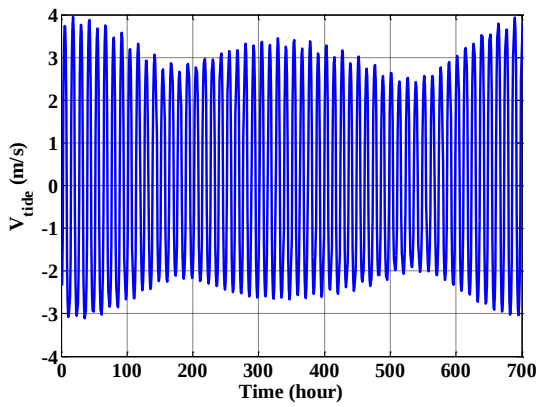

b) Marine current velocity in one month

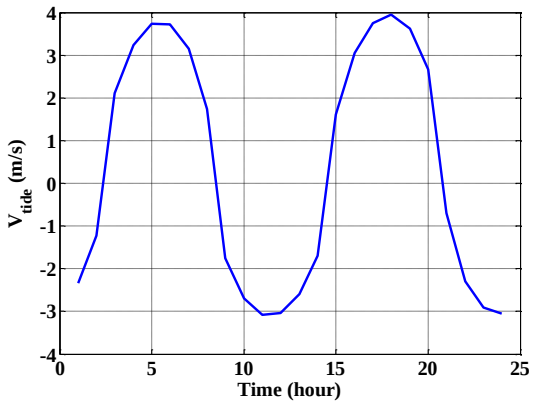

c) Marine current velocity on one day

Fig.II.5 Marine current velocity at Aberdeen, British, in 2011

This model highly depends on the harmonic constituents, as well as the assumption for the channel. The mainly advantage of this method is to calculate the velocity step by step. The obvious disadvantage is that the harmonic constituents of the interested position need to be required.

II.2.2 Practical Model

SHOM, which is Service Hydrographique et Océanographique de la Marine, in France, observes the tide motion for a long time and provides all the marine current data used in the practical model [12] [77]. This model needs the current velocities for spring and neap tides. These values should be given at hourly intervals starting at 6 hours before high waters and ending 6 hours after. Therefore, knowing tide coefficients, it is easy to derive a simple model for tidal current velocity V_{tide}. This equation is given by equation (II.6):

$$V_{tide} = V_{nt} + \frac{(C-45)(V_{st}-V_{nt})}{(95-45)} \quad \text{(II.6)}$$

Where: V_{nt} is the hourly intervals neap tide current velocities, V_{st} is the hourly intervals spring tide current velocities and C is tide coefficient which is defined by astronomic calculation of earth and moon position. In equation (II.6), 95 and 45 are respectively mean spring and neap tide medium coefficients.

This work will choose one site of interest: Penmarc'h, France, which is very near Saint-Nazaire, France. The hourly interval neap and spring current velocities are obtained from SHOM website [77].

Fig.II.6 gives the course of achieving the practical model step by step. The practical model is very simple. It only needs some interval current speeds and tide coefficients which can be gained from SHOM website. However, this method is based on a lot of observations carried out by SHOM, and is more experimental.

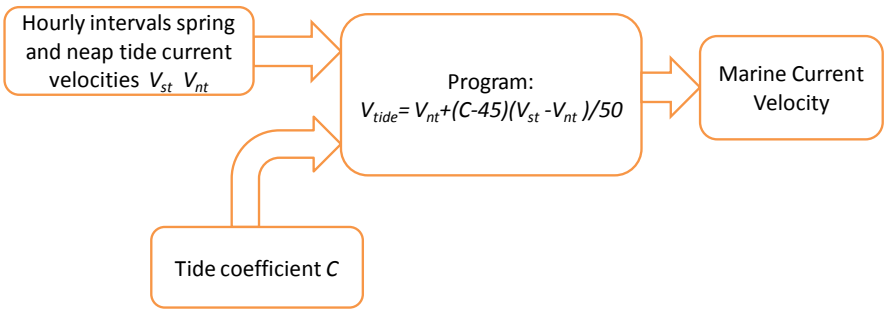

Fig.II.6 Calculate marine current velocity using the practical model

Fig.II.7 a, b and c show respectively the tide velocity at Penmarc'h, in France, for the whole year (2011), for one month (September) and only one day (1st September, 2011), using the practical model.

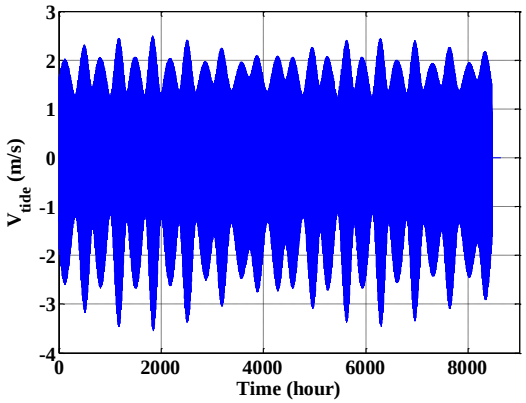

(a) Marine current velocity in one year

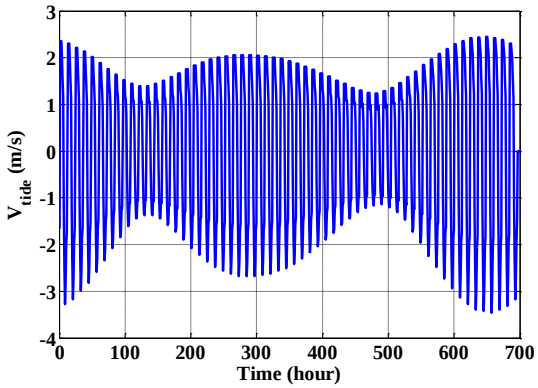

(b) Marine current velocity in one month

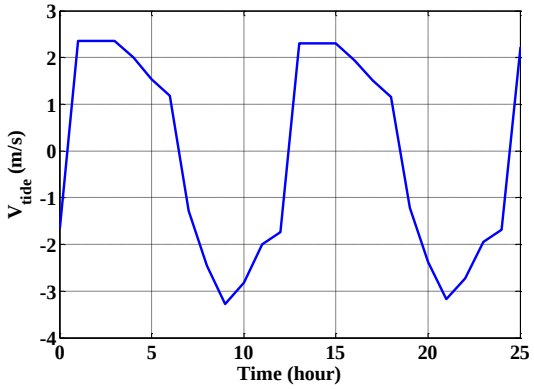

(c) Marine current velocity on one day

Fig.II.7 Marine current velocity at Penmarc'h, France, in 2011

Table II.1 illustrates the resulting estimated extracted power at Penmarc'h, based on the tide coefficients from 2009 to 2011. The marine current energy doesn't have many differences during these 3 years.

Table II.1 Marine current energy for 2009-2011

Year	Power(KWh)	Percentage
2009	$1.4892*10^5$	1
2010	$1.5380*10^5$	+3.28%
2011	$1.5721*10^5$	+2.21%

II.2.3 Conclusion

This part presents the common used methods for modeling the marine current resource: HAM and the practical model.

HAM can easily calculate the height if we know the basic astronomical coefficients for the interested position. With the help of assumptions for a simple mathematical channel model, the current velocity of this imaginary channel can be obtained expediently. This model is more theoretical than others. However, it requires all the harmonic constituents of the interested position.

The practical model is much simpler. All the tide coefficients are provided from SHOM website. All these meaningful data are based on a long term observation carried out by SHOM. This means this model is more experimental and realistic. The only problem of this method is that all the interested sites are only restricted in France. In this report, the practical model based on SHOM data will be used for the resource modeling.

II.3 *Turbine Modeling*

MCECS depends on hydrodynamic forces generated by the marine current over hydrofoil shaped blades to generate electricity. According to section I.5, although there is no overall agreement in the optimum shape of the MCT, however, many of the developers favour the horizontal axis design for marine current energy extraction [35]. Depending on the turbine design, the blades can be designed as either fixed-pitch or variable-pitch. But, due to the uncertain mechanical maintenance requirement caused by the moving parts in the sea water, it's better to design the horizontal turbine with fixed-pitch blades.

This part will present details for the designing of marine current turbine with horizontal axis to extract 10KW.

II.3.1 Kinetic Power Energy

In order to further illustrate how to harness the energy from marine current, this section firstly presents the hydrodynamic characteristics of the water flow. The total kinetic energy in a cylinder of marine current flow is very similar with that of wind. The power for the water flow is governed by equation (II.7).

$$P_{hyd} = \frac{1}{2}\rho A V_{tide}^3 \quad \text{(II.7)}$$

Where: ρ is the density of the ocean water (1024 kg/m^3); A is the cross section of the MCT (m^2); V_{tide} is the tidal current velocity for MCT (m/s) and P_{hyd} is the hydrodynamic power from marine current (W);

The hydrodynamic power mainly depends on the cube of the velocity of the fluid. As a result, a small change in velocity V_{tide} can significantly change a lot of the power. However, regardless of turbine design, only a fraction of hydrodynamic power in the free marine current is recoverable. The power coefficient C_p, which is also called Betz's coefficient, to describe the ratio of recoverable power, is defined as follows:

$$C_p = \frac{P_m}{P_{hyd}} \tag{II.8}$$

Then, the extractable mechanical power P_m of MCT, harnessed from the power in a cylinder of moving fluid, P_{hyd}, by the turbine is expressed by the following relation:

$$P_m = \frac{1}{2} C_p \rho A V_{tide}^3 \tag{II.9}$$

The power coefficient C_p is obtained based on BEM theory. It highly depends on the TSR (Tip Speed Ratio or λ), the pitch angle β, the number and the geometry of the blades. For WECS, C_p has typical values in the range 0.25~0.5. The upper limit is for highly efficient machines with low mechanical losses. For MCECS, C_p is estimated to be in the range 0.35~0.5 [12] [78].

II.3.2 Hydrodynamic Theory

Two theories are used in a combined manner; the first theory is that of the axial flow (the axial momentum theory). In this approach, a one-dimensional model is used to express the energy extracted from the marine current, assuming that the fluid is incompressible. The second theory is the element of the blade (Blade Element Momentum Theory, BEM), which takes account of the rotational component of the fluid due to the rotation of the blades [79] - [81].

II.3.2.1 Momentum Theory

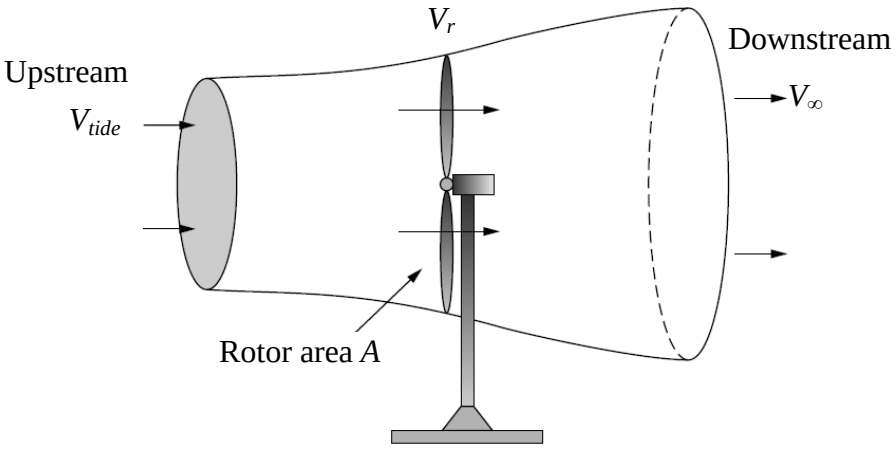

Fig.II.8 Energy extracting stream tube of a turbine.

As shown in Fig.II.8, the flow approaching from the left is slowed down as a portion of its kinetic energy is extracted by the turbine. The fluid leaving the turbine has a lower velocity and its pressure is reduced, causing the fluid to expand downstream of the machine. An envelope drawn around the flow mass that passes through the turbine forms what is called a *stream tube*, as suggested in the figure.

The upstream velocity of the undisturbed fluid is V_{tide}, the velocity of the fluid through the plane of the rotor blades is V_r, and the downstream velocity is V_∞.

The mass flow rate of fluid within the stream tube is everywhere the same. The power extracted by the turbine P_m is equal to the difference in kinetic energy between the upstream and downstream fluid flows. It is given by the following relation:

$$P_m = \frac{1}{2}\rho A V_r (V_{tide}^2 - V_\infty^2) \tag{II.10}$$

If the decreased velocity induced by the rotor is V, then the velocity at the disk is $V_{tide} - V = V_r$, while far downstream the current has been slowed further to velocity V_∞. The difference between the axial component of the current velocity and the axial flow velocity in the rotor plane is usually called the *induced* velocity.

Defining an axial induction factor, a, as the fractional decrease in current velocity between the free stream and the rotor plane represented by:

$$a = \frac{V}{V_{tide}} \tag{II.11}$$

We can write the following relations:

$$V_r = (1 - a)V_{tide} \tag{II.12}$$

$$V_\infty = (1 - 2a)V_{tide} \tag{II.13}$$

Substituting (II.12)and (II.13) into (II.10) gives

$$P_m = \underbrace{\frac{1}{2}\rho A V_{tide}^3}_{Power\ in\ the\ fluid} * \underbrace{4a(1-a)^2}_{Fraction\ extracted} \tag{II.14}$$

From relation (II.14) the efficiency of the rotor, usually designed as C_p can be expressed by

$$C_p = \frac{P_m}{\frac{1}{2}\rho A V_{tide}^3} 4a(1-a)^2 \tag{II.15}$$

The maximum value of the power coefficient C_p occurs when:

$$\frac{dC_p}{da} = 4(1-a)(1-3a) = 0 \tag{II.16}$$

This means the maximum ratio of extracted energy to the total energy equates to 16/27 (0.59259) when a=1/3. This limit is often referred to as the *Betz limit*, or more accurately the *Lanchester-Betz limit*. The power coefficient C_p versus the *axial induction factor a* is shown in Fig.II.9

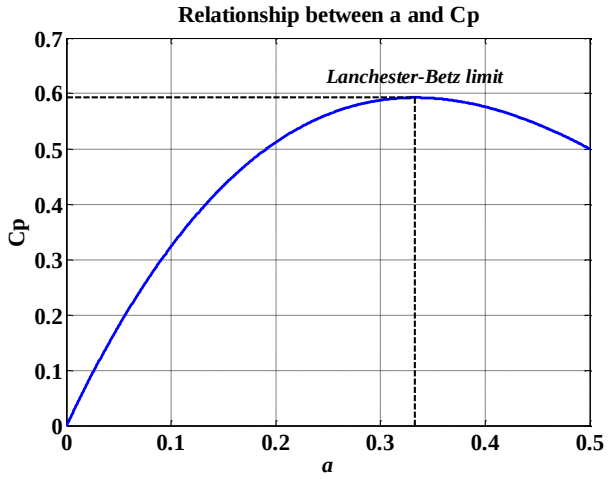

Fig.II.9 Power coefficient Cp as function of the axial induction factor *a*

Additional data that can be derived from this model include the thrust loading on the rotor.

$$T = A\left(\frac{1}{2}\rho V_{tide}^2 - \frac{1}{2}\rho V_{\infty}^2\right) = \frac{1}{2}\rho A V_{tide}^2\,[4a(1-a)] \qquad \text{(II.17)}$$

Moreover, if this thrust loading is considered as a thrust force T on the rotor, the thrust coefficient C_T can be defined in equation (II.18).

$$C_T = \frac{T}{\frac{1}{2}\rho A V_{tide}^2} = 4a(1-a) \qquad \text{(II.18)}$$

The maximum C_T is 1 when a = 1/2 implying zero velocity in the downstream (V_{∞} = 0); meanwhile, C_p will be 0.5. And the thrust coefficient C_T is 8/9 (0.889) at the maximum power coefficient C_p of 0.59259.

The usual way to illustrate rotor efficiency is to present it as a function of tip-speed ratio (TSR). It is the ratio of linear velocity at the blade tip and the fluid velocity, as defined by:

$$\lambda = \frac{R\Omega}{V_{tide}} \qquad \text{(II.19)}$$

Where: R is the radius of the turbine (m) and Ω is the turbine rotational speed (rad/s).

II.3.2.2 Blade Element Momentum Theory

For this theory, each blade will be divided into a sufficient number of elements (usually between ten and twenty). The forces along the blade are then summed together to obtain the lift, drag forces and moments produced by the entire rotor [82].

Based on the momentum theory, all the losses of the pressure or momentum in the rotor is caused by the blade element. The induced velocity in the axial and tangential directions can be calculated from the pressure and momentum loss in the flow. These two induced velocities affect the upstream in the rotor plane, as well as the forces calculated by the BET. This coupling results in an iterative process to determine the hydrodynamic forces and the induced velocities.

BET relies on two key assumptions:

- There are no aerodynamic interactions between elements
- The forces on the blade elements are only determined by the lift and drag coefficients

The advantage of BET is that each blade element is modeled as a two-dimensional airfoil. As a result, in the blade element analysis, lift and drag components can be primitively considered to be perpendicular and parallel to the relative marine current speed direction just as showed in Fig.II.10. It also implies the forces and angles relations which determine the element induced velocities from the wake influence.

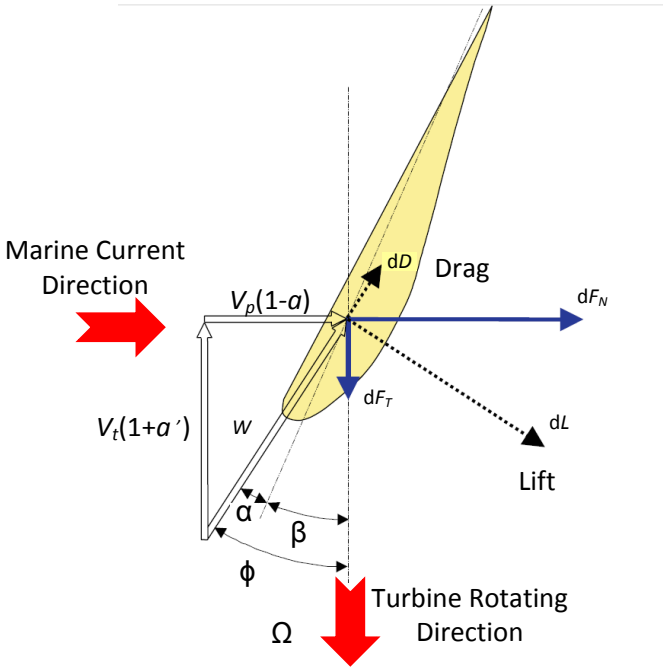

Fig.II.10 Local element velocities, forces and flow angles [83]

dL Blade element lift force (N);

dD Blade element drag force (N);

dF_N Blade element hydrodynamic forces axial components, it can be also noted as one part of element trust dT (N);

dF_T Blade element hydrodynamic forces tangential components (N);

Ω Turbine rotation speed (rad/s);

r Local radius for dr (m);

V_p Local, undisturbed, perpendicular current velocity, it is also regarded as the marine current velocity (V_{tide}) faced to the rotor plane (m/s);

V_t Local, undisturbed, tangential current velocity (m/s);

W Local, undisturbed, marine current velocity (m/s);

a Axial induction factor;

a' Tangential induction factor;

α *W* angle of attack (rad);

β Rotor blade pitch angle (rad);

ϕ *W* direction related to the rotor plane (rad).

The *tangential induction factor a'* is due to a rotation wake at the opposite direction when the marine current passes the blades, just as showed in Fig.II.11. It must be noted that the *tangential induction factor a'* is as a rule smaller than the *axial induction factor a*.

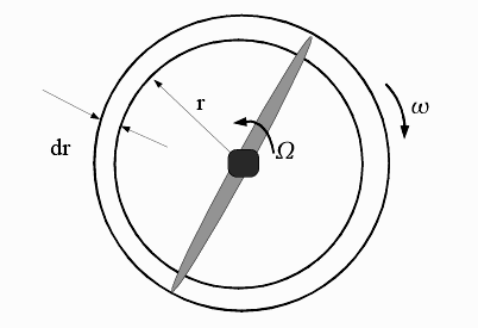

Fig.II.11 Rotating annular stream tube [84]

If ω is defined as tangential induction angular velocity right after the blade, according to the angular momentum, the *tangential induction factor a'* can be obtained in equation (II.20) [73]:

$$a' = \frac{\omega}{2\Omega} \tag{II.20}$$

Thus, the instantaneous relative undisturbed flow velocity experienced by a blade element is:

$$W = \sqrt{\left[V_p(1-a)\right]^2 + [V_t(1+a')]^2} \tag{II.21}$$

This relative velocity affects on the element with an angle on the turbine rotating plane. Based on Fig.II.10, the local flow angle is:

$$\phi = \operatorname{atan}\frac{V_p(1-a)}{V_t(1+a')} = \operatorname{atan}\frac{V_p(1-a)}{\Omega r(1+a')} \tag{II.22}$$

The angle of attack of the relative marine current velocity is determined by the difference between the angle of inflow and the pitch angle:

$$\alpha = \phi - \theta \tag{II.23}$$

The pressure distributions along the profile create forces of lift and drag forces generally applied to the center of thrust. The lift force ($dL \perp dW$) of every blade for dr is [73] [85]:

$$dL = C_L \frac{1}{2}\rho c W^2 dr \tag{II.24}$$

And the drag force ($dD \parallel dW$) for dr is:

$$dD = C_D \frac{1}{2}\rho c W^2 dr \tag{II.25}$$

Where: c is the local blade chord, (varies along the blade: $c = f(r)$); C_L is the blade element 2-D lift coefficient; C_D is the blade element 2-D drag coefficient; dr is the blade section length.

On the other hand, the element torque dΓ is the product of the tangential force dF_T and local radius r. As well, it is determined by the rate of change of angular momentum which is given in equation (II.26) [84].

$$\mathrm{d}\Gamma = N_b \times r \times \mathrm{d}F_T = 2\pi r\rho \mathrm{d}r(1-a)V_p \times 2\Omega a' r^2 \tag{II.26}$$

$$\mathrm{d}F_T = \mathrm{d}L\sin\phi - \mathrm{d}D\cos\phi \tag{II.27}$$

While for the force dF_N, it can be also considered as one part of the element trust force of the rotor plane. Owing to Fig.II.10, this element force is simply written as:

$$\mathrm{d}F_N = \frac{\mathrm{d}T}{\mathrm{N_b}} = \mathrm{d}L\cos\phi + \mathrm{d}D\sin\phi \tag{II.28}$$

Where: $C_{FN} = C_L\cos\phi + C_D\sin\phi$, normal coefficient;

Based on the equations (II.17) and (II.24) to (II.28), the *axial induction factor a* and *tangential induction factor a'* in equation n (II.29).

$$\begin{cases} a = \frac{\sigma_r C_{FN}}{4\sin^2\phi + \sigma_r C_{FN}} \\ a' = \frac{\sigma_r C_{FT}}{4\sin\phi\cos\phi - \sigma_r C_{FT}} \end{cases} \tag{II.29}$$

Where: $C_{FT} = C_L\sin\phi - C_D\cos\phi$, tangential coefficient; $\sin\phi = \frac{V_p(1-a)}{W}$; $\cos\phi = \frac{V_t(1+a')}{W}$; $\sigma_r = \frac{\mathrm{N_b}c}{2\pi r}$, Local Solidity or Chord Solidity; $\mathrm{N_b}$ is the number of rotor blades.

Thus, equation (II.29) determines the dimensionless *induced factor*s *a* and *a'* in case of perpendicular flow. What's more, on account of (II.18) to (II.29), the power and thrust gradients are given in (II.30) and (II.31) [85].

$$\frac{\mathrm{d}C_p}{\mathrm{d}r} = \frac{2\lambda(1-a)^2\sigma_r r C_{FT}}{\pi\sin^2\phi} \tag{II.30}$$

$$\frac{\mathrm{d}C_T}{\mathrm{d}r} = \frac{2(1-a)^2\sigma_r C_{FN}}{\pi\sin^2\phi} \tag{II.31}$$

However, all these results highly depend on the situation without losses and turbulent wake. Losses and turbulent wake corrections are presented in Appendix I.

II.3.3 Calculation of the Element Force

The sections II.3.2.1 and II.3.2.2 describe the principle of the calculation of the element force. From Fig.II.10 and equation (II.21), the instantaneous undisturbed marine current velocity is the vector sum of the perpendicular velocity V_p (V_{tide}), and the tangential velocity V_t. Then, the element life and drag force can be achieved from equations (II.24) and (II.25) once the induction factors are calculated. However, the induction factors are also influenced and restricted by the tip-loss, hub-loss and trust coefficient. As a result, the iterative process to calculate the forces acting on the blade element is showed in Fig.II.12.

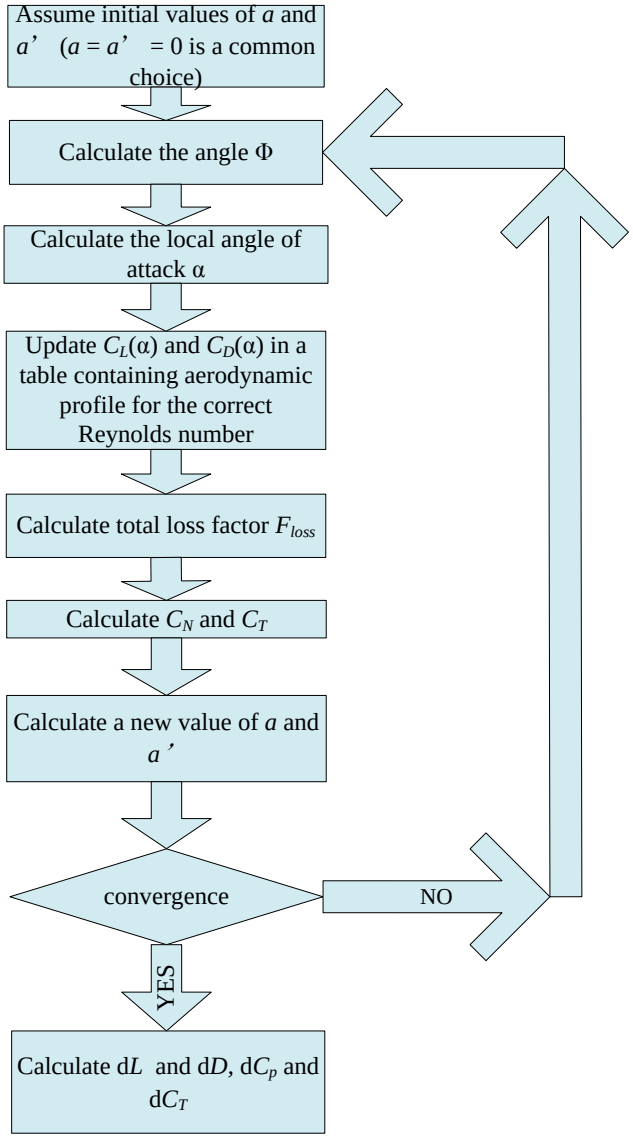

Fig.II.12 Flow chart of calculating C_p

II.3.4 Optimise Turbine for 10 kW System

According to the design requirement of the system and the marine current speed in sections I.4.5 and II.2.2, the nominal speed will be 50 rpm with 10 kW rated power, and the rated marine current velocity will be fixed at 2.5 m/s.

As a result, this system will generate about 10 kW electricity when the marine current is 2.5 m/s, and as well as 50 rpm for the generator. The objective of this section is just to design one form of turbine suitable for this system.

The first question to design the turbine is to determine the number of the blades. As the propeller blades with a number of odd (asymmetric helix) always have a better performance [61], in this study, we will choose 3 blades for the turbine. The second problem is to decide the type of airfoils. Based on the research in [85], [86] and [87], we will adapt NACA 00ZZ (National Advisory Committee for Aeronautics) airfoils as the turbine blade.

The NACA airfoils are airfoil shapes for aircraft wings developed by NACA. The shape of the NACA airfoils is described using a series of digits following the word "NACA". The parameters in the numerical code can be entered into equations to precisely generate the cross-section of the airfoil and calculate its properties [88]. For foil type NACA XYZZ used in this section, each of the 4 parameters present the geometric characteristics, where:

X: First digit describing maximum camber as percentage of the chord;

Y: Second digit describing the distance of maximum camber from the airfoil leading edge in tens of percents of the chord;

ZZ: Last two digits describing maximum thickness of the airfoil as percent of the chord.

As a result, the profile NACA00ZZ means that it is a symmetrical airfoil without cambered surface and ZZ% thickness to chord length. The form can be written as [88]:

$$y_{thk} = \frac{e_{thk}}{0.2} c \left[0.2969 \sqrt{\frac{x}{c}} - 0.1260 \left(\frac{x}{c}\right) - 0.3516 \left(\frac{x}{c}\right)^2 + 0.2843 \left(\frac{x}{c}\right)^3 - 0.1015 \left(\frac{x}{c}\right)^4 \right] \quad \text{(II.32)}$$

Where:

x Position along the chord from 0 to c;

y_{thk} Half thickness at a given value of x (centerline to surface);

e_{thk} Maximum thickness as a fraction of the chord.

For example, if ZZ=15, the plot of NACA0015 foil is presented in Fig.II.13.

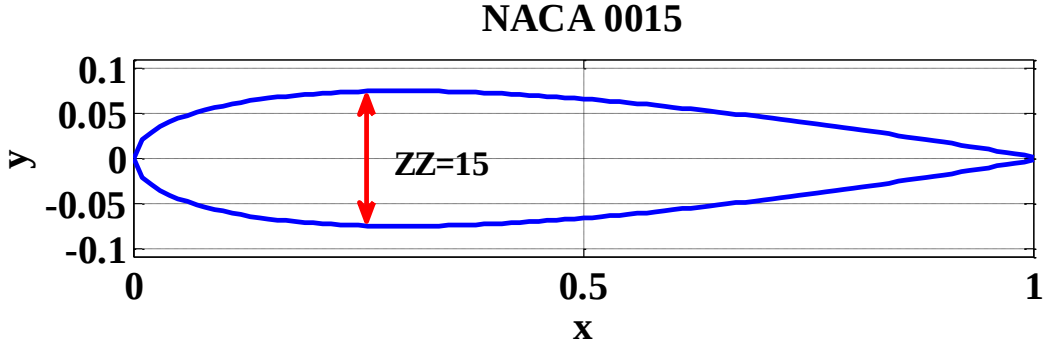

Fig.II.13 NACA 0015 foil

The last question is to design the properties of the blades. On the basis of the equations (II.9) and (II.19) and the system requirements discussed before, the fundamental characteristics must be obeyed the following formula.

$$C_p \lambda^2 = \frac{2P_{mec}\,\Omega^2}{\pi \rho V_{tide}^5} \approx 1.75 \quad \text{(II.33)}$$

In order to satisfy this condition, it is necessary to change the size of the chord at the hub and tip, and as well as the pitch angle. Based on the attempts and theory analysis using Fig.II.12, the principle blade properties of the NACA 00ZZ are showed in Fig.II.14 and Table II.2.

Table II.2 Blade properties: Profile NACA 00ZZ

r/R	c/r (%)	Thickness/c (%)	Twist angle (°)
0.25	15	22.29	0
0.3	14.53	21.60	10.75
0.35	13.6	20.37	8.57
0.4	12.67	19.33	6.82
0.45	11.73	18.46	5.42
0.5	10.80	17.74	4.31
0.55	9.87	17.14	3.44
0.6	8.93	16.62	2.74
0.65	8.00	16.18	2.18
0.7	7.07	15.78	1.73
0.75	6.13	15.39	1.35
0.8	5.20	15.00	1.02
0.85	4.27	14.57	0.74
0.9	3.33	14.08	0.49
0.95	2.40	13.51	0.27
1.0	1.47	12.82	0.1

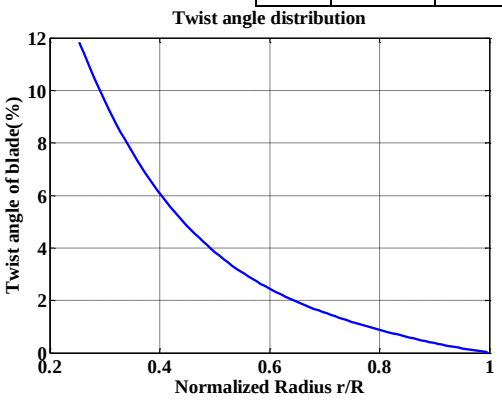

a) Twist angle of the blade element

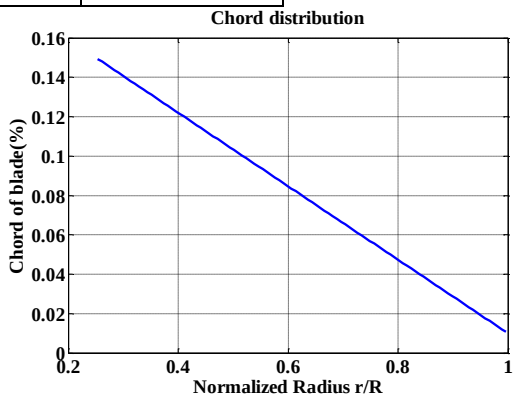

b) Chord of the blade element

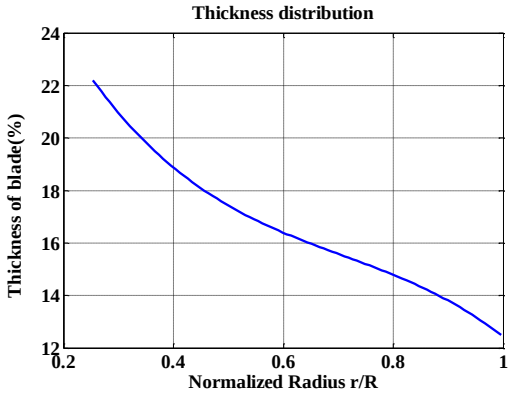

c) Thickness of the blade

Fig.II.14 The geometric parameters of the blade

According to (II.30) and the parameters designed for the system, the power coefficient Cp in the function of λ and β can be showed in Fig.II.15. Some pitch angles are presented in Fig.II.16 and Fig.II.17.

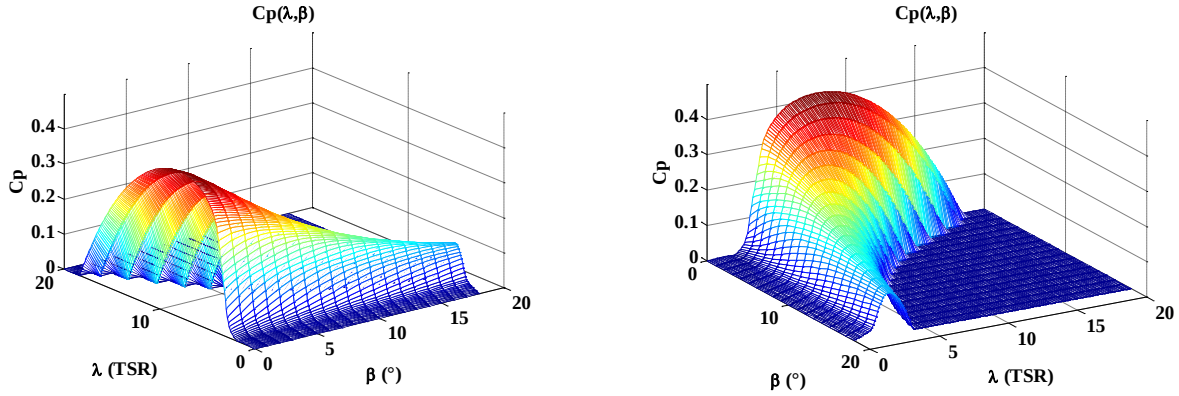

Fig.II.15 Cp (λ,β) curves

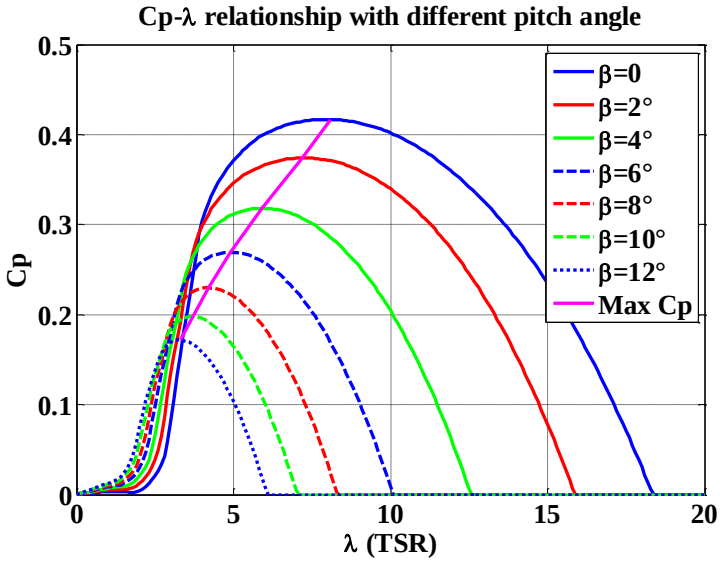

Fig.II.16 Cp-λ curve with different pitch angles β

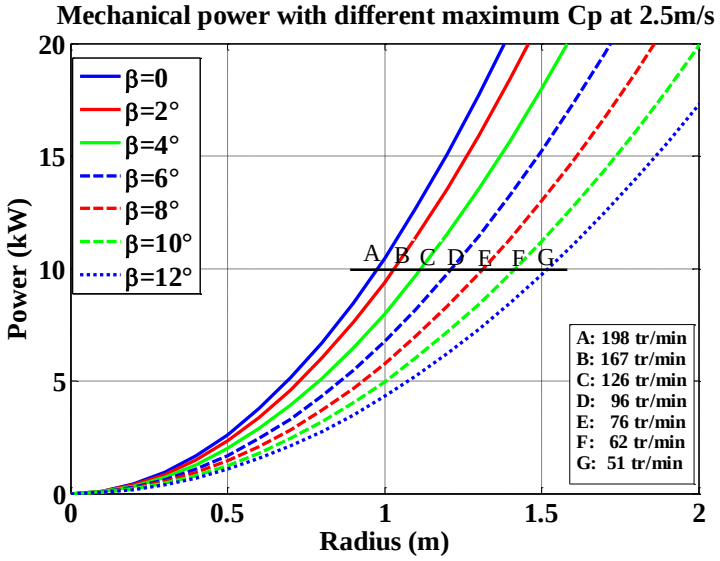

Fig.II.17 Maximum turbine power with different pitch angles β and radius

Fig.II.16 gives the C_p-λ variation with different pitch angle in 2-D view. Fig.II.17 gives the mechanical power for each pitch angle at rated situation with different radius. There is a black

line cross all the curves, the intersection points are noted as: A, B, C, D, E, F, G. From the abscissa of these points, they imply the desired radius for the fixed power 10kW for each pitch angle. It is easy to find that the radius will increase if we raise the pitch angle. In the bottom right corner of Fig.II.17, there are some values which mean the needed rotating speed for the fixed power of each pitch angle. The wanted rotating mechanical speed will decrease if augmenting the pitch angle.

After comparison, for this type of turbine, when pitch angle equates to 12° (λ=3.28, C_p=0.1719), it can well satisfy the formula (II.33). The radius is then determined to be 1.566 m by equation (II.19).

More characteristics of this turbine, such as induction factors, attack angle and coefficients, are showed in Appendix II. Based on these results, it will be useful to develop a MPPT (Maximum Power Point Tracking) strategy for the system.

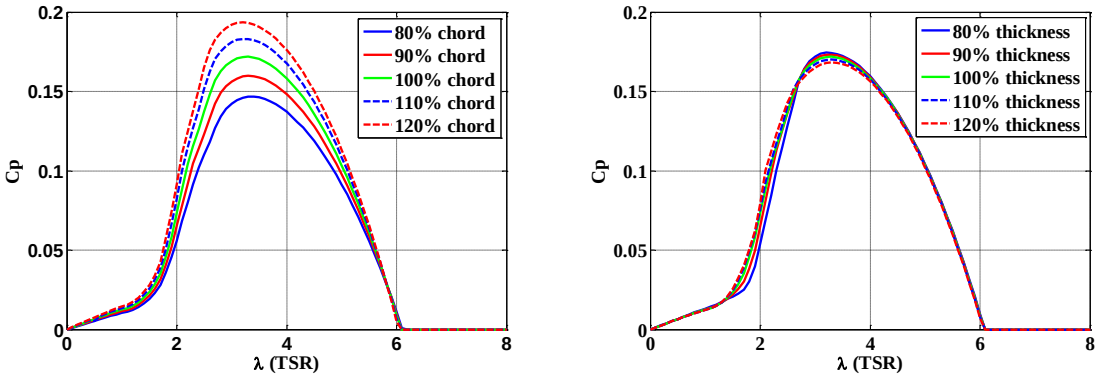

a) Different chord b) Different thickness

Fig.II.18 Cp-λ according to different chord and thickness of blades for β=12°

In accordance with Fig.II.18, we can notice that the increase of the chord can increase the power coefficient Cp significantly. However, the variation of the thickness nearly doesn't change the Cp value. This means the variation of chord has more influence than that of thickness for the Cp-λ curve.

II.4 *Generator Modeling (Doubly Salient Permanent Magnet Generator)*

The objective of this part is to model DSPMG which has been designed as one low speed machine with 10 kW, 50rpm.

II.4.1 Introduction

The research for designing low speed machine in IREENA begins from ten years ago, by developing a new 3-phase VRM (Variable Reluctance Machine) [89]. Theoretically, the velocity of the VRM only depends on the teeth of the rotor as shown in equation (II.34).

$$\Omega = \frac{\omega_e}{N_r} = \frac{2\pi f}{N_r} \quad \text{(II.34)}$$

Where: Ω is the mechanical speed (rad/s); ω_e is the electrical speed (rad/s); f is the electrical frequency (Hz) and N_r represents the number of teeth in the rotor.

This kind of VRM is different from the classical VRM with big teeth in the rotor (for example: 6/4). For a given frequency of the stator current, the rotating speed decreases by increasing the number of the rotor teeth. Fig.II.19 shows a machine with 64 teeth in the rotor, 12 plots and 48 teeth in the stator. It is also called pure VRM which means that the machines are equipped with one single polyphase armature winding circuit. This type of machine has the advantages of robustness and potential low cost [89] [90].

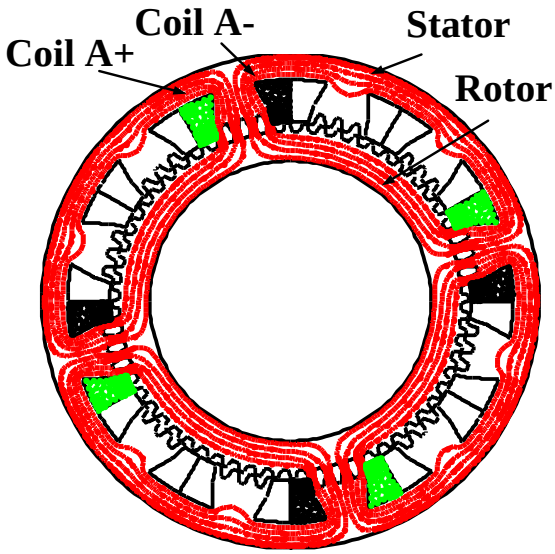

Fig.II.19 64/48 VRM [89]

Nevertheless, various studies show that adding PM (Permanent Magnet) to VRM with doubly salient structure can well improve performance. In [90], Saou has appended four permanent magnets NdFeB to the previous VRM. Whereas, the number of magnets set in the machine must obey the criterion in equation (II.35) [91]. Such kind of VRM is also called hybrid VRM which implies that it is endowed with not only the armature windings but also the magnets.

$$\pm N_s \pm N_r = \pm k_1 p_w \pm k_2 p_m \qquad \text{(II.35)}$$

Where: N_s & N_r are the teeth number in stator and rotor; p_w & p_m are the Pole pair numbers of the coils winding and of the magnets; k_1 & k_2 are the Integers.

In [90], the machine is regarded as member of DSPMG (see Fig.II.20) and is still optimized to maximize torque. Comparing with classic machine, this machine has very interesting performances. Indeed, the active mass torque is 12 Nm/kg; the volume torque is 45.5 kNm/m^3 [90] [91].

This DSPMG has these principle characteristics as follows:

- ✓ There is no magnet in the rotor.
- ✓ The magnets are fixed on the stator. It's much easy to control and cooling the machine.

✓ This machine employs concentrated stator windings. It can reduce the winding mass and the resistance.

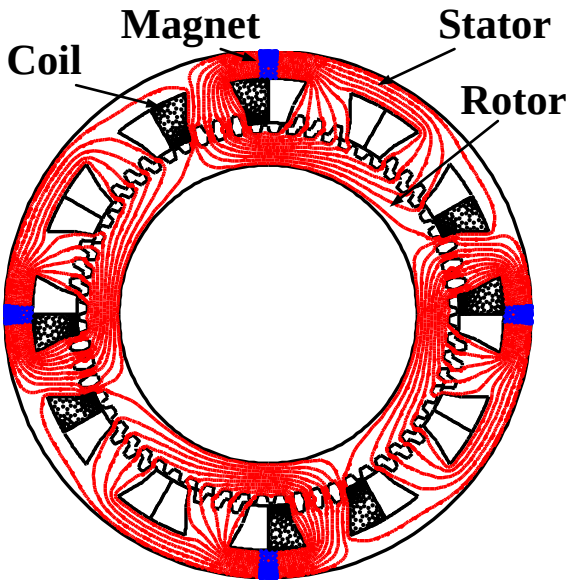

Fig.II.20 DSPMG structure

For purpose of modeling this DSPMG, there are two important positions that are shown in Fig.II.21: conjunction and opposition. For conjunction, it represents the minimum reluctance and then the maximum inductance. While for opposition, it implies the maximum reluctance and minimum inductance. The conjunction position is more stable than opposition.

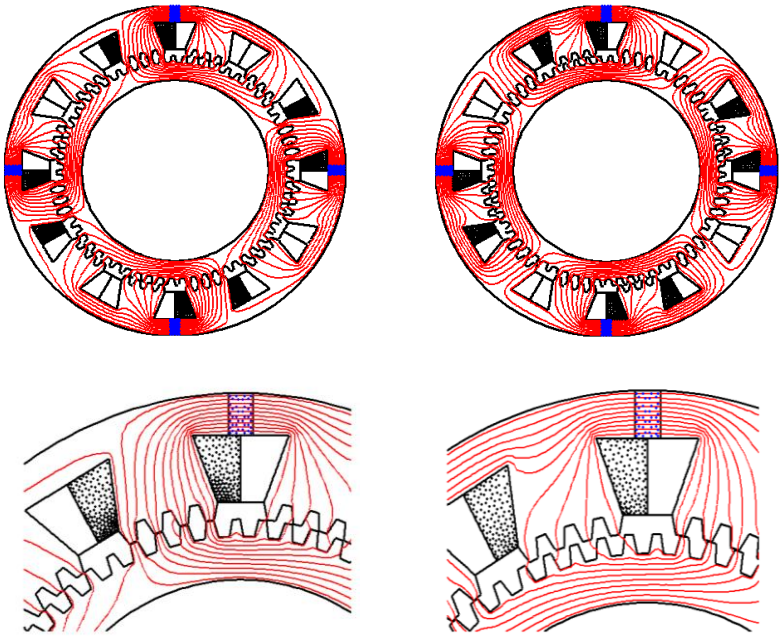

a) Conjunction b) Opposition

Fig.II.21 Two special positions of DSPMG

2D FEM (Finite Element Method) is used to determine the inductance matrix of the machine and the EMF (ElectroMotive Force) at no load. We suppose then that the end effects are neglected, hence the electromagnetic values are invariable in the axial direction (ʒ).

The magnetic vector $\vec{A}$ has only one axial component in the ʒ direction and varies only with x and y.

$$\vec{A} = \begin{bmatrix} 0 \\ 0 \\ \mathrm{A}_{ʒ}(\mathrm{x},\mathrm{y}) \end{bmatrix} \tag{II.36}$$

The flux density $\vec{B}$ has 2 components:

$$\vec{B} = \begin{cases} B_x = \frac{\partial A_ʒ}{\partial y} \\ B_y = -\frac{\partial A_ʒ}{\partial x} \\ B_ʒ = 0 \end{cases} \tag{II.37}$$

We have then to solve the non linear magnet static equations:

$$\frac{\partial}{\partial x}\left(\frac{1}{\mu_o \mu_r}\frac{\partial A_ʒ}{\partial x}\right) + \frac{\partial}{\partial y}\left(\frac{1}{\mu_o \mu_r}\frac{\partial A_ʒ}{\partial y}\right) = J_0 + J_{pm} \tag{II.38}$$

Where: J_0 is the current density of the source (A/m^2); J_{pm} is the current density of the permanent magnet (A/m^2).

The self and mutual inductances of the machine can be determined by the flux.

The flux in the phase A is given by:

$$\varphi_a = L_a i_a + M_{ab} i_b + M_{ac} i_c + \varphi_{ma} \tag{II.39}$$

If the condition is: $i_b = i_c = \varphi_m = 0$, the self inductance L_a is:

$$L_a = \frac{\varphi_a}{i_a} \tag{II.40}$$

And mutual inductance M_{ba} is:

$$M_{ba} = \frac{\varphi_b}{i_a} \tag{II.41}$$

As a result, the characteristics of the self and mutual inductances are given in Fig.II.22 and Fig.II.23. Fig.II.24.a shows the variation of the PM flux linkage calculated by the 2D modeling. Fig.II.24.b shows the consequently EMF. These forms are periodic but are not exactly sinusoidal.

$$e_m = \Omega \frac{d}{d\theta_m}\varphi_m \tag{II.42}$$

The relative permeability is approximated by the Marocco formulation [89]:

$$\frac{1}{\mu_r} = \varepsilon + (c - \varepsilon)\frac{B^{2\alpha}}{B^{2\alpha} + t} \tag{II.43}$$

In this chapter, the parameters of the Silicon steel M40050A can be defined as (SI unit): $\varepsilon = 1.5395 \times 10^{-4}$, $c = 0.1262$ $t = 13.8229$, $\alpha = 4.9948 \times 10^{4}$. The characteristic is presented in Fig.II.25.

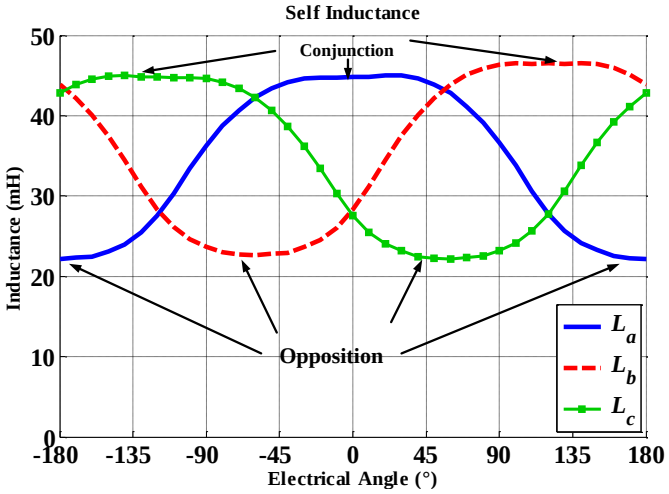

Fig.II.22 Self inductance variations of DSPMG

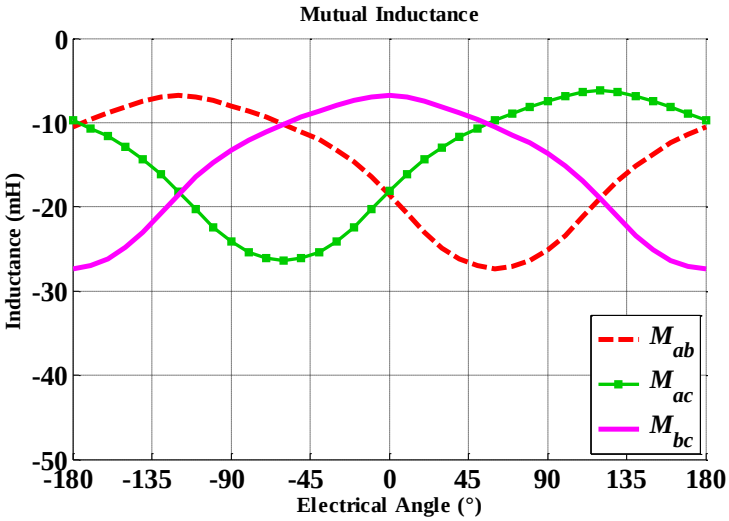

Fig.II.23 Mutual inductance variations of DSPMG

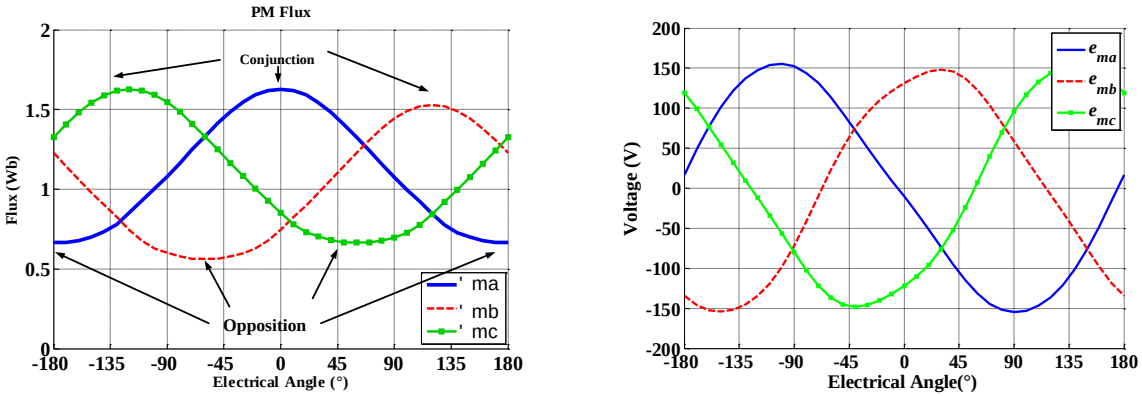

a) PM flux linkage of DSPMG b) EMF of DSPMG

Fig.II.24 PM characteristic of DSPMG

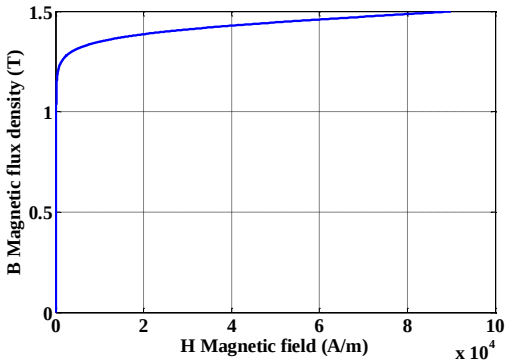

Fig.II.25 B-H characteristic of M40050A

II.4.2 abc Frame Model

On the basis of the inductances and permanent magnet flux characteristics shown in Fig.II.22 to Fig.II.24, FFT (Fast Fourier Transform) is applied to analyze the waveforms in Fig.II.26.

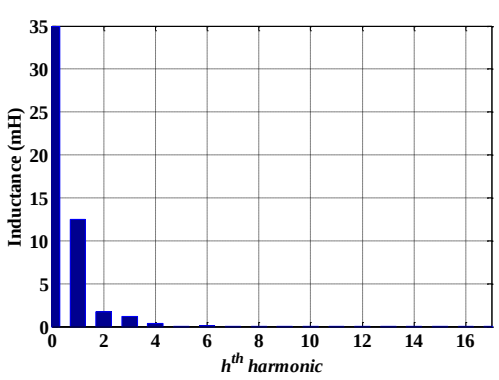

a) Self-inductance L_a

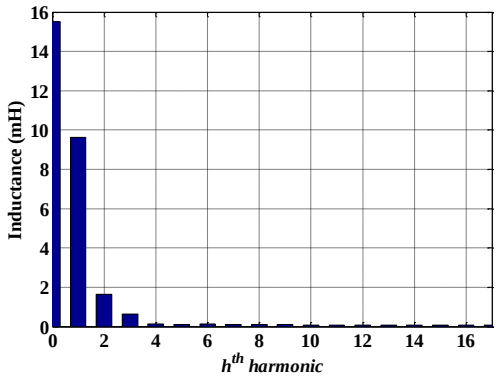

b) Mutual inductance $|M_{ab}|$

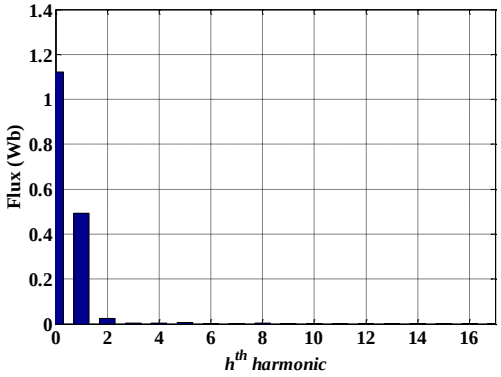

c) PM flux-linkage φ_{ma}

Fig.II.26 FFT for inducance and PM flux-linkage

So, the numerical expression for the 3-phase self-inductances (L_a, L_b and L_c), mutual-inductances (M_{ab}, M_{bc} and M_{ca}) and PM flux-linkage components (φ_{ma}, φ_{mb} and φ_{mc}) for DSPMG can be written as:

$$\begin{cases} L_a = \sum_{h=0}^{\infty} L_{ah} \cos h\theta_e \\ L_b = \sum_{h=0}^{\infty} L_{bh} \cos h\left(\theta_e - \frac{2}{3}\pi\right) \\ L_c = \sum_{h=0}^{\infty} L_{ch} \cos h\left(\theta_e - \frac{4}{3}\pi\right) \end{cases} \quad \text{(II.44)}$$

$$\begin{cases} M_{ab} = M_{ba} = \sum_{h=0}^{\infty} M_{abh} \cos h\left(\theta_e - \frac{4}{3}\pi\right) \\ M_{ac} = M_{ca} = \sum_{h=0}^{\infty} M_{ach} \cos h\left(\theta_e - \frac{2}{3}\pi\right) \\ M_{bc} = M_{cb} = \sum_{h=0}^{\infty} M_{bch} \cos h\theta_e \end{cases} \quad \text{(II.45)}$$

$$\begin{cases} \varphi_{ma} = \sum_{h=0}^{\infty} \varphi_{ah} \cos h\theta_e \\ \varphi_{mb} = \sum_{h=0}^{\infty} \varphi_{bh} \cos h\left(\theta_e - \frac{2}{3}\pi\right) \\ \varphi_{mc} = \sum_{h=0}^{\infty} \varphi_{ch} \cos h\left(\theta_e - \frac{4}{3}\pi\right) \end{cases} \quad \text{(II.46)}$$

$$\Omega = \frac{1}{N_r}\frac{\mathrm{d}\theta_e}{\mathrm{dt}} = \frac{\mathrm{d}\theta_m}{\mathrm{dt}} \quad \text{(II.47)}$$

Where: h=0, continue part; h>1, h^{th} harmonic; θ_e is the electrical position (rad) and θ_m is the mechanical position (rad);

Table II.3 FFT for inductance and flux-linkage

h	L_a (mH)	$\lvert M_{ab}\rvert$ (mH)	φ_{ma} (Wb)
0	34.9519	15.5191	1.1215
1	12.4874	9.6403	0.4937
2	1.7173	1.6551	0.0238
3	1.1567	0.6439	0.0045
4	0.3398	0.1244	0.0029

According to Table II.3, all the other harmonics of the variables are relatively small compared with the fundamental. In order to simplify the model, the 2nd and higher order Fourier terms will be neglected. As a result, the new expressions for the characteristics are written in equations (II.48) to (II.50).

$$\begin{cases} L_a = L_0 + L_1 \cos\theta_e \\ L_b = L_0 + L_1 \cos\left(\theta_e - \frac{2}{3}\pi\right) \\ L_c = L_0 + L_1 \cos\left(\theta_e - \frac{4}{3}\pi\right) \end{cases} \quad \text{(II.48)}$$

$$\begin{cases} M_{ab} = M_{ba} = M_0 + M_1 \cos\left(\theta_e - \frac{4}{3}\pi\right) \\ M_{ac} = M_{ca} = M_0 + M_1 \cos\left(\theta_e - \frac{2}{3}\pi\right) \\ M_{bc} = M_{bc} = M_0 + M_1 \cos\theta_e \end{cases} \quad \text{(II.49)}$$

$$\begin{cases} \varphi_{ma} = \varphi_0 + \varphi_1 \cos\theta_e \\ \varphi_{mb} = \varphi_0 + \varphi_1 \cos\left(\theta_e - \frac{2}{3}\pi\right) \\ \varphi_{mc} = \varphi_0 + \varphi_1 \cos\left(\theta_e - \frac{4}{3}\pi\right) \end{cases} \quad \text{(II.50)}$$

Observing these models, they are so different from that of classic machine model. For the PM-flux linkage expressions in (II.50), the constant components φ_0 which magnetize the DSPMG do not exist in the conventional PMSG (Permanent Magnet Synchronous Generator). From the equations (II.48), (II.49) and (II.50), if L_1 & M_1 and φ_0 are equated to 0, this model will be simplified and will correspond to PMSSG (Permanent Magnet Smooth Synchronous Generator) model. It should be also noted that these self- and mutual- inductances are not like PSPMG (Pole Salient Permanent Magnet Generator) either. For classic PSPMG, the variation of the inductances due to the position is twice of the PM flux-linkage frequency (ex: $L_{a\_PSPMG}=L_0+L_1 \cos 2\theta_e$).

The basic equation for instantaneous electromagnetic torque Γ_{em} is obtained by differentiating the co-energy with constant currents, given by the following relation [93]:

$$\Gamma_{em} = \frac{\partial \widetilde{W}_{em}}{\partial \theta_m} = \frac{p}{2}[i_s]^t \left[\frac{\partial L_s}{\partial \theta_e}\right][i_s] + p[i_s]^t \left[\frac{\partial \varphi_m}{\partial \theta_e}\right] + p\frac{\partial \widetilde{W}_{em\,0}}{\partial \theta_e} \quad \text{(II.51)}$$

Where: p is the number of pole pairs; $\widetilde{W}_{em}$ is the co-energy of the machine; $\widetilde{W}_{em\,0}$ is the co-energy of the machine when all the currents are zero; $[L_s]$ is the Stator inductance matrix; $[i_s]$ is the current vector; $[\varphi_m]$ is the PM flux-linkage vector.

The first term of the torque expression in equation (II.51) is the reluctant torque (or salient torque Γ_r); it is linked to the rotor geometry. The last term is the cogging torque due to the interaction of the magnets with the slots. It is consistently ignored. The second term is the "hybrid" torque (Γ_{pm}) and corresponds to the interaction between the stator currents and the magnet flux. It is the main torque.

It must be noted that, usually, for the alternator mode, in order to keep the total flux in the machine, the researchers prefer to inverse the sign of applied stator voltages and electromagnetic torque. On account of the relation between mechanical and electrical velocities shown in formula (II.34), as well as replace the pole pair by teeth number in rotor. Finally, the torque express for DSPMG can be rewritten simply in equation (II.52).

$$\Gamma_{em} = -\left\{\frac{N_r}{2}[i_s]^t \left[\frac{\partial L_s}{\partial \theta_e}\right][i_s] + N_r[i_s]^t \left[\frac{\partial \varphi_m}{\partial \theta_e}\right]\right\} \quad \text{(II.52)}$$

The electromagnetic torque expression of DSPMG developed in abc frame can be obtained as follow:

$$\Gamma_{em\,DSPMG} = -\left(\Gamma_{r\,DSPMG} + \Gamma_{pm\,DSPMG}\right) \quad \text{(II.53)}$$

Where:

$$\Gamma_{pm\,DSPMG} = -N_r\varphi_1\left[i_a \sin\theta_e + i_b \sin\left(\theta_e - \frac{2\pi}{3}\right) + i_c \sin\left(\theta_e - \frac{4\pi}{3}\right)\right]$$

$$\Gamma_{r\,DSPMG} = -\frac{N_r L_1}{2}\left[i_a^2 \sin\theta_e + i_b^2 \sin\left(\theta_e - \frac{2\pi}{3}\right) + i_c^2 \sin\left(\theta_e - \frac{4\pi}{3}\right)\right]$$
$$-N_r M_1\left[i_a i_b \sin\left(\theta_e - \frac{4\pi}{3}\right) + i_a i_c \sin\left(\theta_e - \frac{2\pi}{3}\right) + i_b i_c \sin\theta_e\right]$$

The three phase voltage and flux expressions of DSPMG can be expressed as follows:

$$\begin{bmatrix}\varphi_a\\ \varphi_b\\ \varphi_c\end{bmatrix}=\begin{bmatrix}\varphi_{ma}\\ \varphi_{mb}\\ \varphi_{mc}\end{bmatrix}+\begin{bmatrix}L_a & M_{ab} & M_{ac}\\ M_{ba} & L_b & M_{bc}\\ M_{ca} & M_{cb} & L_c\end{bmatrix}\begin{bmatrix}i_a\\ i_b\\ i_c\end{bmatrix} \quad \text{(II.54)}$$

$$-\begin{bmatrix}v_a\\ v_b\\ v_c\end{bmatrix}=\begin{bmatrix}e_{ma}\\ e_{mb}\\ e_{mc}\end{bmatrix}+\begin{bmatrix}R_s & 0 & 0\\ 0 & R_s & 0\\ 0 & 0 & R_s\end{bmatrix}\begin{bmatrix}i_a\\ i_b\\ i_c\end{bmatrix}+\frac{d}{dt}\left\{\begin{bmatrix}L_a & M_{ab} & M_{ac}\\ M_{ba} & L_b & M_{bc}\\ M_{ca} & M_{cb} & L_c\end{bmatrix}\begin{bmatrix}i_a\\ i_b\\ i_c\end{bmatrix}\right\} \quad \text{(II.55)}$$

$$e_{mj}=\frac{d}{dt}\varphi_{mj}\quad (j=a,b,c) \quad \text{(II.56)}$$

Where: R_s is the resistance of each phase (Ω); v_j is the phase voltage (V); i_j is the phase current (A); e_{mj} is the EMF induced on stator windings of each phase due to the magnet (V) without load.

So, the output instantaneous power of DSPMG (instantaneous active power) can be also get by formula (II.57).

$$P=v_a i_a+v_b i_b+v_c i_c \quad \text{(II.57)}$$

After development, the instantaneous active power for DSPMG in abc reference frame is obtained in formula (II.58).

$$\begin{aligned}&P_{DSPMG}=\\ &-\left[i_a\frac{\mathrm{d}\varphi_{ma}}{\mathrm{dt}}+i_b\frac{\mathrm{d}\varphi_{ma}}{\mathrm{dt}}+i_{\mathrm{c}}\frac{\mathrm{d}\varphi_{ma}}{\mathrm{dt}}\right]-R_s(i_a^2+i_b^2+i_c^2)\\ &-\left[i_a^2\frac{\mathrm{d}L_a}{\mathrm{dt}}+i_b^2\frac{\mathrm{d}L_b}{\mathrm{dt}}+i_c^2\frac{\mathrm{d}L_c}{\mathrm{dt}}\right]-2\left[i_a i_b\frac{\mathrm{d}M_{ab}}{\mathrm{dt}}+i_a i_c\frac{\mathrm{d}M_{ac}}{\mathrm{dt}}+i_b i_c\frac{\mathrm{d}M_{bc}}{\mathrm{dt}}\right]\\ &-\frac{L_a}{2}\frac{\mathrm{d}}{\mathrm{dt}}i_a^2-\frac{L_b}{2}\frac{\mathrm{d}}{\mathrm{dt}}i_b^2-\frac{L_c}{2}\frac{\mathrm{d}}{\mathrm{dt}}i_c^2-M_{ab}\frac{\mathrm{d}i_a i_b}{\mathrm{dt}}-M_{ac}\frac{\mathrm{d}i_a i_c}{\mathrm{dt}}-M_{bc}\frac{\mathrm{d}i_b i_c}{\mathrm{dt}}\end{aligned} \quad \text{(II.58)}$$

The instantaneous reactive power Q for generator is defined in formula (II.59).

$$Q=-\frac{1}{\sqrt{3}}[(v_a-v_b)i_c+(v_b-v_c)i_a+(v_c-v_a)i_b] \quad \text{(II.59)}$$

The instantaneous reactive power Q in abc frame for DSPMG is written in equation (II.60).

$$\begin{aligned}Q_{DSPMG}&=-\frac{1}{\sqrt{3}}[(v_a-v_b)i_c+(v_b-v_c)i_a+(v_c-v_a)i_b]\\ &=\omega_e\varphi_1\left[i_b\cos\left(\theta_e-\frac{2\pi}{3}\right)-i_c\cos\left(\theta_e-\frac{\pi}{3}\right)+i_a\cos\theta_e\right]\\ &+\frac{1}{\sqrt{3}}\left[(i_c-i_b)\frac{d}{dt}L_a i_a+(i_a-i_c)\frac{d}{dt}L_b i_b+(i_b-i_a)\frac{d}{dt}L_c i_c\right]\\ &+\frac{1}{\sqrt{3}}i_a\frac{d}{dt}[M_{bc}(i_c-i_b)+i_a(M_{ab}-M_{ac})]\\ &+\frac{1}{\sqrt{3}}i_b\frac{d}{dt}[M_{ac}(i_a-i_c)+i_b(M_{bc}-M_{ab})]\\ &+\frac{1}{\sqrt{3}}i_c\frac{d}{dt}[M_{ab}(i_b-i_a)+i_c(M_{ac}-M_{bc})]\end{aligned} \quad \text{(II.60)}$$

From equations (II.53) to (II.60), they are normative expressions of the torque, active and reactive power for all the machines. In the following research, the new expressions on basis of Park reference frame will be displayed.

II.4.3 o-d-q Frame Model

In this section, a dynamic Park model of DSPMG in o-d-q frame is derived.

As showed in Fig.II.27, for DSPMG, the PM-flux linkage has the same period as the inductance.

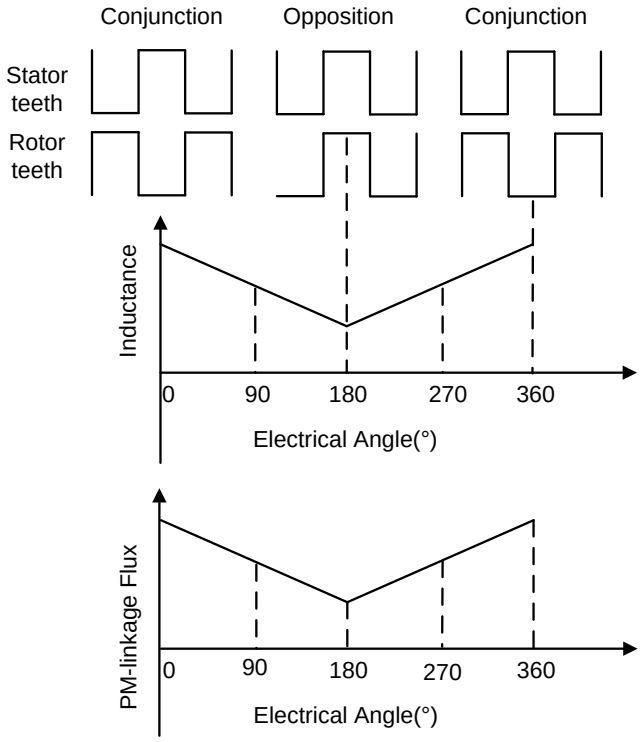

Fig.II.27 Definition of d-q axes positions

The d-q axes of the DSPMG are defined, as shown on Fig.II.28. The d-axis is determined when the PM flux-linkage of phase A is the maximum. As a result, the q-axis is at the position which displaces the d-axis by 90° in electrical degrees anticlockwise. Since the number of teeth in the rotor is 64, the displacement between the d- and q-axis in mechanical degrees will be 1.41°.

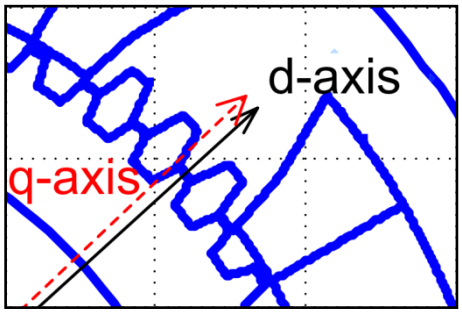

Fig.II.28 d-q axes of the DSPMG

The classical Concordia and Park transformations will be applied for PM flux-linkage and voltage equations in stator reference frame. The Concordia and Park matrix are respectively:

$$T_3 = \frac{1}{\sqrt{3}}\begin{bmatrix} 1 & \sqrt{2} & 0 \\ 1 & -\frac{\sqrt{2}}{2} & \sqrt{\frac{3}{2}} \\ 1 & -\frac{\sqrt{2}}{2} & -\sqrt{\frac{3}{2}} \end{bmatrix} \quad \text{(II.61)}$$

$$R(\theta_e) = \begin{bmatrix} 1 & 0 & 0 \\ 0 & \cos\theta_e & -\sin\theta_e \\ 0 & \sin\theta_e & \cos\theta_e \end{bmatrix} \quad \text{(II.62)}$$

Based on equations (II.54), (II.55), (II.61), (II.62), and by applying successively Concordia and Park rotation to each stator variables, the following o-d-q model can be deduced.

Flux equations in o-d-q model are giving by:

$$\begin{bmatrix} \varphi_o \\ \varphi_d \\ \varphi_q \end{bmatrix} = \begin{bmatrix} L_o & M_{od} & M_{oq} \\ M_{od} & L_d & M_{dq} \\ M_{oq} & M_{dq} & L_q \end{bmatrix} \begin{bmatrix} i_o \\ i_d \\ i_q \end{bmatrix} + \sqrt{3} \begin{bmatrix} \varphi_0 \\ \frac{1}{\sqrt{2}}\varphi_1 \\ 0 \end{bmatrix} \quad \text{(II.63)}$$

Voltage equations are:

$$-\begin{bmatrix} v_o \\ v_d \\ v_q \end{bmatrix} = \begin{bmatrix} e_{mo} \\ e_{md} \\ e_{mq} \end{bmatrix} + [\alpha] \begin{bmatrix} i_o \\ i_d \\ i_q \end{bmatrix} + [\beta] \frac{d}{dt} \begin{bmatrix} i_o \\ i_d \\ i_q \end{bmatrix} \quad \text{(II.64)}$$

With

$$\begin{bmatrix} e_{mo} \\ e_{md} \\ e_{mq} \end{bmatrix} = \sqrt{\frac{3}{2}}\varphi_1 \omega_e \begin{bmatrix} 0 \\ 0 \\ 1 \end{bmatrix};$$

$$[\alpha] = \begin{bmatrix} R_s & 0 & 0 \\ -\omega_e M_{oq} & R_s + 2\omega_e M_{dq} & -\omega_e\left(\frac{3L_d}{2} - \frac{L_q}{2}\right) \\ \omega_e M_{od} & \omega_e\left(\frac{3L_q}{2} - \frac{L_d}{2}\right) & R_s - 2\omega_e M_{dq} \end{bmatrix};$$

$$[\beta] = \left[L_{odq\,DSPMG}\right] = \begin{bmatrix} L_o & M_{od} & M_{oq} \\ M_{od} & L_d & M_{dq} \\ M_{oq} & M_{dq} & L_q \end{bmatrix}$$

$$= \begin{bmatrix} L_0 + 2M_0 & \frac{1}{\sqrt{2}}(L_1 - M_1) & 0 \\ \frac{1}{\sqrt{2}}(L_1 - M_1) & L_0 - M_0 + \left(\frac{L_1}{2} + M_1\right)\cos 3\theta_e & -\left(\frac{L_1}{2} + M_1\right)\sin 3\theta_e \\ 0 & -\left(\frac{L_1}{2} + M_1\right)\sin 3\theta_e & L_0 - M_0 - \left(\frac{L_1}{2} + M_1\right)\cos 3\theta_e \end{bmatrix}$$

Applying Concordia and Park transformations to torque formula (II.52), the torque expressed in o-d-q reference is written is equation (II.65):

$$\Gamma_{em\,DSPMG} = -\left(\Gamma_{pm\,DSPMG} - \frac{\Gamma_{L_{DSPMG}}}{2} + \Gamma_{M_{DSPMG}}\right) \quad \text{(II.65)}$$

Where Γ_{pm}, Γ_L and Γ_M (Γ_L and Γ_M are reluctant torque) are defined as follows:

$\Gamma_{pm\,DSPMG} = \sqrt{\frac{3}{2}} N_r \varphi_1 i_q;$

$\Gamma_{L_{DSPMG}} = N_r (L_d - L_q) i_d i_q;$

$\Gamma_{M_{DSPMG}} = \frac{N_r}{2} M_{dq} (i_d^2 - i_q^2) + N_r M_{od} i_o i_q.$

Based on expressions (II.57) and (II.64), the power in o-d-q frame model can be achieved in formula (II.66).

$$\begin{aligned} P_{DSPMG} &= v_o i_o + v_d i_d + v_q i_q \\ &= -e_{mq} i_q - \left(R_s i_o^2 + R_s i_d^2 + R_s i_q^2\right) \\ &-\omega_e \left[M_{od} i_o i_q + 2M_{dq} (i_d^2 - i_q^2) - 2(L_d - L_q) i_d i_q\right] \\ &- \left[\frac{1}{2} L_o \frac{d i_o^2}{dt} + \frac{1}{2} L_d \frac{d i_d^2}{dt} + \frac{1}{2} L_q \frac{d i_q^2}{dt} + M_{od} \frac{d(i_o i_d)}{dt} + M_{dq} \frac{d(i_d i_q)}{dt}\right] \end{aligned} \quad \text{(II.66)}$$

Based on the electromagnetic torque, the active power *P* of the DSPMG can be rewritten as [110]:

$$P_{DSPMG} = P_{em\,DSPMG} - P_{cu} - P_{f\,DSPMG} \quad \text{(II.67)}$$

With

$P_{em\,DSPMG} = \Omega * \Gamma_{em\,DSPMG}$, electromagnetic power for DSPMG;

$P_{cu} = R_s i_o^2 + R_s i_d^2 + R_s i_q^2$, Joule loss;

$w_{f\,DSPMG} = \frac{1}{2}\{[i_{abc}]^t [L_{abc\,DSPMG}][i_{abc}]\} = \frac{1}{2}\frac{d}{dt}\left\{[i_{odq}]^t [L_{odq\,DSPMG}][i_{odq}]\right\};$

$w_{f\,DSPMG}$ Energy stored in the armature windings of DSPMG.

$$\begin{aligned} P_{f\,DSPMG} &= \frac{d}{dt} w_{f\,DSPMG} \\ &= \frac{3}{2} \mathrm{N_r} \Omega M_{dq} (i_d^2 - i_q^2) - \frac{3}{2} \mathrm{N_r} \Omega (L_d - L_q) i_d i_q \\ &+ \frac{1}{2} L_o \frac{d i_o^2}{dt} + \frac{1}{2} L_d \frac{d i_d^2}{dt} + \frac{1}{2} L_q \frac{d i_q^2}{dt} + M_{od} \frac{d(i_o i_d)}{dt} + M_{dq} \frac{d(i_d i_q)}{dt} \end{aligned} \quad \text{(II.68)}$$

The imaginary power based on (II.59) in o-d-q coordinate for DSPMG will be showed in formula (II.69).

$$\begin{aligned} Q_{DSPMG} &= v_d i_q - v_q i_d \\ &= e_{mq} i_d + \omega_e (L_q i_d^2 + L_d i_q^2) - \left(L_d i_q \frac{d i_d}{dt} - L_q i_d \frac{d i_q}{dt}\right) + \frac{M_{dq}}{2} \left(\frac{d i_d^2}{dt} - \frac{d i_q^2}{dt}\right) \\ &- M_{od} i_q \frac{d i_o}{dt} + \omega_e M_{od} i_d i_o - \omega_e \frac{L_d - L_q}{2} (i_d^2 - i_q^2) - 4\omega_e M_{dq} i_d i_q \end{aligned} \quad \text{(II.69)}$$

From equation (II.65), the DSPMG torque in o-d-q model is not exactly similar with either classic machine. And furthermore, the real power in equation (II.66) is very different from PMSG. While for the imaginary power, there are some parts completely like PMSG, and some parts which don't exist in classic machine simultaneously. All the comparisons will be detailed in the following section.

II.4.4 Comparison with Permanent Magnet Synchronous Generator

For the sake of the comparison, some general expressions of PMSG are recalled on the following:

$$\begin{cases} L_a = L_0 + L_1 \cos 2\theta_e \\ L_b = L_0 + L_1 \cos 2\left(\theta_e - \frac{2}{3}\pi\right) \\ L_c = L_0 + L_1 \cos 2\left(\theta_e - \frac{4}{3}\pi\right) \end{cases} \tag{II.70}$$

$$\begin{cases} M_{ab} = M_{ba} = M_0 + M_1 \cos 2\left(\theta_e - \frac{4}{3}\pi\right) \\ M_{ac} = M_{ca} = M_0 + M_1 \cos 2\left(\theta_e - \frac{2}{3}\pi\right) \\ M_{bc} = M_{bc} = M_0 + M_1 \cos 2\theta_e \end{cases} \tag{II.71}$$

$$\begin{cases} \varphi_{ma} = \varphi_1 \cos \theta_e \\ \varphi_{mb} = \varphi_1 \cos\left(\theta_e - \frac{2}{3}\pi\right) \\ \varphi_{mc} = \varphi_1 \cos\left(\theta_e - \frac{4}{3}\pi\right) \end{cases} \tag{II.72}$$

For PMSG, the o-d-q inductance matrix is presented in equation (II.73).

$$\begin{aligned} \left[L_{odq\,PMGM}\right] &= \begin{bmatrix} L_o & M_{od} & M_{oq} \\ M_{od} & L_d & M_{dq} \\ M_{oq} & M_{dq} & L_q \end{bmatrix} \\ &= \begin{bmatrix} L_0 + 2M_0 & \frac{1}{\sqrt{2}}(L_1 - M_1)\cos 3\theta_e & -\frac{1}{\sqrt{2}}(L_1 - M_1)\sin 3\theta_e \\ \frac{1}{\sqrt{2}}(L_1 - M_1)\cos 3\theta_e & L_0 - M_0 + \left(\frac{L_1}{2} + M_1\right) & 0 \\ -\frac{1}{\sqrt{2}}(L_1 - M_1)\sin 3\theta_e & 0 & L_0 - M_0 - \left(\frac{L_1}{2} + M_1\right) \end{bmatrix} \end{aligned} \tag{II.73}$$

If L_1 and M_1 are equal to zero, this means it is PMSSG.

The torque, the active and reactive powers for PMSG in o-d-q reference frame are obtained in formulas (II.74), (II.75) and (II.78):

$$\Gamma_{em\,PMSG} = -\left\{e_{mq}\, i_q + p\left(L_d - L_q\right) i_d i_q - 2p i_o \left(M_{od}\, i_q - M_{oq}\, i_d\right)\right\} \tag{II.74}$$

$$\begin{aligned} P_{PMSG} &= v_o i_o + v_d i_d + v_q i_q \\ &= -e_{mq}\, i_q - \left(R_s i_o^2 + R_s i_d^2 + R_s i_q^2\right) \\ &\quad -\omega_e\left[-5 i_o \left(M_{od}\, i_q - M_{oq}\, i_d\right) + \left(L_d - L_q\right) i_d i_q\right] \\ &\quad -\left[\frac{1}{2} L_o \frac{d i_o^2}{dt} + \frac{1}{2} L_d \frac{d i_d^2}{dt} + \frac{1}{2} L_q \frac{d i_q^2}{dt} + M_{od} \frac{d\left(i_o i_d\right)}{dt} + M_{oq} \frac{d\left(i_o i_q\right)}{dt}\right] \end{aligned}$$

(II.75)

$$P_{PMSG} = \Omega * \Gamma_{em_{PMSG}} - P_{cu} - P_{f_{PMSG}} \quad \text{(II.76)}$$

With

$P_{em_{PMSG}} = \Omega * \Gamma_{em_{PMSG}}$, electromagnetic power for PMSG;

$$P_{f_{PMSG}} = \frac{\mathrm{d}}{\mathrm{dt}} w_{f_{PMSG}} = -3pi_o\left(M_{od} i_q - M_{oq} i_d\right) + \frac{1}{2} L_o \frac{di_o^2}{dt} + \frac{1}{2} L_d \frac{di_d^2}{dt} + \frac{1}{2} L_q \frac{di_q^2}{dt} + M_{od} \frac{d(i_o i_d)}{dt} + M_{oq} \frac{d(i_o i_q)}{dt} \quad \text{(II.77)}$$

$w_{f_{PMSG}}$ Energy stored in the armature windings of PMSG.

$$\begin{aligned} Q_{PMSG} &= v_d i_q - v_q i_d \\ &= e_{mq} i_d + \omega_e\left(L_d i_d^2 + L_q i_q^2\right) - \left(L_d i_q \frac{di_d}{dt} - L_q i_d \frac{di_q}{dt}\right) \\ &\quad -M_{od} i_q \frac{di_o}{dt} + M_{oq} i_d \frac{di_o}{dt} - 2\omega_e i_o\left(M_{oq} i_q + M_{od} i_d\right) \end{aligned} \quad \text{(II.78)}$$

In order to compare the torque and power of DSPMG to that of classical machines (PMSSG and PSPMG), necessary expressions are summarized in Table II.4. For PMSG, if L_1=M_1=0, the expressions will be suitable for PMSSG; if L_1≠0, M_1≠0, expression will be used for PSPMG.

Table II.4 Inductance and torque expressions [92]

	PMSSG (φ_0=0)	PSPMG (φ_0=0; N_r=p)	DSPMG
L_o	$L_0 + 2M_0$	$L_0 + 2M_0$	$L_0 + 2M_0$
L_d	$L_0 - M_0$	$L_0 - M_0 + \left(\frac{L_1}{2} + M_1\right)$	$L_0 - M_0 + \left(\frac{L_1}{2} + M_1\right)\cos 3\theta_e$
L_q	$L_0 - M_0$	$L_0 - M_0 - \left(\frac{L_1}{2} + M_1\right)$	$L_0 - M_0 - \left(\frac{L_1}{2} + M_1\right)\cos 3\theta_e$
M_{od}	0	$\frac{1}{\sqrt{2}}(L_1 - M_1)\cos 3\theta_e$	$\frac{1}{\sqrt{2}}(L_1 - M_1)$
M_{oq}	0	$-\frac{1}{\sqrt{2}}(L_1 - M_1)\sin 3\theta_e$	0
M_{dq}	0	0	$-\left(\frac{L_1}{2} + M_1\right)\sin 3\theta_e$
Γ_{pm}	$\sqrt{\frac{3}{2}} N_r \varphi_1 i_q$		
Γ_L	$N_r\left(L_d - L_q\right) i_d i_q$		
Γ_M	$\frac{N_r}{2} M_{dq}\left(i_d^2 - i_q^2\right) + N_r M_{od} i_o i_q$		
Γ_{em}	$-\Gamma_{PM}$	$-(\Gamma_{PM} + \Gamma_L)$	$-\left(\Gamma_{PM} - \frac{\Gamma_L}{2} + \Gamma_M\right)$
P_{em}	$\Omega * \Gamma_{em}$		
P_{cu}	$R_s i_o^2 + R_s i_d^2 + R_s i_q^2$ $(R_s i_a^2 + R_s i_b^2 + R_s i_c^2)$		
P	$P = P_{em} - P_{cu} - P_f$		

For conventional generators, d-q axes inductances L_d & L_q are well decoupled and constant, while for DSPMG, they have sinusoidal components with 3 times frequency of EMF. In addition,

the mutual inductances are either constant (M_{od}) or having sinusoidal-variation with 3 times frequency of EMF (M_{dq}) (see Table II.4).

The torque equation can be easily analyzed as follows: for the PMSSG, the torque (Γ_{pm}) is always from PM; for the PSPMG, the torque ($\Gamma_{pm} + \Gamma_L$) is not only from the PM, but also from the reluctance. While for DSPMG, both PM and reluctance can create the torque, and there is also a third term (Γ_M) produced principally by the mutual inductance between d and q axes cross effect [92].

II.5 *Conclusion*

This chapter highly focuses on the modeling of each part of the MCECS: marine current, turbine and DSPMG.

Although several methods to model the marine current exist right now, in the first part of this chapter, only two popular models (HAM and SHOM) are introduced and realized by Matlab/Simulink®. However, considering the SHOM data is based on long term observation and is more experimental and realistic than HAM. The SHOM model is preferred for our study.

Then, the basic theory for the turbine modeling, BEM, is explained in the second section. The tip and hub losses, and as well as the wake state are also considered. Appropriate process to calculate the turbine power coefficient is then presented. Based on these, one theoretical turbine based on the NACA XXYZ blade type is proposed for MCECS (10 kW at marine speed 2.5 m/s).

Finally, the modeling of special low speed generator DSPMG is presented. The classic abc model and one novel dynamic d-q model based on Concordia and Park transformations are all developed. In accordance of the dynamic d-q model, the comparisons of the active power, reactive power and torque between DSPMG and conventional PMSGs (PMSSG and PSPMG) are analyzed. As the power and torque expressions are not exactly as the conventional PMSGs expression, the classic sinusoidal current waveform appears difficult to get the constant torque and power. As a result, the choice of the suitable current for DSPMG is very important.

In the following chapter, the analysis of the current and influence of the inductance will be discussed.

Chapter III

Current Supply Waveforms and Analysis of Generator Performances

NOMENCLATURE

P Active power (W);

Q Reactive power (VAR);

P_{em} Electromagnet power (W);

P_{cu} Joule losses (W);

Γ_{em} Electromagnetic Torque (Nm);

θ_{on} Ignition angle (°);

θ_{off} Extinction angle (°).

GLOSSARY

DSPMG	Doubly Salient Permanent Magnet Generator
EMF	ElectroMotive Force
FFT	Fast Fourier Transform
GWM	Generator With Mutual inductance
GNM	Generator Without Mutual inductance
VRM	Variable Reluctance Machine

III.1 *Introduction*

Until now, there are many researchers studying Doubly Salient Permanent Magnet Generators (DSPMGs) which are the same family as our machine. Many articles focus on the DSPMG design, modeling and control [90] [94] - [101]. However, most of these papers neglect the DSPMG stator mutual inductance influence on the machine performances. Thus, in this chapter, we will focus on this mutual inductance influence based on different stator currents.

In this chapter, the electromagnetic torque is considered as the first criterion. The goal is to obtain a quasi-constant torque in steady state operation. In order to determine the suitable stator current for this special machine, the classical square and sinusoidal current waveforms are first applied and analyzed for generators with (GWM) and without (GNM) mutual inductances between the stator phases. Then, some other special waveforms will be deduced and tested. In order to simplify the analysis, the mechanical (electrical) speed is considered to be constant.

III.2 *Square Current Waveforms*

As presented in Chapter II, the DSPMG is designed on the basis of VRM [89]. In [89], Luc MOREAU has proposed square current phase by phase for VRM. Thus, to analyze performances of DSPMG, the same current waveform is used.

According to the torque expression in (II.51), the reluctant torque is the product of the deviation of the inductance and the square of current; the magnet torque is the product of the deviation of the PM-flux linkage and the current. This means the direction of current only change the PM torque sign. As we have discussed in Chapter II, the PM-flux linkage and the inductance have the same period and variation. Supposing the total torque is always the sum of these two positive parts, the current must be positive and be better to implement when the inductance and PM-flux linkage rise up just as showed in Fig.III.1.

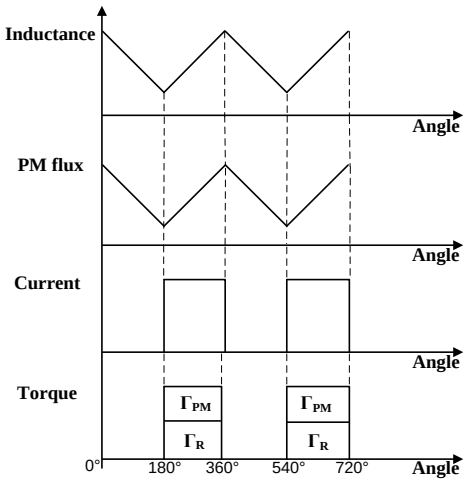

Fig.III.1 DSPMG – inductance, PM-flux linkage, current and torque

Considering that every phase will be supplied by only one current, this means these currents are mutually disjointed and each takes up one third electrical period. The first test current is given in Fig.III.2. The phase current is in phase with relative EMF (ElectroMotive Force) for this kind of current. Each phase of the machine is supplied when the inductance and PM-flux linkage increase. In Fig.III.2, the current of phase A begins at 210° and ends at 330°. In order to bring into correspondence with the conventional notation which always consider the three phase currents begin from phase A, the ignition and extinction angles of phase A are regarded as 180° less than the angle in the coordinate in Fig.III.2. This means the ignition and extinction angles (θ_{on} and θ_{off}) are 30° and 150° respectively.

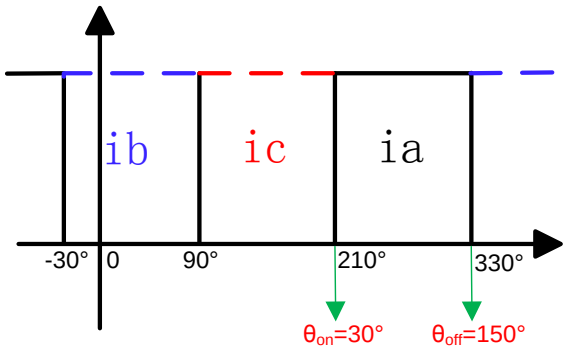

Fig.III.2 Square current waveforms

For the simulation in this chapter, the inductances calculated by taking into account the saturation effect, are considered constant with the variation of the stator current. We suppose then that the saturation state of the machine is imposed by the permanent magnets magnetic flux. The parameters of machine given in chapter 2 are presented in Table III.1.

Table III.1 Electrical parameters of the machine

Rs	φ_0	φ_1	L_0	L_1	M_0 (If necessary)	M_1 (If necessary)
0.08837 Ω	1.455 Wb	0.4805 Wb	25.5 mH	2.5 mH	-12.4 mH	2.5 mH

An ideal simulation results for the square currents are showed in Fig.III.3. A square current with 100 A amplitude and 50 Hz electrical frequency is used. Ideally, the DC-bus voltage is regarded as infinite. The current can jump to the reference value at commutation which will cause a peak in the machine side voltage.

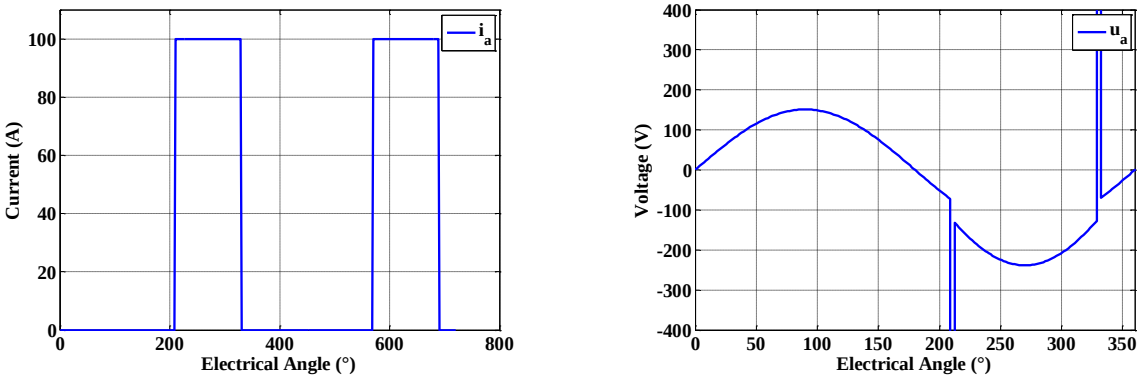

Fig.III.3 Square current and relative voltage

However, in reality, the machine current cannot change greatly in a short time since the DC bus voltage V_{DC} of the converter is limited. If the DC bus voltage is large, the current can increase and decrease quickly; on the contrary, the current will change more slowly. In this section, the DC bus voltage V_{DC} is regarded as constant and equal to 800V which has already presented in [89]. An asymmetrical half bridge circuit converter (see in Fig.III.4) will be adopted to assure interface between DSPMG and a resistive load in the Matlab/Simulink®.

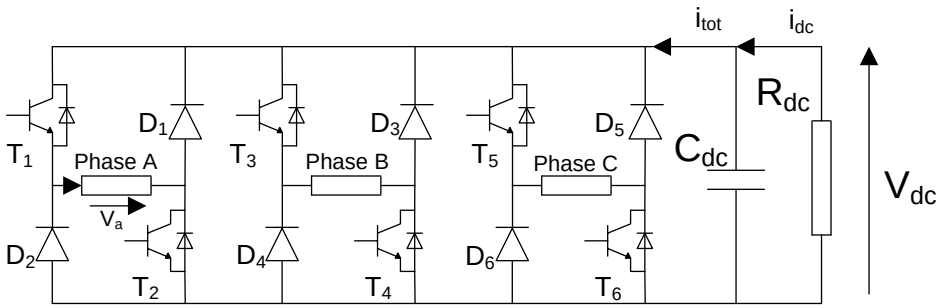

Fig.III.4 Asymmetrical Half Bridge converter

If the current need increase, the positive DC bus voltage V_{dc} is applied to j phase (it means $V_j = V_{dc}$, open the switches T for each phase). If the current needs decrease, the negative DC bus voltage $-V_{dc}$ is applied to j phase (it means $V_j = -V_{dc}$, close the switches T for each phase). If and only if the simulated currents equate to the reference current, only the upper or lower switches are closed (it means $V_j=0$). Assuming that converter losses are neglected, the phase voltage expression is then given in (III.1). The state of the switches is summarized in Table III.2.

$$V_j = S_j V_{dc} \tag{III.1}$$

Table III.2 Principle of Asymmetrical Half Bridge Converter

	Voltage	Closed Switch	S_j
Current: Reference > Simulated	$+V_{dc}$	T_{2k+1}, T_{2k+2}	1
Current: Reference = Simulated	0	T_{2k+1}, D_{2k+2} or D_{2k+1}, T_{2k+2}	0
Current: Reference < Simulated	$-V_{dc}$	D_{2k+1}, D_{2k+2}	-1

Owing to the converter, the machine current needs some time to reach the current reference when closing the switches. As a result, it is possible to find more than one phase current in the machine at some time with certain ignition and extinction current angles. This means the mutual inductance maybe affect the electromagnetic torque and power. Therefore, it is necessary to analyze the influence of the mutual inductance.

In order to simplify the notation, DSPMG with mutual inductance is regarded as: GWM (Generator With Mutual inductance); DSPMG without mutual inductance is noted as: GNM (Generator Without Mutual inductance). The current, voltage and torque for GWM and GNM are showed in Fig.III.5, Fig.III.6 and Fig.III.7.

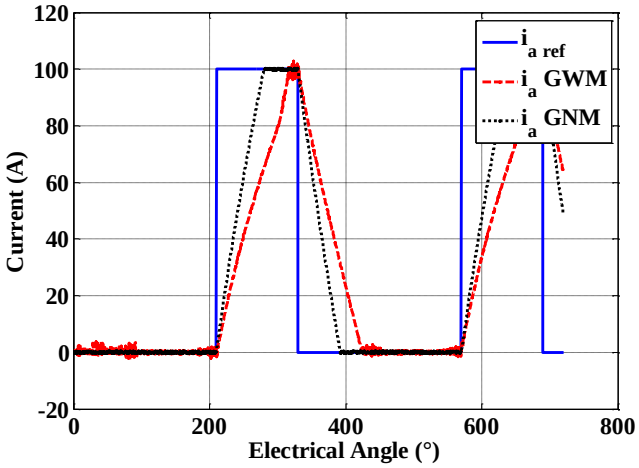

Fig.III.5 Reference and simulated current (100A)

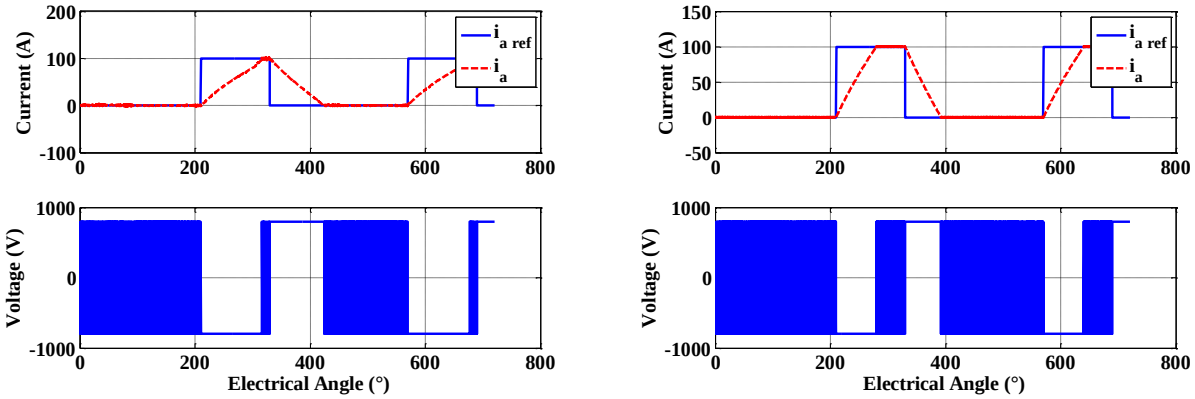

a) For GWM b) For GNM

Fig.III.6 Current and voltage for phase A with converter

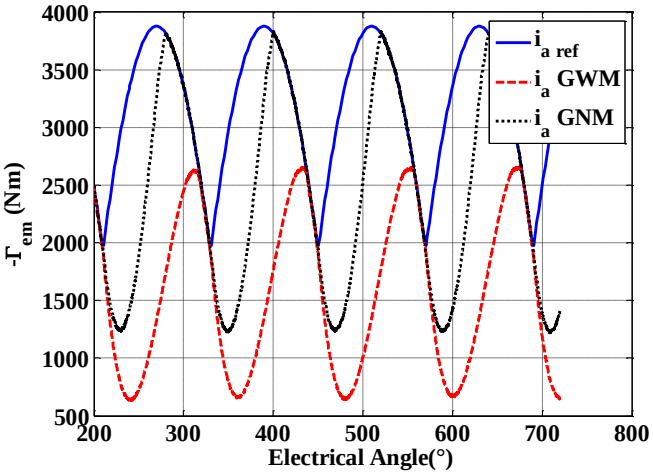

Fig.III.7 Torque for 100 A, 50Hz square waveform current

From Fig.III.5 and Fig.III.6, it is clear that the mutual inductance affects the current reference tracking and the GWM torque is even smaller than that of GNM. Torque and power for both GWM and GNM are presented in Table III.3.

Table III.3 Comparison of the torque for DSPMG with and without mutual inductance

DSPMG	Mean Γ_{em}	Min Γ_{em}	Max Γ_{em}	Kr	Mean P	Mean Q	Mean P_{cu}
GWM	-1597.9	-640.76	-2658.8	126.29%	-7709	35234	569
GNM	-2489.1	-1217.9	-3827.4	104.83%	-12551	26855	699

Where, K_r is the torque ripple coefficient which is defined as:

$$K_r = \left| \frac{\Gamma_{em\ max} - \Gamma_{em\ min}}{\Gamma_{em\ mean}} \right| \quad \text{(III.2)}$$

For the same current reference, the GNM has much more mean torque than GWM, and nearly 20% less ripple. From this table, GNM will increase almost 50% for active power; meanwhile, it can also reduce 30% for reactive power.

As the torque ripple is still very big for both machines, this means that the above selected electrical period (θ_{on}=30° and θ_{off}=150°) is not a good choice for the generator. Therefore, in the following section, the torque ripple will be evaluated for several electrical speed and different ignition and extinction angles for both GWM and GNM. In this simulation, 10 electrical speeds from 5 Hz to 50 Hz, as well as 10 current amplitudes between Im and Im/10 are considered. The ignition angle and extinction angle will be chosen according to [89]:

- $\theta_{on} \in$ [-60°, 80°];
- $\theta_{off} \in$ [100°, 200°];

In our study, the ignition and extinction angles are varied for each square current amplitude and electrical frequency to analyze all the possibilities, and then find out the optimal ignition and extinction angles for different amplitude and electrical frequency after comparison. There are some optimization algorithms to find the optimum angles in order to minimize torque ripple, such as GA (Genetic Algorithm) [89] [90].

III.2.1 Generator with Mutual Inductance

The result of the optimal ignition and extinction angles for the minimum torque ripple are presented in Table III.4 and Table III.5 respectively. The minimum torque ripple coefficients and the corresponding average torque are presented in Table III.6 and Table III.7.

Table III.4 Optimal θ_{on} for GWM (°)

Im (A) / *f* (Hz)	10	20	30	40	50	60	70	80	90	100
5	-2	3	6	8	11	12	11	13	16	16
10	-1	4	7	6	5	9	9	9	11	-36
15	2	2	4	6	7	5	7	-35	-35	-35
20	0	2	4	2	4	6	-35	-34	-36	-37
25	-5	1	4	2	1	4	-36	-36	-37	-37
30	0	0	2	1	3	-35	-35	-35	-35	-36
35	-3	1	-2	1	2	-34	-33	-35	-34	-34
40	0	-2	-1	-5	-34	-35	-32	-31	-32	-30
45	1	-3	3	-6	-33	-32	-31	-29	-26	-23
50	-1	-6	-1	-2	-32	-30	-28	-25	-18	**-11**

Table III.5 Optimal θ_{off} for GWM (°)

Im (A) / *f* (Hz)	10	20	30	40	50	60	70	80	90	100
5	179	174	172	169	167	166	164	162	160	160
10	176	173	171	169	166	165	163	161	158	200
15	176	173	169	166	166	164	162	199	198	198
20	175	172	170	165	164	163	197	197	195	194
25	177	177	167	164	161	161	193	193	192	192
30	178	171	167	165	161	192	192	191	191	190
35	177	174	168	165	161	191	191	189	189	188
40	176	171	167	168	190	188	189	189	187	188
45	180	167	162	165	189	187	187	187	187	189
50	175	168	166	162	187	186	186	184	189	**193**

From Table III.4 and Table III.5, the optimal ignition angles θ_{on} are between -37° and 16°, the extinction angles θ_{off} change from 158° to 199°. The different angles depend on the amplitude and the frequency of the square current reference.

Table III.6 Minimum torque ripple coefficient for GWM (%)

Im (A) / *f* (Hz)	10	20	30	40	50	60	70	80	90	100
5	27.55	24.02	25.86	28.48	32.15	35.88	39.62	43.41	47.31	51.06
10	28.80	23.50	26.08	28.52	32.10	35.82	39.63	43.27	47.30	48.61
15	28.84	24.61	25.79	28.63	32.18	35.80	39.59	41.95	40.84	39.79
20	28.95	24.35	26.21	28.65	31.99	35.92	39.30	37.81	35.37	34.87
25	29.53	24.35	26.14	28.51	31.79	35.48	34.11	33.07	31.61	31.40
30	29.16	24.67	25.78	28.73	31.78	33.41	31.58	30.47	29.40	27.78
35	28.96	24.03	26.27	28.21	32.08	30.25	29.05	27.92	27.78	26.88
40	28.78	24.99	25.99	28.28	30.74	28.26	27.41	27.58	26.60	26.90
45	28.70	23.10	25.93	27.96	28.24	26.72	25.96	25.47	26.76	27.50
50	28.92	24.44	24.59	28.12	26.98	25.13	24.91	25.43	26.45	**28.83**

Table III.7 Average torque Γ_{em} for GWM (Nm)

Im (A) / *f* (Hz)	10	20	30	40	50	60	70	80	90	100
5	-289	-585	-886	-1190	-1501	-1820	-2145	-2483	-2836	-3191
10	-285	-581	-881	-1184	-1492	-1812	-2137	-2470	-2820	-1982
15	-282	-578	-877	-1180	-1490	-1805	-2130	-1699	-1880	-2028
20	-281	-576	-877	-1177	-1488	-1802	-1543	-1732	-1893	-2040
25	-277	-573	-873	-1177	-1482	-1798	-1563	-1741	-1902	-2042
30	-276	-573	-871	-1173	-1481	-1390	-1570	-1754	-1907	-2053
35	-275	-569	-869	-1170	-1476	-1393	-1579	-1749	-1903	-2058
40	-274	-568	-867	-1160	-1188	-1398	-1590	-1749	-1914	-2034
45	-272	-565	-863	-1160	-1194	-1417	-1589	-1750	-1902	-1992
50	-271	-567	-859	-1160	-1206	-1410	-1586	-1787	-1838	**-1808**

The torque ripple will vary between 23.10% and 51.06%. For the nominal function (100A and 50Hz), the optimal ignition and extinction angles are -11° and 193° respectively. The minimum torque ripple coefficient will be 28.83%, and the related average torque is -1808 Nm. The corresponding active, reactive power and the Joule losses are -9441 W, 55 kVAR and 1396 W respectively. Compared with the current reference with conduction time between 30° to 150° as summarized in Table III.3, the torque ripple is much smaller and the average torque is highly

improved. Meanwhile, the active and reactive power, and as well as Joule losses are also increased.

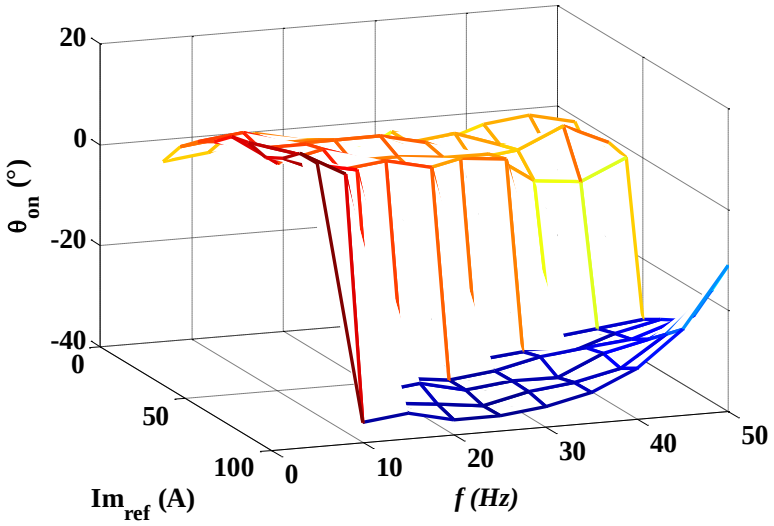

Fig.III.8 θ_{on} for GWM (°)

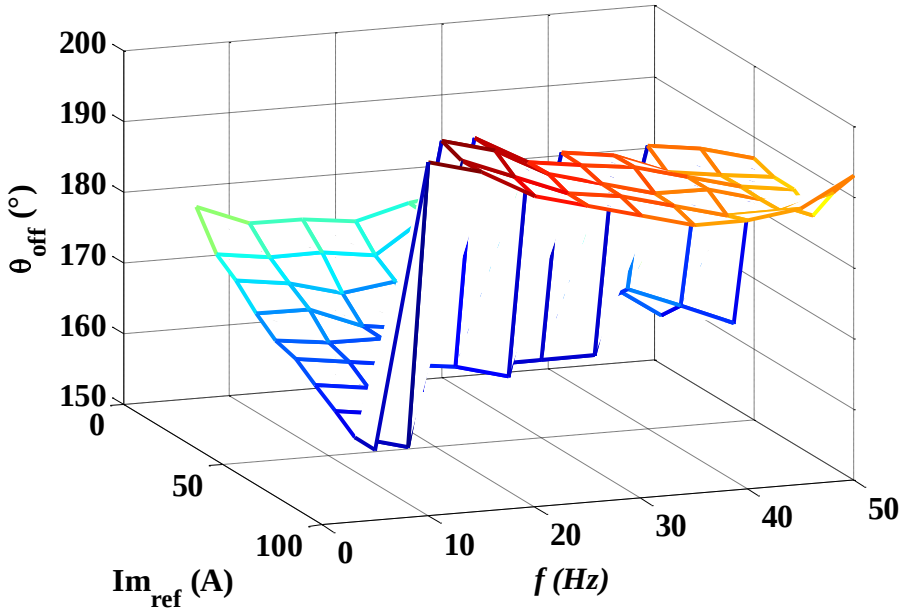

Fig.III.9 θ_{off} for GWM (°)

From Fig.III.8 and Fig.III.9, with the increasing of the amplitude and the frequency of the current, the ignition angle θ_{on} and extinction angle θ_{off} are practically constant firstly. Then θ_{on} decreases and θ_{off} increase depending on the current amplitude and the frequency. If we increase the DC-bus voltage, the conducting time for every current will surely decrease.

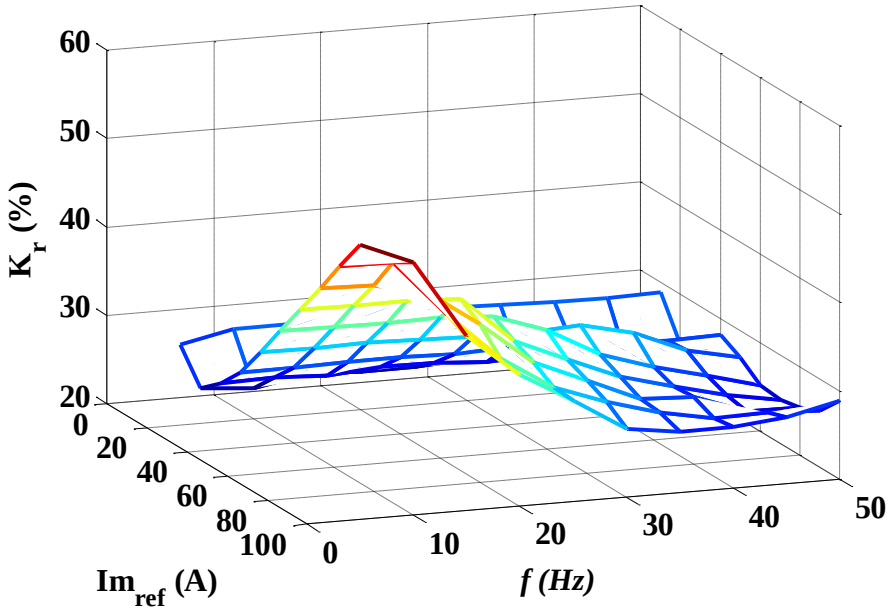

Fig.III.10 Minimum torque ripple coefficient for GWM

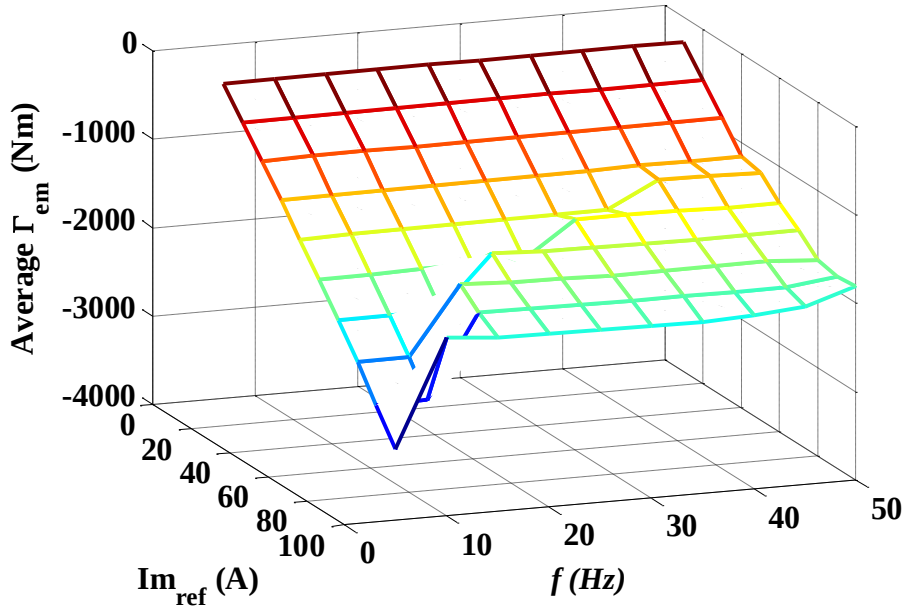

Fig.III.11 Average torque Γ_{em} for GWM

From Fig.III.10 and Fig.III.11, principally, when the current amplitude is relatively small (<50 A), for a given frequency, GWM can get nearly a same torque performances (torque ripple coefficients and average torque).

To minimize the torque ripple, the conducting time increases when the current amplitude is relative big (≥50 A). Normally, the machine with higher current will generate more electromagnetic torque. However, as the DC-bus voltage cannot make the current well track the reference during the small given time, when the electrical frequency increase (the electrical period decrease), the average torque will reduce significantly. For example, the current with 100

A amplitude, the torque changes from -3191 Nm to -1808 Nm form the frequency from 5 Hz to 50 Hz. Simultaneously, the torque ripple coefficient decreases from 51% and 29%.

III.2.2 Generator without Mutual Inductance

The same analysis to find the minimum torque ripple is taken for GNM. From the first two tables, the variation of the optimal ignition angles θ_{on} and the extinction angles θ_{off} is reduced. The ignition angles only changes from -24° to 1° (instead of -37° to 16°) and the extinction angles are between 154° and 180°.

Table III.8 Optimal θ_{on} for GNM (°)

Im (A) / *f* (Hz)	10	20	30	40	50	60	70	80	90	100
5	-2	0	0	-1	-1	-1	-1	-2	-3	-3
10	0	-1	-1	-1	-2	-4	-3	-3	-5	-5
15	-1	-1	-3	-3	-5	-5	-4	-7	-8	-9
20	-3	-3	-2	-4	-6	-7	-9	-9	-9	-11
25	0	-5	-3	-7	-5	-10	-9	-11	-13	-13
30	0	-4	-7	-8	-9	-9	-12	-13	-14	-17
35	1	-2	-4	-6	-10	-11	-11	-16	-17	-19
40	-6	-2	-5	-8	-13	-11	-16	-17	-21	-23
45	-2	-3	-7	-10	-11	-13	-18	-20	-22	-22
50	-4	-7	-7	-11	-14	-15	-19	-24	-24	**-7**

Table III.9 Optimal θ_{off} for GNM (°)

Im (A) / *f* (Hz)	10	20	30	40	50	60	70	80	90	100
5	180	180	180	178	179	178	178	177	179	177
10	179	179	178	178	176	176	177	175	175	174
15	178	177	175	175	176	174	175	172	173	173
20	180	177	175	176	175	172	170	169	169	169
25	179	176	177	176	171	172	170	169	168	165
30	174	174	172	173	173	169	167	166	165	163
35	177	176	172	170	170	166	165	162	162	161
40	180	172	175	168	167	164	165	162	161	159
45	175	173	170	169	165	166	161	159	158	157
50	180	173	173	165	164	161	162	158	154	**167**

Table III.10 Minimum torque ripple coefficient for GNM (%)

Im (A) / *f* (Hz)	10	20	30	40	50	60	70	80	90	100
5	27.82	20.47	18.48	17.62	16.92	16.21	15.84	15.77	15.55	15.41
10	27.22	20.50	18.20	17.15	16.66	16.15	15.91	15.68	15.44	15.40
15	27.48	20.85	18.45	17.44	16.48	16.17	15.87	15.69	15.49	15.39
20	27.05	20.49	18.54	16.99	16.47	16.03	15.90	15.71	15.48	15.37
25	26.74	20.51	18.39	17.36	16.48	16.03	15.88	15.65	15.47	15.47
30	27.38	19.62	18.20	17.14	16.60	16.08	15.80	15.68	15.64	15.53
35	26.20	20.08	18.29	17.25	16.46	16.27	16.04	15.79	15.65	15.60
40	27.47	21.00	18.33	17.38	16.78	16.17	16.02	15.81	15.70	15.61
45	26.60	21.19	18.24	17.22	16.63	16.27	16.12	15.89	15.83	15.73
50	28.40	20.63	18.67	17.42	16.51	16.37	16.14	15.92	15.70	**14.98**

Table III.11 Average torque Γ_{em} for GNM

Im (A) / f (Hz)	10	20	30	40	50	60	70	80	90	100
5	-301	-618	-951	-1297	-1660	-2038	-2430	-2839	-3261	-3701
10	-301	-618	-950	-1297	-1659	-2036	-2428	-2836	-3259	-3696
15	-301	-618	-949	-1296	-1658	-2034	-2425	-2832	-3252	-3687
20	-301	-617	-949	-1295	-1657	-2032	-2422	-2826	-3245	-3677
25	-301	-617	-949	-1294	-1654	-2029	-2418	-2819	-3234	-3662
30	-301	-617	-947	-1293	-1652	-2026	-2412	-2811	-3222	-3645
35	-300	-616-	-947	-1291	-1650	-2021	-2404	-2800	-3208	-3625
40	-299	-615	-946	-1290	-1646	-2015	-2397	-2789	-3190	-3601
45	-299	-615	-945	-1289	-1643	-2010	-2389	-2777	-3172	-3571
50	-299	-615	-944	-1286	-1641	-2005	-2378	-2761	-3152	**-3313**

From Table III.10 and Table III.11, the minimum torque ripple is much smaller than that of GWM, between 14.98% and 28.4%. The minimum torque ripple coefficient for the nominal current (100 A, 50Hz) is only 14.98%, just one half of that of GWM. Meanwhile, the average torque for GNM (-3313 Nm) is much bigger than that of GWM (-1808 Nm). Compared with GWM for the nominal current, GNM can generate more active power (-17 kW) and lead to less reactive power and Joule losses (50 kVAR, 1163 W).

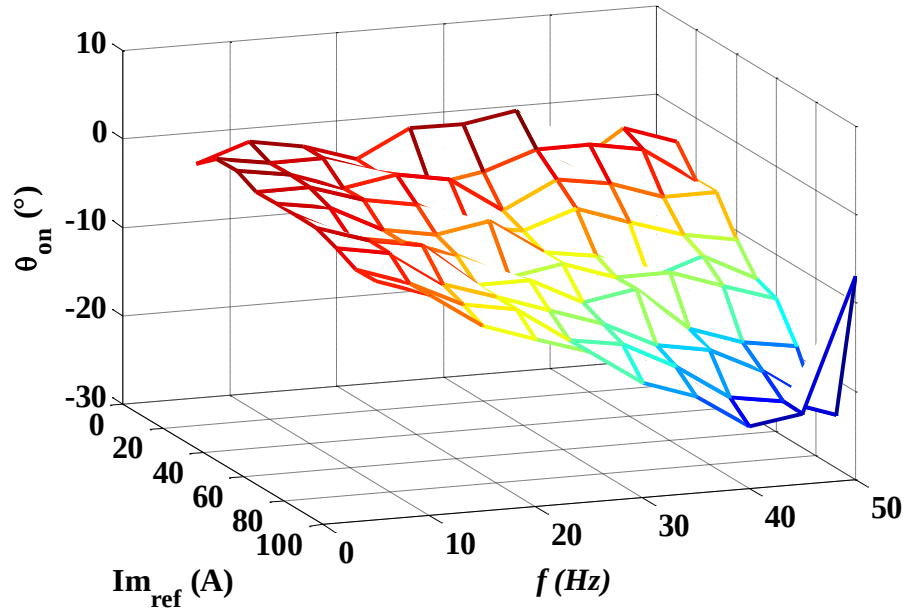

Fig.III.12 θ_{on} for GNM (°)

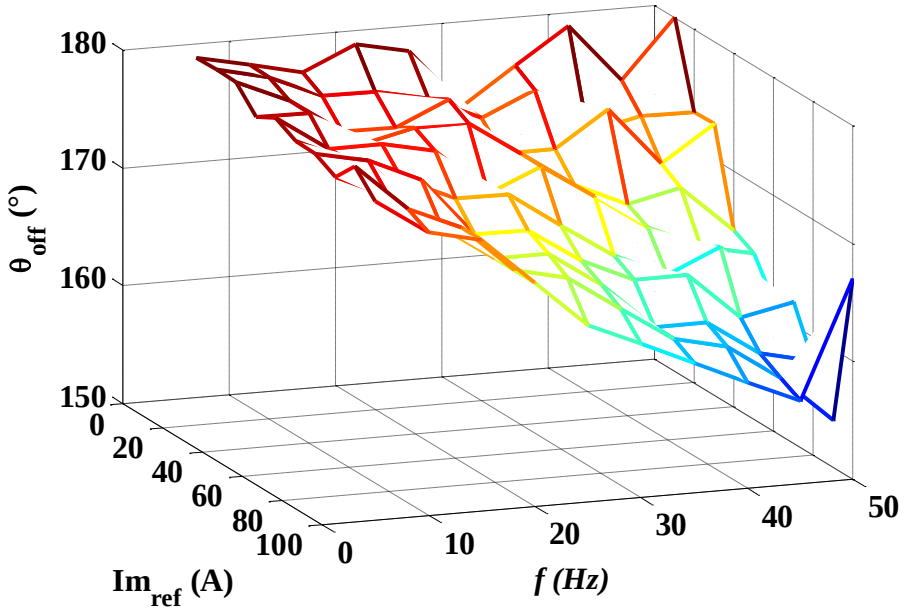

Fig.III.13 θ_{off} for GNM (°)

Thanks to the disappeared mutual inductance, the current can reach the reference more quickly than GWM. As a result, from Fig.III.12 and Fig.III.13, the ignition and extinction angles don't give the same phenomenon as GWM which have an abrupt change increasing the conducting time to reduce the torque ripple when the electrical frequency and amplitude are relatively big.

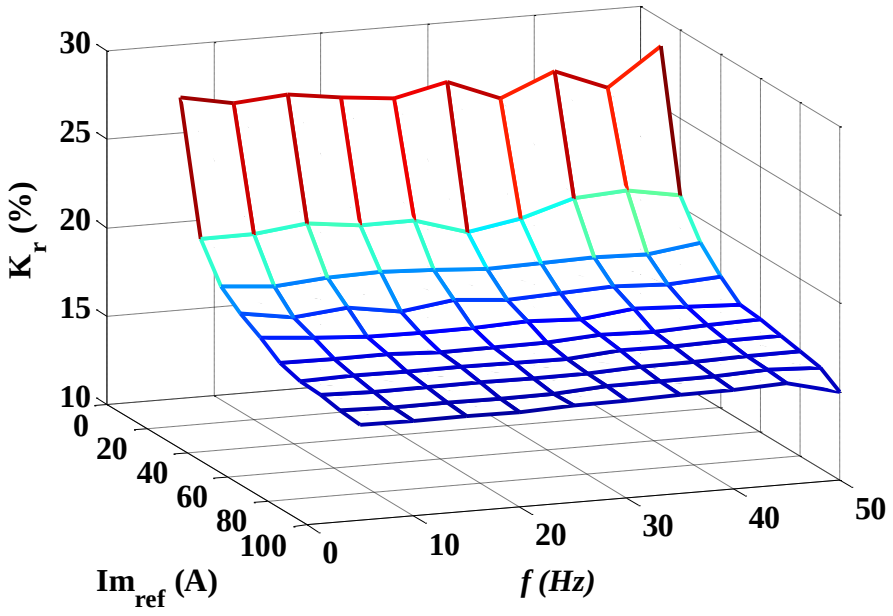

Fig.III.14 Minimum torque ripple coefficient for GNM

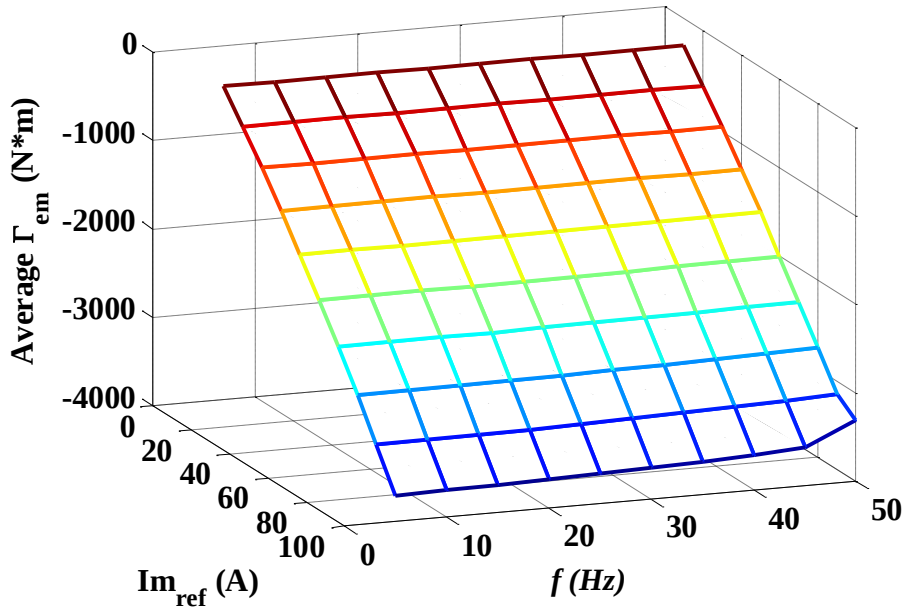

Fig.III.15 Average torque Γ_{em} for GNM

For GNM, the relationship among electrical frequency, current amplitude and the torque is simpler than that of GWM. From Fig.III.14 and Fig.III.15, each current from 10 A to 100 A almost has the same torque ripple coefficients and average torque for the electrical frequency between 10 Hz and 50 Hz. For the same electrical frequency, the torque ripple coefficient will decrease and the average torque will increase when the current amplitude increases. For the same current amplitude, the variation of electrical frequency between 5 Hz and 50 Hz doesn't change the ripple and average torque.

III.2.3 Performances Comparison

Sections III.2.1 and III.2.2 mainly discuss the performances of square waveform current applied to both GWM and GNM. The optimal ignition and extinction angles to minimize torque ripple of these machines are researched.

For each machine, the minimum torque ripples are presented in Table III.6 and Table III.10 respectively. As the existence of the mutual inductance, although the conducting time of GWM is enlarged, the average torque will significantly decrease when the electrical frequency increases. In the case of GNM, for each current amplitude, the average torque can get nearly the same level when the electrical frequency varies between 5 Hz and 50 Hz

Besides, for every current with different amplitude and electrical frequency, the torque ripples of GNM are always smaller than that of GWM.

In conclusion, GNM appears having better torque performance than GWM for the same current amplitude and electrical frequency. It's better to design the machine with the same structure but without mutual inductance.

Some other researches based on the square waveform current to reduce the torque ripple are also carried out (see Appendix V).

III.3 *Sinusoidal Current Waveforms*

In this section, the three-phase sinusoidal waveform currents will be applied to analyse behaviour of DSPMG in terms of average torque and minimisation of ripples. Then, an optimal waveform current will be proposed to enhance the performances.

III.3.1 Basic Sinusoidal Waveform

If a simple balanced three phase sinusoidal waveforms is applied, after transformation, the corresponding homopolar current i_o equates to zero, and the currents in d & q coordinate references will be constant. Therefore, according to electromagnetic torque formula (II.65), the principle torque from the PM-flux linkage is the constant torque, the reluctant torque from the inductance is variable, and can be considered as ripple torque in the condition of constant frequency and current amplitude. In this situation, the rated q-axis current can be written as:

$$i_q = -\sqrt{\frac{2}{3}}\frac{\Gamma_{em}}{N_r \varphi_1} \tag{III.3}$$

For one generator with 10 kW, 50 tr/min, it means the rated current in q-axis (i_q) is 50 A. Later, the problem consists in determining the load angle α between the stator current and EMF. Based on the formula (II.56), the EMF in phase A can be written in (III.4), so the instantaneous current for phase A is given by equation (III.5) with the load angle α.

$$e_{ma} = -\omega_e \varphi_1 \sin\theta_e = -\varphi_1 N_r \Omega \sin\theta_e \tag{III.4}$$

$$i_a = -I_m \sin(\theta_e + \alpha) \tag{III.5}$$

Thus, the Joule losses can be deduced as:

$$P_{cu} = \frac{3}{2} R_s \times I_m^2 = R_s \times \frac{I_q^2}{\cos^2\alpha} \tag{III.6}$$

The power factor cos φ of the machine is simply defined as:

$$\cos\varphi = \left| \frac{P_{mean}}{\sqrt{P_{mean}^2 + Q_{mean}^2}} \right| \tag{III.7}$$

The active and reactive power expressions in (II.66) and (II.69) can be simplified as follows:

$$P_{DSPMG} = -\frac{3}{2} N_r \Omega \varphi_1 I_m \cos\alpha - \frac{3}{2} R_s I_m^2 - 3N_r \Omega \left(\frac{L_1}{2} + M_1\right) I_m^2 \sin(3\theta_e + 2\alpha) \tag{III.8}$$

$$\begin{aligned} Q_{DSPMG} = & -\frac{3}{2}\varphi_1 N_r \Omega I_m + \sin\alpha + N_r \Omega (L_0 - M_0) I_m^2 \\ & + 3N_r \Omega \left(\frac{L_1}{2} + M_1\right) I_m^2 \cos 2\alpha \cos 3\theta_e - 2N_r \Omega \left(\frac{L_1}{2} + M_1\right) \sin 3\theta_e \sin 2\alpha \end{aligned} \tag{III.9}$$

Based on the equations (II.66), (II.69), (III.2), (III.5), (III.6) and (III.7), the variations of current amplitude, Joule losses, active and reactive powers, power factor and torque ripple coefficients versus load angle for both GWM and GNM are showed in Fig.III.16 to Fig.III.21.

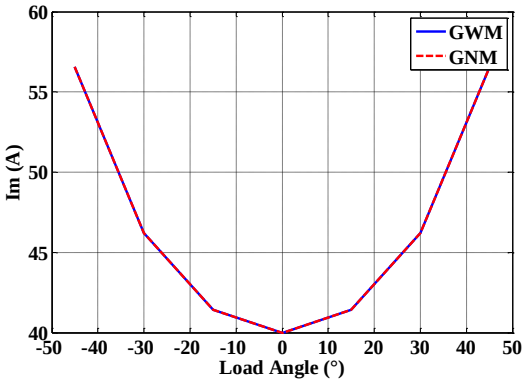

Fig.III.16 Amplitude of current

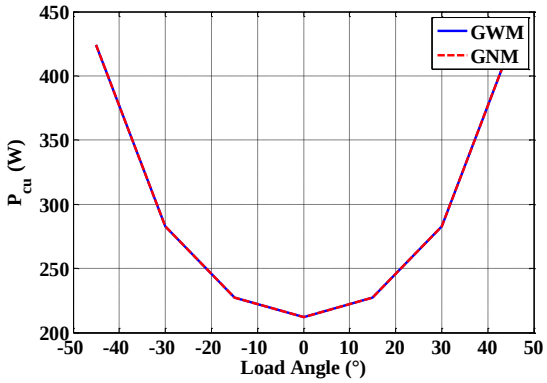

Fig.III.17 Average value of Joule losses

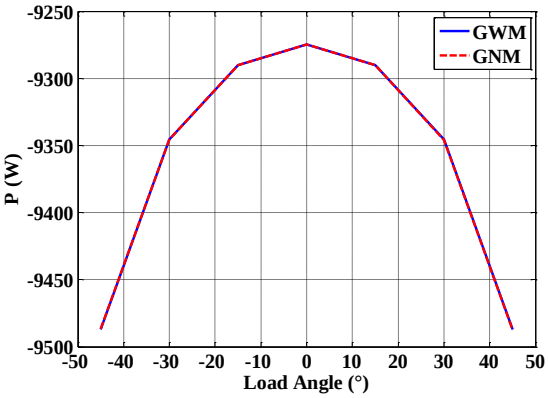

Fig.III.18 Average value of active power

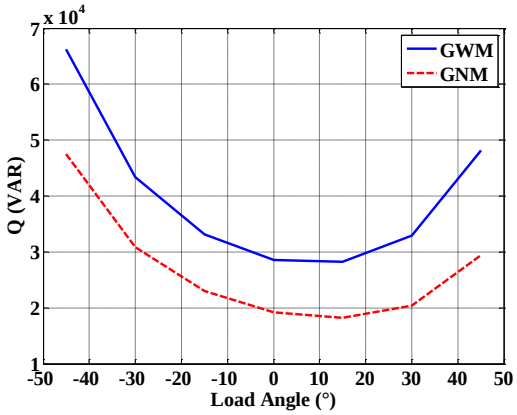

Fig.III.19 Average value of reactive power

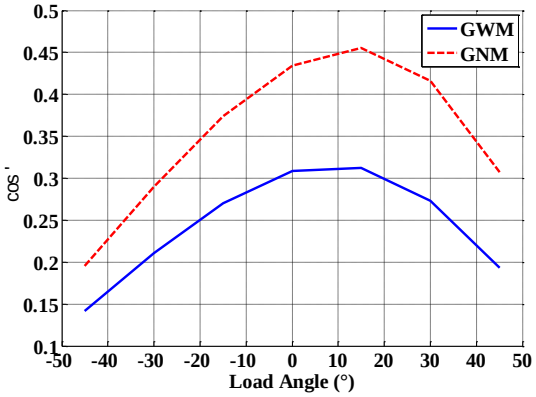

Fig.III.20 Power factor

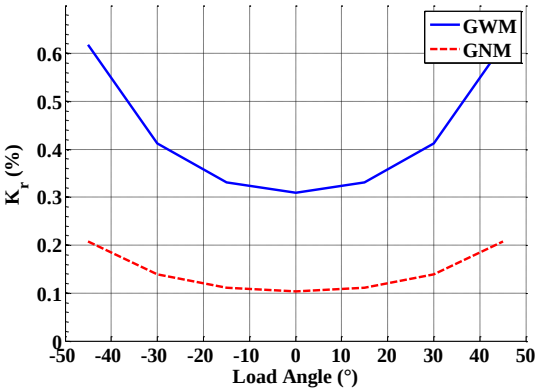

Fig.III.21 Torque ripple coefficient

The current amplitude and losses variations presented in Fig.III.16 and Fig.III.17 have naturally the same forms and are identical for GWM and GNM. From Fig.III.18 and Fig.III.19, although changing the load angle can change the active power, it will vary the reactive power significantly. Fig.III.20 gives the relative power factor for these two DSPMG. Principally, the maximum power factor will happen near the 10°, and GNM usually has bigger power factor for

each load angle than that of GWM. However, the current with 0° load angle possesses the minimum torque ripple for both two machines as shown in Fig.III.21. Due to the mainly objective which minimize the torque ripple and losses, the load angle is considered to be 0°. Then, the nominal amplitude of the sinusoidal current waveform I_m is defined as 40 A in this section.

In order to simplify the simulation period and make the current be in phase with EMF, the sinusoidal waveform is simplified and given as:

$$i_a = -40 \sin \omega_e t \tag{III.10}$$

The voltage, torque and power expressions can be rewritten as:

$$-v_a = \omega_e \left[-\varphi_1 \sin\theta_e - \frac{RI_m}{\omega_e} \sin\theta_e + (-L_0 + M_0) I_m \cos\theta_e - (L_1 + 2M_1) I_m \cos 2\theta_e \right] \tag{III.11}$$

$$\Gamma_{DSPMG} = -\left[\frac{3}{2} N_r \varphi_1 I_m + \frac{3}{4} N_r \left(\frac{L_1}{2} + M_1 \right) \sin 3\theta_e \, I_m^2 \right] \tag{III.12}$$

$$P_{DSPMG} = -\frac{3}{2} N_r \Omega \varphi_1 I_m - \frac{3}{2} R_s I_m^2 - 3N_r \left(\frac{L_1}{2} + M_1 \right) \sin 3\theta_e \, \Omega I_m^2 \tag{III.13}$$

$$\mathrm{Q}_{DSPMG} = \frac{3}{2} N_r \Omega (L_0 - M_0) I_m^2 + 3N_r \Omega \left(\frac{L_1}{2} + M_1 \right) \cos 3\theta_e \, I_m^2 \tag{III.14}$$

From the equation (III.11), the voltage is composed of two parts: one is in function of θ_e; while, the other part varies with $2\theta_e$. This means that although the current reference is sinusoidal, the stator voltage is not sinusoidal and has a 2nd order harmonic component which highly depends on the fundamental of the self and mutual inductances (L_1 and M_1).

According to equations (III.12), (III.13) and (III.14), the instantaneous electromagnetic torque depends on the electrical position. For the active power, if the Joule losses are neglected, it is approximately considered as the product of mechanical speed and one function based on electromagnetic torque. The reactive power can be regarded as the product of the mechanical velocity and one simple function determined by the current amplitude and electrical position.

The voltage, torque, active and reactive power variations versus electrical angle are presented in Fig.III.22 to Fig.III.25.

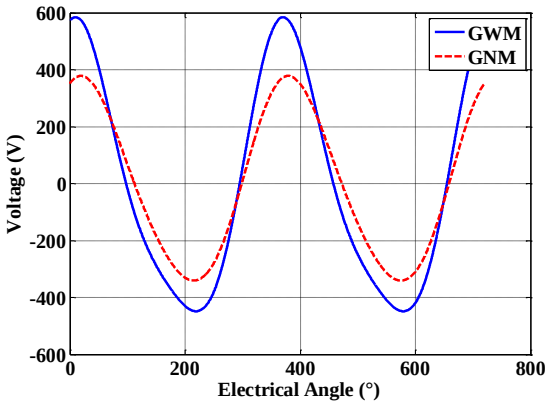

Fig.III.22 Voltage for phase A

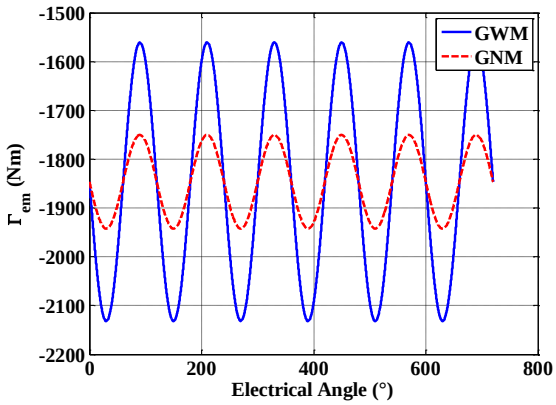

Fig.III.23 Electromagetic torque

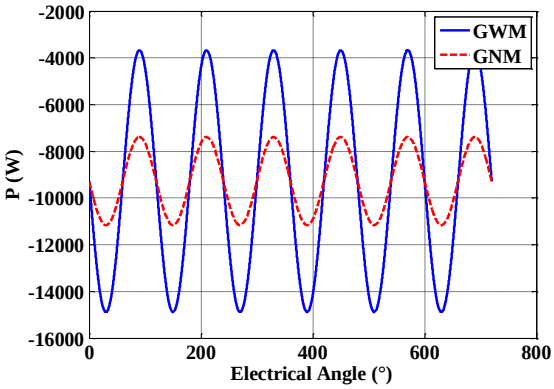

Fig.III.24 Active power

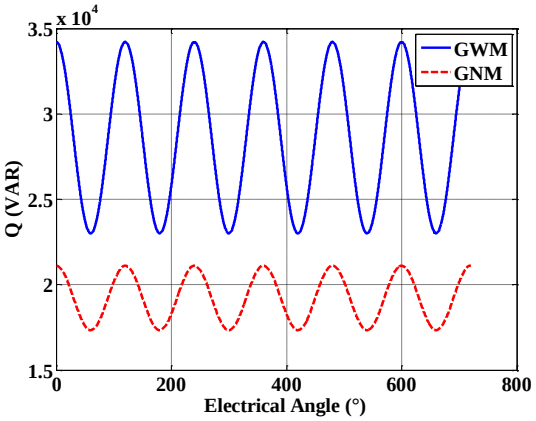

Fig.III.25 Reactive power

Table III.12 FFT for v_a (Sinusoidal waveform)

	GNM	GWM
Continuous Component	0	0
Fundamental (50Hz)	355.8 (100%)	501.3 (100%)
2nd harmonic (100Hz)	31.4 (8.83%)	93.4 (18.63%)
3rd harmonic (150Hz)	0	0
4th harmonic (200Hz)	0	0
THD	8.83%	18.63%

From Table III.12 and Fig.III.22, obviously, the phase voltage of GNM has lower amplitude and is more sinusoidal because the 2nd order harmonic is much smaller (8.83% instead of 18.63%). In addition, this machine reduces ripples in the torque and powers, as well as the mean value of reactive power. However, the mean values for torque and active power are the same for both machines as the main parts of mean values are determined by the permanent magnet.

The active and reactive power ripple coefficients K_P and K_Q can be deduced based on the same principle than for torque (III.2).

For the simple sinusoidal current waveform, K_r, K_P and K_Q will be simplified in equations (III.15), (III.16) and (III.17).

$$K_P = \left|\frac{P_{max} - P_{min}}{P_{mean}}\right| = \frac{4\Omega N_r I_m \left(\frac{L_1}{2} + M_1\right)}{N_r \Omega \varphi_1 + R_s I_m} \quad \text{(III.15)}$$

$$K_Q = \left|\frac{Q_{max} - Q_{min}}{Q_{mean}}\right| = \frac{4\left(\frac{L_1}{2} + M_1\right)}{L_0 - M_0} \quad \text{(III.16)}$$

$$K_r = \left|\frac{\Gamma_{em\ max} - \Gamma_{em\ min}}{\Gamma_{em\ mean}}\right| = \frac{I_m \left(\frac{L_1}{2} + M_1\right)}{\varphi_1} \quad \text{(III.17)}$$

If the Joule losses are neglected, formula (III.15) can be rewritten as:

$$K_P \approx \frac{4 I_m \left(\frac{L_1}{2} + M_1\right)}{\varphi_1} \quad \text{(III.18)}$$

From equations (III.17) and (III.18), for the sinusoidal current waveform, we observe that $K_P/K_R \approx 4$

Expressions (III.12) and (III.13) show(III.18) that if the amplitude of the current is increased by *k* times, the average torque and the average active power is *k* times higher, meanwhile their ripples will be k^2 times higher.

Based on the formula (III.14), both the mean value and ripple of the reactive power depend on the square of the current amplitude. As a result, the K_Q will be constant for the machine with given parameters.

Moreover, equations (III.17) and (III.18) contain one common part: the fundamentals of the self and mutual inductances ($L_1/2+M_1$). As L_1 and M_1 have practically the same values (see Table III.1), the mutual inductance fundamental takes more important role than that of self inductance for the torque and power ripple.

Table III.13 gives the simulation details of the power and torque comparisons between these two generators for 40 A amplitude 50 Hz sinusoidal current waveform. As already discussed, K_P is nearly four times of K_r (40.65% to 10.4% for GNM, 120.87% to 30.92% for GWM).

Table III.13 Comparison of DSPMG for simple sinusoidal current

	GNM	GWM	Ratio GNM/GWM
Max Γ_{em}	-1942.3	-2131.7	1.10
Min Γ_{em}	-1750.3	-1560.8	0.89
Mean Γ_{em}	-1846.3	-1846.3	1
K_r	10.4%	30.92%	2.97
Max P	-11160	-14880	1.33
Min P	-7390.0	-3669.7	0.50
Mean P	-9275	-9275	1
K_P	40.65%	120.87%	2.97
Max Q	21112	34217	1.62
Min Q	17342	23006	1.32
Mean Q	19227	28612	1.48
K_Q	19.61%	39.2%	2
P_{cu}	212.0880	212.0880	1

From Table III.13, the existence of mutual inductance (M_0 & M_1) will increase both the average value of the reactive power (from 19227 var to 28612 var) and K_Q (from 19.61% to 39.2%). It implies that GWM needs more energy from the grid to magnetize the machine.

In order to analyze the DSPMG performances with different sinusoidal current waveforms, two new parameters called Active Power Constant C_{ap} and Reactive Power Constant C_{rp} are introduced in equations (III.19) and (III.20). These two parameters multiplying the electrical speed will get the active and reactive power respectively.

$$C_{ap} = \frac{P}{\omega_e} \quad (W * s/rad) \tag{III.19}$$

$$C_{rp} = \frac{Q}{\omega_e} \quad (VAR * s/rad) \tag{III.20}$$

The power ripple coefficients K_P and K_Q can be expressed as a function of C_{ap} and C_{rp} in formulas (III.21) and (III.22).

$$K_P \approx \left| \frac{C_{ap\,max} - C_{ap\,min}}{C_{ap\,mean}} \right| \quad \text{(III.21)}$$

$$K_Q = \left| \frac{C_{rp\,max} - C_{rp\,min}}{C_{rp\,mean}} \right| \quad \text{(III.22)}$$

The sinusoidal waveform currents with 0° load angle by changing the amplitudes (from 5A to 50A) are then tested for these two DSPMG. More details are presented in Table III.14 and Table III.15. These two tables can well verify the machine performance we have summarized before.

Table III.14 GWM coefficients for different current amplitudes

		5A	10A	15A	20A	25A	30A	35A	40A	45A	50A
Γ_{em}	Min	-226.3	-443.7	-652.2	-851.8	-1042.4	-1224.1	-1396.9	-1560.8	-1715.8	-1861.8
	Max	-235,2	-479.4	-732,5	-994.5	-1265,4	-1545.3	-1834,1	-2131.7	-2438.4	-2753.9
	Mean	-230,8	-461.6	-692,4	-923.1	-1153,9	-1384.7	-1615,5	-1846.3	-2077.1	-2307.8
K_r		3.87%	7.7%	11.6%	15.5%	19.33%	23.2%	27.1%	30.9%	34.8	38.7%
C_{ap}	Min	3.34	6.14	8.40	10.13	11.32	11.98	12.10	11.68	10.73	9.24
	Max	3.90	8.37	13.42	19.05	25.26	32.05	39.42	47.36	55.89	64.99
	Mean	3.62	7.25	10.91	14.59	18.29	22.01	25.76	29.52	33.31	37.11
K_P		15.4%	30.7%	46.0%	61.1%	76.2%	91.2%	106.1%	120.9%	135.6%	150.2%
C_{rp}	Min	1.14	4.58	10.30	18.31	28.61	41.19	56.07	73.23	92.69	114.42
	Max	1.70	6.81	15.32	27.23	42.55	61.27	83.39	108.91	137.85	170.18
	Mean	1.42	5.69	12.81	22.77	35.58	51.23	69.73	91.07	115.27	142.30
K_Q		39.2%	39.2%	39.2%	39.2%	39.2%	39.2%	39.2%	39.2%	39.2%	39.2%
P_{cu}		3.31	13.25	29.82	53.02	82.85	119.30	162.38	212.09	268.42	331.39

Table III.15 GNM coefficients for different current amplitudes

		5A	10A	15A	20A	25A	30A	35A	40A	45A	50A
Γ_{em}	Min	-229.3	-455.6	-678.9	-899.1	-1116.4	-1330.7	-1542	-1750.3	-1955.6	-2157.8
	Max	-232.3	-467.6	-705.9	-947.1	-1191.4	-1438.7	-1689	-1942.3	-2198.6	-2457.8
	Mean	-230.8	-461.6	-692.4	-923.1	-1153.9	-1384.7	-1615.5	-1846.3	-2077.1	-2307.8
K_r		1.3%	2.6%	3.9%	5.2%	6.5%	7.8%	9.1%	10.4%	11.7%	13.0%
C_{ap}	Min	-3.52	-6.88	-10.07	-13.09	-15.95	-18.64	-21.16	-23.52	-25.71	-27.74
	Max	-3.71	-7.63	-11.76	-16.09	-20.64	-30.35	-25.39	-35.52	-40.90	-46.49
	Mean	-3.62	-7.25	-10.91	-14.59	-18.29	-22.01	-25.76	-29.52	-33.31	-37.11
K_P		5.18%	10.3%	15.5%	20.6%	25.6%0	30.7%	35.7%	40.7%	45.6%	50.5%
C_{rp}	Min	0.86	3.45	7.76	13.80	21.56	31.05	42.26	55.20	69.86	86.25
	Max	1.05	4.20	9.45	16.80	26.25	37.80	51.45	67.20	85.05	105.00
	Mean	0.96	3.83	8.61	15.30	23.91	34.43	46.86	61.20	77.46	95.63
K_Q		19.6%	19.6%	19.6%	19.6%	19.6%	19.6%	19.6%	19.6%	19.6%	19.6%
P_{cu}		3.31	13.25	29.82	53.02	82.85	119.30	162.38	212.09	268.42	331.39

In conclusion, in accordance with the analysis and comparison based on sinusoidal current waveform with 0° load angle in this section, two important conclusions can be obtained. Firstly, the ripples of the power are determined by the current and are independent of speed. Secondly,

GNM has much better performance than GWM for this kind of current as it generates less ripples for electromagnetic torque and active power and as well as reactive power.

III.3.2 Quasi-Sinusoidal Waveform

As discussed in the previous section, the torque ripple highly depends on the current amplitudes. If the machine is at rated operating condition, the sinusoidal waveform current cannot get the torque ripple coefficient less than 10% even for GNM. In this section, a new current reference waveform is analyzed in order to further reduce the torque ripple. We assume that appropriate harmonic current components must be injected. This new current will be regarded as the product of one simple sinusoidal function with variable current amplitude (which is function of electrical angle).

The three phase currents based on the above assumption are given in formula (III.23).

$$\begin{cases} i_a = -I_{\mathrm{m}}(\theta_e)\sin(\theta_e+\alpha) & = \sum_{h=0}^{\infty} I_{mh}\sin(h\theta_e+\alpha_h) \\ i_b = -I_{\mathrm{m}}(\theta_e)\sin\left(\theta_e-\frac{2\pi}{3}+\alpha\right) & = \sum_{h=0}^{\infty} I_{mh}\sin\left(h\theta_e-\frac{2h\pi}{3}+\alpha_h\right) \\ i_c = -I_{\mathrm{m}}(\theta_e)\sin\left(\theta_e-\frac{4\pi}{3}+\alpha\right) & = \sum_{h=0}^{\infty} I_{mh}\sin\left(h\theta_e-\frac{4h\pi}{3}+\alpha_h\right) \end{cases} \quad \text{(III.23)}$$

Where: h=0, continuous part; h>1, h^{th} harmonic component; I_{mh} is the amplitude of harmonic component for rank h; α_h is the phase angle for harmonic component for rank h.

The basic torque expression (II.65) can be rewritten as:

$$\Gamma_{em} = -\left[\frac{3}{2}N_r\varphi_1\cos\alpha\, I_m(\theta_e)+\frac{3}{4}\mathrm{N_r}\left(\frac{1}{2}L_1+M_1\right)\sin(3\theta_e+2\alpha)\, I_m^2(\theta_e)\right] \quad \text{(III.24)}$$

As the current must be some real value, in accordance with the principle of quadratic equation, the equation (III.24) must obey the following inequality (III.25).

$$\Gamma_{em} \le \frac{\frac{3}{4}\mathrm{N_r}{\varphi_1}^2\cos^2\alpha}{\frac{1}{2}\mathrm{L_1}+\mathrm{M_1}} \quad \text{(III.25)}$$

Our objective is to obtain a constant torque, thus, the current amplitude solution for formula (III.24) can be written as:

$$I_m(\theta_e) = \frac{-\frac{3}{2}\mathrm{N_r}\varphi_1\cos\alpha+\sqrt{\left(\frac{3}{2}\mathrm{N_r}\varphi_1\cos\alpha\right)^2-4\times\frac{3}{4}\mathrm{N_r}\left(\frac{1}{2}L_1+M_1\right)\sin(3\theta_e+2\alpha)*\Gamma_{em}}}{2\times\frac{3}{4}\mathrm{N_r}\left(\frac{1}{2}L_1+M_1\right)\sin(3\theta_e+2\alpha)} \quad \text{(III.26)}$$

The formula (III.25) explains the restricted condition to maintain the torque during every time. This means if the desired torque is bigger than this restricted value, the machine cannot find the appropriate current to obtain this torque. This limitation is determined by the characteristics of the machine and as well as the load angle. Obviously, the limited value of torque will be much bigger when the mutual inductance is zero.

For this machine, if the desired torque is -1845 Nm which is equal to the rated torque in Fig.III.23, according to formula (III.25), the maximum load angle α for GNM to obtain the desired torque is 63°, while it is 38° for GWM. Hence, to study the influence of the load angle α

on the machine performances, we choose the load angle between ±45°for GNM and ±30° for GWM. We observe that the current amplitude given by equation (III.26) depend on the load angle α.

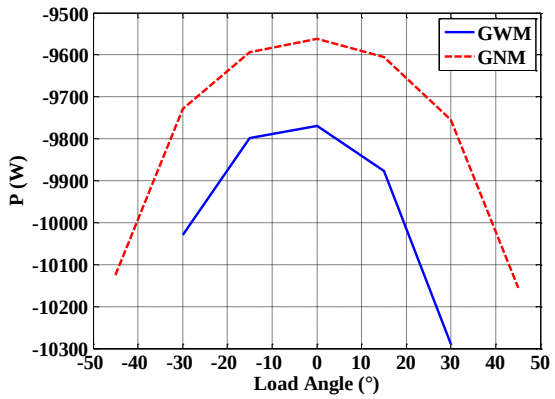

Fig.III.26 Average value of active power

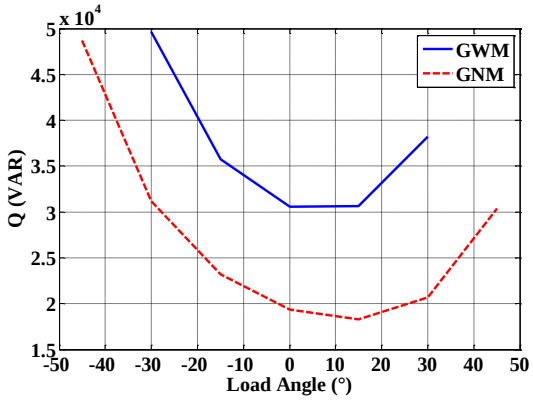

Fig.III.27 Average value of reactive power

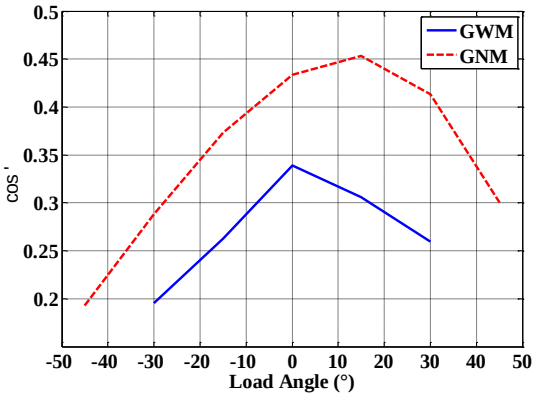

Fig.III.28 Power factor

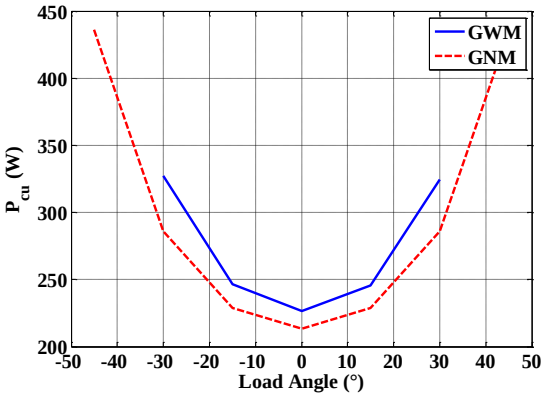

Fig.III.29 Joule losses

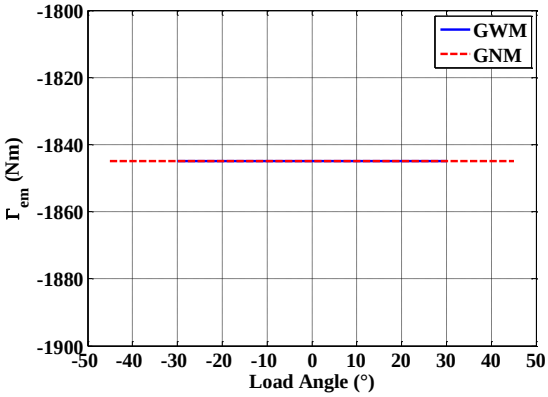

Fig.III.30 Electromagnetic torque

From Fig.III.26 to Fig.III.30, this designed quasi-sinusoidal current waveform can get the constant torque with the different load angles under the restrict condition in equation (III.25). GNM always produce less powers and Joule losses for every load angle. When the load angle is 0°, each machine has the minimum losses, and nearly the maximum power factor. For simplicity

and based on the same criterion as for sinusoidal current waveform to reduce the torque ripple and losses, the load angle for quasi-sinusoidal current waveform is chosen as 0°.

III.3.2.1 Quasi-Sinusoidal current waveform for GWM

The quasi-sinusoidal current waveform i_a based on formula (III.26) for -1845 Nm and 50 Hz is shown in Fig.III.31. After applying FFT, the amplitudes and phase angles of current harmonic parts are detailed in Fig.III.32 and Table III.16.

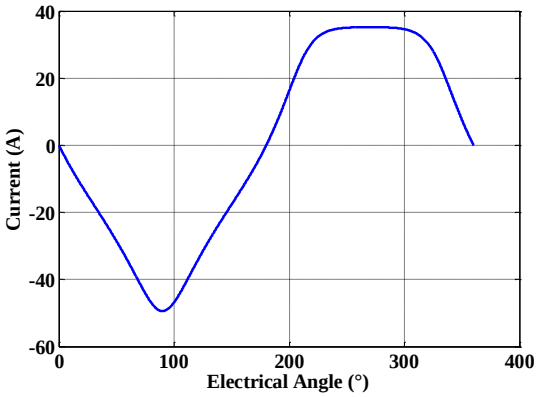

Fig.III.31 Current in phase A (GWM)

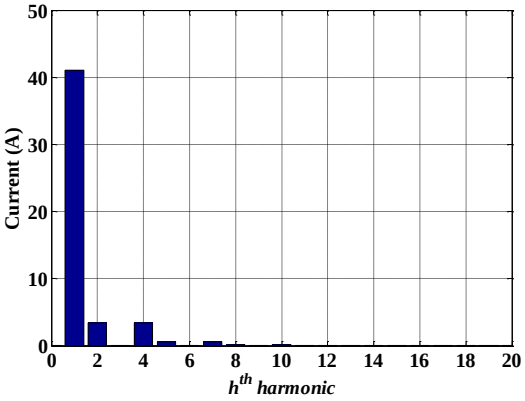

Fig.III.32 FFT for i_a (GWM)

Based on FFT, the current harmonics h can be summarized as:

$$h = 3k \pm 1;\ k \in \mathbb{N} \qquad \text{(III.27)}$$

In Table III.16, we just present the most important harmonic terms of the harmonics.

Table III.16 FFT for i_a (GWM)

	Amplitude (I_{mh})	Phase Angle α_h (°)
Fundamental (50 Hz)	41.0757 (100%)	180
2nd harmonic (100 Hz)	3.4240 (8.34%)	90
4th harmonic (200 Hz)	3.4240 (8.34%)	-90
5th harmonic (250 Hz)	0.5793 (1.41%)	180
7th harmonic (350 Hz)	0.5793 (1.41%)	0

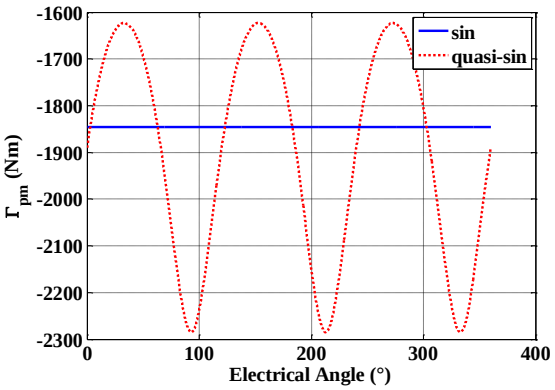

Fig.III.33 Magnet torque comparison (GWM)

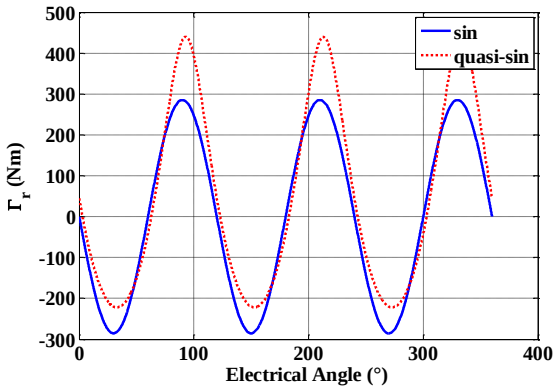

Fig.III.34 Reluctant torque comparison (GWM)

Fig.III.33 and Fig.III.34 just give the comparison of the sinusoidal and quasi-sinusoidal waveform currents for permanent magnet torque and reluctant torque. We observe that the injected harmonics will increase the magnet torque ripple and change the reluctant torque ripple.

For the simple sinusoidal current waveform, the magnet torque is constant as the q axis current is constant (solid lines in Fig.III.33). The reluctant torque will be periodic term with zero mean value (solid line in Fig.III.34).

To obtain the constant torque, we observe from Table III.16 that the fundamental of the quasi-sinusoidal current waveform (41 A) is slightly greater than the sinusoidal case (40 A).

Moreover, we can also notice that the magnet and reluctant torques for this quasi sinusoidal current are not symmetrical. This is because this quasi-sinusoidal current waveform contains the even harmonic currents with big amplitude (2^{nd} and 4^{th} harmonic current components) (see in Table III.16).

In conclusion, the injected harmonic currents will increase the permanent magnet torque ripple and change the reluctant torque to maintain the total electromagnetic torque constant.

Using results given in Table III.16, the current i_a can be approximately as i_a':

$$i_a \approx i_a' = I_{m1}\sin(\theta_e + \pi) + I_{m2}\sin\left(2\theta_e + \frac{\pi}{2}\right) + I_{m4}\sin\left(4\theta_e - \frac{\pi}{2}\right)$$
$$= -I_{m1}\sin\theta_e + I_{m2}\cos 2\theta_e - I_{m4}\cos 4\theta_e \qquad \text{(III.28)}$$

Based on this approximation (III.28), the performances of original current (i_a) and fitting current (i_a') are compared in Fig.III.35 to Fig.III.40 and Table III.17.

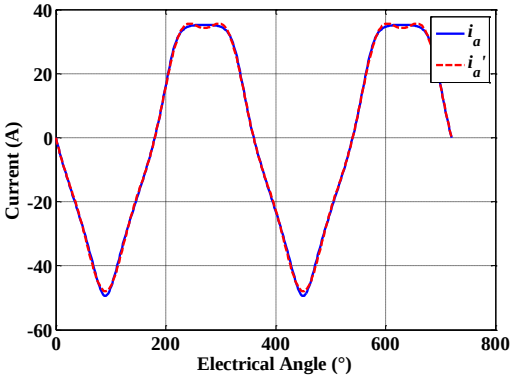

Fig.III.35 i_a and i_a' (GWM)

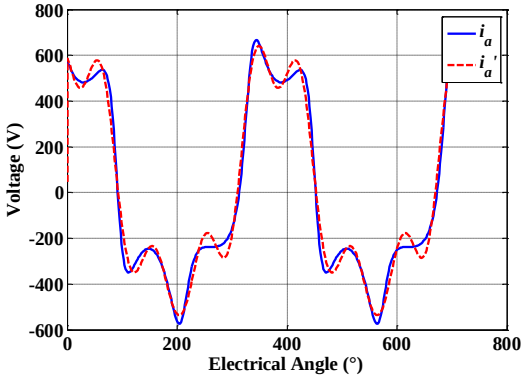

Fig.III.36 Phase voltage v_a for ia and i_a' (GWM)

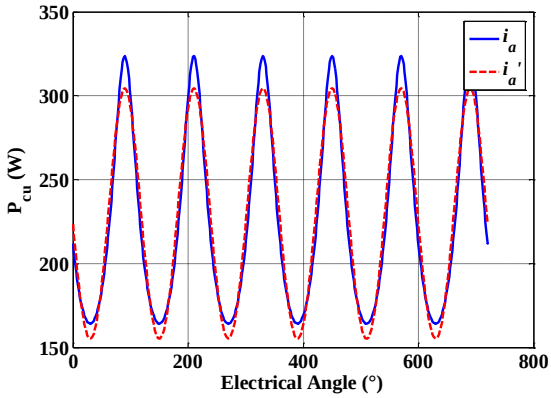

Fig.III.37 Joule loss for i_a and i_a' (GWM)

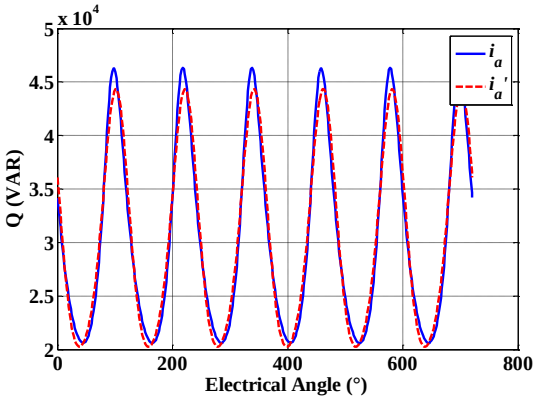

Fig.III.38 Reactive power for i_a and i_a' (GWM)

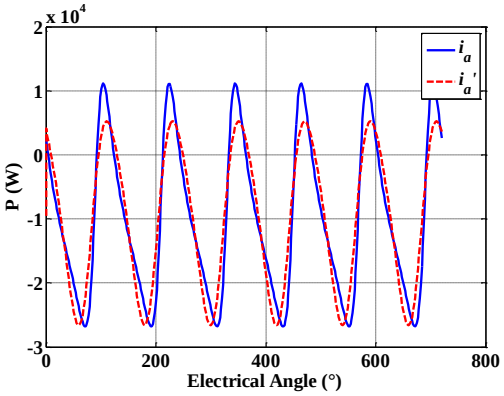

Fig.III.39 Active power for i_a and i_a' (GWM)

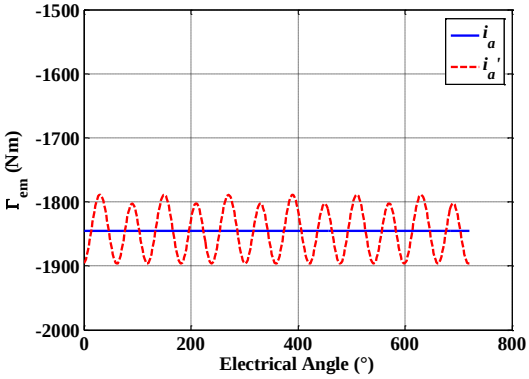

Fig.III.40 Electromagnetic torque for i_a and i_a' (GWM)

Table III.17 Comparison of original current i_a and fitting current i_a' (GWM)

	Original current i_a	Fitting current i_a'
Max Γ_{em}	-1845	-1896
Min Γ_{em}	-1845	-1789
Mean Γ_{em}	-1845	-1846
Kr	0	5.8%
Max P	-26793	-26591
Min P	11128	522
Mean P	-9769	-9723
K_P	388%	279%
Max Q	46316	44334
Min Q	20608	20252
Mean Q	30591	30603
K_Q	84.04%	78.7%
P_{cu}	226.8	226.7

From these figures and Table III.17, intuitively, the fitting current i_a' leads practically to the same average values of the power, torque and Joule losses because i_a' still keeps the main part of the original current i_a. However, it is precisely because of lacking of the neglected small 5th and 7th harmonic components, the fitting current i_a' brings about 6% torque ripple. Meanwhile, the fitting current i_a' gives fewer ripples for both active and reactive powers.

For the sinusoidal current waveform, the voltage is composed of fundamental and 2nd harmonic (see equation (III.11)). Compared with the Fig.III.22 and Fig.III.36, we observe the voltage corresponding to currents i_a and i_a' are more distorted than the one corresponding to the sinusoidal current waveform.

In the following, we analyse the influence of each harmonic component of the fitting current i_a'. The relevant simulation results are shown from Fig.III.41 to Fig.III.46.

As the torque ripple is the first criterion of our study, if the i_a' is used to supply DSPMG, the torque equation (II.53) can be developed as:

$$\begin{aligned}\Gamma_{em} = & -\frac{3}{2}N_r I_{m1}\left(\varphi_1 - \frac{L_1 I_{m2}}{2} - M_1 I_{m2}\right) - \left(\frac{3L_1}{8} + \frac{3M_1}{4}\right)N_r I_{m1}^2 \sin 3\theta_e \\ & + N_r \sin 3\theta_e \left(\frac{3\varphi_1}{2} I_{m2} + \frac{3L_1}{8} I_{m2}^2 - \frac{3M_1}{4} I_{m2}^2\right) \\ & + N_r \left(\frac{3\varphi_1}{2}\sin 3\theta_e \, I_{m4} + \frac{3L_1}{8}\sin 9\theta_e \, I_{m4}^2 + \frac{3M_1}{4}\sin 9\theta_e \, I_{m4}^2\right) \\ & - N_r L_1 \left(\frac{3}{4}\cos 6\theta_e \, I_{m1} + \frac{3}{8}\sin 3\theta_e \, I_{m2}\right) I_{m4} \\ & - N_r M_1 \left(\frac{3}{2}\cos 6\theta_e \, I_{m1} + \frac{3}{2}\sin 3\theta_e \, I_{m2}\right) I_{m4} \end{aligned} \quad \text{(III.29)}$$

The first term of the formula (III.29) is the average torque of GWM. The other parts are the total torque ripple. The injected currents lead to reduce this ripple. Based on the harmonic currents calculated by FFT in Table III.16, the average total torque is -1846.4 Nm. This is not exactly equal to the theoretical value -1845 Nm. This means the other harmonics which we have neglected still produce the opposite torque to reach the reference. Nevertheless, the torque difference is too small to the reference; it will be neglected in the study.

To studying the influence of the 2nd and 4th harmonics, we introduce the currents i_{a1}' and i_{a2}' (see equations (III.30) and (III.31)). i_{a1}' contains fundamental and the 4th harmonic current; while, i_{a2}' contains fundamental and the 2nd harmonic current. The torque performance of these fitting currents can be analyzed theoretically from expression (III.29).

$$i_{a1}' = -I_{m1}\sin\theta_e - I_{m4}\cos 4\theta_e \quad \text{(III.30)}$$

$$i_{a2}' = -I_{m1}\sin\theta_e + I_{m2}\cos 2\theta_e \quad \text{(III.31)}$$

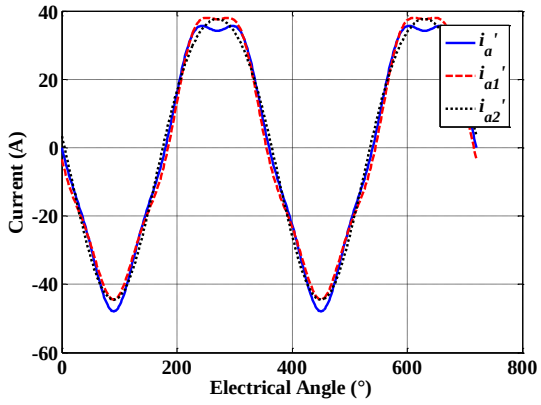

Fig.III.41 i_a', i_{a1}' & i_{a2}' (GWM)

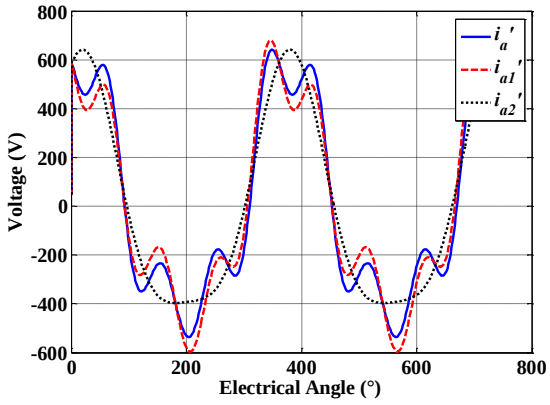

Fig.III.42 v_a for i_a', i_{a1}' & i_{a2}' (GWM)

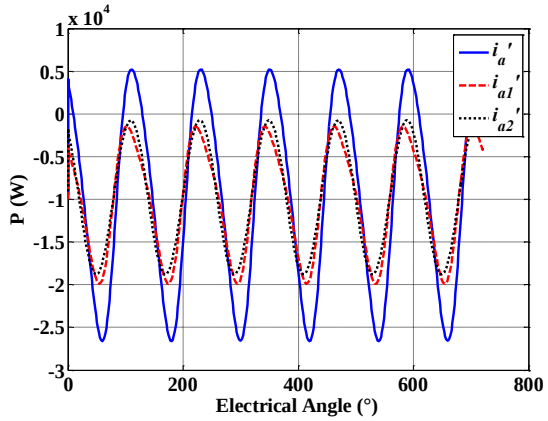

Fig.III.43 Active power for i_a', i_{a1}' & i_{a2}' (GWM)

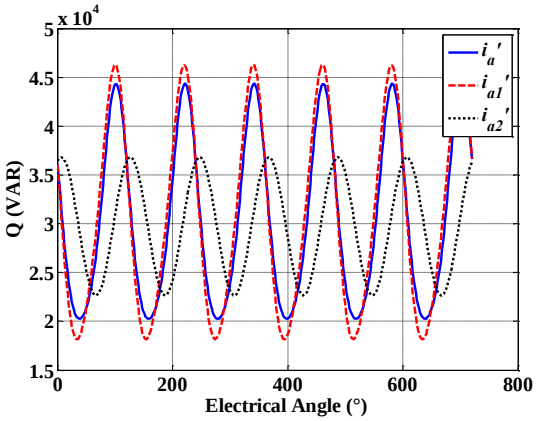

Fig.III.44 Reactive power for i_a', i_{a1}' & i_{a2}' (GWM)

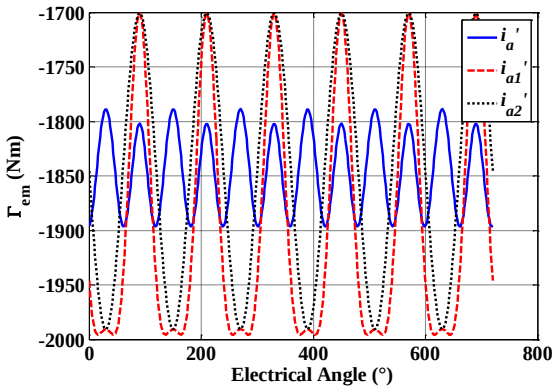

Fig.III.45 Electromagnetic torque for i_a',i_{a1}' & i_{a2}' (GWM)

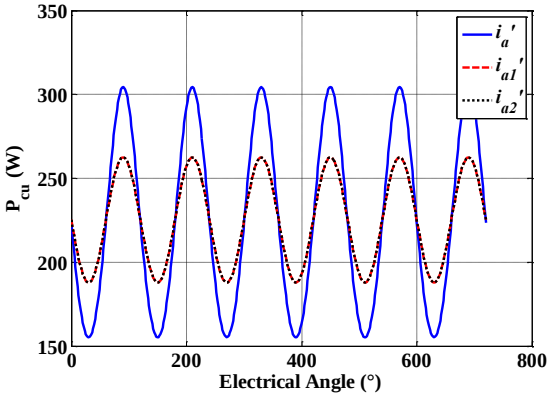

Fig.III.46 Joule losses for i_a',i_{a1}' & i_{a2}' (GWM)

As the two current harmonics are nearly 8% of the fundamental, we can easily find the difference between these three currents in Fig.III.41. There are also different ripples for the other variables. More details of the voltage, power and torque for these three currents will be presented in Table III.18 and Table III.19.

Table III.18 FFT for v_a (quasi-sinusoidal waveform, GWM)

	i_a'	i_{a1}'	i_{a2}'	Sinusoidal
Continuous Component	0	0	0	0
Fundamental (50Hz)	514.7 (100%)	513.5 (100%)	514.7 (100%)	501.3 (100%)
2nd harmonic (100Hz)	125.6 (24.4%)	95.9 (18.7%)	125.7 (24.4%)	93.4 (18.63%)
3rd harmonic (150Hz)	0	0.05 (0%)	0.05 (0%)	0
4th harmonic (200Hz)	163.3 (31.8%)	163.3 (31.8%)	0	0
5th harmonic (250Hz)	20.0 (3.9%)	20.0 (3.9%)	0	0
6th harmonic (300Hz)	0	0	0	0
THD	40.22%	37.08%	24.41%	18.63%

From Fig.III.42, i_{a1}' and i_a' have similar voltage form but with different ripple. This means the voltage for i_{a1}' have the same terms of harmonic as that of i_a'. Meanwhile, i_{a2}' gives the voltage which is less distorted and more similar to the sinusoidal waveform.

Thanks to Table III.18, i_{a1}' which contains the 4th current harmonic brings 2nd, 4th and 5th voltage harmonics. For i_{a2}', the 2nd current harmonic only gives the 2nd harmonic in the voltage. Although, the 2nd voltage harmonic produced by i_{a2}' is nearly one fourth (24.4%) of the voltage

fundamental, the THD (Total Harmonic Distortion) of i_{a2}' is still smaller than that of i_{a1}'. Table III.18 shows also that, compared to the sinusoidal current waveform, i_{a2}' leads to practically the same voltage harmonics and a slightly bigger THD. We observe that both i_{a1}' and i_{a2}' give a 3rd voltage harmonic which are very small and can be neglected.

Table III.19 Analysis of current harmonics influence on torque and power (GWM)

	i_a'	i_{a1}'	i_{a2}'	Sinusoidal
Max Γ_{em}	-1896	-1995.7	-1990.8	-2131.7
Min Γ_{em}	-1789	1700.6	-1700	-1560.8
Mean Γ_{em}	-1846	-1896.3	-1845	-1846.3
Kr	5.8%	15.56%	15.72%	30.92%
Max P	-26591	-19897	-18791	-14880
Min P	522	-1462.4	-753	-3669.7
Mean P	-9723	-10027	-9732	-9275
K_P	279%	184%	185%	120.87%
Max Q	44334	46258	36794	34217
Min Q	20252	18166	22659	23006
Mean Q	30603	31026	29760	28612
K_Q	78.7%	90.5%	47.5%	39.2%
P_{cu}	226.7	225.2	225.2	212.0880

Table III.19 gives some details of the power and torque. From this table, the average values of the torque, power and losses are almost the same for the four currents including the sinusoidal waveform current. This is mainly because these four currents have nearly the same major component. The only big difference between these currents is the ripples of each variable.

We notice that the simulated torque ripples generated by i_{a1}' and i_{a2}' correspond exactly to the mathematic analysis (equation (III.29)). The torque ripples corresponding to i_{a1}' and i_{a2}' are still much smaller than that of sinusoidal waveform (30.92%). This means the injected currents is a good choice for GWM.

For both the active and reactive power, cancelling either harmonic of i_a' will change the power ripples (K_P varies from 279% to 184% and 185% respectively, K_Q varies from 78.7% to 90.5% and 47.5% respectively), and the sinusoidal waveform will appear the minimum ripples among these four currents (120.87% K_P, 39.2% K_Q).

Compared to the sinusoidal current waveform, the injected harmonic currents increase both mean active and mean reactive power. Therefore, the choice of current is a work full of compromise. Although the current i_{a2}' increase torque ripple compared to i_a', it will highly decrease the THD of the voltage, and as well as the power ripple. As a result, i_{a2}' which is composed of one simple sinusoidal and 2nd harmonic waveform is considered as the best choice for GWM.

III.3.2.2 Quasi-Sinusoidal Waveform for GNM

In accordance of equation (III.23), if the reference torque and electrical frequency are -1845 Nm and 50Hz respectively, the quasi-sinusoidal waveform i_a current for GNM are given in Fig.III.47. Notwithstanding this current is still not absolutely symmetrical, it is much more sinusoidal than that of GWM in Fig.III.31.

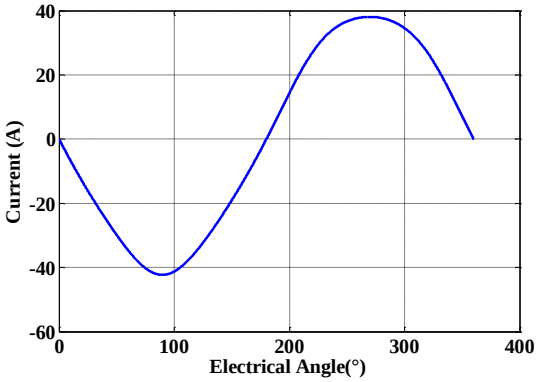

Fig.III.47 Current in phase A (GNM)

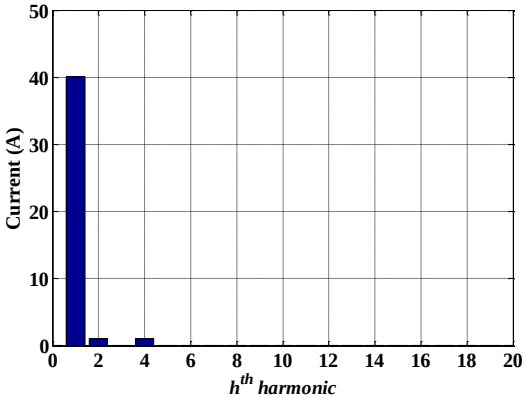

Fig.III.48 FFT for i_a (GNM)

Table III.20 FFT for i_a (GNM)

	Amplitude (I_{mh})	Phase Angle α_h(°)
Fundamental (50 Hz)	40.0819 (100%)	180
2nd harmonic (100 Hz)	1.0492 (2.62%)	90
4th harmonic (200 Hz)	1.0492 (2.62%)	-90
5th harmonic (250 Hz)	0.0550 (0.14%)	180
7th harmonic (350 Hz)	0.0550 (0.14%)	0

Table III.20 also presents the first 5 import harmonic current of the quasi sinusoidal current for GNM. From this table, the current harmonics for GNM are much smaller than that of GWM, so the magnet and reluctant torque ripples should be smaller than GWM, just as given in Fig.III.49 and Fig.III.50 (III.29).

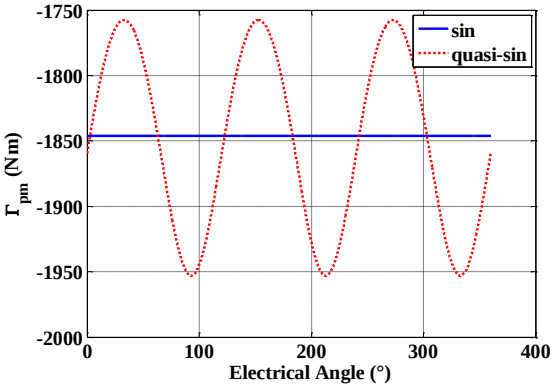

Fig.III.49 Magnet torque comparison (GNM)

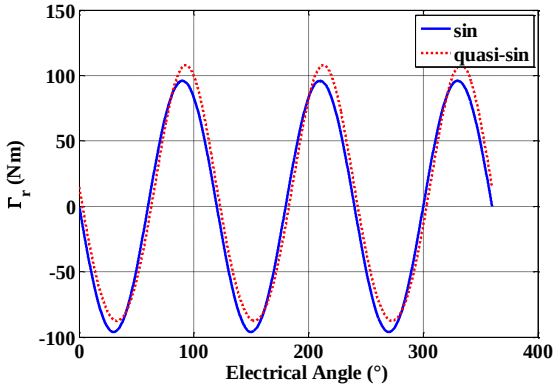

Fig.III.50 Reluctant torque comparison (GNM)

In comparison with that of GWM, the magnet torque ripple for quasi-sinusoidal current has been highly reduced (between -1757 Nm and -1953 Nm), as well as the reluctant torque ripple.

That means the mutual inductance leads to more current harmonics to compensate the torque ripple.

From Fig.III.48 and Table III.20, the 5th and 7th harmonic current components of GNM can be neglected. The fitting current i_a' for GNM is summarized exactly as the formula (III.28) which has already used for GWM.

Fig.III.51 to Fig.III.56 shows that the currents i_a and i_a' result in practically the same performances. More details are given in Table III.21.

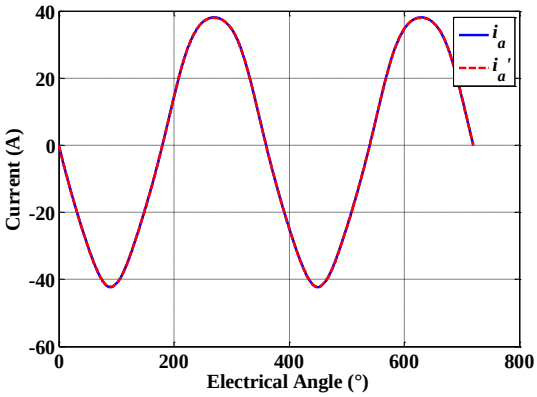

Fig.III.51 i_a and i_a' (GNM)

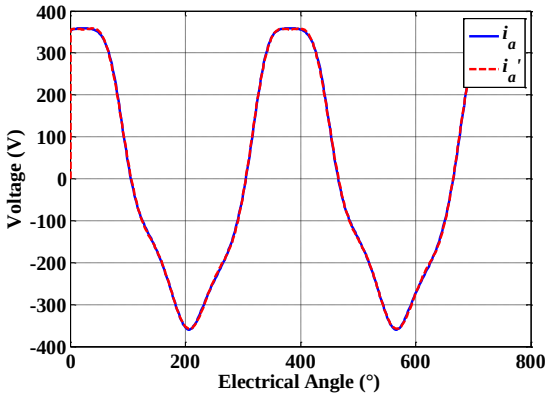

Fig.III.52 Phase voltage v_a for i_a and i_a' (GNM)

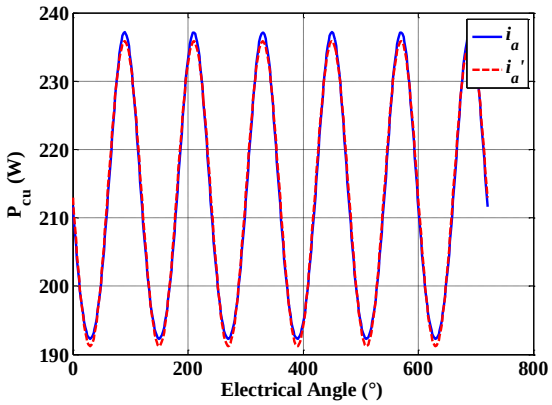

Fig.III.53 Joule Loss for i_a and i_a' (GNM)

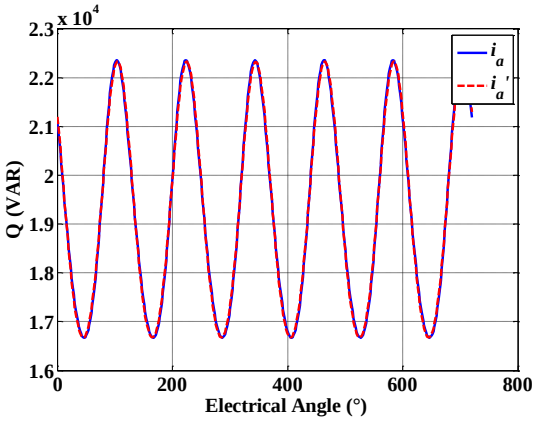

Fig.III.54 Reactive power for i_a and i_a' (GNM)

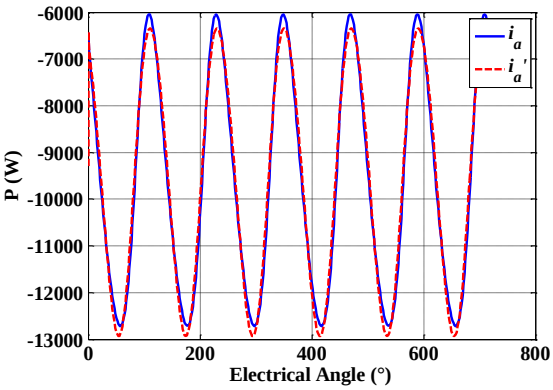

Fig.III.55 Active power for i_a and i_a' (GNM)

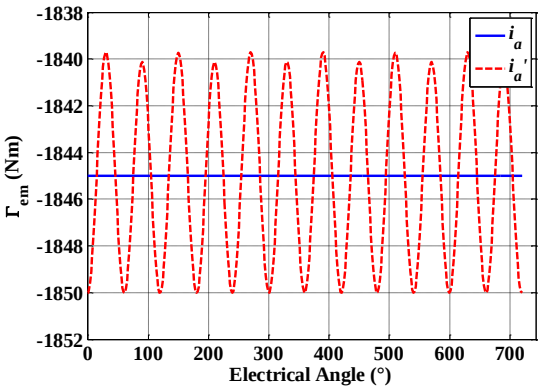

Fig.III.56 Electromagnetic torque for i_a and i_a' (GNM)

Table III.21 Comparison of original i_a and fitting current i_a' (GNM)

	Original i_a	i_a'
Max Γ_{em}	1845	1850
Min Γ_{em}	1845	1839.7
Mean Γ_{em}	1845	1845
Kr	0%	0.56%
Max P	-12715	-12932
Min P	-6043.9	-6344.5
Mean P	-9561.7	-9553.5
K_P	69.77%	68.9%
Max Q	22359	22327
Min Q	16671	16676
Mean Q	19335	19335
K_Q	29.42%	29.23%
P_{cu}	213.2	213.2

If there is no mutual inductance, equation (III.29) can be simplified as:

$$\Gamma_{em} = -\frac{3}{2}N_r I_{m1}\left(\varphi_1 - \frac{L_1 I_{m2}}{2}\right) - \frac{3N_r L_1 \sin 3\theta_e}{8} I_{m1}^2 + N_r \sin 3\theta_e \left(\frac{3\varphi_1}{2} I_{m2} + \frac{3L_1}{8} I_{m2}^2\right) + N_r \left(\frac{3\varphi_1}{2} \sin 3\theta_e \, I_{m4} + \frac{3L_1}{8} \sin 9\theta_e \, I_{m4}^2\right) - N_r L_1 \left(\frac{3}{4}\cos 6\theta_e \, I_{m1} + \frac{3}{8}\sin 3\theta_e \, I_{m2}\right) I_{m4} \quad \text{(III.32)}$$

Then, the effect of the two harmonics (2nd & 4th) will be analyzed as in section III.3.2.1. The voltage, power and torque for the three analyzed currents (i_a', i_{a1}' and i_{a2}') are shown in Fig.III.57 to Fig.III.62.

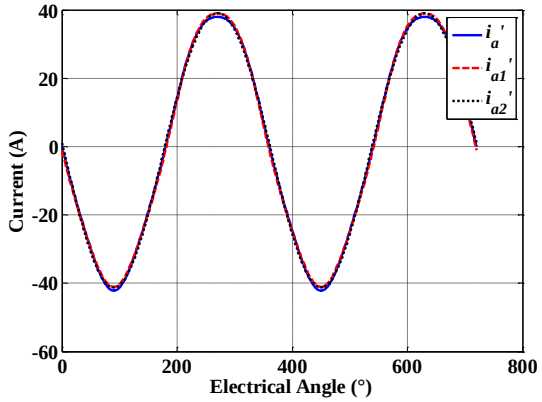

Fig.III.57 i_a', i_{a1}' and i_{a2}' (GNM)

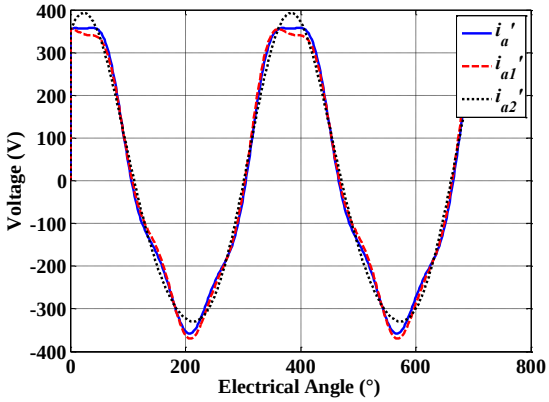

Fig.III.58 Phase Voltage v_a for i_a', i_{a1}' and i_{a2}' (GNM)

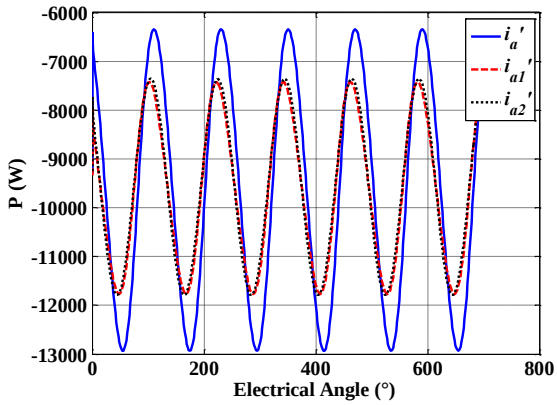

Fig.III.59 Active power for i_a', i_{a1}' and i_{a2}' (GNM)

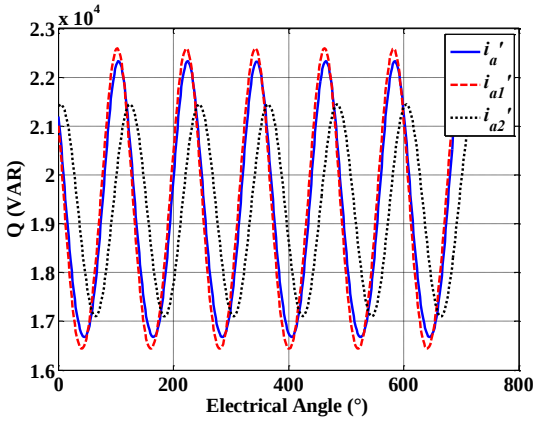

Fig.III.60 Reactive power for i_a', i_{a1}' and i_{a2}' (GNM)

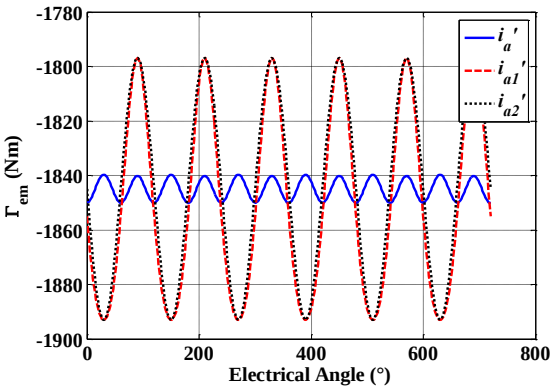

Fig.III.61 Γ_{em} for i_a', i_{a1}' and i_{a2}' (GNM)

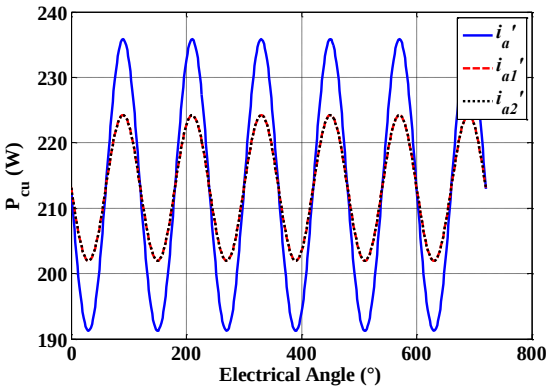

Fig.III.62 P_{cu} for i_a', i_{a1}' and i_{a2}' (GNM)

Because the current harmonics of GNM are relatively small, there is no big difference for the 3 currents (see Fig.III.57). However, the voltage, power and torque are still different. Some more details are given in Table III.22 and Table III.23.

Table III.22 FFT for v_a (quasi-sinusoidal waveform, GNM)

	i_a'	i_{a1}'	i_{a2}'	Sinusoidal
Continuous Component	0	0	0	0
Fundamental (50Hz)	356.6 (100%)	356.4 (100%)	356.6 (100%)	355.8 (100%)
2nd harmonic (100Hz)	35.6 (10.0%)	31.5 (8.8%)	35.6 (9.97%)	31.4 (8.83%)
3rd harmonic (150Hz)	0	1.21 (0.3%)	1.21 (0.3%)	0
4th harmonic (200Hz)	33.6 (9.4)	33.6 (9.4%)	0	0
5th harmonic (250Hz)	2.1 (0.6%)	2.1 (0.6%)	0	0
6th harmonic (300Hz)	0	0	0	0
THD	13.74%	12.93%	9.98%	8.83%

The similar results are found for GNM. i_{a2}' always presents the best performance in the voltage. The voltage THD (9.98%) is more close to the sinusoidal waveform than the other two currents (i_a' and i_{a1}'). As for GWM, i_{a1}' and i_{a2}' also generate 3rd voltage harmonic. Although it's bigger than that for GWM, it can be also neglected compared to the other harmonics.

Table III.23 Analysis of current harmonics influence on torque and power (GNM)

	i_a'	i_{a1}'	i_{a2}'	Sinusoidal
Max Γ_{em}	-1850	-1890	-1893	-1942.3
Min Γ_{em}	-1839.7	-1796.9	1796.9	-1750.3

Mean Γ_{em}	-1845	-1850	-1845	-1846.3
K_r	0.56%	5.19%	5.21%	10.4%
Max P	-12932	-11766	-11790	-11160
Min P	-6344.5	-7424.4	-7357.7	-7390.0
Mean P	-9553.5	-9592.7	-9564.6	-9275
K_P	68.9%	45.26%	46.34%	40.65%
Max Q	22327	22591	21442	21112
Min Q	16676	16438	17103	17342
Mean Q	19335	19362	19284	19227
K_Q	29.23%	31.78%	22.51%	19.61%
P_{cu}	213.2	213.09	213.09	212.0880

From Table III.23, the current harmonics for GNM also take some effects on the ripple coefficients like GWM. Compared to the sinusoidal current waveform, the injection of 2^{nd}, 4^{th} or both harmonics decrease K_r and increase K_P, K_Q. In consideration of the voltage THD and the ripples of torque and power, the fitting current i_{a2}' (composed of fundamental and 2^{nd} harmonic) appears the best choice for GNM.

III.3.3 Comparison

From the analysis and comparison for GWM and GNM applying both sinusoidal and quasi-sinusoidal waveform currents achieved in the above sections, GNM always appears having better performance than GWM (fewer ripples and less average reactive power). The only difference between these two machines concerns the existence of the stator mutual inductance or not. As a result, we can conclude that the existence of the mutual inductance will bring many ripples for the voltage, torque and power and as well as the level of reactive power. It will be better to design a similar machine without mutual inductance.

The currents based on sinusoidal waveform are also well compared. Different factors are taking into consideration such as: THD of the voltage, ripples and level of reactive power. According to Table III.19 and Table III.23, we find i_{a2}' which is composed of fundamental and 2^{nd} harmonic current components appears as the best solution for both machines (GWM and GNM) that can get the best comprehensive performance.

In conclusion, GNM supplied by i_{a2}' is the best solution for the machine side system.

The amplitudes of the i_{a2}' components (GNM) for the torque from 0 to 2500 Nm obtained from equations (III.23) and (III.26) are given in Fig.III.63.a. Fig.III.63.b to Fig.III.63.d show the details of Fig.III.63.a.

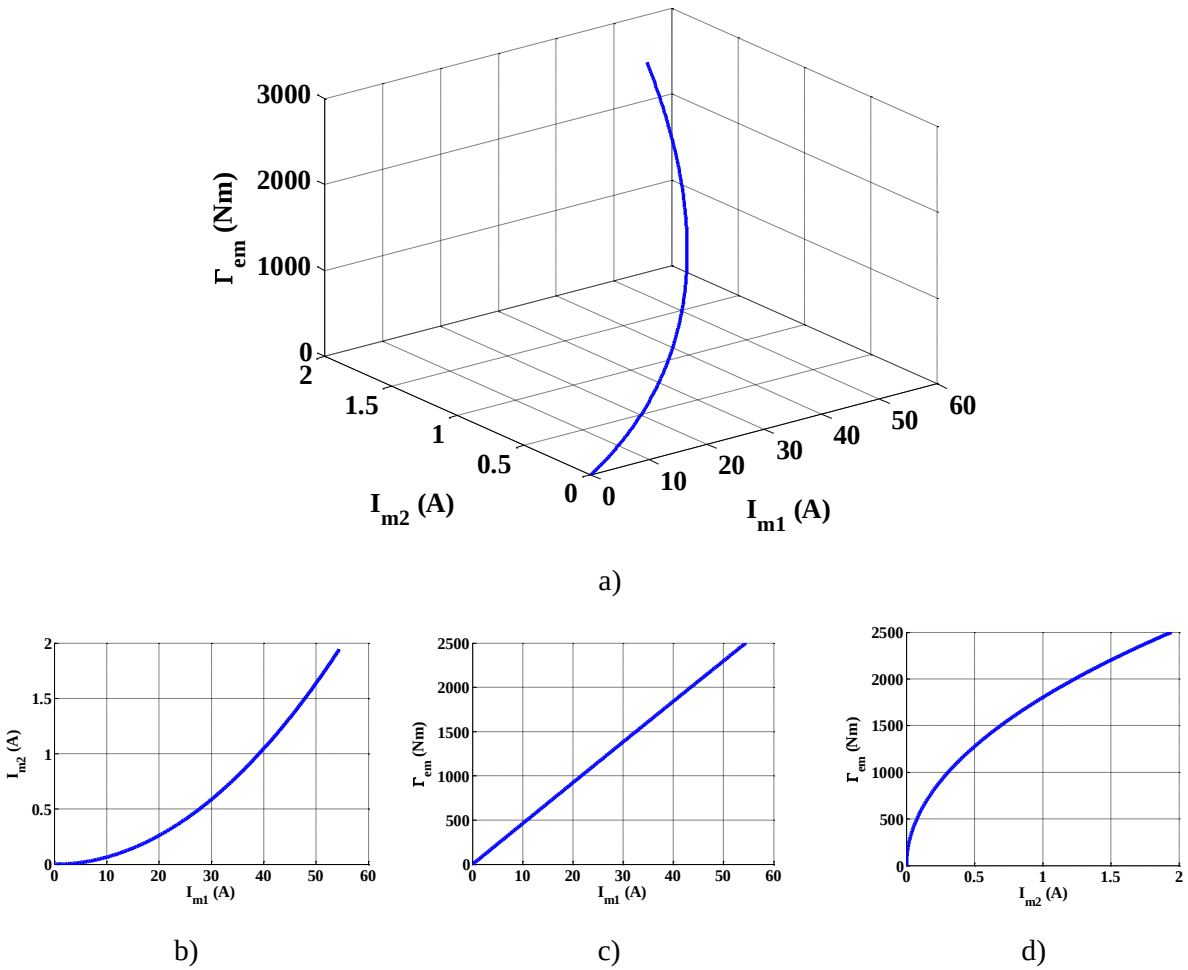

Fig.III.63 The relationship between the torque and harmonic amplitudes (GNM).

III.4 *Conclusion*

This chapter mainly discusses 2 problems in the condition of constant speed: firstly, which kind of current is suitable for DSPMG in order to obtain quasi constant torque; secondly, the influence of mutual inductance in DSPMG.

For the current, 2 basic current waveforms are proposed in this chapter: square and sinusoidal waveforms. And then, quasi-sinusoidal waveforms are also presented. Based on the assumption of DSPMG with and without mutual inductance, the performances of the machine in terms of mean and torque ripple are discussed taken into account the voltage and powers variations (mean values, THD and ripples).

For each current, DSPMG without mutual inductance presents much more performance than machine with mutual inductance. This machine can get the best results in comprehensive consideration of torque, voltage and powers when the current reference waveform is composed of fundamental and 2nd harmonic components. Therefore, in the following Chapter IV, the generator used for the MCECS is DSPMG without mutual inductance.

Chapter IV

Control of Marine Current Energy Conversion System

NOMENCLATURE

V_{DC} DC-bus voltage (V);

V_c carrier wave voltage (V);

V_{ma} machine side voltage for phase A (V);

V_{ca} control voltage for phase A (V);

I_{ref} Stator current reference, $I_{ref} = \left[i_{o_{ref}} \quad i_{d_{ref}} \quad i_{q_{ref}}\right]^t$;.

I Simulated current, $I = [i_o \quad i_d \quad i_q]^t$;

Γ_m Mechanical torque from MCT (Nm);

Γ_{em} Electromagnetic torque from generator (Nm);

Ω Mechanical speed (rad/s);

J_m Moment of inertia (kg*m^2);

f_v Coefficient of friction (Nm*s/rad);

Cp Power coefficient;

P_m Mechanical power (W);

P_{em} Electromagnetic power (W);

$P_{m\,loss}$ Mechanical losses (W);

GLOSSARY

EMF	ElectroMotive Force;
DSPMG	Doubly Salient Permanent Magnet Generator;
MPPT	Maximum Power Point Tracking;
CPC	Constant Electromagnetic Power Control;
PWM	Pulse Width Modulation;
GNM	Generator No Mutual inductance;
MCECS	Marine Current Energy Conversion System;
WECS	Wind Energy Conversion System;
TSR	Tip Speed Ratio;
P&O	Perturbation and Observation;
HCS	Hill-Climb Searching;
SMC	Sliding Mode Control;
PI	Proportional Integral;

IV.1 *Introduction*

In order to maximize the torque, minimize the torque ripples and the Joule losses simultaneously, the currents analyzed in Chapter III will be applied. The current reference will be in phase with ElectroMotive Force (EMF). The Maximum Power Point Tracking (MPPT) control strategy is used to find the optimum rotor speed and extract the maximum marine current energy at low marine current speeds. When the marine current speed is high, Constant Electromagnetic Power Control (CPC) strategy is proposed. In order to deliver the energy to the grid, a 6-switch Back-to-Back Pulse Width Modulation (PWM) converter will be used. The machine side converter will mainly focus on mechanical speed control. The grid side will mainly focus on the DC-bus voltage control and the power factor on the grid side.

The main results, based on the Generator model without stator mutual inductance (GNM) developed in Chapter II, are presented and analyzed with the help of Matlab/Simulink® simulation assessment.

IV.2 *Machine Side System Design*

The control strategy of the machine side system is shown in Fig.IV.1. It is divided into two parts, like for conventional machines, internal current loop and external speed loop (torque loop). In the following sections, the control strategy and system design for each part will be introduced respectively.

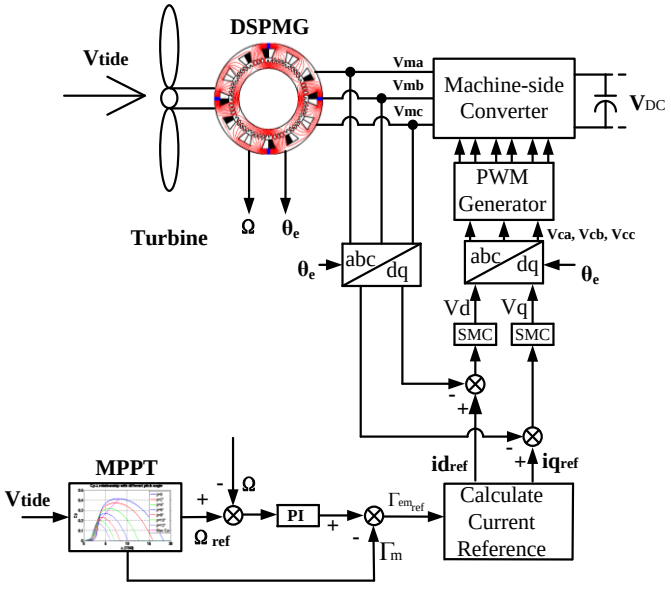

Fig.IV.1 Control strategy of the machine-side converter

IV.2.1 Control Strategy for Machine Side System

For conventional machines, the three phase sinusoidal waveform stator currents are transformed into two continuous parts owing the Concordia and Park transformations. Then the AC machines are controlled using field oriented approach as DC machines.

For Doubly Salient Permanent Magnet Generator (DSPMG), the same principle will be also used. However, as discussed in Chapter III, the stator quasi sinusoidal current which is composed of one simple sinusoidal waveform with 50 Hz frequency and 2nd harmonic component at 100 Hz frequency is the best choice for GNM at the nominal function condition to reduce the torque ripple and keep the stator voltage performance. In this section, the load angle of the quasi-sinusoidal current waveforms is considered as 0° for the minimum losses per torque. This means the fundamental of this current is in phase with EMF. The d-q axis currents are given in Fig.IV.2 and Fig.IV.3. The mean value of each current component is determined by the fundamental current and the ripples are due to the 2nd current harmonic.

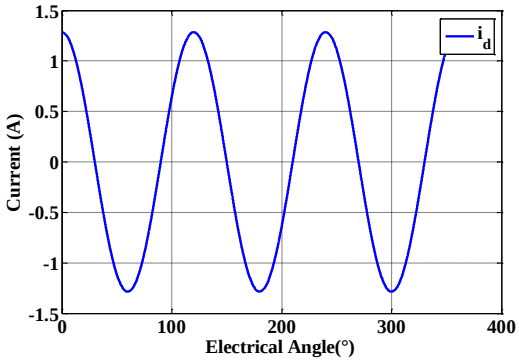

Fig.IV.2 d axis current for quasi-sinusoidal

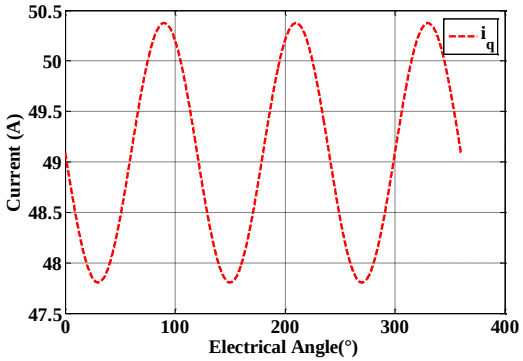

Fig.IV.3 q axis current for quasi-sinusoidal

For the external loop, in order to determine the optimal operating point of the marine current turbine at low marine current speeds, MPPT strategy for the speed loop is used.

Based on the literature, until now, many algorithms have been proposed and used in WECS in order to extract the maximum power from the fluid. The principle algorithms are: Tip Speed Ratio (TSR) control, Optimal Torque (OT) control, Power Signal Feedback (PSF) control, Perturbation and Observation (P&O) control, also called Hill-Climb Searching (HCS) method [102] [103].

In our study, TSR control is preferred as its fast convergence speed and good performance under varying marine current speed. The optimal TSR for a given turbine is fixed constant regardless of marine current speed which can be determined experimentally and theoretically. The extracted energy can be guaranteed to be maximized theoretically if TSR keeps the optimal value. As a result, this method just seeks to force the energy conversion system to always work at this optimal point by comparing it with the actual value and feeding this difference to the controller. Then, the controller changes the speed control signal of the generator to reduce the error. Therefore, the speed reference based on the optimal point can be deduced as shown in equation (IV.1).

$$\Omega_{ref} = \frac{\lambda_{opt} V_{tide}}{R} \quad \text{(IV.1)}$$

For the turbine that we analyzed in section II.3.4, λ_{opt}=3.28, C_{p_max}=0.1719, and the radius of the turbine R is 1.5661 m.

As the power varies with the cube of the marine current velocity, if the marine current speed changes a little, the hydrodynamic power will alter apparently. As a result, when the marine current speed is high, MPPT strategy must be changed as the maximum mechanical power is too big to the system. In our study, a Constant Power Control (CPC) strategy is adopted.

If we consider the converter gain equates to 1, the machine side double loop control block can be simplified as represented in Fig.IV.4.

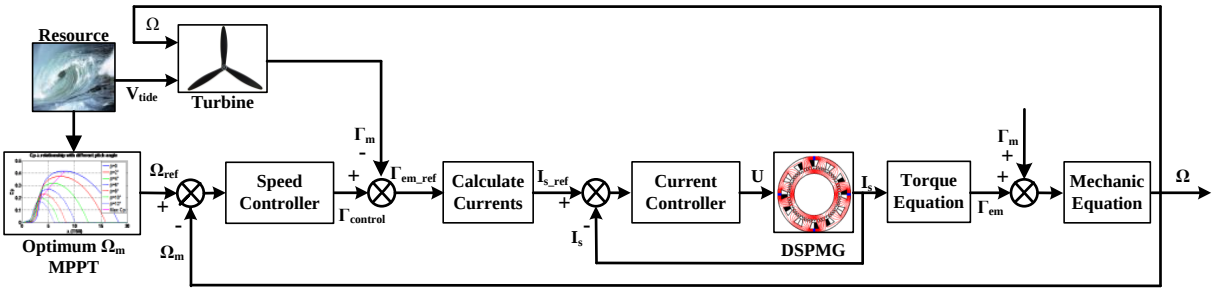

Fig.IV.4 Control schematic of Marine Current Energy Conversion System (MCECS)

IV.2.2 Current control

Based on the analysis in Chapter II, the d-q model of DSPMG is a nonlinear time-variant model. In this part, the nonlinear and robust Sliding Mode Control (SMC) is introduced. Then, the current performance will be compared with the classical Proportional Integral (PI) controller.

IV.2.2.1 Sliding Mode Control

SMC is a standard systematic approach to tackle the parametric and modeling uncertainties of a nonlinear system. It alters the dynamics of a nonlinear system by application of a discontinuous control signal that forces the system to slide along a cross-section. It switches from one continuous structure to another based on the current position in the state space which is to say that SMC is a variable structure control method. The motion of the system sliding along the boundaries is so called sliding mode which is unaffected by the disturbances. These boundaries are called sliding surface [104] - [107].

The voltage equation for DSPMG in equation (II.64) can be also written as:

$$\begin{cases} -v_o = e_o + \beta_{11} * \frac{d}{dt} i_0 + \beta_{12} * \frac{d}{dt} i_d + \alpha_{11} * i_0 \\ -v_d = e_d + \beta_{21} * \frac{d}{dt} i_o + \beta_{22} * \frac{d}{dt} i_d + \beta_{23} * \frac{d}{dt} i_q + \alpha_{22} * i_d + \alpha_{23} * i_q \\ -v_q = e_q + \beta_{32} * \frac{d}{dt} i_d + \beta_{33} * \frac{d}{dt} i_q + \alpha_{31} * i_o + \alpha_{32} * i_d + \alpha_{33} * i_q \end{cases} \quad \text{(IV.2)}$$

Where:

$$[\alpha]=\begin{bmatrix} R_s & 0 & 0 \\ -\omega_e M_{oq} & R_s+2\omega_e M_{dq} & -\omega_e\left(\frac{3L_d}{2}-\frac{L_q}{2}\right) \\ \omega_e M_{od} & \omega_e\left(\frac{3L_q}{2}-\frac{L_d}{2}\right) & R_s-2\omega_e M_{dq} \end{bmatrix}=\begin{bmatrix}\alpha_{11} & \alpha_{12} & \alpha_{13}\\ \alpha_{21} & \alpha_{22} & \alpha_{23}\\ \alpha_{31} & \alpha_{32} & \alpha_{33}\end{bmatrix};$$

$$[\beta]=\begin{bmatrix} L_0+2M_0 & \frac{1}{\sqrt{2}}(L_1-M_1) & 0 \\ \frac{1}{\sqrt{2}}(L_1-M_1) & L_0-M_0+\left(\frac{L_1}{2}+M_1\right)\cos 3\theta_e & -\left(\frac{L_1}{2}+M_1\right)\sin 3\theta_e \\ 0 & -\left(\frac{L_1}{2}+M_1\right)\sin 3\theta_e & L_0-M_0-\left(\frac{L_1}{2}+M_1\right)\cos 3\theta_e \end{bmatrix}$$
$$=\begin{bmatrix}\beta_{11} & \beta_{12} & \beta_{13}\\ \beta_{21} & \beta_{22} & \beta_{23}\\ \beta_{31} & \beta_{32} & \beta_{33}\end{bmatrix}.$$

In order to control the DSPMG, a state space model can be deduced from equation (IV.2). It is given by equation (IV.3).

$$\dot{X}=AX+BU+B_1E \tag{IV.3}$$

Where:

$X=[i_o \quad i_d \quad i_q]^t$; $U=[v_o \quad v_d \quad v_q]^t$; $E=[e_o \quad e_d \quad e_q]^t$;

$A=-[\beta]^{-1}[\alpha]$; $B=B_1=-[\beta]^{-1}$;

The developed non-linear control law is established using Lyapunov's Second theorem of stability. For designing the SMC, there are two important points: firstly, how to choose the sliding surface; secondly, how to get the control laws [92].

In our study a Reaching law based on SMC scheme has been applied to control the inner loop current performance. The purpose of our system is to well trace the current, according to [105] and [106], the sliding surface is developed as:

$$\sigma=I_{ref}-I \tag{IV.4}$$

Where: I_{ref} is the stator current reference, $I_{ref}=\left[i_{o_{ref}} \quad i_{d_{ref}} \quad i_{q_{ref}}\right]^t$; I is the Simulated current, $I=[i_o \quad i_d \quad i_q]^t$.

Satisfying the reaching condition of sliding mode, the control law is designed such as the time taken for reaching the sliding mode is very fast. According to [106], a reaching law approach can be written as follow:

$$\dot{\sigma}=-k\sigma-\varepsilon\, sign(\sigma) \tag{IV.5}$$

Where the constants $\varepsilon>0$, $k>0$, the reaching time criterion is given as [105]:

$$t_r=\frac{1}{k}Ln\left(\frac{k|\sigma_0|+\varepsilon}{\varepsilon}\right) \tag{IV.6}$$

Where: σ_0 is the initial value of trajectory.

Signum function is defined as:

$$sign(\sigma) = \begin{cases} 1 & \sigma > 0 \\ -1 & \sigma < 0 \end{cases} \quad \text{(IV.7)}$$

So, in our case, the dynamic SMC is designed as the following equation:

$$U = [\beta] * \left(-k\sigma - \varepsilon\, sign(\sigma) - \dot{I}_{ref}\right) - [\alpha] * I - E \quad \text{(IV.8)}$$

The structure of the SMC scheme of the current control Loop is presented in Fig.IV.5 and is simulated on Matlab/Simulink® by considering the simple sinusoidal and quasi sinusoidal current form given in Chapter III.

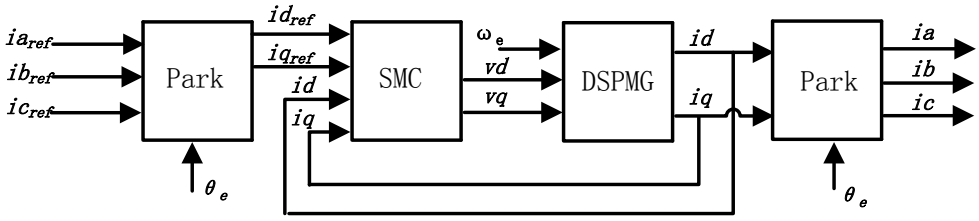

Fig.IV.5 Structure of the current control loop (SMC)

Based on the introduction of SMC, the performance of the currents will be presented and compared with that of PI controller for both sinusoidal current waveform and the quasi sinusoidal current waveform containing fundamental and 2nd current harmonic for -1845 Nm. The simulation results are given in Fig.IV.6 to Fig.IV.9

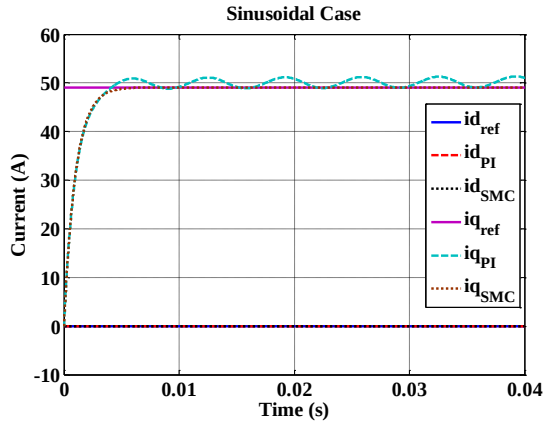

Fig.IV.6 d-q axis currents

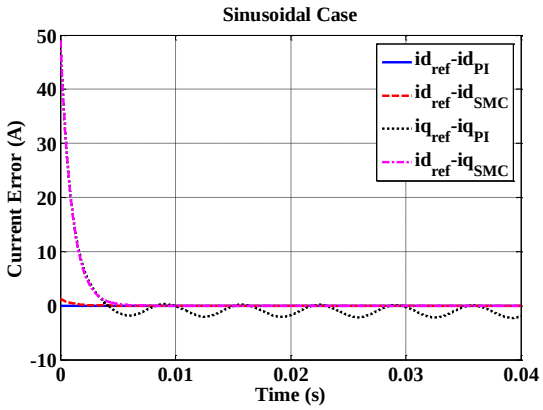

Fig.IV.7 Current error in d-q axis

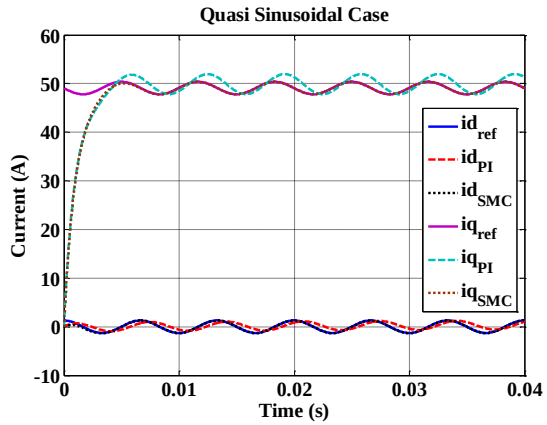

Fig.IV.8 d-q axis currents

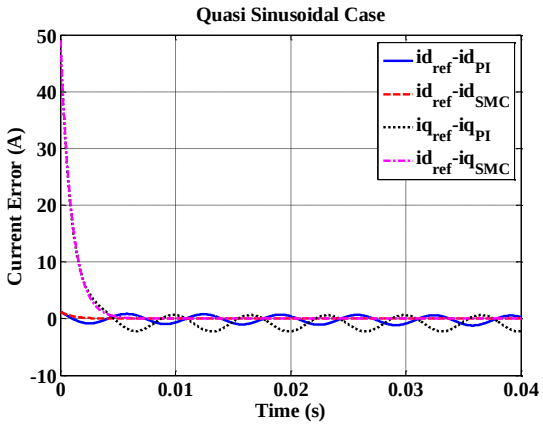

Fig.IV.9 Current error in d-q axis

For the sinusoidal current waveform, the d-q axis currents are constant (see Fig.IV.6). The PI controller can well trace the d axis current but cannot keep the q axis current equate to the reference. SMC appears a good performance for the sinusoidal current waveform in Fig.IV.6 and Fig.IV.7. For the proposed current, as the existence of the 2nd current harmonic, the d-q axis currents are not constant. PI controller cannot well trace both d-q axis currents; however, SMC still presents good performance with zero current errors.

In conclusion, PI controller is no longer suitable to the nonlinear system. SMC has proved the high performance dynamic characteristics for the nonlinear time variant system even for the variable reference. SMC is a good choice for the inner current loop control. Some robust analysis of SMC for current loop is presented in Appendix IX.

IV.2.3 Speed Control

In section IV.2.1, we have discussed MPPT for MCECS. The maximum power from the marine current is determined by the turbine rotating speed for the given turbine. Thus, the way to harness the maximum power is just to control the mechanical speed of the turbine (generator) at the optimum speed. Therefore, the schematic of the external speed control strategy is simplified in Fig.IV.10. Here, we assume that the transfer function of internal current loop was perfect.

In this section, PI controller based on pole placement method is proposed for the speed loop control. As the marine current has a very slow variation during the daytime, usually, we can consider that the marine current speed is constant during few minutes. However, due to the existence of the swell effect in some special sites, the speed can change in a short time.

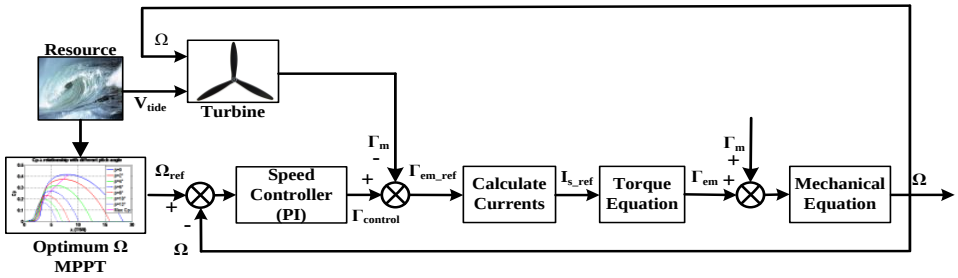

Fig.IV.10 Structure of the speed control loop

The mechanical equation for the generator can be written as:

$$\Gamma_m + \Gamma_{em} = J_m \frac{d\Omega}{dt} + f_v \Omega \tag{IV.9}$$

Where: Γ_m is the mechanical torque from MCT (Nm); Γ_{em} is the electromagnetic torque from generator (Nm); Ω is the mechanical speed (rad/s); J_m is the moment of inertia (kg*m^2); f_v is the coefficient of friction (Nm*s/rad).

After Laplace transformation, the mechanical expression in (IV.9) can be written as:

$$G_m(s) = \frac{\frac{1}{f_v}}{1+\frac{J_m}{f_v}s} \tag{IV.10}$$

IV.2.3.1 PI controller

For our study, PI controller is used for the speed loop which is given in equation (IV.11).

$$G_{cm}(s) = k_{pm} + \frac{k_{im}}{s} \tag{IV.11}$$

Where: k_{pm} and k_{im} are the proportional and integral constant for speed loop.

The second order close loop transfer function for PI controller with pole placement method is given in formula (IV.12).

$$F_{cm}(s) = \frac{F_{om}(s)}{1+F_{om}(s)} = \frac{\frac{k_{im}}{J_m}}{S^2+\frac{k_{pm}+f_v}{J_m}s+\frac{k_{im}}{J_m}}\left(1+\frac{k_{pm}}{k_{im}}s\right) \tag{IV.12}$$

Two parameters of PI controller: proportional part and integral part are calculated by formula (IV.13).

$$\begin{cases} k_{pm} = 2\xi\omega_n J_m - f_v \\ k_{im} = J_m\omega_n^2 \\ \omega_n = \frac{3}{t_r} \\ \xi = 0.707 \end{cases} \tag{IV.13}$$

In this simulation, the machine mechanical speed begins from 4.19 rad/s (marine current speed V_{tide}= 2 m/s) and increases to 5.24 rad/s when the marine current speed reaches the nominal condition (V_{tide}= 2.5 m/s). At last, the mechanical speed decreases to 3.15 rad/s (V_{tide}= 1.5 m/s). The simulation results are given in Fig.IV.11.

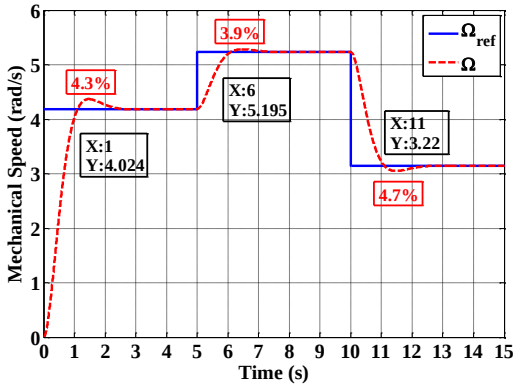

Fig.IV.11 Mechanical performace for PI controller

Three text boxes in the figure give the information for each response time (1 s, 6 s, 11 s). From these values, although the second order system brings relative small overshoots (4.3%, 3.9%, 4.7%) (see Fig.IV.11), PI controller can get the 95% of the reference values during the mechanical response time. It approves good performance in tracking the mechanical speed. The external PI mechanical speed controller is theoretically ideal.

IV.2.3.2 Robust Analysis for Speed Loop

The robust analysis of PI controller for the mechanical parameters will be presented in this part. Firstly, the influence of coefficient of friction is explained; then the moment of inertia is discussed. The variation will be between 80%~120%. Fig.IV.12 and Fig.IV.13 present respectively the influences of the friction coefficient and moment of inertia for PI controller.

Based on these figures, the bigger friction coefficient and smaller moment of inertia will decelerate the system and decrease the overshoot (see Fig.IV.12). On the contrary, the smaller friction coefficient or bigger moment of inertia will accelerate the system and increase the overshoot (see Fig.IV.13).

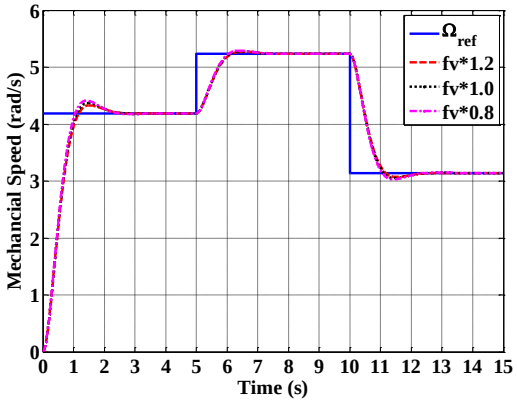

Fig.IV.12 Influence of the friction coefficient

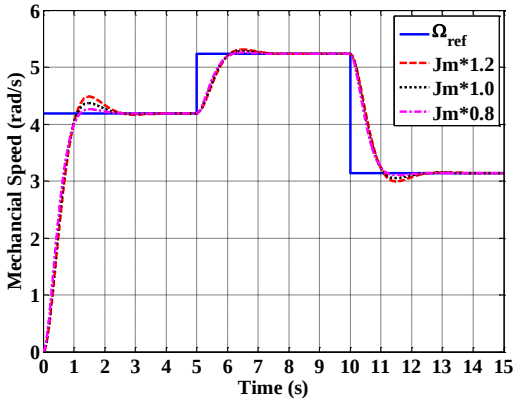

Fig.IV.13 Influence of moment of inertia

IV.2.3.3 Control Strategies for High Marine Current Speed

The turbine maximum speed to follow MPPT is 5.24 rad/s for a marine current of 2.5 m/s. When the marine current speed exceeds 2.5 m/s, the extracted power will be limited to 10 kW by CPC strategy (see Fig.IV.14).

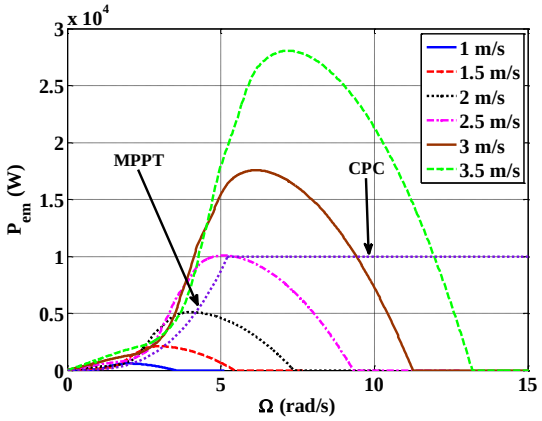

Fig.IV.14 Electromagnetic power

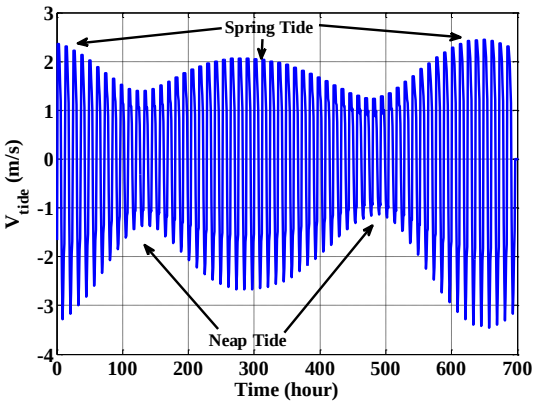

Fig.IV.15 Marine current velocity

According to the marine current speed in Fig.IV.15 for Penmarc'h, France, for this example, the peak marine current speed will reach 3.5 m/s. If the MPPT strategy is still used, the maximum extracted power will be over 29 kW.

In accordance of the Cp-λ curve in Fig.IV.16, we observe that for every given Cp value, there are two possibilities existing in both Zones I and II.

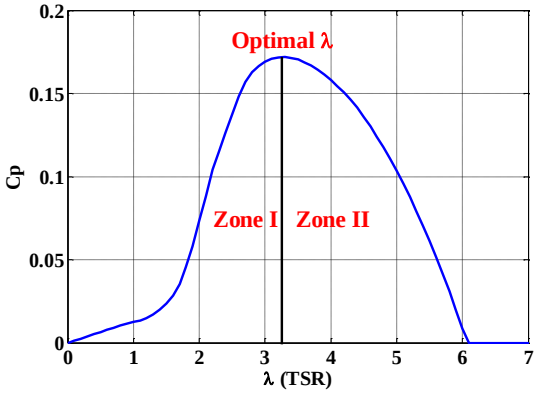

Fig.IV.16 Cp-λ curve

For Zone I, if the marine speed increases, the mechanical power will increase immediately because of the same power coefficient. Consequently the mechanical speed increase as the electromagnetic torque is considered constant for a short time. Then the power coefficient Cp and mechanical power P_m still increases and reaches the optimal Cp-λ point, working as MPPT.

The same situation happens in the Zone II. If the mechanical speed and TSR increase, the power coefficient and mechanical power will decrease. This tendency will make the system work near the original mechanical power. This zone is more stable for the small variation of the marine current speed.

The variation of the marine current speed is simplified in the following:

Zone I: $V_{tide} \nearrow \rightarrow P_m \nearrow \rightarrow \Omega \nearrow \rightarrow \lambda \nearrow \rightarrow Cp \nearrow \rightarrow P_m \nearrow$;

Zone II: $V_{tide} \nearrow \rightarrow P_m \nearrow \rightarrow \Omega \nearrow \rightarrow \lambda \nearrow \rightarrow Cp \searrow \rightarrow P_m \searrow$.

IV.2.3.3.1 CPC strategy

In order to get constant the electromagnetic power of the generator for high marine current speeds, the new reference mechanical rotating speed must be calculated. If each side of the mechanical equation (IV.9) is multiplied by mechanical speed Ω, it can be rewritten as:

$$P_m + P_{em} = J_m \Omega \frac{d\Omega}{dt} + f_v \Omega^2 \qquad \text{(IV.14)}$$

For a small variation of the machine current speed, equation (IV.14) can be simplified as:

$$P_{em} = \underbrace{f_v \Omega^2}_{P_{m\ loss}} - \underbrace{C_p P_{hyd}}_{P_m} \qquad \text{(IV.15)}$$

Based on equation (IV.15), the proposed mechanical speed reference for CPC can be obtained as shown in Fig.IV.17. In this scheme, for each given marine current speed, the hydrodynamic power (P_{hyd}) is calculated firstly; then λ increases from 3.28 which means the function point is in Zone II ($\lambda > \lambda_{opt}$); the relative mechanical speed Ω and C_p are achieved to get the electromagnetic power P_{em}; if the difference between this value and the power limitation $P_{em\ lim}$ (10 kW) is bigger than ΔP, λ continues to increase ($\lambda_n=\lambda_{n-1}+\Delta\lambda$) until P_{em} converges to the power limitation. In this way, the suitable mechanical speed for overrated marine current speed can be obtained.

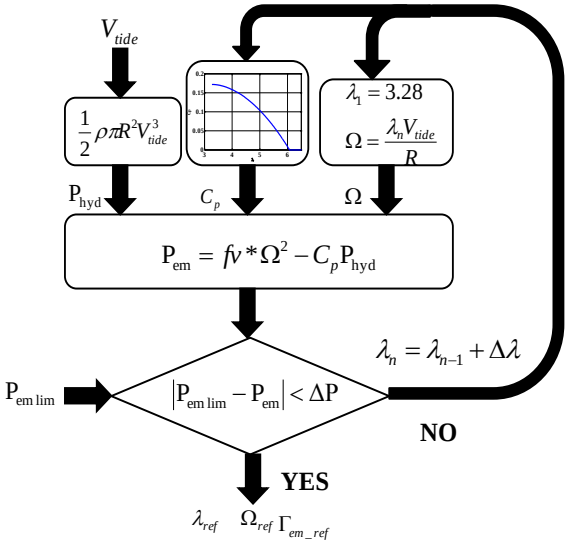

Fig.IV.17 Mechanical speed reference calculation for CPC

Based on the scheme in Fig.IV.17, the suitable λ and mechanical speed reference Ω_{ref} for each high marine current speed between 2.5 m/s and 3.5 m/s are given in Fig.IV.18 and Fig.IV.19.

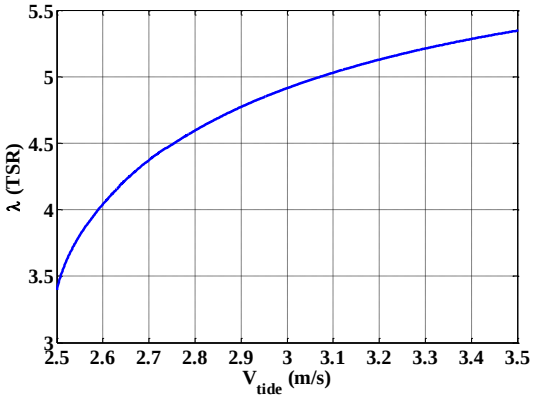

Fig.IV.18 Suitable λ (CPC)

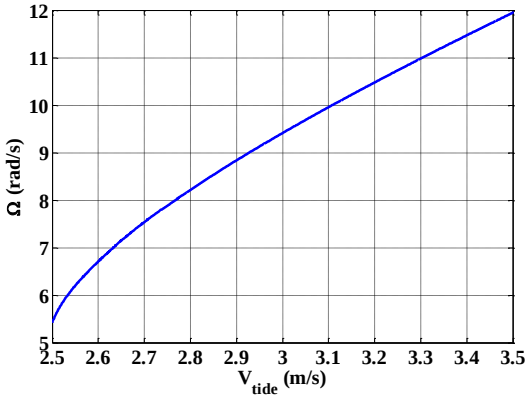

Fig.IV.19 Suitable mechanical speed (CPC)

According to these two figures, when the marine current speed increases, the suitable tip speed ratio λ and the mechanical speed Ω increase. Hence, the power coefficient Cp in Zone II will decrease as shown in Fig.IV.20. The variations of the mechanical power P_m electromagnetic power P_{em} and mechanical loss P_{m_loss} with the marine current speed are presented in Fig.IV.20. As the electromagnetic power is constant and the mechanical speed increases, it leads to the decrease of the electromagnetic torque which is shown in Fig.IV.22.

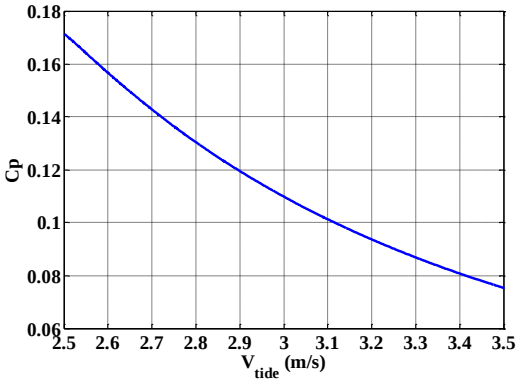

Fig.IV.20 Suitable Cp (CPC)

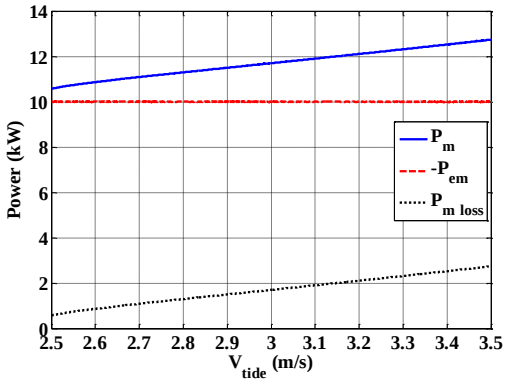

Fig.IV.21 Power (CPC)

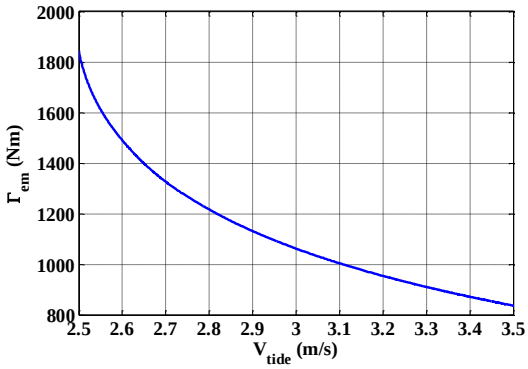

Fig.IV.22 Electromagnetic torque (CPC)

On the following, the MPPT and CPC strategies performances with the marine current speed increasing are presented. For the simulation, the marine current speed is initially set at 2.5 m/s and rises to 3.5 m/s during 10 s to 40 s as shown in Fig.IV.23. After 10 s, the current speed is bigger than the rated value (2.5 m/s) and the power limitation control strategy should be applied. Although this marine current speed is not very realistic (as the marine current speed periodic changes slowly during approximately half a day in reality), it enables to test the performances of the two strategies.

Figures, from Fig.IV.24 to Fig.IV.27, present the power coefficient C_p, average electromagnetic power P_{em}, electromagnetic torque Γ_{em} and the suitable mechanical speed Ω respectively.

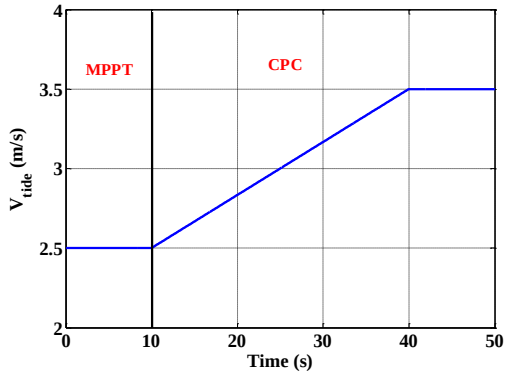

Fig.IV.23 Marine current speed

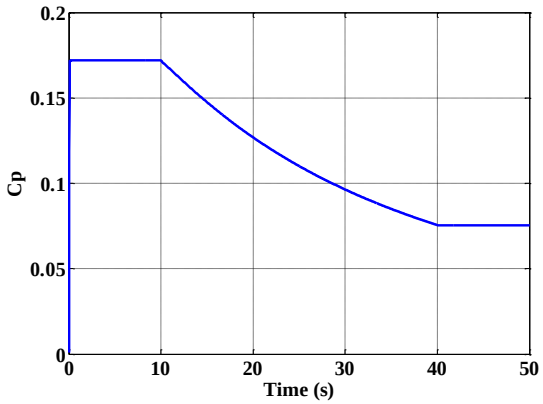

Fig.IV.24 Cp for CPC

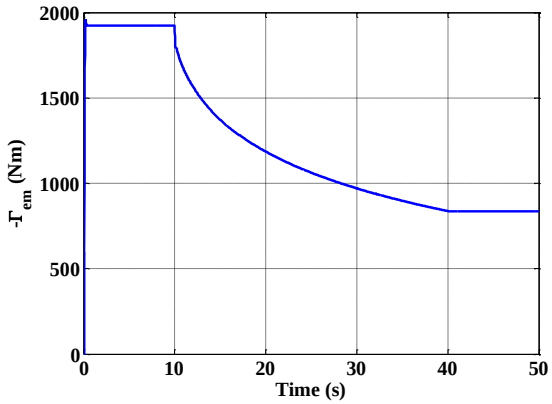

Fig.IV.25 Electromagnetic torque for CPC

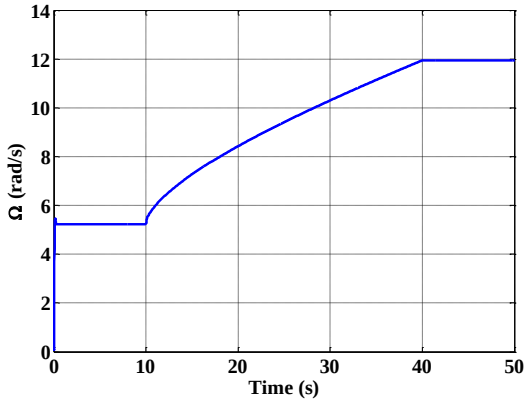

Fig.IV.26 Mechanical speed for CPC

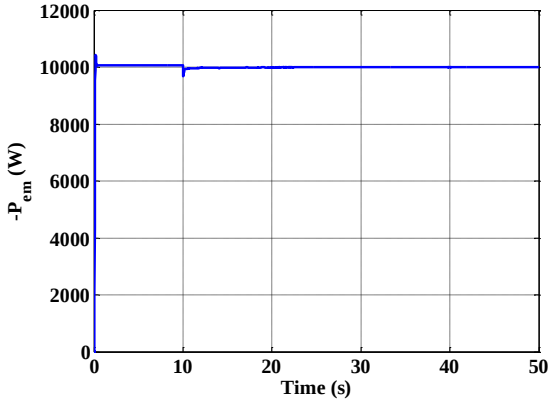

Fig.IV.27 Electromagnetic power for CPC

From Fig.IV.24, before 10 s, the Cp is fixed at the maximum value. Then Cp decreases as CPC strategy is used for high marine current speed (>2.5 m/s). After 10 s, the marine current speed begins to increase, the mechanical speed and electromagnetic torque increase smoothly (see Fig.IV.25 and Fig.IV.26). There are no big variations for the strategy change. Fig.IV.27 presents the electromagnetic power of the machine. It can be seen that, the power is kept constant for the marine current speed between 2.5 m/s and 3.5 m/s. In conclusion, this strategy is suitable for the high marine current speed and it doesn't bring big variation for the strategy change.

IV.2.3.3.2 Stator Current for High Marine Current Speed

According to Fig.IV.19, the suitable mechanical speed increases when the marine current speed increases. However, the EMF of the machine will also increase which leads to a high machine voltage. Therefore, it's necessary to define the suitable machine current to get the desired torque and limit the machine voltage.

The voltage expression of DSPMG supplied by the quasi sinusoidal current waveform is very complex. Hence, a numerical method to analyze the machine current for high marine current speed is proposed. The scheme to calculate the current is given in Fig.IV.28.

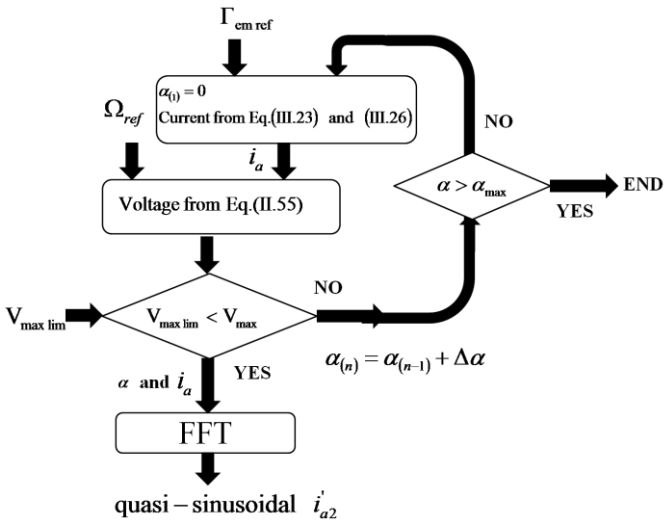

Fig.IV.28 Scheme to calculate the quasi sinusoidal current waveform

The suitable electromagnetic torque and mechanical speed for each marine current speed (see Fig.IV.19 and Fig.IV.22) are used to calculate the voltage (load angle α begins from 0°). If the maximum phase voltage is bigger than the designed value $V_{max\ lim}$, α increases until the maximum phase voltage is smaller than this value. Then, quasi sinusoidal current waveform containing fundamental and 2nd harmonic are determined.

The DC bus voltage is chosen taking into account the output limit stator voltage as indicated in formula (IV.16) [108].

$$V_{DC} \geq \frac{1.634*\sqrt{3}}{\sqrt{2}} V_{max\ \ lim} \tag{IV.16}$$

Thanks to the flowchart on Fig.IV.28, the load angle and the relative maximum voltage variations for the flux weakening strategy are given on Fig.IV.29 and Fig.IV.30. From these two figures, for CPC strategy, the load angle is first equal to 0, after it always increases with the increase of marine current speed. Using the load angle, the amplitudes of currents for CPC strategy are given in Fig.IV.31.

The load angle and the maximum phase voltage obtained by scheme in Fig.IV.28 are presented in the following:

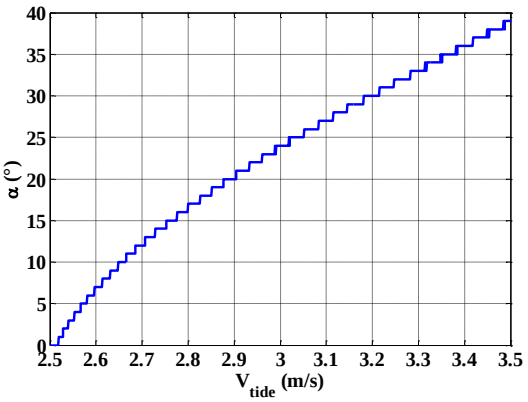

Fig.IV.29 Load angle for flux weakening

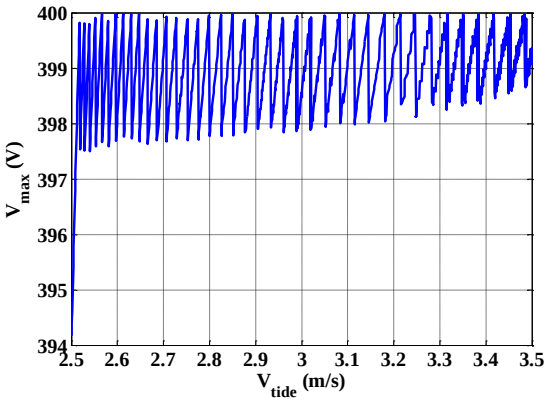

Fig.IV.30 Maximum voltage for the load angle

However, as we have discussed in Chapter III, the quasi sinusoidal current we used in this chapter will surely slight increase the maximum voltage.

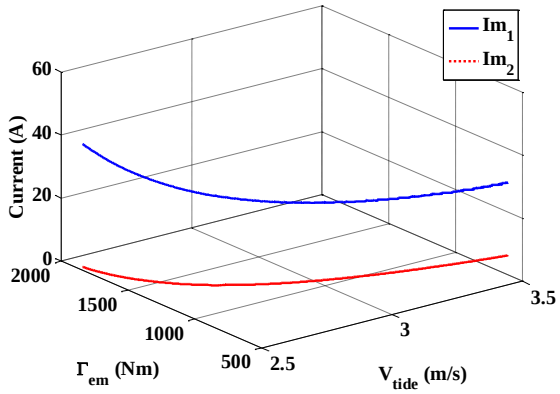

a) Harmonic currents for CPC strategy 3D

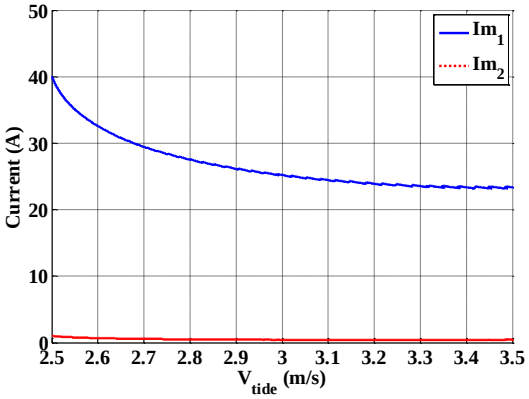

b) Harmonic currents versus marine current speed

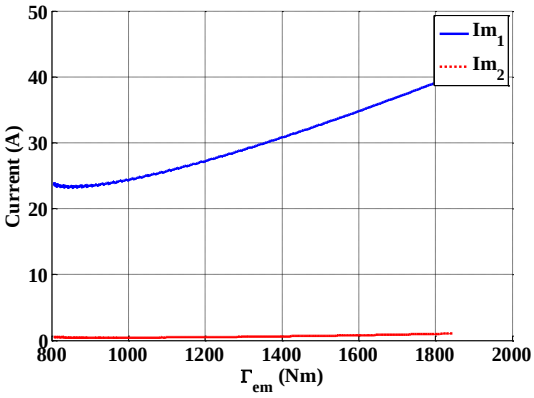

c) Harmonic currents versus electromagnetic torque

Fig.IV.31 Harmonic currents with the relationship of Marine current speed and Torque

IV.2.4 Current and Speed Closed Loop Decoupling Control

For the double loop control, the mechanical speed reference is determined by marine current speed and different control strategies (MPPT for low speed, CPC for high speed). Then the torque reference is obtained by the mechanical torque and speed control output. At last, the machine current reference to produce the desired torque is obtained from Fig.III.63 or Fig.IV.31.

The marine current speed varies very slowly during the daytime. We can consider it is constant for several minutes. Firstly, a ramp form marine current speed is used for the machine side system. Although this form is not realistic for marine current speed, it enables to study the machine performances with the quick marine current speed variation in the simulation. Then, the realistic marine current speed based on SHOM data [77] will be tested.

We consider the ramp form marine current speed is 2.5 m/s at the beginning, then increases to 3.5 m/s slowly from 1s to 4 s as showed in Fig.IV.32. Fig.IV.33 reveals the mechanical speed Ω. The machine side double loop can well track the mechanical speed reference.

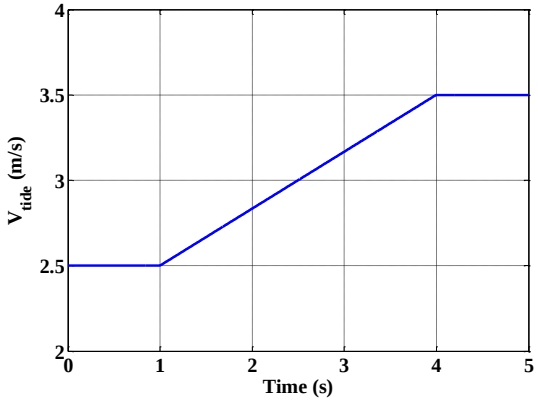

Fig.IV.32 Marine current speed

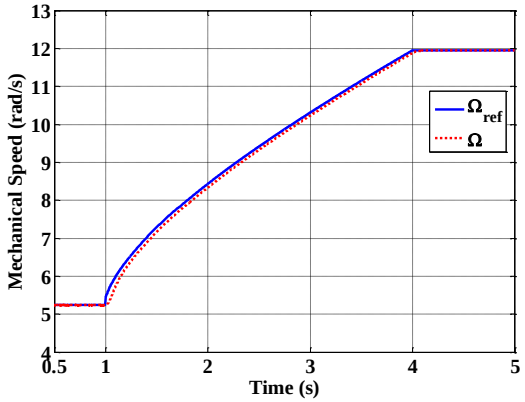

Fig.IV.33 Mechanical speed

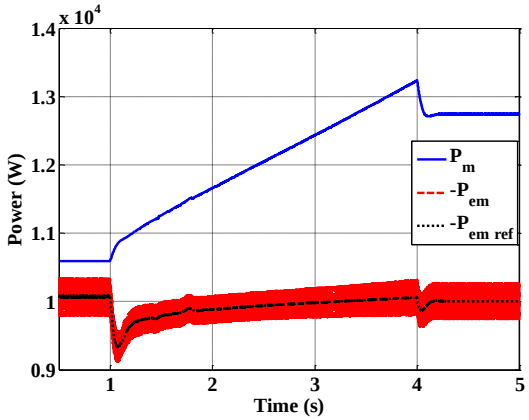

Fig.IV.34 Power

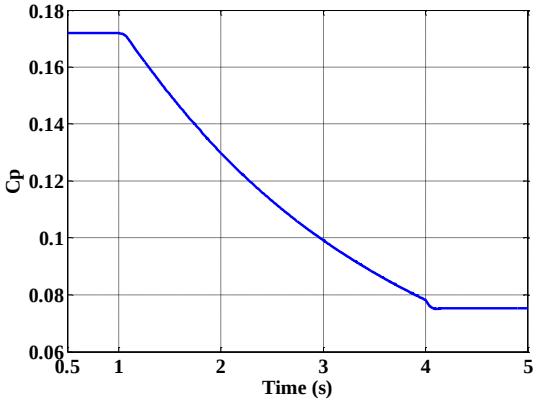

Fig.IV.35 Power coefficient

As the variation of the marine current speed is much more slowly than before, there is no big power fluctuation. The power and torque are smoother than before. Fig.IV.34 gives the mechanical power and electromagnetic power of the machine side system. In accordance of CPC strategy, the average value of electromagnetic power is nearly 10 kW. The difference of the mechanical and electromagnetic powers increases as the mechanical losses rise with the mechanical speed increasing. In accordance of the CPC strategy when the marine current speed is higher than 2.7 m/s, the power coefficient Cp will decrease as shown in Fig.IV.35.

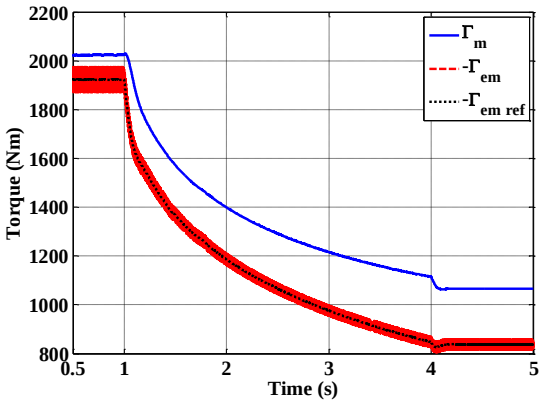

Fig.IV.36 Torque

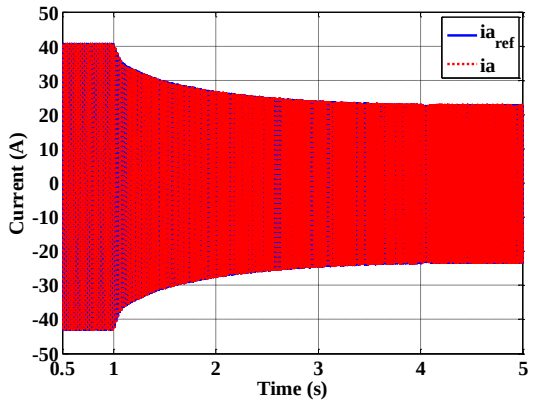

Fig.IV.37 Current for phase A (i_a)

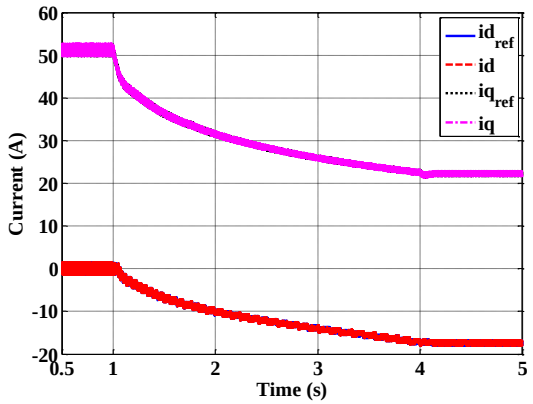

Fig.IV.38 d-qaxis current

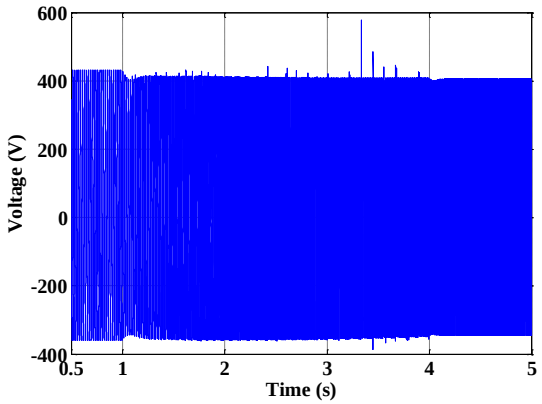

Fig.IV.39 Phase voltage for phase A (v_a)

On Fig.IV.36, we can see that the electromagnetic torque will decrease to maintain the electromagnetic power when the mechanical speed increases. As the current is the function of the electromagnetic torque, therefore, the current has the same variation like the torque (see Fig.IV.37 and Fig.IV.38). The relative voltage of the phase A is given in Fig.IV.39.

From the simulation results, the machine side double loop system appears good performances to track the mechanical speed, electromagnetic torque and the current. For the sake of simulate the whole day, marine current speed based on realistic date [SHOM] is considered as represented in Fig.IV.40.

As the marine current speed is smaller than 1 m/s, the extracted power is nearly zero. Thus, the mechanical speed reference is considered as zero. Fig.IV.41 just shows the relative mechanical speed based MPPT and CPC strategies. Fig.IV.42 and Fig.IV.43 present the torque and power respectively.

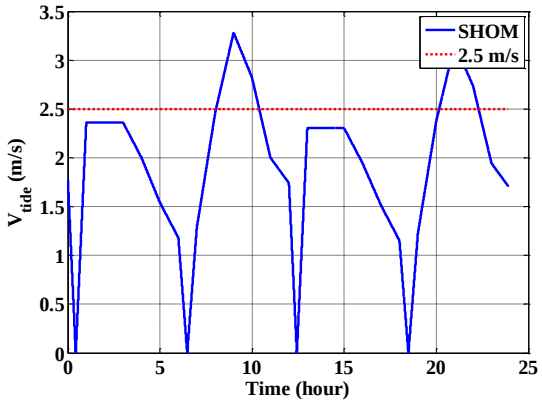

Fig.IV.40 Marine current speed (SHOM)

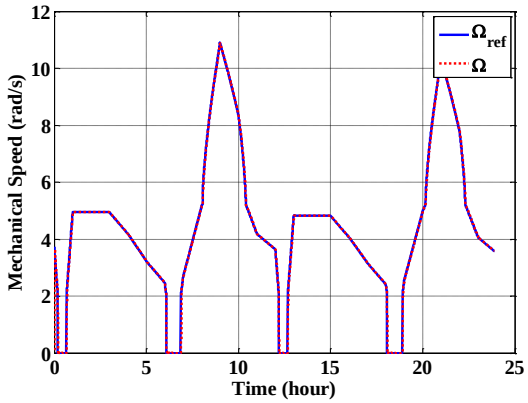

Fig.IV.41 Mechanical speed

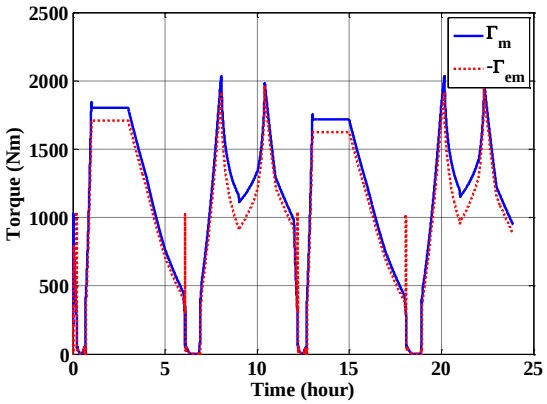

Fig.IV.42 Torque (SHOM)

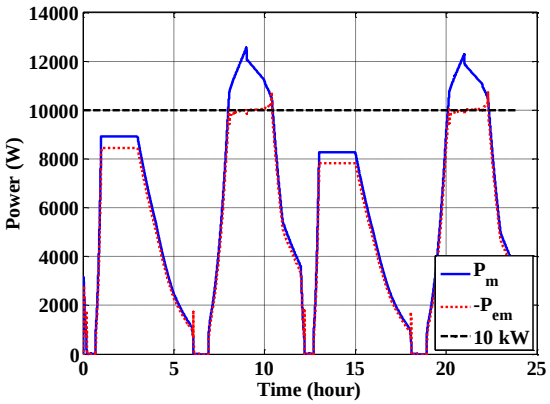

Fig.IV.43 Power (SHOM)

IV.2.5 Influence of the AC/DC Converter

In Chapter I, 4 mainly converter topologies are briefly introduced. In our study, the full power converter with 6-switch, back-to-back bridge and DC-link capacitor are adopted. The losses in the converters are neglected during our research. The machine side converter is presented in Fig.IV.44.

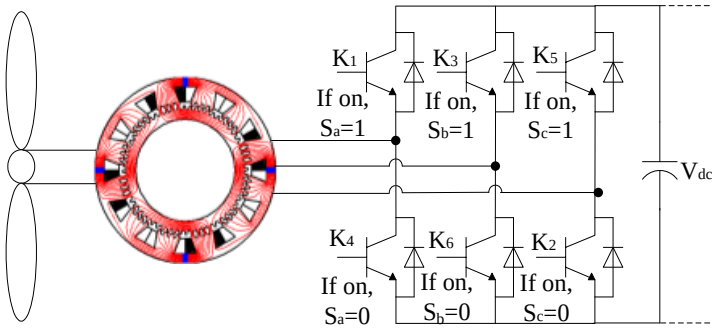

Fig.IV.44 Machine side converter

Where: K1~K6 are the switches; V_{DC} is the DC-bus voltage.

The AC (Alternating Current) side voltage can be represented with eight possibilities (six active and two zero) described by:

$$V_{i+1} = \begin{cases} \frac{2}{3} V_{dc} e^{j\frac{i\pi}{3}} & i \in [0,5] \\ 0 \end{cases} \qquad \text{(IV.17)}$$

To make the converter works properly, the PWM pattern must generate a fundamental with the same frequency as the power source. Changing the amplitude of this fundamental and its phase shift with respect to the mains, the converter can be controlled to operate in the four quadrants: leading power factor converter, lagging power factor converter, leading power factor inverter, and lagging power factor inverter. Changing the pattern of modulation modifies the magnitude of fundamental. Displacing the PWM pattern changes the phase shift [109].

So as to model the PWM converter mathematically, it is obliged to describe the input voltage in PWM converter. The phase voltages are given by:

$$\begin{bmatrix} v_a \\ v_b \\ v_c \end{bmatrix} = \frac{V_{DC}}{3} \begin{bmatrix} 2 & -1 & -1 \\ -1 & 2 & -1 \\ -1 & -1 & 2 \end{bmatrix} \begin{bmatrix} S_a \\ S_b \\ S_c \end{bmatrix} \quad \text{(IV.18)}$$

The details of the voltages and switches are given in the Table IV.1.

Table IV.1 The relationship between the AC and DC voltage of the converter

Switch			Phase voltage V			Line to line voltage U		
S_a	S_b	S_c	v_a	v_b	v_c	u_{ab}	u_{bc}	u_{ca}
0	0	0	0	0	0	0	0	0
1	0	0	$2/3\,V_{DC}$	$-1/3\,V_{DC}$	$-1/3\,V_{DC}$	V_{DC}	0	$-V_{DC}$
1	1	0	$1/3\,V_{DC}$	$1/3\,V_{DC}$	$-2/3\,V_{DC}$	0	V_{DC}	$-V_{DC}$
0	1	0	$-1/3\,V_{DC}$	$2/3\,V_{DC}$	$-1/3\,V_{DC}$	$-V_{DC}$	V_{DC}	0
0	1	1	$-2/3\,V_{DC}$	$1/3\,V_{DC}$	$1/3\,V_{DC}$	$-V_{DC}$	0	V_{DC}
0	0	1	$-1/3\,V_{DC}$	$-1/3\,V_{DC}$	$2/3\,V_{DC}$	0	$-V_{DC}$	V_{DC}
1	0	1	$1/3\,V_{DC}$	$-2/3\,V_{DC}$	$1/3\,V_{DC}$	V_{DC}	$-V_{DC}$	0
1	1	1	0	0	0	0	0	0

The state of the switches S_a, S_b , S_c are presented in equations (IV.19), (IV.20) and (IV.21)

$$S_a = \begin{cases} 0 & (K_1 \text{ off}, \ K_4 \text{ on}) \\ 1 & (K_1 \text{ on}, \ K_4 \text{ off}) \end{cases} \quad \text{(IV.19)}$$

$$S_b = \begin{cases} 0 & (K_3 \text{ off}, \ K_6 \text{ on}) \\ 1 & (K_3 \text{ on}, \ K_6 \text{ off}) \end{cases} \quad \text{(IV.20)}$$

$$S_c = \begin{cases} 0 & (K_5 \text{ off}, \ K_2 \text{ on}) \\ 1 & (K_5 \text{ on}, \ K_2 \text{ off}) \end{cases} \quad \text{(IV.21)}$$

Besides the mathematical model of the converter, the trigger methods are also significant in the design of the control system. Normally, there are three main control methods in the industry application, such as Phase Amplitude Control (PAC), fixed frequency triangular wave comparison control and hysteretic current comparison control. Due to the characters of fixed frequency of the second method, it is used in our study. The whole marine current energy harness system is divided into separated part, and at last they will be integrated. The DC voltage is assumed to be well controlled by grid-side inverter [72].

The converter gain can be summarized in equation (IV.22):

$$V_{ma} = \frac{V_{DC}}{2V_c} V_{ca} \quad \text{(IV.22)}$$

If the converter gain is 1, it means the DC-bus voltage V_{DC} must equate to two time of the carrier wave voltage V_c. As a result, the machine side phase A voltage V_{ma} is exactly equal to the phase A control voltage V_{ca}.

The same marine current speed in Fig.IV.32 is also applied in this part. The performances of the system with converter especially for 2.5 m/s and 3.5 m/s marine current speed are shown in Fig.IV.45 to Fig.IV.48.

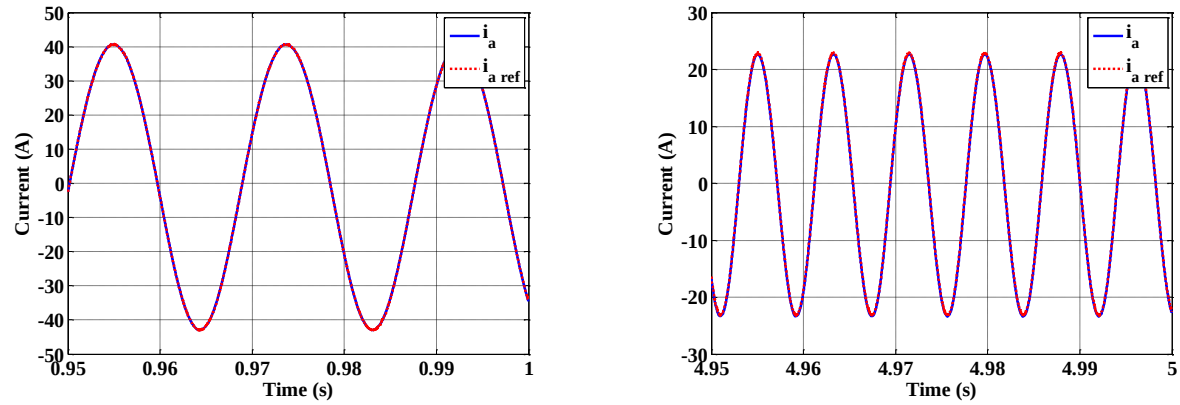

a) for 2.5 m/s b) for 3.5 m/s

Fig.IV.45 Current waveforms (with converter)

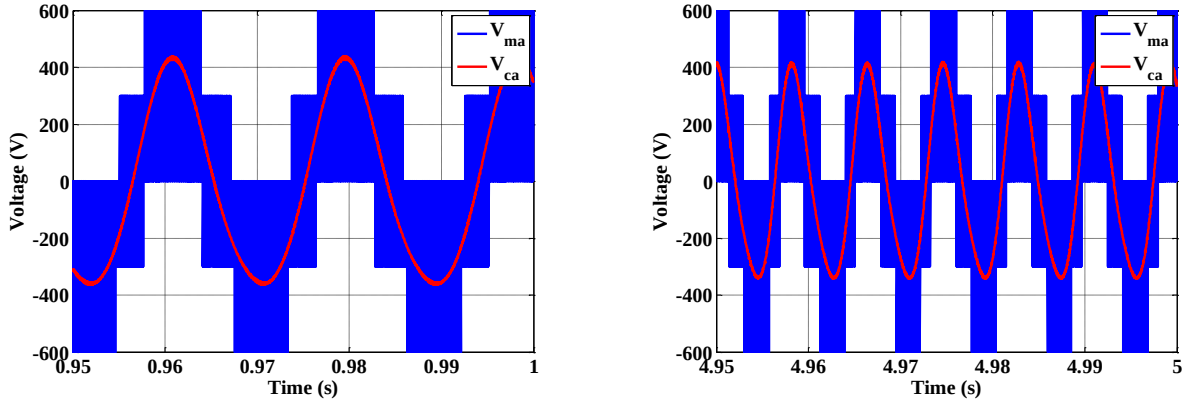

a) for 2.5 m/s b) for 3.5 m/s

Fig.IV.46 Voltage waveforms (with converter)

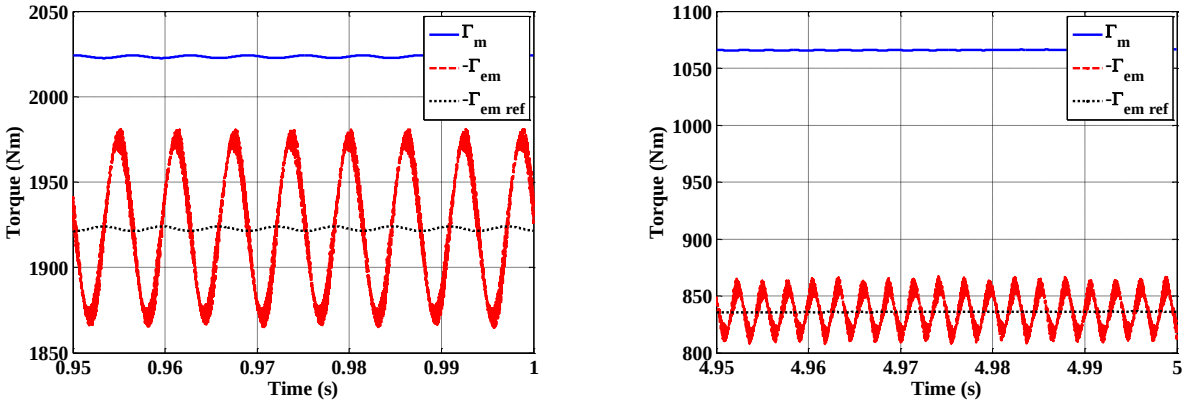

a) for 2.5 m/s b) for 3.5 m/s

Fig.IV.47 Torque performances (with converter)

From Fig.IV.45 and Fig.IV.46, we observe that the current and voltage are well controlled. The electrical frequency of the current and voltage at 2.5 m/s marine current speed is much smaller than that at 3.5 m/s. Fig.IV.47 and Fig.IV.48 present the torque and power. They imply

that the frequencies of the torque and power are practically three times than that of current as expected. For our strategy, when the marine current speed is bigger than 2.5 m/s, the machine current decreases (see Fig.IV.37). This can explain why the torque and power ripples at 3.5 m/s marine current speed are smaller than that at 2.5 m/s.

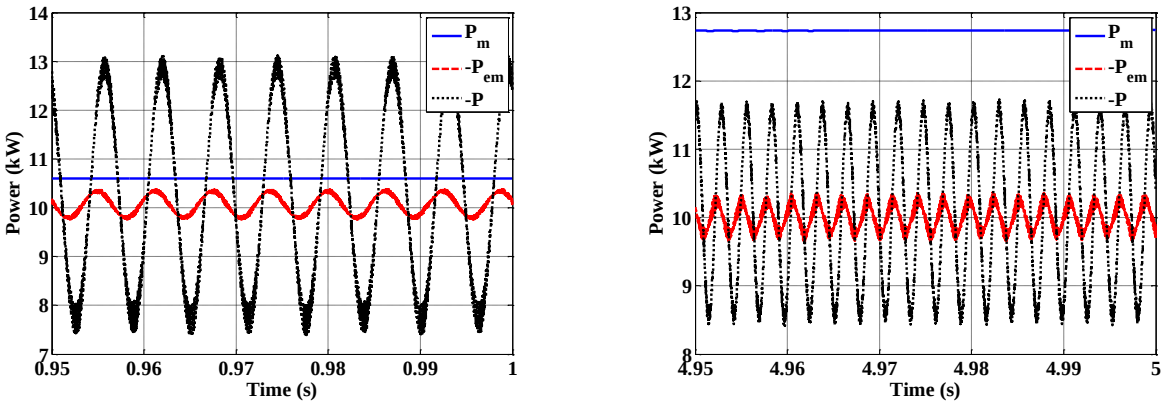

a) for 2.5 m/s b) for 3.5 m/s

Fig.IV.48 Power performances (with converter)

IV.3 *Grid Side System Design*

In section IV.2, the machine side converter was designed under the condition of constant DC-bus voltage being 900 V. Thus, the control object of grid side converter is to control and maintain the DC-bus voltage constant and assure a unity power factor on the grid side. For this purpose, an internal current loop and external voltage loop control strategy was introduced in this section. A schematic of the system was shown in Fig.IV.49.

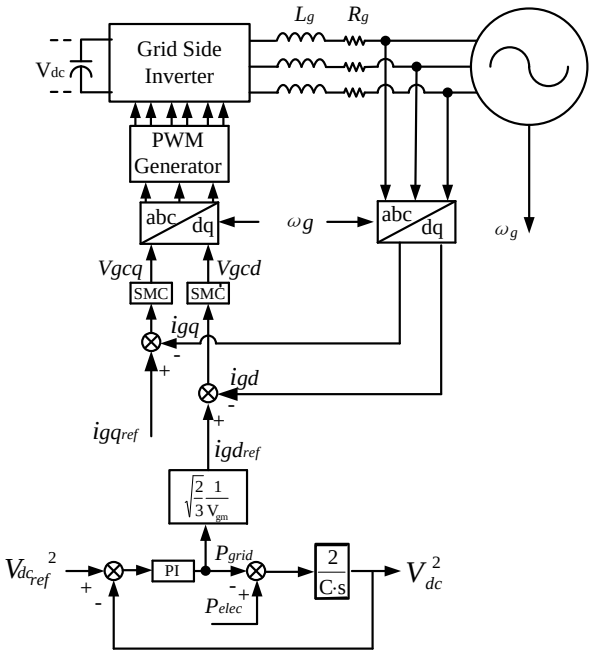

Fig.IV.49 Grid side system block diagram

IV.3.1 Passive Elements Calculation

Fig.IV.50 shows representation of the converter topology which is very similar to the machine side converter. L_g and R_g represent respectively the line inductance and resistance. i_{mdc} is the current out of the machine-side converter, i_{gdc} is the current into the grid-side inverter and i_{dc} is the current into the DC-bus capacitor.

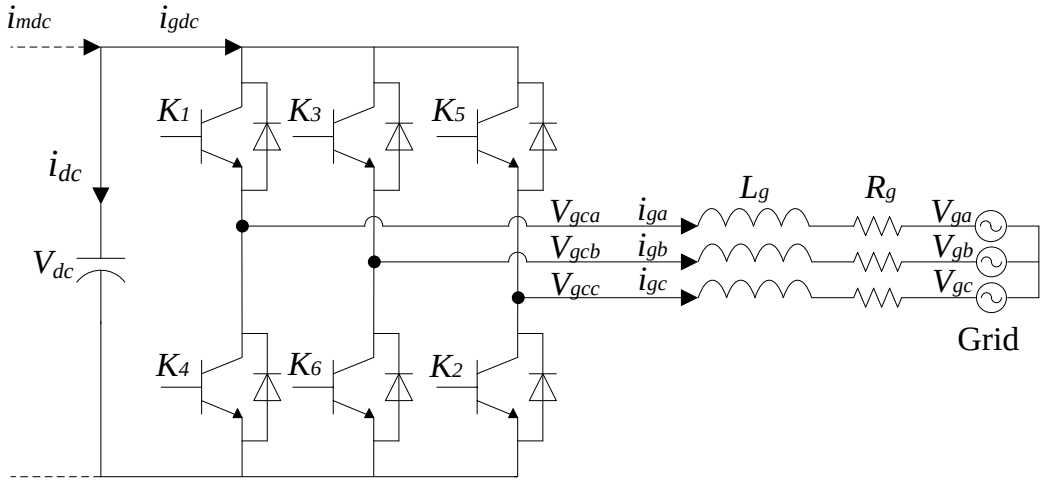

Fig.IV.50 Grid side inverter

The grid side voltage equations can be written as:

$$\begin{cases} V_{gca} = V_{ga} + R_g i_{ga} + L_g \frac{di_{ga}}{dt} \\ V_{gcb} = V_{gb} + R_g i_{gb} + L_g \frac{di_{gb}}{dt} \\ V_{gcc} = V_{gc} + R_g i_{gc} + L_g \frac{di_{gc}}{dt} \end{cases} \quad \text{(IV.23)}$$

The current relationship for the grid side is:

$$i_{mdc} - i_{gdc} = i_{dc} = C \frac{dV_{dc}}{dt} \quad \text{(IV.24)}$$

Where C is the capacitance of the DC bus capacitor.

If the converter power losses are neglected, then:

$$P_{grid} = V_{ga} i_{ga} + V_{gb} i_{gb} + V_{gc} i_{gc} = V_{dc} i_{gdc} \quad \text{(IV.25)}$$

After Concordia and Park transformations, in the d-q coordinates which rotate synchronously with an electrical angular velocity ω, the state equation of the converter based on (IV.23) is expressed as:

$$\begin{bmatrix} V_{gcd} \\ V_{gcq} \end{bmatrix} = \begin{bmatrix} V_{gd} \\ V_{gq} \end{bmatrix} + \begin{bmatrix} R_g & -\omega_g L_g \\ \omega_g L_g & R_g \end{bmatrix} \begin{bmatrix} i_{gd} \\ i_{gq} \end{bmatrix} + L_g \frac{d}{dt} \begin{bmatrix} i_{gd} \\ i_{gq} \end{bmatrix} \quad \text{(IV.26)}$$

Where: ω_g is the electrical speed of the grid side voltage (rad/s).

Theoretically, the grid side power need equate to the machine side power. Therefore, the nominal grid side power is 10 kW.

$$P_{grid} = P_{em} = 3\,\frac{V_{gm}\,I_{gm}}{2} = 10\text{ kW} \quad \text{(IV.27)}$$

Where: V_{gm} is the amplitude of the grid side voltage (V); I_{gm} is the amplitude of the grid side Current (A);

If we considered the grid side phase voltage V_{gm} is 311 V (RMS 220V), the nominal grid side current can be calculate as follows:

$$I_{gm\_max} = \frac{2P_{grid}}{3V_{gm\_max}} = 21.4\text{ A} \quad \text{(IV.28)}$$

If the current ripple in the grid side ΔI_g =0.05*Ig, the grid side inductance is given in formula (IV.29) [108].

$$L_g = \frac{\sqrt{3}*220}{6\sqrt{2}*f_s*\Delta I_g} \quad \text{(IV.29)}$$

Where: L_g is the grid side inductance, 5.9 mH; f_s is the switch frequency, 10 kHz.

According to [108], the minimum DC-bus capacity C_{dc_min} is presented in formula (IV.30).

$$C_{dc\_min} = \frac{I_{gm\_max} + \frac{P_{grid}}{V_{dc}}}{2\Delta V_{dc}*f_s} \quad \text{(IV.30)}$$

In our study, the value of the capacity is fixed to 200 µF.

IV.3.2 Internal Current Loop

To assure a unity power factor in the grid side, the q-axis current needs to be zero. For the current loop controller, SMC and the same reaching law approach than for machine side system will also be applied. Based on SMC formula (IV.8) and grid side voltage equation (IV.26), the grid current controller can be showed in:

$$\begin{bmatrix} V_{gcd} \\ V_{gcq} \end{bmatrix} = -L_g\left(\dot{\sigma}_g - \dot{I}_{g\_ref}\right) + \begin{bmatrix} R_g & -\omega_g L_g \\ \omega_g L_g & R_g \end{bmatrix}\begin{bmatrix} i_{gd} \\ i_{gq} \end{bmatrix} + \begin{bmatrix} V_{gd} \\ V_{gq} \end{bmatrix} \quad \text{(IV.31)}$$

The sliding surface σ_g is:

$$\dot{\sigma}_g = -k\sigma - \varepsilon\, sign(\sigma) = \dot{I}_{g\_ref} - \dot{I}_g \quad \text{(IV.32)}$$

IV.3.3 External Voltage Loop

As the analysis of the DC bus circuit in (IV.24), this equation is able to be used to deduce the control strategy for DC bus voltage [72]. If the transient output active power of the generator converter is calculated as P_{elec} ($P_{elec} = i_{mdc}\,V_{dc}$), and the transient power at the DC side of the grid-connected converter is P_{grid} ($P_{grid} = V_{dc}\,i_{gdc}$), the equation can be rewritten as:

$$i_{mdc} - i_{gdc} = \frac{P_{elec}}{V_{dc}} - \frac{P_{grid}}{V_{dc}} = i_{dc} = C\,\frac{dV_{dc}}{dt} \quad \text{(IV.33)}$$

After Laplace transformation, equation (IV.34) can be written as:

$$\frac{V_{dc}^2(s)}{P_{elec}(s)-P_{grid}(s)} = \frac{2}{CS} \tag{IV.34}$$

Thus, it is obvious that the under-control object is a first order system, and it is possible to design a PI controller to improve the state response. Here, we assume that the phase voltage output from the three phase grid-connected converter is ideally sinusoidal wave without distortion or noise which given in formula (IV.35).

$$\begin{cases} V_{ga} = V_{gm}\cos\omega_g t \\ V_{gb} = V_{gm}\cos(\omega_g t - \frac{2\pi}{3}) \\ V_{gc} = V_{gm}\cos(\omega_g t - \frac{4\pi}{3}) \end{cases} \tag{IV.35}$$

So that the transient value of the d axis voltage is the same as the root mean square value of the voltage. The Concordia and Park transformations are utilized to convert the three phase AC voltage to d-q axis voltage. The d-q axis current is presented in (IV.36):

$$\begin{cases} V_{gd} = \sqrt{\frac{3}{2}}V_{gm} \\ V_{gq} = 0 \end{cases} \tag{IV.36}$$

In order to get the unity power factor, the grid-side current will be in phase of the grid side voltage. Therefore, the q-axis current reference for the internal loop could be calculated by:

$$i_{gd\_ref} = \frac{P_{grid}}{V_{gd}} = \sqrt{\frac{2}{3}}\frac{P_{grid}}{V_{gm}} \tag{IV.37}$$

IV.3.4 Simulation Results

The grid side current loop using converter will be tested firstly. According to the equation (IV.28), the nominal maximum grid side current is 21.4 A. As a result, in the simulation, we assume that the initial amplitude value I_{gm} is 21.4 A and decreases to 10.7 A at 0.04 s. Meanwhile, the grid side current load angle also changes. At the beginning, the load angle is zero; it increases to 30° at 0.02 s; at 0.06 s, the load angle is 60°. During these time, ω_g=50*2*π rad/s and the DC-bus voltage is 900 V. The phase A current and the relative d-q current simulation result is shown in Fig.IV.51 and Fig.IV.52.

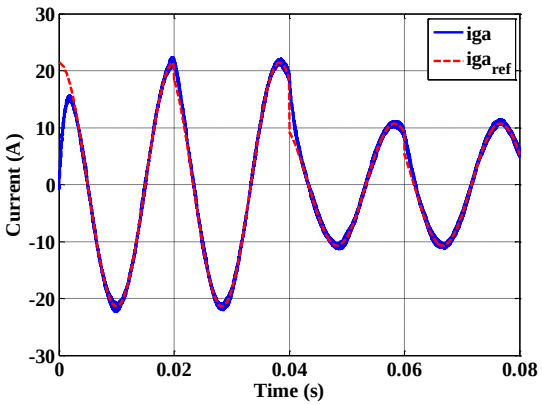

Fig.IV.51 Grid-side phase A current control

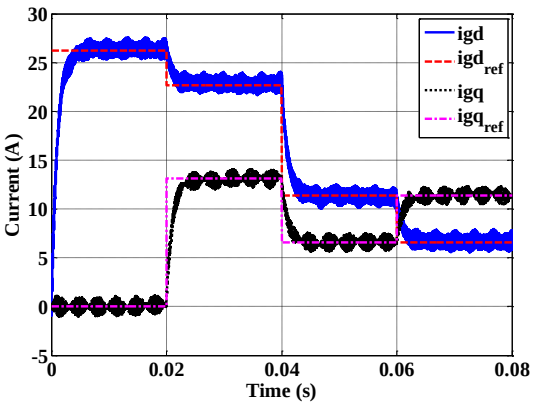

Fig.IV.52 Grid-side d-q current control

From Fig.IV.51 and Fig.IV.52, the grid side currents are well regulated. This means the parameters of the SMC and grid side inductance are well chosen.

On the following, the grid side double loop system is analysed. As the machine side active power is not constant for a given marine current speed, a low-pass filter is adopted in the grid side current control. The current reference is calculated by the following relation:

$$i_{gd\_ref} = \frac{1}{Ts+1}\sqrt{\frac{2}{3}}\frac{P_{grid}}{V_{gm}} \quad \text{(IV.38)}$$

The average electrical power value changes from -8 kW to -10 kW at 0.1 s, and decreases to -5 kW at 0.2 s. The power form the machine P and the grid side power P_{grid} are shown in Fig.IV.53.

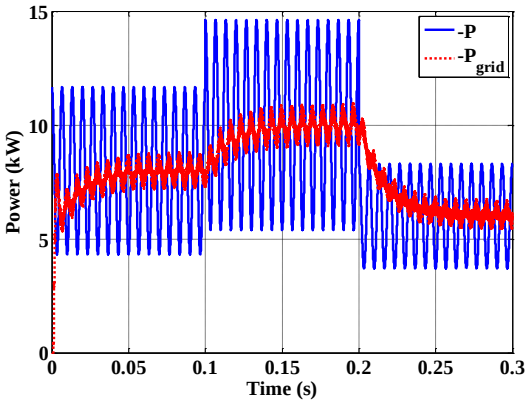

Fig.IV.53 Machine and grid sides powers

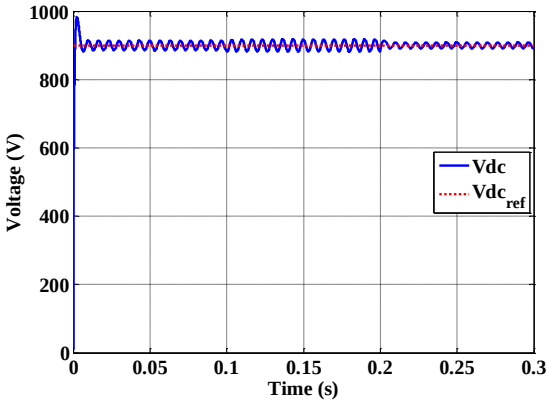

Fig.IV.54 DC-bus voltage

The resulting DC-bus voltage, grid current and grid voltage variations are shown in Fig.IV.54 to Fig.IV.56.

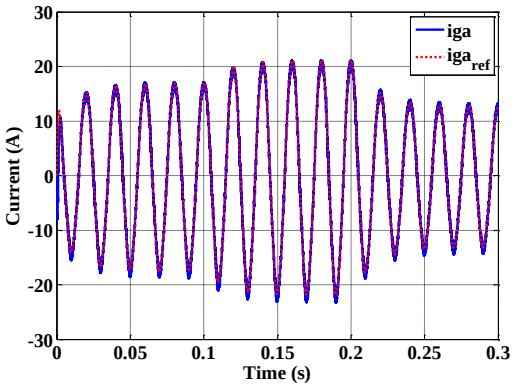

Fig.IV.55 Grid side current

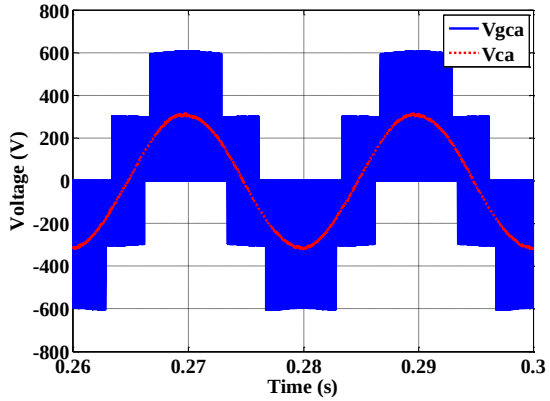

Fig.IV.56 Control and converter voltages

IV.4 *Global Simulation of MCECS*

In the end of this chapter, the system simulation results will be presented. The marine current speed in Fig.IV.32 is taken in this part. In order to reduce the simulation time, the converters gains are kept as unity.

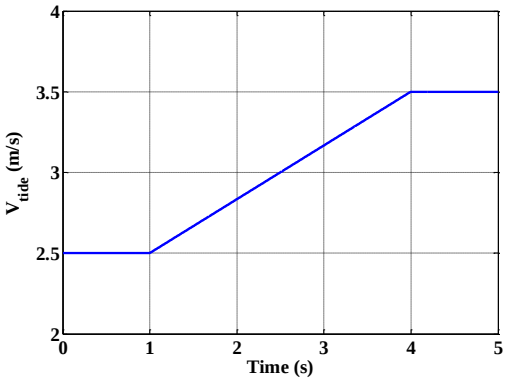

a) Marine current speed

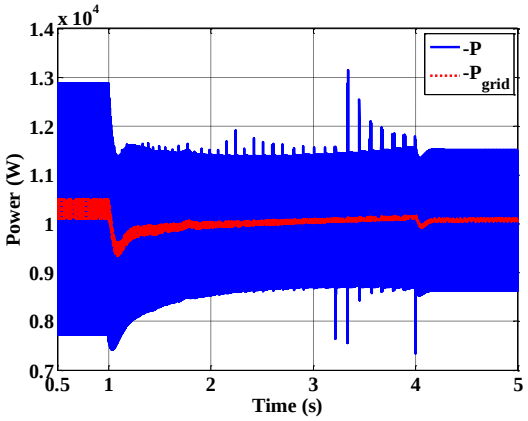

b) Powers variations

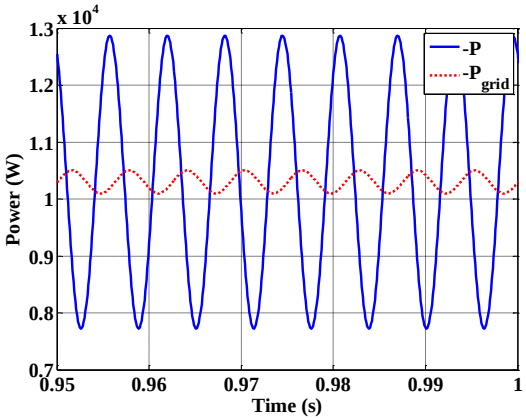

c) for 2.5 m/s marine current speed

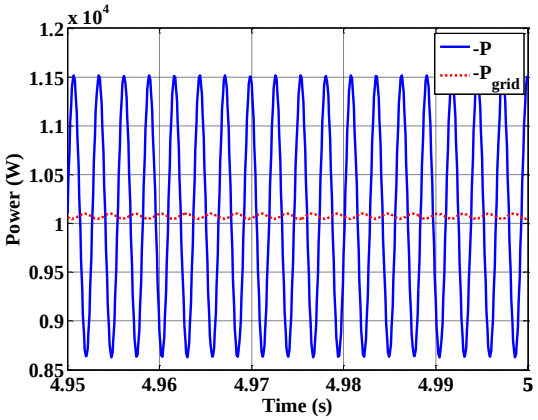

d) for 3.5 m/s marine current speed

Fig.IV.57 Generator power and grid side power

The generator output power P and the grid side power P_{grid} are shown in Fig.IV.57. From Fig.IV.57.c and d, during 0.95 s and 1 s (MPPT control), the machine side power is about 10.305 kW, and the grid side power is nearly the same (10.3 kW). Between 4.95 s and 5 s (CPC control), the powers are also almost the same (10.09 kW and 10.07 kW respectively).

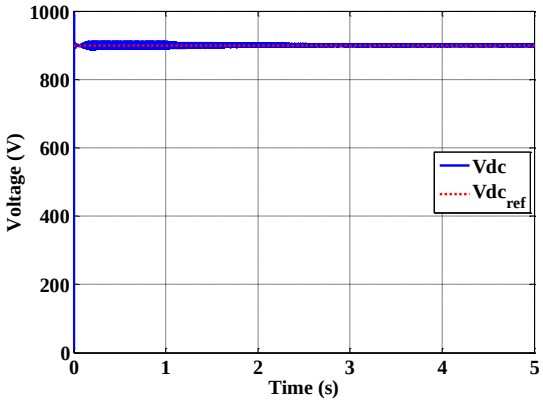

a) DC-bus voltage variation

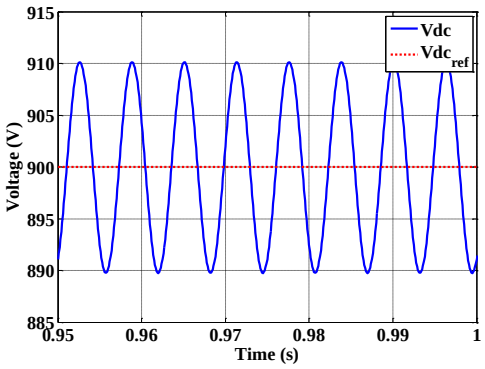

b) for 2.5 m/s marine current speed

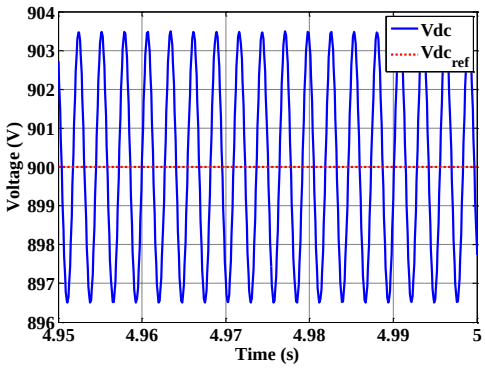

c) for 3.5 m/s marine current speed

Fig.IV.58 DC-bus voltage

Fig.IV.58 presents the DC-bus voltage performance. There is a small ripple in the voltage which means that it is well controlled. From this figure, we can observe that the DC-bus voltage ripple highly depends on the machine side power. In our simulation, the maximum voltage ripple is 10 V (1%) when the marine current speed is 2.5 m/s; if the marine current reaches 3.5 m/s, the ripple is only 3.5 V.

The grid side voltage and current are given in Fig.IV.59. As the power is about 10 kW (see Fig.IV.58), the maximum value of the grid side current is always 21 A (see Fig.IV.59).

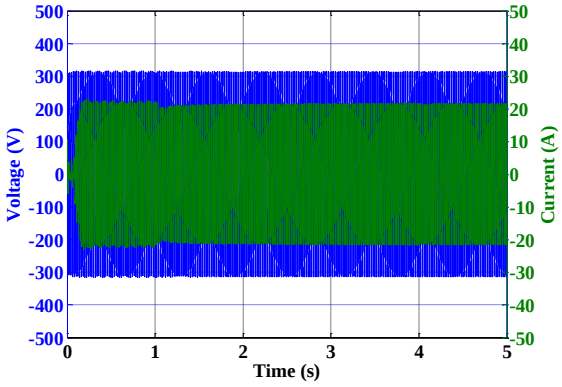

a) for all the marine current speed

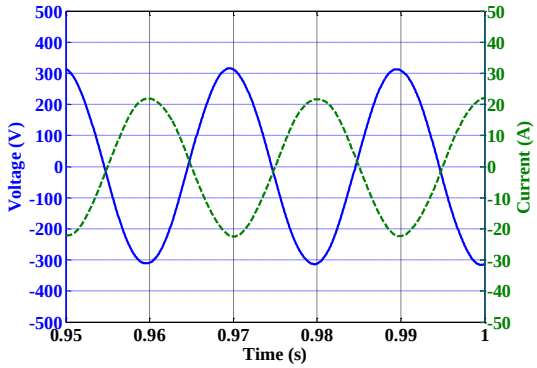

b) for 2.5 m/s marine current speed

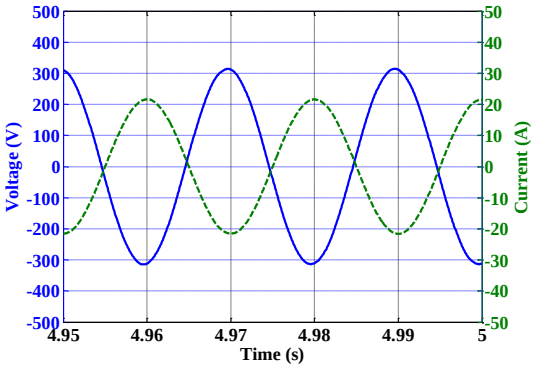

c) for 3.5 m/s marine current speed

Fig.IV.59 Grid side voltage and current

From these simulation results, we can conclude that the system is well controlled. Simulation results taking into account power converters are presented in Appendix XI for a small marine current variation (2.5 m/s to 2.6 m/s).

IV.5 *Conclusion*

This chapter mainly focuses the MCECS model, control methods and strategies.

The first part of this chapter shows the machine side system design. As we have discussed in Chapter II, the d-q DSPMG model is no linear and time-variant. Thus, one robust controller SMC is proposed for the current loop and compared with classical PI controller. The robustness is also analyzed in the same section. PI controller is only used for the external speed loop. The suitable current which contains fundamental and 2^{nd} current harmonic analyzed in Chapter III is applied for DSPMG. When the marine current speed is low, MPPT is always the best choice to extract the maximum power; on the contrary, when the marine current speed is high, CPC is preferred to maintain the power constant.

For the second part, we discussed the grid side system. Like for the machine side system, SMC is used for the internal current loop to get a unity power factor and a PI controller is proposed for the external DC-bus voltage loop.

The modeling of the whole chain: marine current turbine, generator, power electronics and associated control strategies are developed and tested on Matlab/Simulink® environment. All results appear good performances which mean that the controllers and strategies have been well designed.

General Conclusions and Perspectives

In this thesis, a modeling and control of Marine Current Energy Conversion System (MCECS) based on Doubly Salient Permanent Magnet Generator (DSPMG) has been developed. The work focuses on MCECS control strategy and also the DSPMG performances.

At the beginning of the thesis, an introduction of the marine current energy is given and the hydrodynamic characteristics are described. Due to the high density of water, the marine current turbine blade is smaller than that of wind turbine for the same power. As almost the same theory to harness the kinetic energy, the mature technologies which have been used in Wind Energy Conversion System (WECS) can also be employed in MCECS. Different projects are synthesised and classified according to their technology challenge, turbine concept and used generators/power electronics interfaces. This synthesis shows that Direct Drive Permanent Magnet Generator (DDPMG) reduces mechanical maintenance problems and seems the best choice for MCECS.

Each part of the whole system is modelled in Chapter II, including marine current resource, marine current turbine and low speed DSPM Generator. The main used methods for modeling the resource, HAM and SHOM, are analysed. The SHOM approach, more experimental and realistic than HAM, is preferred do its simplicity. The basic turbine modeling theory BEM is then explained to develop the suitable blade for studied system (10 kW at 2.5 m/s marine current speed). Taking into account the tip and hub losses, as well as the wake state, the suitable NACA blade form is determined. Finally, dynamic abc and d-q models of DSPMG are developed. The comparison with conventional generators (PMSG) shows the complexity and the particularity of the DSPMG.

Chapter III mainly discusses DSPMG performances with different supply current waveforms in order to achieve a quasi-constant torque. The stator mutual inductance influence is also studied. Classical currents waveforms (square and sinusoidal waveforms) are first used to analyze the machine behavior. Simulation results allow to high torque ripples exceeding 10 %. Then, a quasi-sinusoidal current waveform is proposed to reduce the torque ripples. This current, limited to a fundamental and 2^{nd} harmonic components, gives the best performances in term of torque ripples and also voltage THD and powers ripples. This study is realized for both DSPMG with or without stator mutual inductance noted respectively GWM and GNM, and shows the superiority of GNM.

The system control methods, strategies and simulation results are presented in Chapter IV. Because of the nonlinear time variant machine system, robust Sliding Mode Controller is used for the current loop and compared with the classical PI controller performances. A PI controller is proposed for the speed loop. For low speeds marine current, an MPPT strategy is applied for

the machine side system to get the maximum power. For high speed marine current speeds a Constant Power Control strategy is preferred. For both cases, the grid side converter is controlled to maintain the DC bus voltage constant and assure a unit power factor on the grid. Exhaustive results are presented and discussed confirming good performance for MCECS and the validity of the developed simulation tool.

During this work, DSPMG has been studied and compared. The suitable current applied for DSPMG is also analyzed. Besides, DSPMG based MCECS is researched and simulated. However,

There are still some developments to improve this work:

- Refine simulation results taking into account power converters and realistic data.
- An experimental bench is under realization in IREENA laboratory. It will serve to validate the developed models and control strategies.
- Based on simulation results in Appendix VI, the relative important self-inductance leads to a poor power factor. It appears important to design the machine by optimizing the volume power and the stator inductance simultaneously.
- As deduced from the comparison between GNM and GWM in Chapter III, it will be interesting to design and optimize the similar machine without mutual inductance which gives better performances.

Résumé en Français

Ce mémoire de thèse rédigé en langue anglaise s'achève par un résumé en langue français conformément aux conditions de l'école doctorale Sciences & Technologies de l'Information et Mathématiques (STIM) de l'université de Nantes.

Modélisation et commande d'une chaîne de conversion d'énergie hydrolienne à base de machine synchrone à aimants permanents doublement saillante.

SOMMAIRE

INTRODUCTION

Les océans, qui occupent deux tiers du globe, captent et emmagasinent des quantités colossales d'énergie. Plusieurs sources d'énergie sont exploitables : l'énergie des marées, de la houle, du vent, de la biomasse, des courants marins et du soleil (sous forme de chaleur). Seule l'extraction de l'énergie des courants marins par hydrolienne est considérée dans cette étude. Cette énergie suscite un intérêt particulier du fait de ses nombreux avantages. En effet, la force et la vitesse des courants de marée, phénomène prédictible, peuvent être connues à l'avance. Il est donc possible, par opposition aux autres énergies renouvelables, dépendant des conditions météorologiques, de connaître à tout moment quelle sera la puissance extractible.

Une hydrolienne est un système de conversion de l'énergie des courants marins en énergie électrique. Cette conversion se décompose en plusieurs étapes :

◦ Conversion de l'énergie des courants en énergie mécanique, cette conversion est assurée par une hélice marine;

◦ Conversion de l'énergie mécanique en énergie électrique, celle-ci est effectuée par une génératrice électrique;

◦ L'adaptation de la puissance électrique en sortie de la génératrice au réseau électrique, il s'agit du rôle des convertisseurs de puissance qui permettront, grâce à une commande adaptée, d'assurer le transfert maximal d'énergie.

L'objectif de ces travaux de thèse est d'apporter une contribution à la modélisation et à la commande d'une chaîne de conversion d'énergie hydrolienne. Pour ce faire notre choix s'est porté sur une hydrolienne à base d'une génératrice lente non-conventionnelle synchrone à aimants permanents doublement saillante.

Le premier chapitre consiste à dresser un état de l'art des technologies et concepts des systèmes hydroliennes ainsi que les différents projets existants ou en cours.

Le deuxième chapitre présente d'une part un rappel sur le principe de la conversion de l'énergie cinétique véhiculée par les courants de marée en énergie électrique, la modélisation de la ressource et de la turbine. D'autre part le modèle dynamique de la génératrice basé sur la méthode des éléments finis et de la transformation de Park est développé.

Dans le troisième chapitre une analyse des courants d'alimentation de la génératrice est détaillée. Des formes particulières de courants sont testées par simulation en vue de délivrer un couple quasi constant.

Le dernier chapitre est consacré au contrôle global de la chaîne de conversion par hydrolienne, allant de la ressource jusqu'à l'intégration au réseau. Les résultats des simulations réalisées (pour un fonctionnement en MPPT ou défluxé), sont présentés et discutés.

I. ENERGIE HYDROLIENNE: ETAT DE L'ART

Le principe de récupération de l'énergie des courants de marées par les hydroliennes est globalement similaire à celui des éoliennes. Les principaux éléments constituants la chaîne de conversion d'une hydrolienne peuvent regrouper les mêmes éléments que la chaîne de conversion d'une éolienne, à savoir, un capteur mécanique (turbine), une génératrice électrique, des convertisseurs statiques et des moyens de stockage d'énergie (figure 1).

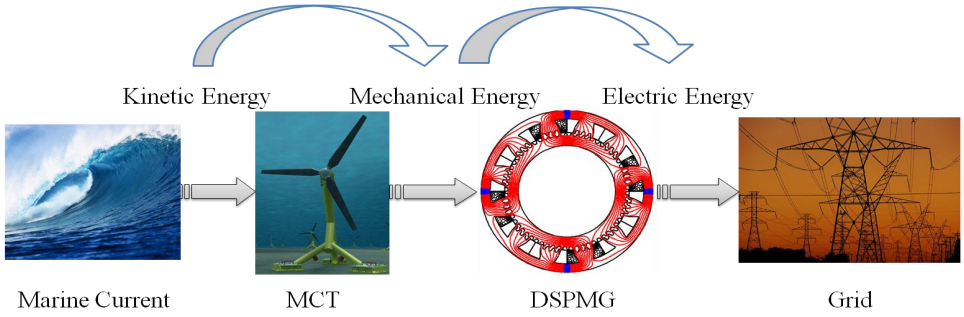

Fig. 1 Structure d'une chaîne de conversion d'énergie de courants marins

La puissance récupérable P_{hyd} s'exprime par l'équation suivante:

$$P_{hyd} = \frac{1}{2}\rho A V_{tide}^3 \quad (1)$$

Cette puissance dépend de la masse volumique de l'eau (ρ), de la surface (A) balayée par l'hélice marine, et du cube de la vitesse du fluide V_{tide}; ainsi une faible variation de la vitesse V peut entraîner une forte variation de la puissance. Cependant seule une partie de cette puissance est récupérable P_m, le coefficient de Betz C_p donne le ratio de la puissance récupérable donné par:

$$P_m = \frac{1}{2}\rho A C_p V_{tide}^3 \quad (2)$$

Ce coefficient C_p dépend du type d'hélice, du nombre de pales et du coefficient de la vitesse spécifique notée λ. Cet dernier est le rapport entre la vitesse linéaire en bout de pale et la vitesse du fluide:

$$\lambda = \frac{R\Omega}{V_{tide}} \quad (3)$$

La relation (2) permet d'établir un ensemble de caractéristiques donnant la puissance disponible en fonction de la vitesse de rotation de la turbine pour différentes vitesses de l'eau.

Différentes technologies de turbines hydroliennes sont aujourd'hui développées afin de récupérer l'énergie cinétique des courants de marées. Ces turbines sont principalement regroupées en trois types : hydrolienne à axe horizontal à axe vertical et à battement caudal. Les hydroliennes être placées en surface, au fond et entre deux eaux.

Un état de l'art de ces concepts, utilisés dans différents projets industriels et universitaires, une synthèse des systèmes d'entrainement directs ou avec multiplicateurs de vitesse ainsi qu'un état sur les générateurs électriques associés sont présentés. Nous nous sommes intéressés aux hydroliennes les plus courantes, à axe horizontal placées au fond des eaux.

II. MODELISATION DE LA CHAINE DE CONVERSION

Cette modélisation multiphysique concerne à la fois la ressource, la turbine et la génératrice.

En effet, avant d'installer une hydrolienne, il est nécessaire d'étudier précisément les ressources du lieu considéré. Pour cela, il faut connaître le phénomène physique des courants de marée et mesurer la vitesse des courants. Générés par le phénomène des marées, les courants de marée sont périodiques, et ils se manifestent différemment au large et près des côtes. La vitesse d'un courant de marée est proportionnelle à l'amplitude de la marée et varie selon la morphologie côtière.

Il est possible de calculer la vitesse du courant à un moment donné et en un point donné, en fonction du coefficient de marée et de l'heure qu'il est par rapport à la pleine mer. En France, les courants marins ainsi que les marées sont étudiés et prédis par le Service Hydrographique et Océanographique de la Marine (SHOM). Ce service propose la formule suivante pour déterminer la vitesse du courant:

$$V_{tide} = V_{nt} + \frac{(C-45)(V_{st}-V_{nt})}{(95-45)} \quad (4)$$

où les coefficients C, V_{st} et V_{nt} représentent respectivement : le coefficient de la marée, la vitesse en eau vive et la vitesse en eau morte.

Dans notre étude, on s'est basé sur les données 2011 du site Penmarc'h en Bretagne (France).

Concernant la turbine, le rendement énergétique et la rentabilité économique d'une hydrolienne repose en grande partie sur les performances hydrodynamiques de son capteur. Ainsi le dimensionnement de la forme géométrique de la pale requiert une attention particulière, d'une part pour son impact majeur sur la puissance récupérée et d'autre part pour la complexité de sa modélisation hydrodynamique.

Les efforts sur une pale d'hydrolienne étant similaires à ceux subis par une éolienne ou une aile d'avion, nous avons appliqué la même approche qualitative. Les efforts de portance et de trainée permettent ainsi de déterminer le couple fourni par l'hélice. Le modèle de simulation développé, à partir de l'étude bibliographique, est basé sur deux théories combinées:

◦ La théorie de l'écoulement axial, "Axial Momentum Theory (AMT)";

◦ La théorie de l'élément de pale, "Blade Element Theory (BEM)".

La mise en œuvre de cette méthode (utilisée par l'industrie éolienne) a permis de modéliser l'hélice à partir des courbes de performances en fonction des caractéristiques géométriques des profils hydrodynamiques.

La turbine étudiée dans notre cas est employée avec une génératrice lente innovante de type synchrone à aimants permanents doublement saillante fournissant 10 kW pour une vitesse de 50 tr/mn.

Cette machine triphasée possède 48 dents répartis sur 12 plots qui portent le bobinage. Elle est excitée par 4 aimants placés au stator. Son rotor est passif et possède 64 dents.

Dans une première partie une modélisation 2D par éléments finis est développée pour identifier les paramètres de la machine et établir un modèle dans le repère abc. En vue de commander la machine son modèle dynamique est développé dans le repère odq en appliquant la transformation de Park.

Les résultats obtenus sont comparés à ceux de génératrices synchrones à aimants permanents classiques montrant ainsi l'originalité, la complexité et les principales caractéristiques de la structure proposée. L'analyse de l'impact de la mutuelle inductance entre les phases statoriques, souvent non pris en compte dans la littérature sur les performances de la machine est détaillée.

III. COURANTS D'ALIMENTATION ET ANALYSE DE PERFORMANCES

Dans le but de déterminer la forme convenable des courants d'alimentation statoriques pour cette machine spéciale, une analyse des performances de la génératrice alimentée par des courants classiques sinusoïdaux et carrés d'abord abordée. Compte tenu des ondulations obtenues pour le couple, une forme d'onde spécifique pour les courants d'alimentation est calculée et proposée pour les réduire tout en tenant en compte l'influence sur les puissances active et réactive (valeurs moyennes et ondulation) et le taux de distorsion harmonique de la tension délivrée.

Pour chaque type de courant, l'étude et l'analyse, en simulation, a été menée en tenant compte de l'impact de l'inductance mutuelle entre les phases du stator sur les performances de la machine. On montre ainsi qu'il est avantageux d'utiliser une machine sans couplage magnétique entre les phases statoriques.

IV. COMMANDE DE LA CHAINE DE CONVERSION D'ENERGIE HYDROLIENNE

Les stratégies de commande des systèmes hydroliens sont basées sur les courbes donnant les caractéristiques de puissance mécanique en fonction de la vitesse du courant marin et de la puissance électrique en fonction de la vitesse de rotation (Figure 2).

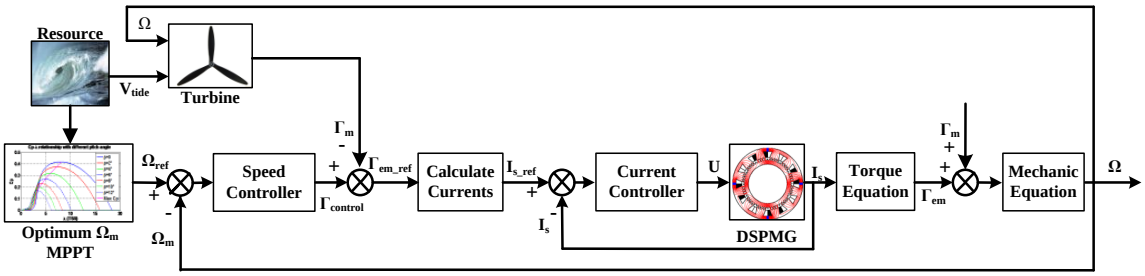

Figure 2. Principe commande de la chaîne de conversion d'énergie hydrolienne à base DSPMG

Côté machine, les cas des faibles vitesses et des vitesses élevées des courants marins sont analysées, évaluées et comparées.

Lorsque la vitesse du courant marin est inférieure à la vitesse nominale, la commande spécifique connue sous la terminologie Maximum Power Point Tracking (MPPT) est utilisée. Elle consiste à contrôler le couple afin de régler la vitesse de rotation de la génératrice. Connaissant la caractéristique donnant le coefficient de puissance C_p en fonction de la vitesse du courant marin (supposée mesurable), mesurable, la vitesse de rotation de la génératrice peut être contrôlée en maintenant la vitesse spécifique à λ_{opt} par conséquent C_p à sa valeur maximale.

Lorsque la vitesse des courants marins est supérieure à la valeur nominale, le mode de MPPT est changé en mode de limitation de puissance. Dans ce cas la valeur requise de C_p est d'abord calculée par la limitation de puissance du générateur et de la vitesse des courants marins à partir de la relation (1), le coefficient de vitesse spécifique λ se situe sur la partie droite des caractéristiques donnant Cp ($\lambda > \lambda_{opt}$). La puissance du générateur peut être alors commandée à la valeur limite.

Pour la boucle interne de courant deux régulateurs ont été testés : PI par compensation de pôles et un régulateur par mode glissant. Pour la régulation de vitesse un régulateur type PI, synthétisé par placement de pôles et compensation de pôles a été mis en œuvre.

Le côté réseau est régulé de façon à maintenir la tension DC du bus continu constante et un facteur de puissance unitaire.

CONCLUSION ET PERSPECTIVES

Dans cette thèse, un modèle basé sur Matlab/Simulink® pour les systèmes de conversion d'énergie hydrolienne à base de machine synchrone à aimants permanents doublement saillante a été élaboré. Les principaux résultats, basés sur l'outil de simulation développé incluant un modèle multiphysique de la turbine, une caractérisation réaliste de la ressource, un générateur à basse vitesse (DSPMG) non conventionnel, des interfaces d'électronique de puissance et des algorithmes de contrôle appropriés, sont présentés et discutés.

Les perspectives envisagées pour la suite peuvent être résumées comme suit :

- Le banc expérimental en cours de réalisation en laboratoire IREENA servira à valider les modèles développés et des stratégies de contrôle.

- Sur la base des résultats de simulation à l'annexe V, une importante valeur des inductances propres conduit à un mauvais facteur de puissance. Il semble important de concevoir la machine en optimisant la puissance volumique et des inductances statoriques propres simultanément.
- Comme déduit à partir de la comparaison entre le générateur GNM et GWM dans le chapitre III, il serait intéressant de concevoir et d'optimiser une machine similaire, sans inductance mutuelle qui donne de meilleures performances.

References

[1] H. Chen et *al.* "Marine tidal current systems: State of the art", In Proceeding of 21st IEEE International ISIE 2012, pp.1431-1437, Hangzhou, China, 28-31 May, 2012.

[2] http://en.wikipedia.org/wiki/Marine_energy (Last accessed May 2014)

[3] http://www.pelamiswave.com/ (Last accessed May 2014)

[4] EU Commission, "The exploitation of tidal marine currents", Report EUR16683EN, 1996.

[5] http://www.marineturbines.com (Last accessed May 2014)

[6] http://www.greenoptimistic.com/2011/08/31/korea-biggest-tidal-power-plant/ (Last accessed May 2014)

[7] http://www.see.murdoch.edu.au/resources/info/Tech/tidal/ (Last accessed May 2014)

[8] http://www.dvice.com/archives/2009/11/worlds_first_os.php (Last accessed May 2014)

[9] http://news.cnet.com/8301-11128_3-10404158-54.html (Last accessed May 2014)

[10] H. Kobayashi et *al*., "The Present Status and Features of OTEC and Recent Aspects of Thermal Energy Conversion Technologies", 24th Meeting of the UJNR Panal on Marine Facilities, Honolulu, USA, 2004.

[11] T.J. Hammons, "Tidal power," Proceeding of IEEE, vol. 3, no. 8,pp. 419-433, 1993.

[12] S. Benelghali, "On multiphysics modeling and control of marine current turbine systems", Ph.D thesis, Université de Bretagne Occidentale, 2009, France.

[13] https://earthsciencenhs.wikispaces.com/Tides (Last accessed May 2014)

[14] http://www.oc.nps.edu/nom/day1/partc.html (Last accessed May 2014)

[15] http://co-ops.nos.noaa.gov/restles4.html (Last accessed May 2014)

[16] A. C. Baker, "The development of functions relating cost and performance of tidal power schemes and their application to small-scale sites", in Tidal Power. London: Thomas Telford, 1986.

[17] T. Cornelius, M. Smith, “Presentation To Offshore Engineering Society Tidal Stream Energy”, 7th October 2009.

[18] http://atlantisresourcesltd.com (Last accessed May 2014)

[19] M. Benoit et *al*., “Energies marines hydrolienne et houlomotrice. Exemples de projets et de travaux de R&D”. Conférence Institut Coriolis, 24 septembre 2010, France.

[20] P.L. Fraenkel, “Power from marine currents”, Proc. IMechE, Part A: Journal of Power and Energy, vol. 216, n°1, pp. 1-14, 2002.

[21] S. Love, “A Channel Model Approach to Determine Power Supply Profiles and the Potential for Embedded Generation”, Ph.D thesis, Department of Mechanical Engineering University of Strathclyde, Scotland, 2005.

[22] K. Thomas, “Low Speed Energy Conversion from Marine Currents”, Ph.D thesis, Uppsala University, Sweden, 2007.

[23] http://www.esru.strath.ac.uk/EandE/Web_sites/09-10/MCT/html/Home (Last accessed May 2014)

[24] SeaGen Environmental Monitoring Programme Final Report, “Marine Current Turbines”, 16 January 2011.

[25] F. Akwensivie, “In the wake of a marine current turbine”, master thesis, University of Strathclyde, 2004, Scotland.

[26] A.S. Bahaj, L.E. Myers, “Fundamentals applicable to the utilisation of marine current turbines for energy production”, Renewable Energy, vol. 28, issue 14, pp 2205–2211, 2003.

[27] Mårten Grabbe Urban Lundin and Mats Leijon, “Ocean Energy”, Department of Electricity and Lightning Research, Uppsala University, Sweden.

[28] P.L Fraenkel, “Marine Current Turbines: an emerging technology”, Renewable Energy – Hydraulic Applications – Theory and Practice, Paper for Scottish Hydraulics Study Group Seminar in Glasgow on 19 March 2004.

[29] G. Hagerman, et *al*., “Methodology for Estimating Tidal Current Energy Resources and Power Production by Tidal In-Stream Energy Conversion (TISEC)”, Project: EPRI North American Tidal In Stream Power Feasibility Demonstration Project, Report: EPRI – TP – 001 NA Rev 2, June 14, 2006.

[30] http://www.emec.org.uk (Last accessed May 2014)

[31] J.A. Clarke, et *al*., “Regulating the output characteristics of tidal current power stations to facilitate better base load matching over the lunar cycle”, Renewable Energy, vol. 31, pp. 173–180, 2006.

[32] K. Tushar et *al*. "Energy Resources and Systems, Volume 2: Renewable Resources", Springer Dordrecht Heidelberg London New York, 2011.

[33] Renewable UK the voice of wind & marine energy, "Wave and Tidal Energy in the UK State of the industry", report, March 2011.

[34] K. Thomas, "Low Speed Energy Conversion from Marine Currents", Ph.D thesis, Uppsala University, Sweden, 2007.

[35] F. O'Rourke, et *al.*, "Marine Current Energy Devices: Current Status and Possible Future Applications in Ireland", Renewable and Sustainable Energy Reviews, vol.14, N°3, pp. 1026-1036, 2010.

[36] http://knowledge.allianz.com/environment/energy/?580/marine-power-a-renewab le -that -is-here-to-say (Last accessed May 2014)

[37] http://www.sabella.fr/fiche.php?id=1 (Last accessed May 2014)

[38] http://en.wikipedia.org/wiki/Sabella_%28company%29#cite_note-1 (Last accessed May 2014)

[39] http://www.cleancurrent.com/ (Last accessed May 2014)

[40] http://www.rechargenews.com/news/americas/article1278698.ece (Last accessed May 2014)

[41] ICF Marbek, "Review of Selected Tidal Power Technologies, Final Report", September 20, 2012.

[42] B. Polagye, et *al*., "Environmental Effects of Tidal Energy Development'', Scientific Workshop University of Washington, Seattle, Washington, USA, 2010.

[43] http://www.openhydro.com/ (Last accessed May 2014)

[44] http://www.envento-windenergie.com/20_faqs.php (Last accessed May 2014)

[45] O. Yaakob et *al*., "Experimental Studies O Savonius-Type Vertical Axis Turbine For Low Marine Current Velocity", International Journal of Engineering-Transactions A: Basics, vol.26, no.1, pp. 91-98, 2013.

[46] S. Kiho, et *al*., "The power generation from tidal currents by Darrieus turbine", Renewable energy, vol. 9, issue 1-4, pp. 1242-1245, 1996.

[47] A. L. Niblick, "Experimental and Analytical Study of Helical Cross-Flow Turbines for a Tidal Micropower Generation System", Thesis University of Washington, 2012.

[48] http://www.gcktechnology.com/GCK/pg2.html (Last accessed 2014)

[49] European commission 6th framework programme co-ordinated action on ocean energy tidal renewable energy research, development and demonstration roadmap, Energy Systems Research Unit, Department of Mechanical Engineering, University of Strathclyde, Glasgow, UK, December 2007.

[50] http://www.orpc.co/default.aspx (Last accessed 2014)

[51] K. Jahangir et *al*., "Ocean Energy: Global Technology Development Status", DOC. TO104, IEA-OES, 2009.

[52] O Rourke, et *al*., "Tidal energy update 2009", Applied Energy, vol.87, issue 2, pp. 398-409, 2010.

[53] A. Testa et *al*., "High efficiency field oriented control of an induction generator for a tidal current turbine", EPE'09, 13th European Conference on Power Electronics and Applications, IEEE, pp. 1-10, Barcelona, Spain, 2009.

[54] E. Segergren, et *al*., "Design of a Very Low Speed PM Generator for the Patented KOBOLD Tidal Current Turbine", Proceedings of Energy Ocean, Florida, USA, 2004.

[55] "Marine Renewable Energy – Wave, Tidal and Water Current", Canadian Technology Status Report, Natural Resources Canada, 2010.

[56] Johnson J B, et *al*., "tidal and ocean current hydrokinetic energy technologies: Status and future opportunities in Alaska", Alaska centre for energy and power, Alaska, USA, pp. 1-28, 2010.

[57] http://www.bluenergy.com/index.html (Last accessed May 2014)

[58] http://www.biopowersystems.com/ (Last accessed May 2014)

[59] http://www.flumill.com/ (Last accessed May 2014)

[60] http://www.minesto.com/index.html (Last accessed May 2014)

[61] H. Chen, "Modeling and Control of a Chain of Energy Production by Marine Current Turbine", Ph.D First Year Report, Université de Nantes, 2011.

[62] http://www.lunarenergy.co.uk/productOverview.htm (Last accessed May 2014)

[63] N. Mehmood, et *al*., "Harnessing Ocean Energy by Tidal Current Technologies", Research Journal of Applied Sciences, Engineering and Technology, vol 4, Issue 18, pp. 3476-3487, 2012.

[64] H. Polinder, et *al.*, "Comparison of direct-drive and geared generator concepts for wind turbines," IEEE Transactions on Energy Conversion, vol. 21, no. 3, pp. 725-733, 2006.

[65] M. Leijon and K Nilsson, "Direct electric energy conversion system for energy conversion from marine currents", Proc. IMechE vol. 221, Part A: Journal of Power and Energy, 2007.

[66] S. Moury, M.T. Iqbal, "A Permanent Magnet Generator with PCB Stator for Low Speed Marine Current Applications", International Conference on the Developments in Renewable Energy Technology (ICDRET) 17-19 Dec. 2009.

[67] A. Grauers, "Design of Direct-driven Permanent-magnet Generators for Wind Turbines", Technical report, School of Electrical and Computer Engineering, Chalmers, University of Technology, Göteborg, Sweden, 1996.

[68] L. Drouen, et al. "Study of an innovative electrical machine fitted to marine current turbines", OCEANS 2007-Europe. IEEE, 2007.

[69] S. Djebarri et *al*. "Rough design of a double-stator axial flux permanent magnet generator for a rim-driven marine current turbine", In Proceeding of 21st IEEE International ISIE 2012, pp.1431-1437, Hangzhou, China, 28-31 May, 2012.

[70] http://mreworldmap.com/

[71] J.A. Baroudi, et *al.*, "A review of power converter topologies for wind generators", Renewable Energy, vol. 32, Issue14, pp. 2369-2385, 2007.

[72] J. Li, "Study and control of a chain of energy production by marine current turbine", Report, Ecole Polytechnique de l'Université de Nantes, 2009.

[73] O. Ceyhan, "Aerodynamic design and optimization of horizontal axis wind turbines by using BEM theory and genetic algorithm", Middle East Technical University, Ankara, 2008.

[74] G.H. Darwin, "Tides", in Encyclopaedia Britannica, R.S. Peale & Co.Chicago, vol. XXIII, pp. 353-381, 1890.

[75] Admiralty Tide Tables, vol.3, 2002.

[76] T.J. GAY, "Assessment of tidal stream energy potential for Marine Corps Recruit Depot Parris Island", Master of science of School of Civil & Environmental Engineering, Georgia Institute of Technology December 2010.

[77] www.shom.fr/ (Last accessed May 2014)

[78] S. Benelghali et *al.* "Comparison of PMSG and DFIG for marine current turbine applications", 2010 XIX International Conference on In Electrical Machines (ICEM), pp. 1-6, Rome, Italy, 6-8 Sept, 2010.

[79] S. Benelghali et *al*. "A simulation model for the evaluation of the electrical power potential harnessed by a marine current turbine", IEEE Journal of Oceanic Engineering, vol. 32, no. 4, pp. 786-797, 2007.

[80] G. INGRAM, "Wind Turbine Blade Analysis using the Blade Element Momentum Method", Durham University, Great Britain, 2011.

[81] T. Burton et *al.*, "Wind Energy Handbook", John Wiley and Sons, 2001.

[82] P.J MORIARTY, A.C Hansen, "AeroDyn theory manual", Technical report, National Renewable Energy Laboratory, 2005.

[83] D. P Molenaar, “Cost-effective design and operation of variable speed wind turbines”, Delft University Press, 2003.

[84] A. Abdul Aziz, “Development of a ducted horizontal axis marine current turbine rotor”, Universiti Teknologi Malaysia, Faculty of Mechanical Engineering, 2010.

[85] W. M. J. BATTEN, et *al.*, “The prediction of the hydrodynamic performance of marine current turbines”, Renewable Energy, vol. 33, no 5, pp. 1085-1096, 2008.

[86] A. S. BAHAJ, et *al.*, “Power and thrust measurements of marine current turbines under various hydrodynamic flow conditions in a cavitation tunnel and a towing tank”, Renewable energy, vol. 32, no 3, p. 407-426, 2007.

[87] G. WASSELYNCK, “Etude d’association convertisseur – machine -commande pour la production d’énergie par hydrolienne”, Rapport Master, Ecole Polytechnique de l’université de Nantes, 2008.

[88] http://en.wikipedia.org/wiki/NACA_airfoil (Last accessed May 2014)

[89] L. Moreau, “Modélisation, conception et commande de génératrices à réluctance variable basse vitesse”, Thèse de l’université de Nantes, 2005.

[90] R. Saou “Modélisation et optimisation de machines lentes a aimants permanents: machines à double saillance et à inversion de flux”, Thèse Ecole Nationale Polytechnique d’Alger, Novembre 2008.

[91] A. Rezzoug, M.E.H Zaim, “Non-conventional Electrical Machines” John Wiley and Sons, 2011.

[92] H. Chen, et *al.*, “Modeling and current control of a double salient permanent magnet generator (DSPMG)”, In proceeding of Power Electronics and Applications (EPE), 15th European Conference on, pp. 1-10, Lille, France, 2013.

[93] R. Le Doeuff, M. E. H. Zaïm, “Rotating Electrical Machines”, Wiley & sons, 2009.

[94] W. Hua, et *al.*, “A new model of vector-controlled doubly-salient permanent magnet motor with skewed rotor”, In Electrical Machines and Systems (ICEMS) IEEE International conference, pp. 3026-3031, Wuhan, China, 2008.

[95] K. T Chau, et *al.*, “Torque ripple minimization of doubly salient permanent-magnet motors”, IEEE Transactions on Energy Conversion, vol.20, no.2, pp. 352-358, 2005.

[96] S.Y Chen, et *al.*, “Research on Relationship Between Reluctant Torque and Torque Ripple for Doubly Salient Permanent Magnet Motor”, Proceedings-Chinese Society of Electrical Engineering, vol.28, no.9, pp. 76, 2008.

[97] M. Cheng et *al.*, “Variable parameter PI control of a novel doubly salient permanent magnet motor drive ”, Power Electronics and Drive Systems (PEDS), IEEE International Conference on, vol. 1, pp. 698-703, 2003.

[98] M. Cheng et *al*., "A simple method to improve the sinusoidal static characteristics of doubly-salient PM machine for brushless AC operation", In Electrical Machines and Systems (ICEMS) IEEE International Conference, pp. 665-669, Seoul, South Korean 2007.

[99] M. Cheng et *al*., "Design and analysis of a new doubly salient permanent magnet motor", IEEE Transactions on Magnetics, vol.37, no.4, pp. 3012-3020, 2001.

[100] C. Martis et *al*., "On the dynamic model of a doubly-salient permanent-magnet motor", IEEE Mediterranean Electrotechnical Conference (MELECON), vol.1, pp. 410-414, Tel-Aviv, Israel, 1998.

[101] F. Blaabjerg, et *al*., "New advanced control methods for doubly salient permanent magnet motor", Industry Applications Conference (IAS), IAS annual meeting, vol. 1, pp. 222-230, Orlando, USA, 1995.

[102] M.A. Abdullah, et *al*., "A review of maximum power point tracking algorithms for wind energy systems", Renewable and Sustainable Energy Reviews, vol.16, issue 5, pp. 3220-3227, 2012.

[103] M.A. Abdullah, et *al*., "A study of maximum power point tracking algorithms for wind energy system", IEEE First Conference on. Clean Energy and Technology (CET), pp. 321-326, 2011.

[104] J.J.E. Slotine, W. Li, "Applied nonlinear control", Prentice-Hall, 1991.

[105] W. Gao, J.C Hung, "Variable structure control of nonlinear systems: a new approach", IEEE Transactions on Industrial Electronics, vol. 40, Issue 1, pp. 45-55, 1993.

[106] S Zhang, X Ma., "A PMSM Sliding-mode Control System Based-on Exponential Reaching Law", Computational Aspects of Social Networks (CASoN), International Conference on. IEEE, Sep. 26-28, pp. 412-414, Taiyuan, China, 2010.

[107] J. K Liu, "Matlab Simulation for Sliding Mode Control", Tsinghua University Press, 2005.

[108] T. Bouaouiche, "Commande à structure variable et étude de l'intégration d'éolienne à base de machine asynchrone à double alimentation sur le réseau électrique", Thèse université de Nantes, 2007.

[109] M.H Rashid, "Power electronics handbook", Academic Press, 2001.

[110] Y. Li, and T.A. Lipo, "A doubly salient permanent magnet motor capable of field weakening", Power Electronics Specialists Conference, PESC'95 Record., 26th Annual IEEE. vol. 1, pp. 565 – 57, Altlanta, USA, 1995.

Appendix

Appendix I *Losses and turbulent wake state*

Losses coefficients

The correction factors to the induced velocity for the tip-loss model and hub-loss model are respectively designed as [82]:

- ***Tip-Loss Model***

$$F_{tip} = \frac{2}{\pi}\frac{1}{\cos\left(e^{-f_{tip}}\right)} \quad \text{(A.1)}$$

$$\text{Where } f_{tip} = \frac{N_b}{2}\frac{R-r}{r\sin\phi} \quad \text{(A.2)}$$

- ***Hub-Loss Model***

$$F_{hub} = \frac{2}{\pi}\frac{1}{\cos\left(e^{-f_{hub}}\right)} \quad \text{(A.3)}$$

$$\text{Where } f_{hub} = \frac{N_b}{2}\frac{r-R_{hub}}{R_{hub}\sin\phi} \quad \text{(A.4)}$$

With R_{hub} the radial position of start root loss (typically 10% to 30% of the blade radius for wind turbine) [83]. We have no typically values for marine current turbines. So for our modelisation, we choose R_{hub}=25%.

- ***Total Loss***

For a given element, according to Eggleston and Stoddard [83], the effective total loss factor is the product of the hub-loss and hub-loss correction factors which is showed in equation (A.5).

$$F_{loss} = F_{tip} \times F_{hub} \quad \text{(A.5)}$$

Turbulent wake state

Another correction also needs to take into account when the induction factor value is higher than about 0.4. Since then, the momentum theory and vortices theory is no longer applicable

because of the predicted reversal of flow in the turbine wake. The turbine is now operating in the so-called “turbulent wake state”.

There are several high induction corrections which are available in the literature. They are: Glauert correction; Spera Correction; DTU course Correction; Modified Glauert Correction; RISOE empirical relation. In this part, the method used is Modified Glauert Correction.

The Modified Glauert Correction is a model which combines of the loss model and the Glauert correction. As the induced velocity near the tip is relative high, the possibility of the turbulent wake state will increase. Therefore, the Modified Glauert Corrention with loss and Glauert Correction can be summarized as follows.

According to equations (II.18) and (II.28), the trust coefficient C_T can use the following expression.

$$C_T = \frac{\sigma_r(1-a)^2}{\sin^2\phi} C_{FN} \tag{A.6}$$

If C_T<0.96F, the standard BEM theory is used to calculate the induction factors:

$$\begin{cases} a = \dfrac{\sigma_r C_{FN}}{4F_{loss}\sin^2\phi+\sigma_r C_{FN}} \\ a' = \dfrac{\sigma_r C_{FT}}{4F_{loss}\sin\phi\cos\phi-\sigma_r C_{FT}} \end{cases} \tag{A.7}$$

If C_T<0.96F, the Modified Glauert Correction will be used to determine the new axial induction factor in equation

$$a = \frac{18F-20-3\sqrt{C_T(50-36F_{loss})+12F(3F_{loss}-4)}}{36F-50} \tag{A.8}$$

Appendix II *Characteristics of the turbine*

Some more characteristics of the turbine discussed in Chapter II, are showed in Fig.A.1.

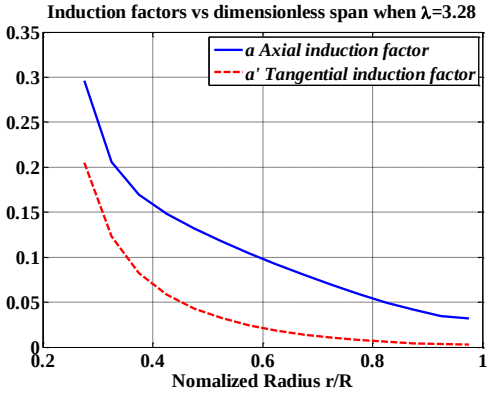

a) Induction factors *a* & *a*'

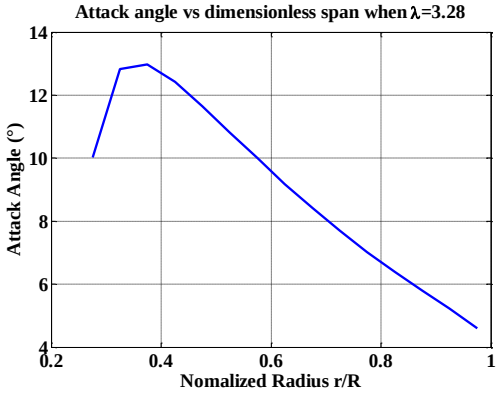

b) Attack angle α

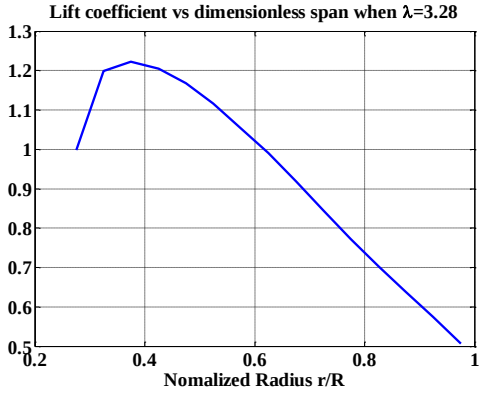

c) Lift coefficient C_L

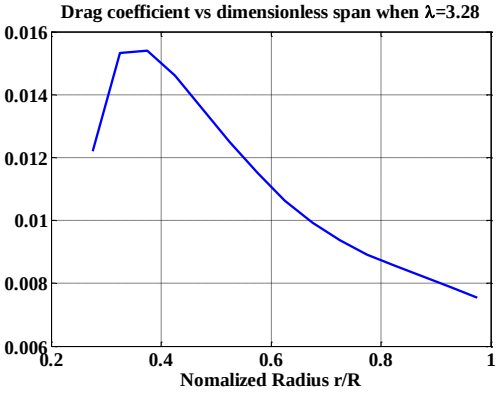

d) Drag coefficient C_D

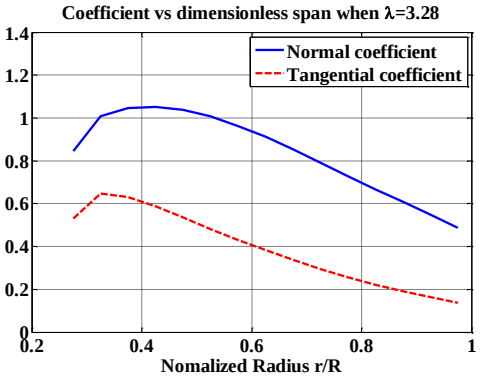

e) Normal and Tangential coefficients CFN & C_{FT}

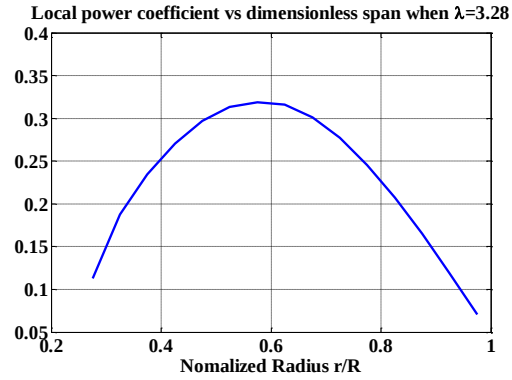

f) Local power coefficient dC_P

Fig.A.1 Performance at pitch angle of 12°

The loss factor of this turbine is simply showed in Fig.A.2. If the loss factor is 1, it means there is no loss in this position. Form this figure; the hub loss has very big influence at the root and nearly has no influence in the tip. Conversely, the tip loss doesn't have any effects at the root part, while takes a very important part in the disturbance. The green line in Fig.A.2 gives the total loss factor along the radius. There are many losses in the tip and as well as the root part, and

there is nearly no loss at the centre of the blade. This well explains why the centre of the radius always has the largest local power coefficient in Fig.A.1.

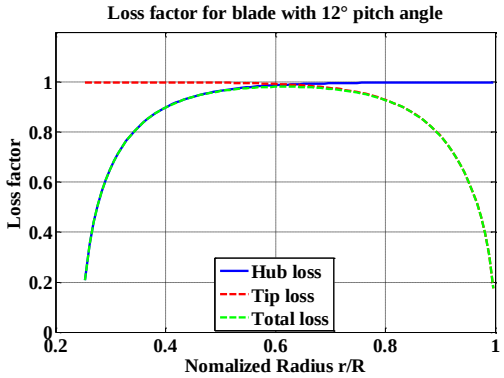

Fig.A.2 Loss factor

Appendix III *Calculation of DSPMG o-d-q frame model*

The DSPMG flux equation is:

$$\begin{bmatrix}\varphi_a\\ \varphi_b\\ \varphi_c\end{bmatrix}=\begin{bmatrix}L_a & M_{ab} & M_{ac}\\ M_{ba} & L_b & M_{bc}\\ M_{ca} & M_{cb} & L_c\end{bmatrix}\begin{bmatrix}i_a\\ i_b\\ i_c\end{bmatrix}+\begin{bmatrix}\varphi_{am}\\ \varphi_{bm}\\ \varphi_{cm}\end{bmatrix} \tag{A.9}$$

We only consider the fundamental and the 2nd inductance harmonics as presented in Chapter II.

$$[\varphi_{abc}]=T_3\begin{bmatrix}\varphi_o\\ \varphi_{\alpha\beta}\end{bmatrix}\quad[i_{abc}]=T_3\begin{bmatrix}i_o\\ i_{\alpha\beta}\end{bmatrix}\quad[\varphi_{abc}]=T_3R(\theta_e)\begin{bmatrix}\varphi_o\\ \varphi_{dq}\end{bmatrix}\quad[i_{abc}]=T_3R(\theta_e)\begin{bmatrix}i_o\\ i_{dq}\end{bmatrix}$$

Where: T_3 and $R(\theta_e)$ are the Concordia and Park transformation matrix respectively.

$$\varphi_o=T_{31}^t[L_s]T_{31}i_o+T_{31}^t[L_s]T_{32}P(\theta_e)\begin{bmatrix}i_d\\ i_q\end{bmatrix}-P(-\theta_e)T_{31}^t[\varphi_m] \tag{A.10}$$

$$\begin{bmatrix}\varphi_d\\ \varphi_q\end{bmatrix}=P(-\theta_e)T_{32}^t[L_s]T_{31}i_o+P(-\theta_e)T_{32}^t[L_s]T_{32}P(\theta_e)\begin{bmatrix}i_d\\ i_q\end{bmatrix}+P(-\theta_e)T_{32}^t[\varphi_m] \tag{A.11}$$

Where: $[L_s]=\begin{bmatrix}L_a & M_{ab} & M_{ac}\\ M_{ba} & L_b & M_{bc}\\ M_{ca} & M_{cb} & L_c\end{bmatrix}$, $P(\theta)=\begin{bmatrix}\cos\theta_e & -\sin\theta_e\\ \sin\theta_e & \cos\theta_e\end{bmatrix}$; $[\varphi_m]=\begin{bmatrix}\varphi_{am}\\ \varphi_{bm}\\ \varphi_{cm}\end{bmatrix}$.

As a result the o-d-q frame flux components are given by:

$$\begin{bmatrix}\varphi_o\\ \varphi_d\\ \varphi_q\end{bmatrix}=\begin{bmatrix}L_o & M_{od} & M_{oq}\\ M_{od} & L_d & M_{dq}\\ M_{oq} & M_{dq} & L_q\end{bmatrix}\begin{bmatrix}i_o\\ i_d\\ i_q\end{bmatrix}+\begin{bmatrix}e_{mo}\\ e_{md}\\ e_{mq}\end{bmatrix}=\begin{bmatrix}L_{odq}\end{bmatrix}\begin{bmatrix}i_o\\ i_d\\ i_q\end{bmatrix}+\begin{bmatrix}e_{mo}\\ e_{md}\\ e_{mq}\end{bmatrix}$$

$$=\begin{bmatrix}L_0+2M_0 & \frac{1}{\sqrt{2}}(L_1-M_1) & 0\\ \frac{1}{\sqrt{2}}(L_1-M_1) & L_0-M_0+\left(\frac{L_1}{2}+M_1\right)\cos 3\theta_e & -\left(\frac{L_1}{2}+M_1\right)\sin 3\theta_e\\ 0 & -\left(\frac{L_1}{2}+M_1\right)\sin 3\theta_e & L_0-M_0-\left(\frac{L_1}{2}+M_1\right)\cos 3\theta_e\end{bmatrix}\begin{bmatrix}i_o\\ i_d\\ i_q\end{bmatrix}$$

$$-\sqrt{3}\begin{bmatrix}\varphi_0\\ \frac{1}{\sqrt{2}}\varphi_1\\ 0\end{bmatrix} \tag{A.12}$$

The DSPMG voltage equation in abc reference frame is:

$$-\begin{bmatrix}v_a\\ v_b\\ v_c\end{bmatrix}=\begin{bmatrix}R_s & 0 & 0\\ 0 & R_s & 0\\ 0 & 0 & R_s\end{bmatrix}\begin{bmatrix}i_a\\ i_b\\ i_c\end{bmatrix}+\begin{bmatrix}e_{ma}\\ e_{mb}\\ e_{mc}\end{bmatrix}+\frac{d}{dt}\left\{\begin{bmatrix}L_a & M_{ab} & M_{ac}\\ M_{ba} & L_b & M_{bc}\\ M_{ca} & M_{cb} & L_c\end{bmatrix}\begin{bmatrix}i_a\\ i_b\\ i_c\end{bmatrix}\right\} \tag{A.13}$$

The voltage equation in o-d-q reference frame is:

$$-\begin{bmatrix}v_o\\ v_d\\ v_q\end{bmatrix}=\begin{bmatrix}R_s & 0 & 0\\ 0 & R_s & 0\\ 0 & 0 & R_s\end{bmatrix}\begin{bmatrix}i_o\\ i_d\\ i_q\end{bmatrix}+\frac{d}{dt}\begin{bmatrix}\varphi_o\\ \varphi_d\\ \varphi_q\end{bmatrix} \tag{A.14}$$

$$-v_o=R_si_o+\frac{d}{dt}\varphi_o=R_si_o+(L_0+2M_0)\frac{d}{dt}i_o+\frac{1}{\sqrt{2}}(L_1-M_1)\frac{d}{dt}i_d \tag{A.15}$$

$$-v_{dq} = R_s \begin{bmatrix} i_d \\ i_q \end{bmatrix} + \omega_e \begin{bmatrix} 0 & -1 \\ 1 & 0 \end{bmatrix} \begin{bmatrix} \varphi_d \\ \varphi_q \end{bmatrix} + \frac{d}{dt} \begin{bmatrix} \varphi_d \\ \varphi_q \end{bmatrix} \tag{A.16}$$

$$\omega_e \begin{bmatrix} 0 & -1 \\ 1 & 0 \end{bmatrix} \begin{bmatrix} \varphi_d \\ \varphi_q \end{bmatrix} = \omega_e \begin{bmatrix} -\varphi_q \\ \varphi_d \end{bmatrix} = \omega_e \begin{bmatrix} -M_{oq} & -M_{dq} & -L_q \\ M_{od} & L_d & M_{dq} \end{bmatrix} \begin{bmatrix} i_o \\ i_d \\ i_q \end{bmatrix} - \begin{bmatrix} e_{mo} \\ e_{md} \\ e_{mq} \end{bmatrix} \tag{A.17}$$

$$\frac{d}{dt}\varphi_{dq} = \frac{d}{dt}\left\{ \begin{bmatrix} M_{od} & L_d & M_{dq} \\ M_{oq} & M_{dq} & L_q \end{bmatrix} \begin{bmatrix} i_o \\ i_d \\ i_q \end{bmatrix} \right\} - \frac{d}{dt} \begin{bmatrix} e_{mo} \\ e_{md} \\ e_{mq} \end{bmatrix}$$

$$= \begin{bmatrix} M_{od} & L_d & M_{dq} \\ M_{oq} & M_{dq} & L_q \end{bmatrix} \frac{d}{dt} \begin{bmatrix} i_o \\ i_d \\ i_q \end{bmatrix} + \omega_e \begin{bmatrix} 0 & -3\left(\frac{L_1}{2} + M_1\right)\sin 3\theta_e & -3\left(\frac{L_1}{2} + M_1\right)\cos 3\theta_e \\ 0 & -3\left(\frac{L_1}{2} + M_1\right)\cos 3\theta_e & 3\left(\frac{L_1}{2} + M_1\right)\sin 3\theta_e \end{bmatrix} \begin{bmatrix} i_o \\ i_d \\ i_q \end{bmatrix} \tag{A.18}$$

Finally, DSPMG o-d-q reference frame in (II.64) can be verified:

$$-\begin{bmatrix} v_o \\ v_d \\ v_q \end{bmatrix} = \begin{bmatrix} e_{mo} \\ e_{md} \\ e_{mq} \end{bmatrix} + [\alpha] \begin{bmatrix} i_o \\ i_d \\ i_q \end{bmatrix} + [\beta] \frac{d}{dt} \begin{bmatrix} i_o \\ i_d \\ i_q \end{bmatrix} \tag{A.19}$$

Appendix IV *Calculation of DSPMG torque expression in o-d-q frame model*

The basic electromagnetic torque expression for generator can be written as:

$$\Gamma_{em} = -\left\{\frac{N_r}{2}[i_s]^t\left[\frac{\partial L_s}{\partial\theta_e}\right][i_s] + N_r[i_s]^t\left[\frac{\partial\varphi_m}{\partial\theta_e}\right]\right\} \quad (A.20)$$

The inductance matrix is:

$$[L_s] = \left[L_{abc\,DSPMG}\right] = \begin{bmatrix} L_a & M_{ab} & M_{ac} \\ M_{ba} & L_b & M_{bc} \\ M_{ca} & M_{cb} & L_c \end{bmatrix} \quad (A.21)$$

According to the DSPMG model developed in Chapter II, the first term, which is called the reluctant torque or salient torque Γ_r, can be developed as follows:

$$\Gamma_r = \frac{N_r}{2}[i_s]^t\left[\frac{\partial L_s}{\partial\theta_e}\right][i_s] = \frac{N_r}{2\omega_e}\left[i_{odq}\right]^t R^t(\theta_e)T_3^t\frac{\partial}{\partial t}\left\{\begin{bmatrix} L_a & M_{ab} & M_{ac} \\ M_{ba} & L_b & M_{bc} \\ M_{ca} & M_{cb} & L_c \end{bmatrix}\right\}T_3R(\theta_e)\left[i_{odq}\right] \quad (A.22)$$

$$\Gamma_r = \frac{N_r}{2}\left[i_{odq}\right]^t\begin{bmatrix} 0 & 0 & \frac{\sqrt{2}}{2}(L_1 - M_1) \\ 0 & -\left(\frac{1}{2}L_1 + M_1\right)\sin 3\theta_e & -\left(\frac{1}{2}L_1 + M_1\right)\cos 3\theta_e \\ \frac{\sqrt{2}}{2}(L_1 - M_1) & -\left(\frac{1}{2}L_1 + M_1\right)\cos 3\theta_e & \left(\frac{1}{2}L_1 + M_1\right)\sin 3\theta_e \end{bmatrix}\left[i_{odq}\right] \quad (A.23)$$

As a result, the reluctant torque can be written as:

$$\Gamma_r = \frac{N_r}{2}\left[2M_{od}\,i_o\,i_q - \left(L_d - L_q\right)i_d\,i_q + M_{dq}\left(i_d^2 - i_q^2\right)\right] \quad (A.24)$$

The second term of the expression is the "hybrid" torque Γ_{pm}. It corresponds to the interaction of the stator currents with the rotor flux. This is the main torque. It can develop as:

$$\Gamma_{pm} = N_r[i_s]^t\left[\frac{\partial\varphi_m}{\partial\theta_e}\right] = -N_r\left[i_{odq}\right]^t R^t(\theta_e)T_3^t\begin{bmatrix} \varphi_1\sin\theta_e \\ \varphi_1\sin\left(\theta_e - \frac{2}{3}\pi\right) \\ \varphi_1\sin\left(\theta_e - \frac{4}{3}\pi\right) \end{bmatrix} \quad (A.25)$$

As a result, the main torque can be written as:

$$\Gamma_{pm} = -\sqrt{\frac{3}{2}}N_r\varphi_1\left[i_{odq}\right]^t\begin{bmatrix} 1 & 0 & 0 \\ 0 & \cos\theta_e & \sin\theta_e \\ 0 & -\sin\theta_e & \cos\theta_e \end{bmatrix}\begin{bmatrix} 0 \\ \sin\theta_e \\ -\cos\theta_e \end{bmatrix} = \sqrt{\frac{3}{2}}N_r\varphi_1 i_q \quad (A.26)$$

The DSPMG electromagnetic torque is obtained as:

$$\Gamma_{em} = -(\Gamma_{em} + \Gamma_r) \quad (A.27)$$

Appendix V *Other current waveforms*

In the beginning of Chapter III, we have analyzed the square current form. Even for this kind of current reference, there are many torque ripples. We have researched some other kinds of currents which are based on the square current to get the constant electromagnetic torque. Some examples are presented in this Appendix. For all these current, the analyses begin from the basic electromagnetic torque in equation (A.28).

$$\Gamma_{em} = -\left\{\frac{N_r}{2}[i_s]^t\left[\frac{\partial L_s}{\partial \theta_e}\right][i_s] + N_r[i_s]^t\left[\frac{\partial \varphi_m}{\partial \theta_e}\right]\right\} \quad \text{(A.28)}$$

- Step-by-Step Current

The idea of this current is exactly the same as the current used in the beginning of section III.2. We consider three currents will be supplied phase by phase. In this situation, the sum of three currents is not zero (see Fig.A.3).

$$i_a + i_b + i_c \neq 0 \quad \text{(A.29)}$$

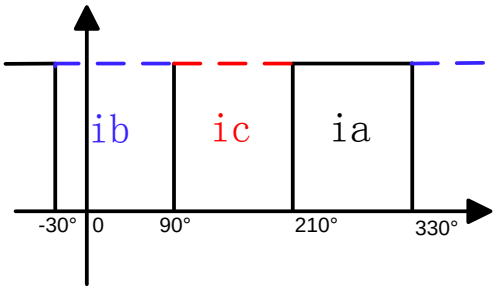

Fig.A.3 Step by step current

In this assumption, there is only one current in the 3 phases at every time. So the torque is always produced by only one current. As a result, if the current only exists in phase A (Ia=Im(θ); Ib=Ic=0), the torque expression in (A.28) can be rewritten as:

$$\Gamma_{em} = \mathrm{N_r}\varphi_1 i_a \sin\theta_e + \frac{\mathrm{N_r}}{2}L_1 i_a^2 \sin\theta_e \quad \text{(A.30)}$$

One example given in Fig.A.3, we consider phase A begins from 210° and ends at 330°; Phase B begins from -30° (330°) and ends at 90°; Phase C begins from 90°and ends at 210°.

So the current in each phase can be calculated as:

For phase A, 210° and ends at 330°

$$i_a^2 + 2\frac{\varphi_1}{L_1}i_a - \frac{2\Gamma_{em}}{L_1 \mathrm{N_r}\sin\theta_e} = 0 \quad \text{(A.31)}$$

The current in phase A is:

$$i_a = \frac{-2\varphi_1 + \sqrt{4\varphi_1^2 + \frac{8\Gamma_{em}L_1}{\mathrm{N_r}\sin\theta_e}}}{2L_1} \quad \text{(A.32)}$$

The current for phase B, -30° (330°) and ends at 90°:

$$i_b = \frac{-2\varphi_1 + \sqrt{4\varphi_1^2 - \frac{8\Gamma_{em} L_1}{N_r \sin\left(\theta_e - \frac{2\pi}{3}\right)}}}{2L_1} \quad \text{(A.33)}$$

The current for phase C, begins from 90° and ends at 330°:

$$i_c = \frac{-2\varphi_1 + \sqrt{4\varphi_1^2 - \frac{8\Gamma_{em} L_1}{N_r \sin\left(\theta_e - \frac{4\pi}{3}\right)}}}{2L_1} \quad \text{(A.34)}$$

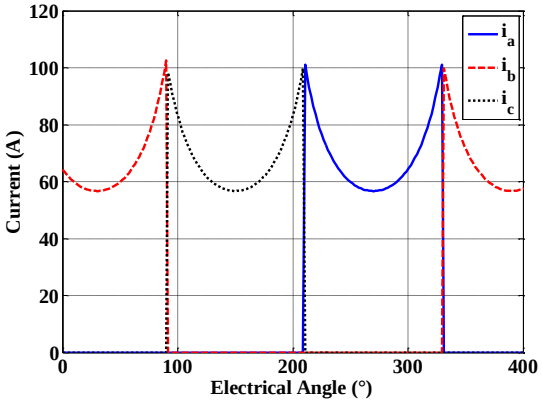

Fig.A.4 Example for the step by step current

- Two-Current

In this part, we always consider the sum of the three currents is 0.

$$i_a + i_b + i_c = 0 \quad \text{(A.35)}$$

The expression of the electromagnetic torque can be written as these forms:

$$\Gamma_{em} = -\left[\frac{N_r}{2}\left(\frac{L_1}{2} + M_1\right)(i_b^2 + 4i_b i_c + i_c^2) + \frac{3}{2}N_r\varphi_1(-i_b - i_c)\right]\sin\theta - \left[\frac{N_r}{2}\left(\frac{L_1}{2} + M_1\right)\sqrt{3}(-i_b^2 + i_c^2) + \frac{\sqrt{3}}{2}N_r\varphi_1(-i_b + i_c)\right]\cos\theta_e \quad \text{(A.36)}$$

If there are always two currents in the machine, one possibility is given in Fig.A.5

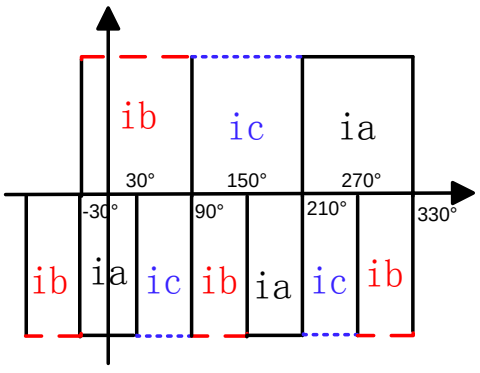

Fig.A.5 Two-current in the machine

-30° (330°) and 30°:

$$i_b = \frac{-\mathrm{N_r}\varphi_1\left[\frac{3}{2}\sin\theta + \frac{\sqrt{3}}{2}\cos\theta_e\right] - \sqrt{\left[\mathrm{N_r}\varphi_1\left(\frac{3}{2}\sin\theta_e + \frac{\sqrt{3}}{2}\cos\theta_e\right)\right]^2 - 2\mathrm{N_r}\Gamma_{em}\left(\frac{L_1}{2}+M_1\right)\left[\sin\theta_e - \sqrt{3}\cos\theta_e\right]}}{-\mathrm{N_r}\left(\frac{L_1}{2}+M_1\right)\left[\sin\theta_e - \sqrt{3}\cos\theta_e\right]} \quad (A.37)$$

$$i_a = -i_b;\ i_c = 0;$$

30° and 90°:

$$i_b = \frac{-\sqrt{3}\mathrm{N_r}\varphi_1\cos\theta_e + \sqrt{\left[\sqrt{3}\mathrm{N_r}\varphi_1\cos\theta_e\right]^2 + 4\mathrm{N_r}\Gamma_{em}\left(\frac{L_1}{2}+M_1\right)\sin\theta_e}}{2\mathrm{N_r}\left(\frac{L_1}{2}+M_1\right)\sin\theta_e} \quad (A.38)$$

$$i_c = -i_b;\ i_a = 0;$$

90° and 150°:

$$i_b = \frac{-\sqrt{3}\mathrm{N_r}\varphi_1\cos\theta_e - \sqrt{\left[\sqrt{3}\mathrm{N_r}\varphi_1\cos\theta_e\right]^2 + 4\mathrm{N_r}\Gamma_{em}\left(\frac{L_1}{2}+M_1\right)\sin\theta_e}}{2\mathrm{N_r}\left(\frac{L_1}{2}+M_1\right)\sin\theta_e} \quad (A.39)$$

$$i_c = -i_b;\ i_a = 0;$$

150° and 210°:

$$i_c = \frac{\mathrm{N_r}\varphi_1\left[\frac{3}{2}\sin\theta_e - \frac{\sqrt{3}}{2}\cos\theta_e\right] - \sqrt{\left[\mathrm{N_r}\varphi_1\left(\frac{3}{2}\sin\theta_e - \frac{\sqrt{3}}{2}\cos\theta_e\right)\right]^2 - 2\mathrm{N_r}\Gamma_{em}\left(\frac{L_1}{2}+M_1\right)\left[\sin\theta_e + \sqrt{3}\cos\theta_e\right]}}{-\mathrm{N_r}\left(\frac{L_1}{2}+M_1\right)\left[\sin\theta_e + \sqrt{3}\cos\theta_e\right]} \quad (A.40)$$

$$i_a = -i_c;\ i_b = 0;$$

210° and 270°:

$$i_c = \frac{\mathrm{N_r}\varphi_1\left[\frac{3}{2}\sin\theta_e - \frac{\sqrt{3}}{2}\cos\theta_e\right] + \sqrt{\left[\mathrm{N_r}\varphi_1\left(\frac{3}{2}\sin\theta_e - \frac{\sqrt{3}}{2}\cos\theta_e\right)\right]^2 - 2\mathrm{N_r}\Gamma_{em}\left(\frac{L_1}{2}+M_1\right)\left[\sin\theta_e + \sqrt{3}\cos\theta_e\right]}}{-\mathrm{N_r}\left(\frac{L_1}{2}+M_1\right)\left[\sin\theta_e + \sqrt{3}\cos\theta_e\right]} \quad (A.41)$$

$$i_a = -i_c;\ i_b = 0;$$

270° and 330°:

$$i_b = \frac{-\mathrm{N_r}\varphi_1\left[\frac{3}{2}\sin\theta_e + \frac{\sqrt{3}}{2}\cos\theta_e\right] + \sqrt{\left[\mathrm{N_r}\varphi_1\left(\frac{3}{2}\sin\theta_e + \frac{\sqrt{3}}{2}\cos\theta_e\right)\right]^2 - 2\mathrm{N_r}\Gamma_{em}\left(\frac{L_1}{2}+M_1\right)\left[\sin\theta_e - \sqrt{3}\cos\theta_e\right]}}{-\mathrm{N_r}\left(\frac{L_1}{2}+M_1\right)\left[\sin\theta_e - \sqrt{3}\cos\theta_e\right]} \quad (A.42)$$

$$i_a = -i_b;\ i_c = 0;$$

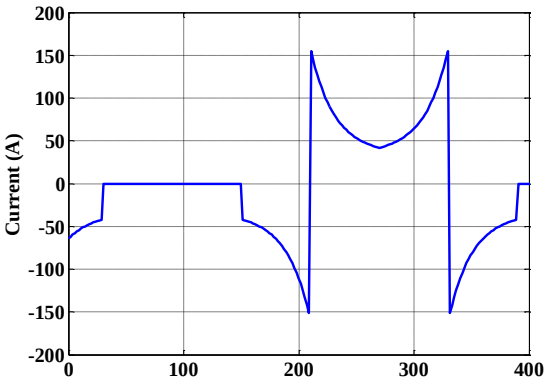

Fig.A.6 Example for two-current (i_a)

- Three-current

This idea is just to simple the torque equation based on the step-by-step current. In this idea, we will consider during π/6 and 5π/6, the current in phase A Ia=Im, while Ib=Ic=-Im/2.

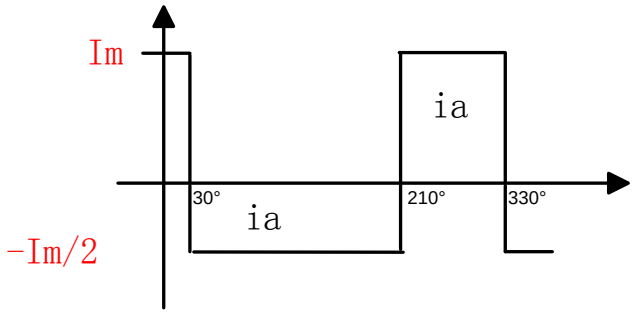

Fig.A.7 Three-current in the machine

The electromagnetic torque can be written as:

$$\Gamma_{em} = -\left[\frac{N_r}{2}\left(\frac{L_1}{2}+M_1\right)(i_b^2+4i_b i_c+i_c^2)+\frac{3}{2}N_r\varphi_1(-i_b-i_c)\right]\sin\theta_e$$
$$-\left[\frac{N_r}{2}\left(\frac{L_1}{2}+M_1\right)\sqrt{3}(-i_b^2+i_c^2)+\frac{\sqrt{3}}{2}N_r\varphi_1(-i_b+i_c)\right]\cos\theta_e$$

For the current:

-30° and 90°:

$$i_b = \frac{-3\varphi_1+\sqrt{[3\varphi_1]^2-\frac{8\Gamma}{N_r\sin\left(\theta_e-\frac{2\pi}{3}\right)}\left(\frac{3}{4}L_1+\frac{3}{2}M_1\right)}}{3\left(\frac{L_1}{2}+M_1\right)} \quad (A.43)$$

$$i_a = i_c = -\frac{i_b}{2};$$

90° and 210°:

$$i_c = \frac{-3\varphi_1+\sqrt{[3\varphi_1]^2-\frac{8\Gamma}{N_r\sin\left(\theta_e-\frac{4\pi}{3}\right)}\left(\frac{3}{4}L_1+\frac{3}{2}M_1\right)}}{3\left(\frac{L_1}{2}+M_1\right)} \quad (A.44)$$

$$i_b = i_c = -\frac{i_a}{2};$$

For 210° and 330°:

$$i_a = \frac{-3\varphi_1 + \sqrt{[3\varphi_1]^2 - \frac{8\Gamma_{em}}{N_r \sin\theta_e}\left(\frac{3}{4}L_1 + \frac{3}{2}M_1\right)}}{3\left(\frac{L_1}{2} + M_1\right)} \tag{A.45}$$

$$i_b = i_c = -\frac{i_a}{2};$$

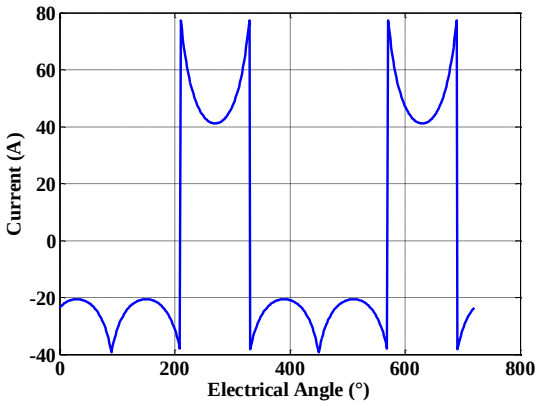

Fig.A.8 Example for three-current (i_a)

Appendix VI *Influence of the self inductance*

From the analysis of the square current, sinusoidal waveform current and quasi-sinusoidal waveform current, we find that the reactive power is much bigger than active power even for GNM. It implies that the power factor is very low in the designed nominal operation condition (see in Table A.1).

Indeed, the machine has a relative great self inductance value because it was designed to maximise the volume power [90] [103] without any constraint on its inductance.

Table A.1 Power factor cos φ

	Sinusoidal	i_{a2}'
GWM	0.31	0.31
GNM	0.43	0.44

In Chapter III, we have already observed that GNM always obtains the better performances. Thus, in this part, only GNM is considered. According to equations (III.13) and (III.14), the average value of the active power is independent of inductance; the mean value of reactive power highly depends on the fundamental of the self inductance (for GNM). The amplitude of the sinusoidal current waveform varies from 5 A to 60A (230 Nm to 2769 Nm), the current i_{a2}' is designed based on the relative torque for sinusoidal current waveform. The variations of the power factors for different self inductances are given in Fig.A.9 and Fig.A.10 respectively.

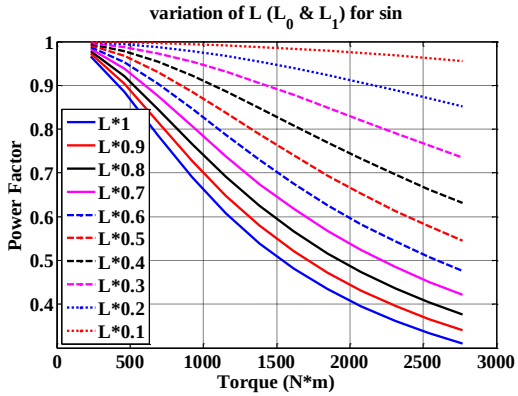

Fig.A.9 Power factor for different L (sin)

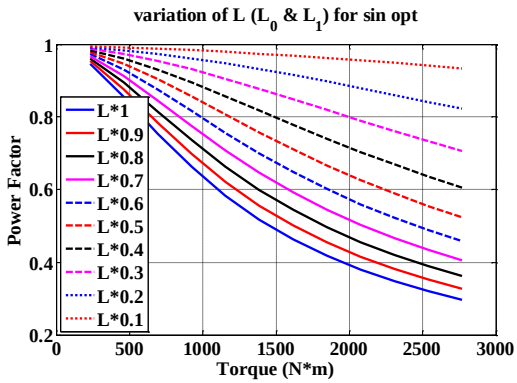

Fig.A.10 Power factor for different L (i_{a2}')

From figures Fig.A.9 and Fig.A.10, for both sinusoidal and i_{a2}' waveform currents, the smaller self inductance always brings higher power factor. For the identical inductance, the small current will get the higher power factor. There are two possibilities to increase the power factor: reduce the self inductance value; operate the machine in a lower power condition.

Appendix VII *Influence of the airgap, yoke thickness, magnet thickness*

There are 16 parameters for design DSPM, [90] has well explain the choice of these parameters determined to get the maximum active masses torque (12.6 Nm/kg). The overall structure is fully defined by the following 16 parameters in Fig.A.11 and Fig.A.12.

- The width of the rotoric and statoric yokes: Er and Es;
- The height of slot hb;
- The opening of slot β;
- The position of point A (Ra, βa) with the radius Ra;
- The rotor and stator radius: Rr and Rc;
- The parameters of the trapezoidal teeth hs, hr α_{r1}, α_{s1}, α_{r2} and α_{s2};
- Thickness of the magnet Em.

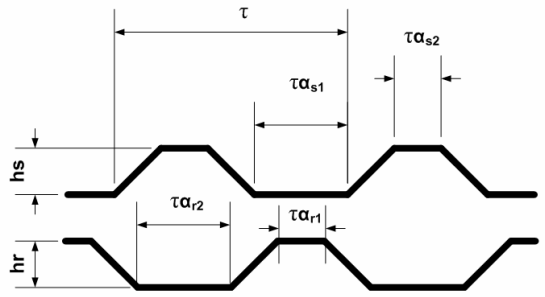

Fig.A.11 Trapezoidal teeth in rotor and stator [90]

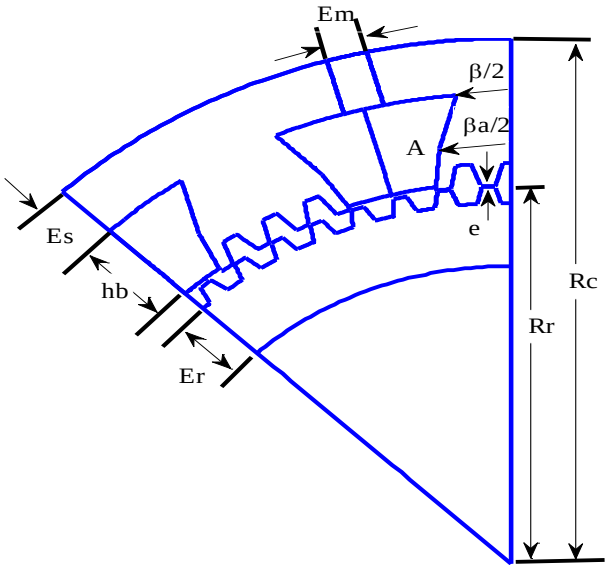

Fig.A.12 Global design parameters

As we present in Appendix VI, the self inductance takes a very important role for GNM in the power factor (mean value of active and reactive power). This definition of power factor in

equation (III.7) is suitable for the condition with sinusoidal waveform current and voltage, but it is not exactly correct for the current or voltage non-sinusoidal. If the voltage and current are not sinusoidal waveforms, the real power factor is much complex. The factor also depends on the power ripples. Thus, the influence of the parameters for the power ripple will be analyzed firstly.

Based on the torque, active and reactive powers expression in equations (III.12), (III.13) and (III.14) for GNM applying the sinusoidal current waveform, we observe that the main torque and active power depend on the fundamental of the PM flux linkage (φ_1); the fundamental of the self inductance (L_1) will determine the ripples of the torque and powers; the average values of the reactive power is highly determined by the continuous part of the self inductance (L_0); the continuous part of the PM flux linkage (φ_0) doesn't change the performance of the machine.

The performances for GNM applying quasi-sinusoidal current waveform are very complicated; as a result, it is not easy to find the exact expression as for sinusoidal current waveform. Thus, some variation for the φ_0, φ_1, L_0 and L_1 will be test. As the torque for this kind of current is always constant, we will only present the performances for the powers for the given torque -1845 Nm with 50 Hz frequency.

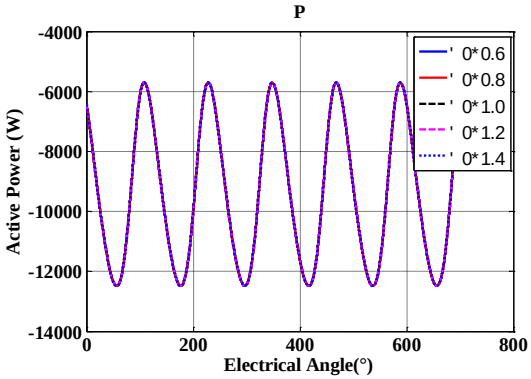

Fig.A.13 Variation of φ_0 versus P

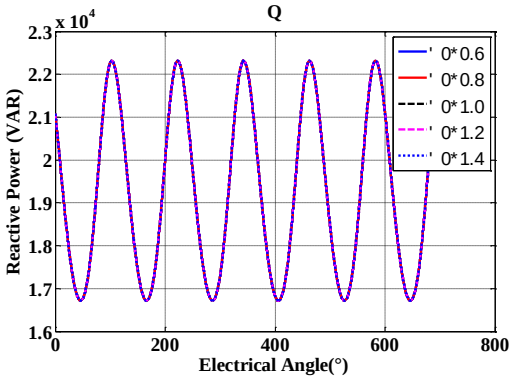

Fig.A.14 Variation of φ_0 versus Q

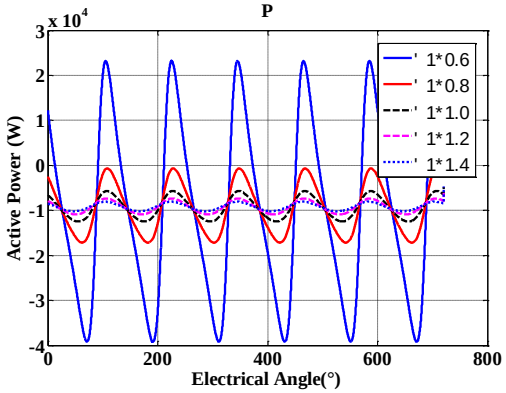

Fig.A.15 Variation of φ_1 versus P

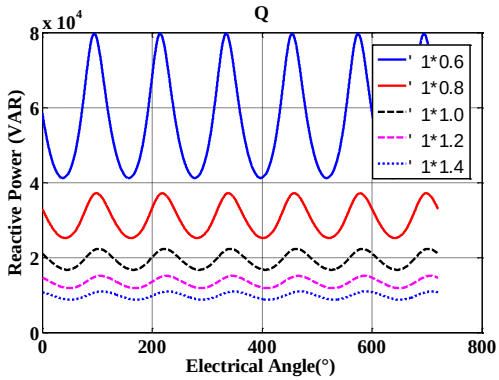

Fig.A.16 Variation of φ_1 versus Q

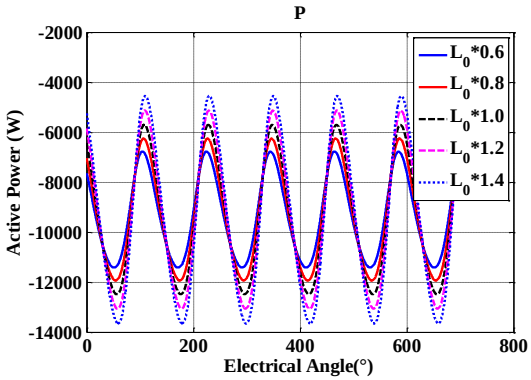

Fig.A.17 Variation of L_0 versus P

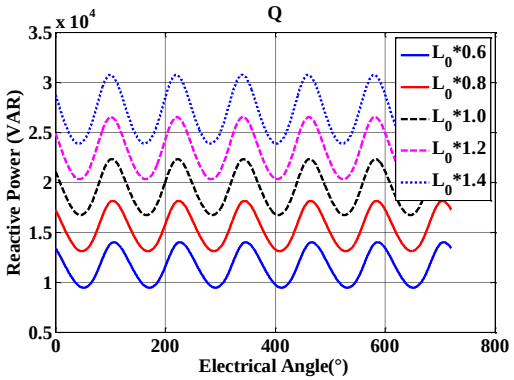

Fig.A.18 Variation of L_0 versus Q

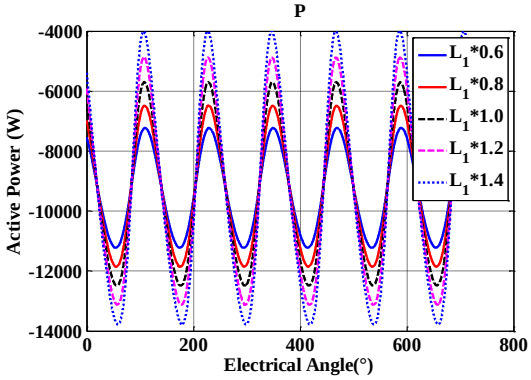

Fig.A.19 Variation of L_1 versus P

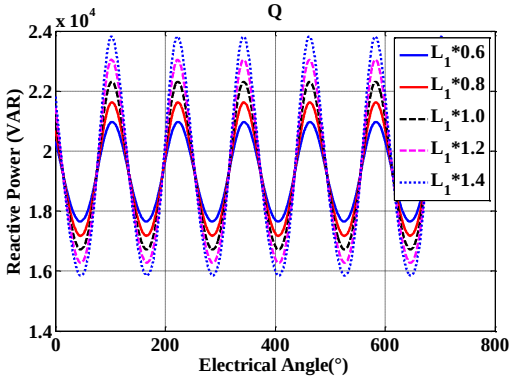

Fig.A.20 Variation of L_1 versus Q

From Fig.A.13 and Fig.A.14, it is not difficult to find that the variation of φ_0 cannot affect the performances of the powers. Fig.A.15 and Fig.A.16 shows the variation of the φ_1. The increase of φ_1.can greatly decrease the ripples of both active and reactive powers, moreover, it can highly reduce the level of reactive power. The influences of the powers for the variation of L_0 are given in Fig.A.17 and Fig.A.18. The smaller L_0 will bring smaller active power ripples and smaller mean value of reactive power. L_0 cannot change the ripple of the reactive power. Fig.A.19 and Fig.A.20 imply that the smaller the L_1 is, the smaller ripples for active and reactive power will be.

In accordance of the analysis above, in conclusion, it is better to decrease L_0 and L_1, as well as increase φ_1. In this section, we will just vary some of the machine structure parameters to see the variation of the flux linkage (φ_1) and inductance (L_0 and L_1). We define the objective function in equation (A.46) to evaluate the performance. We want to get the bigger value of this function.

$$F_{opt} = \frac{\varphi_1}{L_1} + \frac{\varphi_1}{L_0} \tag{A.46}$$

Comparing the machine with the same level torque, it means all the machines must have the same MMF (MagnetoMotive Force). All the variation of the structure must obey the equation (A.47).

$$k * J_s * S_{slot} = NI = \text{constant} \tag{A.47}$$

Where: k is the filling factor; J_s is the current density (A/mm^2); N is the number of the spire; I is the current (A); S_{slot} is the surface of the slot (m^2).

The self inductance L is bound to reluctance of the corresponding magnetic circuit by the equation (A.48) [93].

$$L = \frac{N^2}{\Re} \tag{A.48}$$

If we want to decrease the inductance, it is necessary to decrease the number of the spire or increase the reluctance of the machine. For DSPMG, the airgap reluctance is not easily to calculate analytically. In our study, we consider that the reluctance of the machine mainly depends on the airgap (e), surface of the airgap and the magnet (S_e and S_m=Es*$L_{machine}$), and the magnet thickness (Em). In the following, these parameters will be changed individually (e, Em and Es) firstly, then Em and Es are modified together.

For classic machine, the bigger airgap leads to the smaller inductance. Thus, the DSPMG airgap will be increased. For the original machine, the airgap is 0.5 mm. In our work, two values 0.75 mm and 1 mm will be analyzed. The PM flux linkage and self inductance are given in Table A.2.

Table A.2 Variation of the airgap e

airgap e (mm)	0.5 (original)	0.75	1
φ_0 (wb)	0.8479	0.8101 (95.54%)	0.7764 (91.57%)
φ_1 (wb)	0.4815	0.3910 (81.20%)	0.3136 (65.13%)
L_0 (mH)	29.6399	28.1673 (95.03%)	26.1113 (88.10%)
L_1 (mH)	7.6402	7.3584 (96.31%)	6.3142 (82.64%)

From Table A.2, if we increase the airgap of the machine, the PM flux linkage (φ_0 and φ_1) and self inductance (L_0 and L_1) will both decrease. The φ_1 will reduce greater than the other variables. The objective function for the variation of the airgap is given in Fig.A.21. It can be observed that the objective function value will reduce with the airgap increasing.

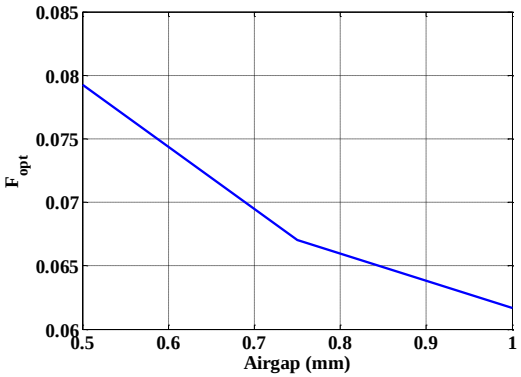

Fig.A.21 F_{opt} for the variation of airgap

The reluctance of the magnet can be summarized in equation (A.49).

$$\Re_m = \frac{E_m}{\mu_0 E_s * L_{machine}} \tag{A.49}$$

$$\xi = \frac{B_r}{\mu_0} E_m \tag{A.50}$$

The thickness of the magnet Em will increase the magnet reluctance (see equation (A.49)) and also increases the MMF of the magnet (see equation (A.50)). However it is possible to give the analytic expression for airgap reluctance like equation (A.50) . In our study, the variation of Em is chosen between 0.5 and 1.5. The flux and inductance are given in Table A.3; the objective function is shown in Fig.A.22. The objective function value will increase with the growing of the Em. We observe that if we augment the thickness of the permanent magnet Em from the original value to 150% of the value, the objective function value only increase 0.002 (see Fig.A.22). The values of φ_1, L_0 and L_1 don't change a lot and are almost the same as the original values (see Table A.3). It implies that the growth of the magnet thickness cannot greatly vary the object function.

Table A.3 Variation of the magnet height Em

	Em=k_{Em}*Em (original)										
k_{Em}	0.5	0.6	0.7	0.8	0.9	1	1.1	1.2	1.3	1.4	1.5
L_0	30.2	30.0	29.9	29.8	29.7	29.6	29.6	29.5	29.5	29.5	29.4
L_1	7.8	7.7	7.7	7.7	7.7	7.6	7.6	7.6	7.6	7.6	7.5
φ_0	0.8051	0.8189	0.8290	0.8367	0.8429	0.8478	0.8519	0.8554	0.8586	0.8613	0.8636
φ_1	0.4684	0.4733	0.4767	0.4787	0.4804	0.4816	0.4824	0.4832	0.4837	0.4841	0.4845

Considering keep the same MMF of the machine, if the height of the magnet Es reduces, the surface and the number of the coil will both increase. This results in the slightly growth of the PM flux linkage (φ_0 and φ_1) and greatly growth of self inductance (L_0 and L_1). Thus, the variation is taken from 1 to 1.5. The electrical variables of the machine are presented in Table A.4. The objective function of k_{Es} is shown in Fig.A.23. The values will cut down and then rise again with the increasing of Es.

Table A.4 Variation of the magnet height Es

	Es=k_{Es}*Es (original)										
k_{Es}	1	1.05	1.1	1.15	1.2	1.25	1.3	1.35	1.4	1.45	1.5
L_0	29.6	27.9	26.2	24.5	22.9	21.3	19.8	18.3	16.8	15.2	13.7
L_1	7.6	7.5	7.4	7.2	7.0	6.8	6.6	6.3	5.9	5.5	5.0
φ_0	0.8478	0.8444	0.8365	0.8253	0.8116	0.7953	0.7762	0.7542	0.7297	0.7022	0.6728
φ_1	0.4816	0.4677	0.4505	0.4310	0.4110	0.3902	0.3696	0.3485	0.3281	0.3087	0.2896

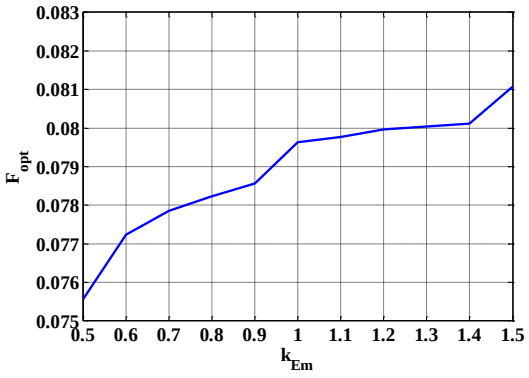

Fig.A.22 F_{opt} for the variation of Em

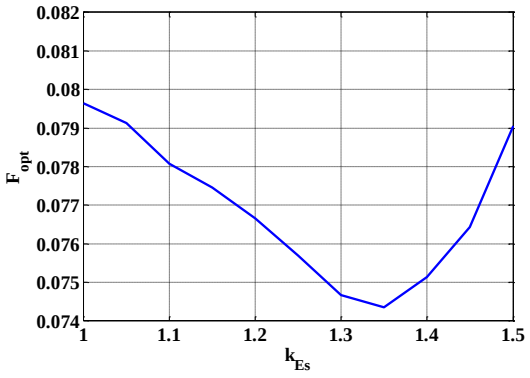

Fig.A.23 F_{opt} for the variation of Es

As the variation of these two structure parameters Em and Es respectively cannot change the objective function value significantly, in the following section, these two parameters will be

modified together. The PM flux linkage (φ_0 and φ_1) and self inductance (L_0 and L_1) are given in Table A.5, Table A.6, Table A.7 and Table A.8.

Table A.5 φ_0 for variation of Em and Es

φ_0 (Wb)		k_{Em}										
		0.5	0.6	0.7	0.8	0.9	1	1.1	1.2	1.3	1.4	1.5
k_{Es}	1	0.805	0.819	0.829	0.837	0.843	0.848	0.852	0.855	0.8596	0.861	0.864
	1.1	0.796	0.809	0.818	0.826	0.832	0.837	0.841	0.844	0.847	0.850	0.852
	1.2	0.772	0.784	0.793	0.801	0.807	0.812	0.816	0.820	0.823	0.825	0.827
	1.3	0.737	0.749	0.758	0.766	0.771	0.776	0.780	0.784	0.787	0.790	0.792
	1.4	0.694	0.705	0.714	0.720	0.725	0.730	0.733	0.737	0.740	0.742	0.744
	1.5	0.642	0.652	0.659	0.665	0.669	0.673	0.676	0.679	0.681	0.684	0.686

Table A.6 φ_1 for variation of Em and Es

φ_1 (Wb)		k_{Em}										
		0.5	0.6	0.7	0.8	0.9	1	1.1	1.2	1.3	1.4	1.5
k_{Es}	1	0.468	0.473	0.477	0.479	0.480	0.482	0.482	0.483	0.484	0.484	0.485
	1.1	0.448	0.449	0.450	0.451	0.450	0.451	0.450	0.450	0.450	0.450	0.450
	1.2	0.414	0.414	0.413	0.413	0.412	0.411	0.410	0.410	0.409	0.409	0.408
	1.3	0.376	0.374	0.373	0.372	0.370	0.370	0.369	0.368	0.367	0.366	0.365
	1.4	0.337	0.334	0.332	0.331	0.329	0.328	0.327	0.326	0.326	0.325	0.324
	1.5	0.299	0.296	0.294	0.292	0.291	0.290	0.288	0.287	0.286	0.286	0.285

Table A.7 L_0 for variation of Em and Es

L_0 (mH)		k_{Em}										
		0.5	0.6	0.7	0.8	0.9	1	1.1	1.2	1.3	1.4	1.5
k_{Es}	1	30.2	30.0	29.9	29.8	29.7	29.6	29.6	29.5	29.5	29.5	29.4
	1.1	26.7	26.5	26.4	26.3	26.2	26.2	26.1	26.1	26.0	26.0	26.0
	1.2	23.4	23.2	23.1	23.0	22.9	22.9	22.8	22.8	22.8	22.7	22.7
	1.3	20.3	20.2	20.0	19.9	19.8	19.8	19.7	19.7	19.6	19.6	19.5
	1.4	17.4	17.2	17.1	17.0	16.8	16.8	16.7	16.6	16.6	16.5	16.4
	1.5	14.5	14.3	14.1	14.0	13.8	13.7	13.7	13.6	13.5	13.4	13.4

Table A.8 L_1 for variation of Em and Es

L_1 (mH)		k_{Em}										
		0.5	0.6	0.7	0.8	0.9	1	1.1	1.2	1.3	1.4	1.5
k_{Es}	1	7.83	7.77	7.73	7.69	7.66	7.64	7.61	7.60	7.58	7.56	7.55
	1.1	7.63	7.56	7.51	7.47	7.43	7.40	7.37	7.35	7.33	7.31	7.30
	1.2	7.32	7.24	7.18	7.13	7.09	7.05	7.02	7.00	6.97	6.95	6.93
	1.3	6.90	6.82	6.74	6.68	6.63	6.58	6.54	6.51	6.47	6.44	6.41
	1.4	6.37	6.24	6.15	6.06	5.99	5.92	5.86	5.80	5.76	5.71	5.68
	1.5	5.63	5.46	5.32	5.20	5.10	5.01	4.94	4.87	4.82	4.76	4.72

The PM flux linkage and the inductance are.

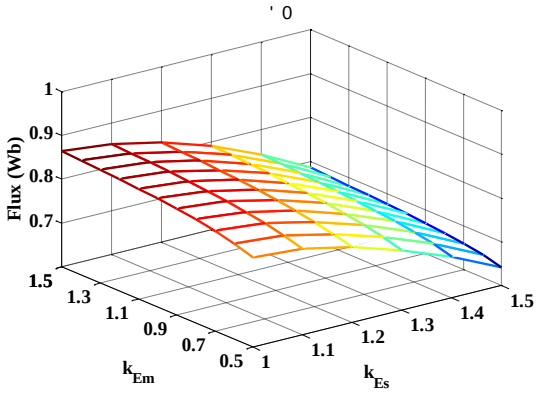

Fig.A.24 φ_0 for the variation of Em and Es

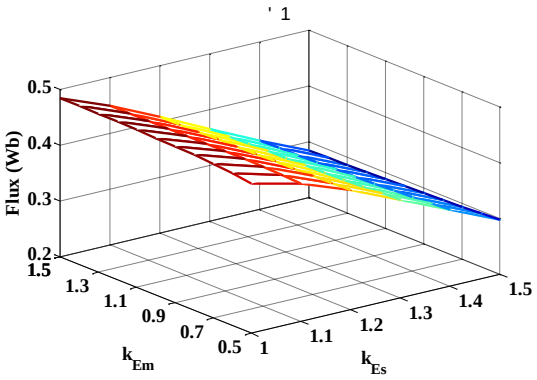

Fig.A.25 φ_1 for the variation of Em and Es

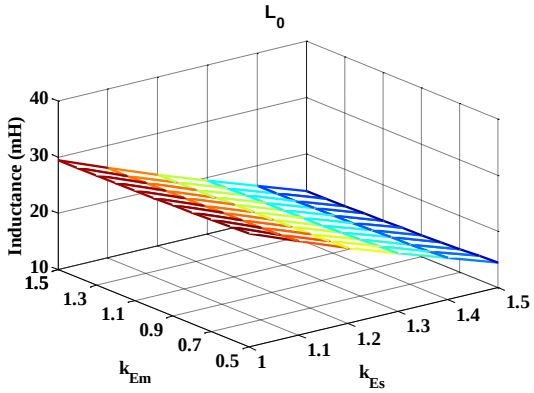

Fig.A.26 L_0 for the variation of Em and Es

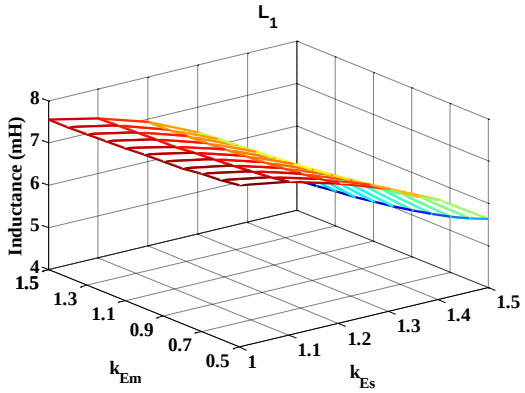

Fig.A.27 L_1 for the variation of Em and Es

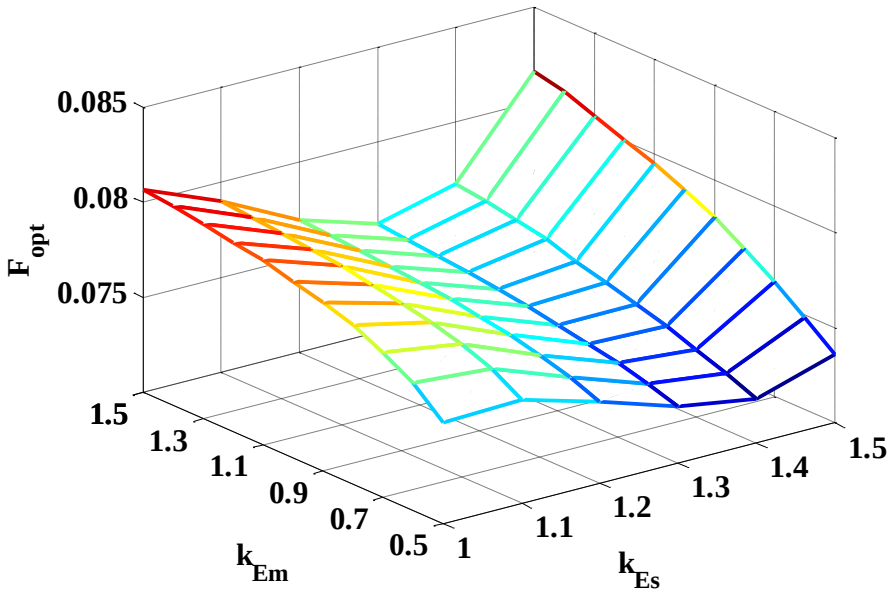

Fig.A.28 F_{opt} for the variation of Em and Es

From Fig.A.28, if we want to maximize the optimal function value F_{opt}, it is better to increase Em and decrease Es.

Appendix VIII *Current PI control*

The general form of the PI controller is determined as follows:

$$G_c(s) = k_p + \frac{k_i}{s} \tag{A.51}$$

Where s is the Laplace operator, the k_p is the proportional constant and the k_i is the integral constant.

In the voltage equation (II.64) of the DSPMG, they (the d and q current components) are still coupled so that it cannot be possible to design the controller directly for each axis.

$$\begin{cases} -v_o = e_o + \beta_{11} * \frac{d}{dt} i_0 + \beta_{12} * \frac{d}{dt} i_d + \alpha_{11} * i_0 \\ -v_d = e_d + \beta_{21} * \frac{d}{dt} i_o + \beta_{22} * \frac{d}{dt} i_d + \beta_{23} * \frac{d}{dt} i_q + \alpha_{22} * i_d + \alpha_{23} * i_q \\ -v_q = e_q + \beta_{32} * \frac{d}{dt} i_d + \beta_{33} * \frac{d}{dt} i_q + \alpha_{31} * i_o + \alpha_{32} * i_d + \alpha_{33} * i_q \end{cases} \tag{A.52}$$

A decouple method was introduced for the design of the internal current controller with an assumption that the initial value of the electrical speed ω_e is 0. The voltage equation in (II.64) can be written as follows:

$$\begin{cases} v_o' = -e_o - v_o - \beta_{12} * \frac{d}{dt} i_d & = \beta_{11} * \frac{d}{dt} i_0 + \alpha_{11} * i_0 \\ v_d' = -e_d - v_d - \beta_{21} * \frac{d}{dt} i_o - \beta_{23} * \frac{d}{dt} i_q - \alpha_{23} * i_q & = \beta_{22} * \frac{d}{dt} i_d + \alpha_{22} * i_d \\ v_q' = -e_q - v_q - \beta_{32} * \frac{d}{dt} i_d - \alpha_{31} * i_o - \alpha_{32} * i_d & = \beta_{33} * \frac{d}{dt} i_q + \alpha_{33} * i_q \end{cases} \tag{A.53}$$

Where:

$$[\alpha] = \begin{bmatrix} R_s & 0 & 0 \\ -\omega_e M_{oq} & R_s + 2\omega_e M_{dq} & -\omega_e \left(\frac{3L_d}{2} - \frac{L_q}{2}\right) \\ \omega_e M_{od} & \omega_e \left(\frac{3L_q}{2} - \frac{L_d}{2}\right) & R_s - 2\omega_e M_{dq} \end{bmatrix} = \begin{bmatrix} \alpha_{11} & \alpha_{12} & \alpha_{13} \\ \alpha_{21} & \alpha_{22} & \alpha_{23} \\ \alpha_{31} & \alpha_{32} & \alpha_{33} \end{bmatrix};$$

$$[\beta] = \begin{bmatrix} L_o & M_{od} & M_{oq} \\ M_{od} & L_d & M_{dq} \\ M_{oq} & M_{dq} & L_q \end{bmatrix} = \begin{bmatrix} \beta_{11} & \beta_{12} & \beta_{13} \\ \beta_{21} & \beta_{22} & \beta_{23} \\ \beta_{31} & \beta_{32} & \beta_{33} \end{bmatrix}.$$

So, equation (A.53) can be rewritten into Laplace transfer function as follows:

$$\begin{cases} G_o(s) = \frac{i_o(s)}{v_o'(s)} = \frac{1}{\alpha_{11} + \beta_{11} s} \\ G_d(s) = \frac{i_o(s)}{v_d'(s)} = \frac{1}{\alpha_{22} + \beta_{22} s} \\ G_q(s) = \frac{i_q(s)}{v_q'(s)} = \frac{1}{\alpha_{33} + \beta_{33} s} \end{cases} \tag{A.54}$$

A pole-compensate method, so that the open loop transfer function $F_o(s)$ is a first-order system which is given in formula (A.55).

$$\begin{cases} F_{oo}(s) = G_{co}(s) * G_o(s) = k_{io} * \left(\frac{1+\frac{k_{po}}{k_{io}}s}{s}\right) * \frac{\frac{1}{\alpha_{11}}}{1+\frac{\beta_{11}}{\alpha_{11}}s} = \frac{k_{io}}{\alpha_{11}*s} \\ F_{od}(s) = G_{cd}(s) * G_d(s) = k_{id} * \left(\frac{1+\frac{k_{pd}}{k_{id}}s}{s}\right) * \frac{\frac{1}{\alpha_{22}}}{1+\frac{\beta_{22}}{\alpha_{22}}s} = \frac{k_{id}}{\alpha_{22}*s} \\ F_{oq}(s) = G_{cq}(s) * G_q(s) = k_{iq} * \left(\frac{1+\frac{k_{pq}}{k_{iq}}s}{s}\right) * \frac{\frac{1}{\alpha_{33}}}{1+\frac{\beta_{33}}{\alpha_{33}}s} = \frac{k_{iq}}{\alpha_{33}*s} \end{cases} \quad \text{(A.55)}$$

So, the relationship between proportional and integral parameters k_p and k_i for each equation are:

$$\begin{cases} k_{po} = \frac{\beta_{11}}{\alpha_{11}} k_{io} \\ k_{pd} = \frac{\beta_{22}}{\alpha_{22}} k_{id} \\ k_{pq} = \frac{\beta_{33}}{\alpha_{33}} k_{iq} \end{cases} \quad \text{(A.56)}$$

In this case, the close loop Laplace transfer functions $F_{co}(s)$ $F_{cd}(s)$ $F_{cq}(s)$ are written:

$$\begin{cases} F_{co}(s) = \frac{F_{oo}(s)}{1+F_{oo}(s)} = \frac{1}{1+\frac{\alpha_{11}*s}{k_{io}}} \\ F_{cd}(s) = \frac{F_{od}(s)}{1+F_{od}(s)} = \frac{1}{1+\frac{\alpha_{22}*s}{k_{id}}} \\ F_{cq}(s) = \frac{F_{oq}(s)}{1+F_{oq}(s)} = \frac{1}{1+\frac{\alpha_{33}*s}{k_{iq}}} \end{cases} \quad \text{(A.57)}$$

So far, the system has a first-order response with the PI controller. The electrical equations are coupled by the d and q axis current actually. Based on the controlling theory, if the response time t_r is fixed, the time constant τ for each electrical equation is:

$$\tau = \frac{\alpha_{11}}{k_{io}} = \frac{\alpha_{22}}{k_{id}} = \frac{\alpha_{33}}{k_{iq}} = \frac{t_r}{3} \quad \text{(A.58)}$$

The simple sinusoidal current waveform is firstly applied to the machine, the simulation results are showed in Fig.A.29 and Fig.A.30.

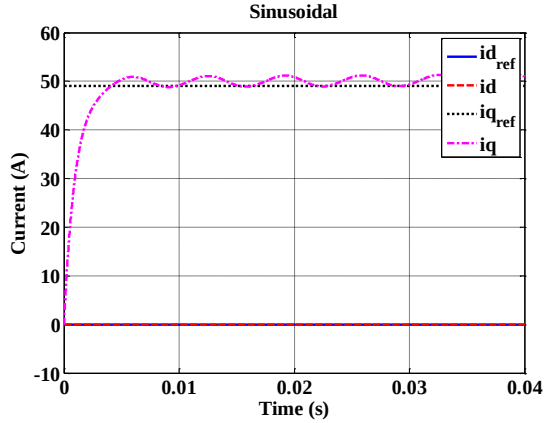

Fig.A.29 d-q axis currents (PI)

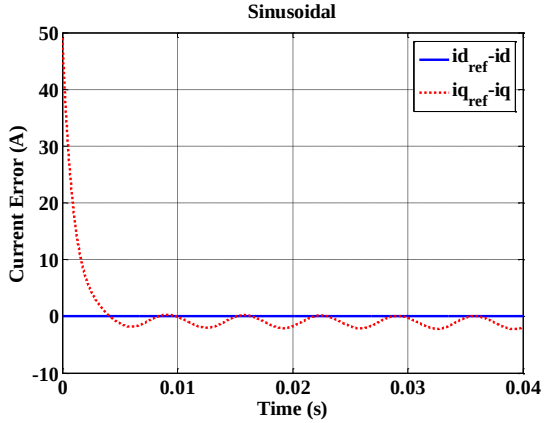

Fig.A.30 Current error in d-q axis (PI)

For the simple sinusoidal waveform current, after transformation, the d-q axis current will be constant. Even for these two constant references, PI controller cannot appear good performance. The controller in d-axis can work well and keep the current equate to zero. However, the controller in q-axis cannot well track the reference with error between -1 A and 1.3A.

Then, the proposed fitting current which is composed of fundamental and 2nd harmonic component is tested. The simulation results are given in Fig.A.31 and Fig.A.32.

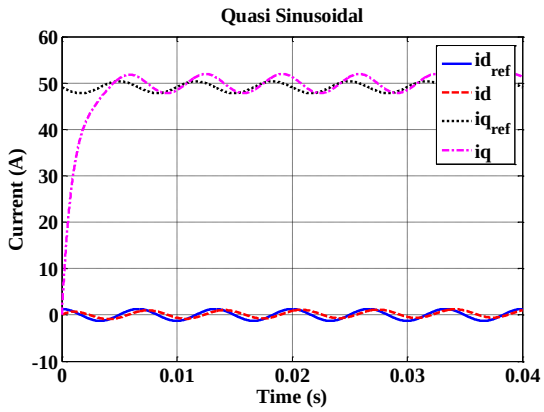

Fig.A.31 d-q axis currents (PI)

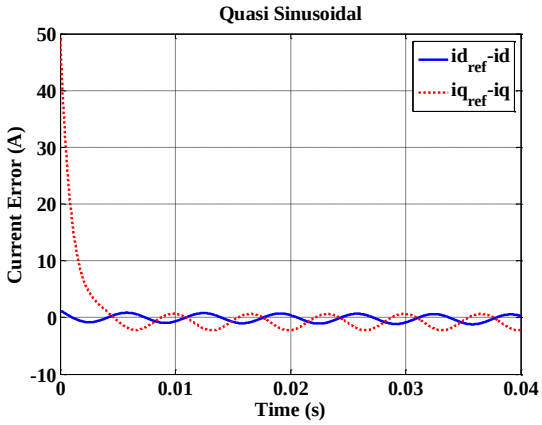

Fig.A.32 Current error in abc axis (PI)

If the harmonic is injected to the fundamental, the d-q axis currents are no longer constant. The PI controller cannot tackle the two variable d-q currents which leads to the current error between -1.5 A and 2 A in the steady state.

Based on the simulation results from Fig.A.29 to Fig.A.32, the classical PI controller cannot give a good performance in the time-variant nonlinear system Therefore, the nonlinear and robust controller SMC is applied.

Appendix IX *Robust Analysis of SMC for Current Loop*

In this part, the robustness of SMC is briefly evaluated according to some parameters variations: controller parameters, machine stator resistance and inductance. The analysis for these three parts is detailed in the following.

- **Influence of SMC parameters**

The controller parameters are varied and their effect on the settling time of the response is presented in Fig.A.33 and Fig.A.34 for both sinusoidal and quasi sinusoidal currents.

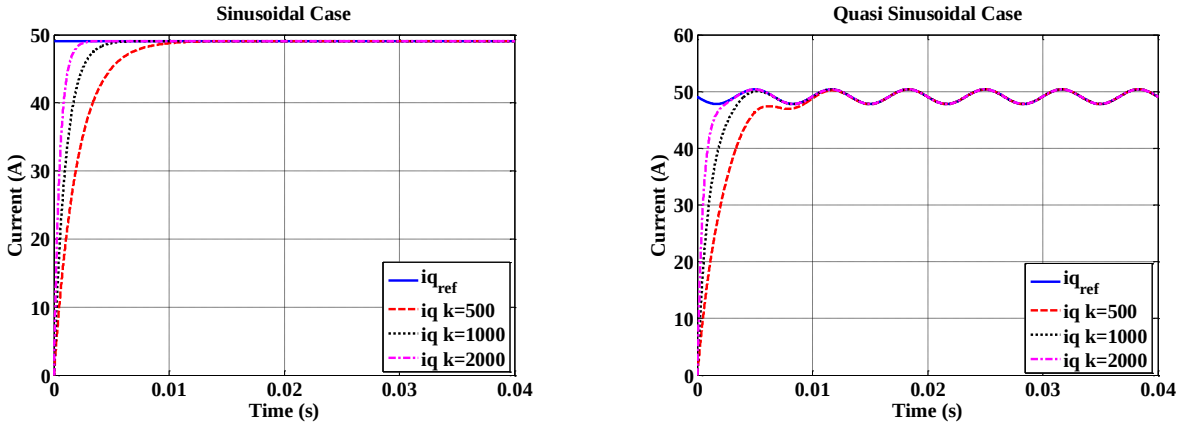

a) q axis current b) q axis current

Fig.A.33. Influence of the variation of k (ε is fixed, 0.01)

Form these two figures, it can be concluded that with increasing the value of the parameter k, the settling time decreases; with increasing the value of ε, it causes more chattering in steady state as shown in Fig.A.41.b.

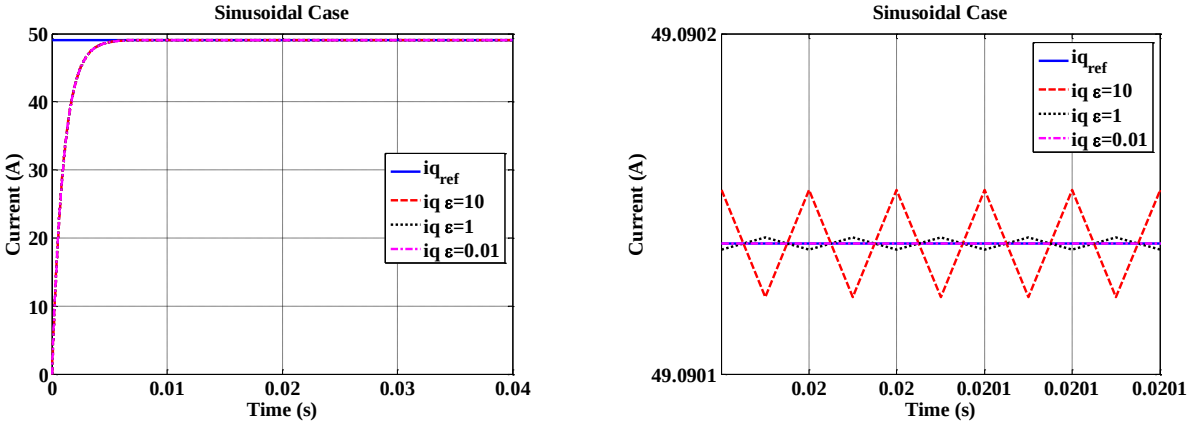

a) q axis current b) Zoom of Steady state

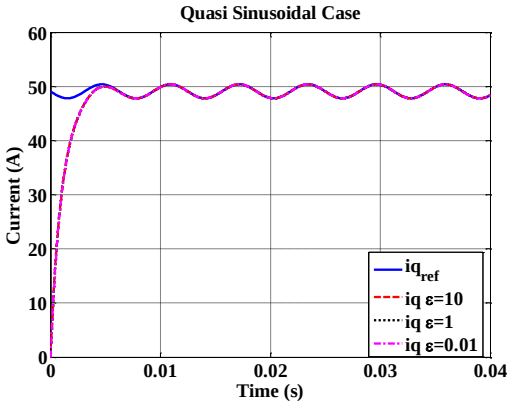

c) q axis current

Fig.A.34. Influence of the varation of ε (k is fixed, 1000)

- **Influence of Stator Resistance**

In this part, the parameters in the controller keep as the original values (both for parameters ε and k), while the resistance in the machine model will change from 80% to 120% of its initial value.

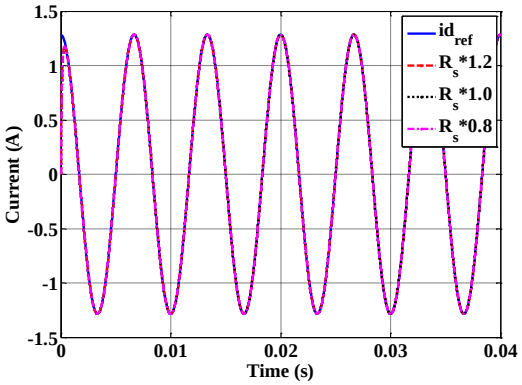

Fig.A.35 Robustness of R_s for i_d

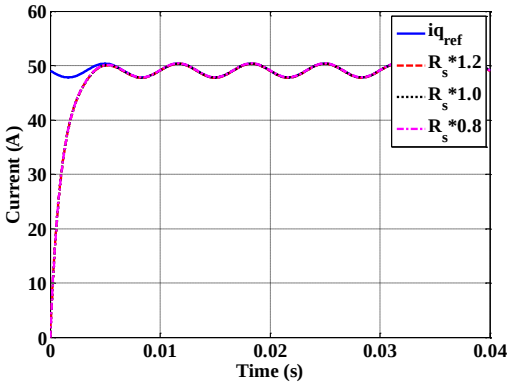

Fig.A.36 Robustness of R_s for i_q

For these two figures (Fig.A.35 and Fig.A.36), in spite of the resistance variation in the machine model, the SMC shows a good tracking performances. For all the different resistance, SMC can nearly reach the reference at the same response time and well trace the reference.

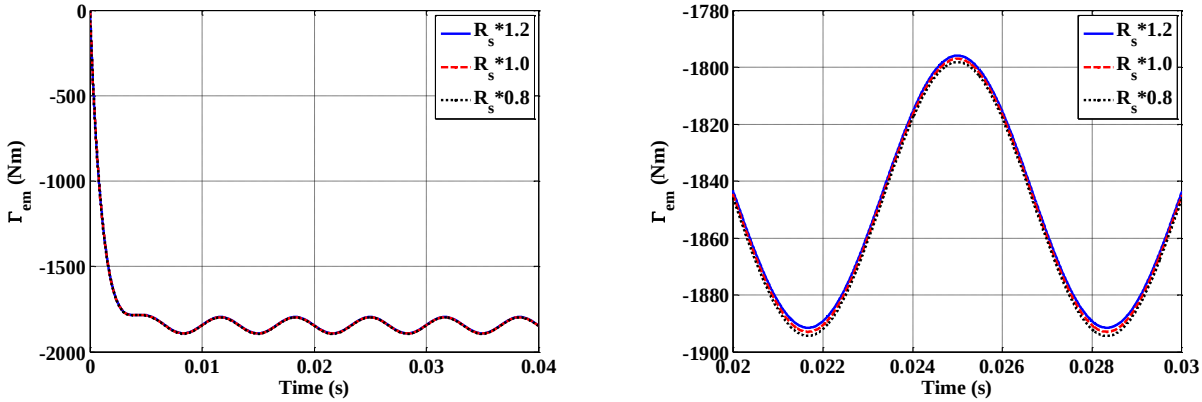

Fig.A.37 Torque for different resistance

Fig.A.37 gives the corresponding electromagnetic torque variation for different stator resistance values. Indeed, SMC can well trace the reference; however, as there are small errors between the reference and simulated currents, they bring a little difference for the electromagnetic torque which can be neglected comparing to the reference value (1845 Nm).

- **Influence of Stator Inductance**

The same principle is taken for the stator inductance variation (L_0 & L_1). Assuming controller parameters are kept as before, the inductance varies from 120% to 80% of its original value. The current and torque performances are given in Fig.A.45 to Fig.A.47.

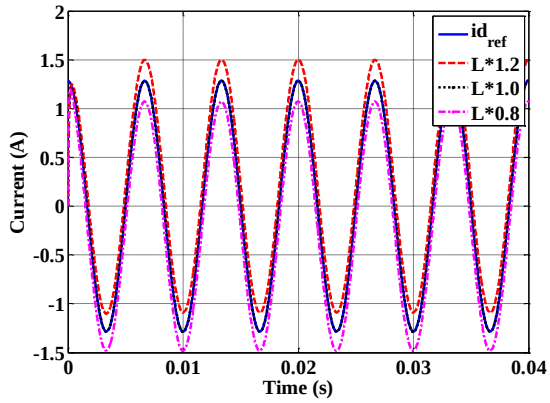

Fig.A.38 Robustness of L for i_d

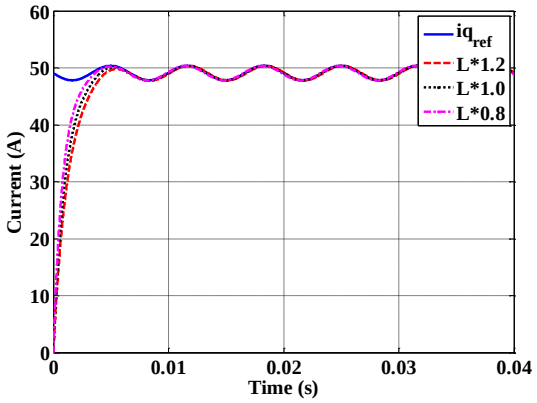

Fig.A.39 Robustness of L for i_q

From Fig.A.38 and Fig.A.39, we observe that inductance variation takes a slight error in d-q axis current which is not like that of resistance variation. However, this small error doesn't generate big difference in the electromagnetic torque in Fig.A.40. This means SMC is robust for the inductance variation.

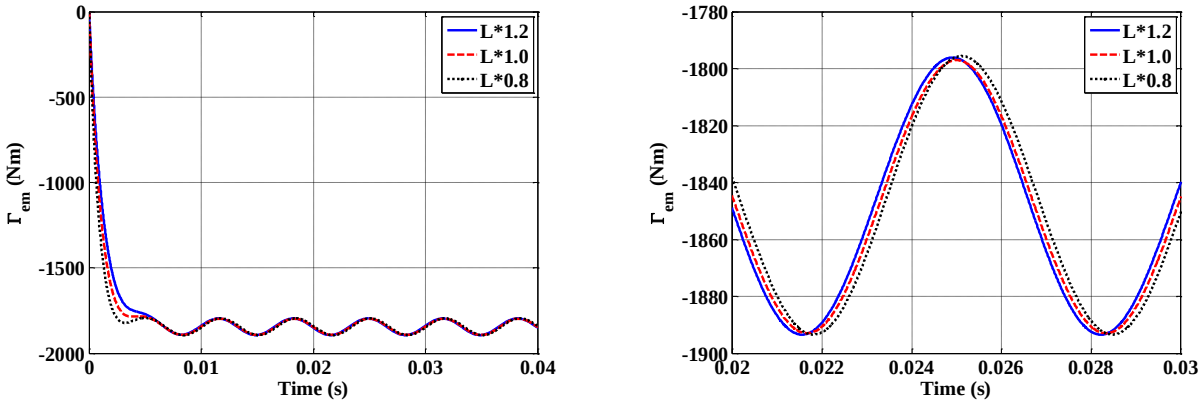

Fig.A.40 Torque for different inductance

Appendix X *Speed PI controller with pole compensation method*

The open loop for speed control is:

$$F_{om}(s) = G_m(s)G_{cm}(s) = k_{im} * \left(\frac{1+\frac{k_{pm}}{k_{im}}s}{s}\right) * \frac{\frac{1}{f_v}}{1+\frac{J_m}{f_v}s} \tag{A.59}$$

PI controller contains two parts: proportional part and integral part. In this part, two methods to calculate the proportional and integral parameters are detailed: pole-cancellation method and pole-placement method. The mainly difference of these two methods is: the close loop transfer function based on a pole-cancellation method is a first order system; while that of pole-placement method is a second order system.

If pole-compensation method is used, the open loop transfer function must satisfy the condition as follows:

$$1 + \frac{k_{pm}}{k_{im}}s = 1 + \frac{J_m}{f_v}s \tag{A.60}$$

As a result, the close loop transfer function is:

$$F_{cm}(s) = \frac{G_{om}(s)}{1+G_{om}(s)} = \frac{1}{\frac{f_v}{k_i}s+1} \tag{A.61}$$

With $\frac{k_{pm}}{k_{im}} = \frac{J_m}{f_v}$.

According to the control theory, for the first order system, the response time is:

$$t_r = 3\frac{f_v}{k_{im}} \tag{A.62}$$

Therefore, the parameters for PI controller based on pole compensation method are:

$$\begin{cases} k_{im} = 3\frac{f_v}{t_r} \\ k_{pm} = 3\frac{J_m}{t_r} \end{cases} \tag{A.63}$$

As the rated speed of marine current for MCECS is 2.5 m/s, the marine current will be 2.5 m/s at the beginning, then, increase to 2.8 m/s at 5 s, at last, it reduces to 2 m/s. According to the Cp-λ curve in Fig.II.16, the speed reference changes from 5.236 rad/s to 5.864 rad/s and finally goes to 4.189 rad/s. The results for reference and simulated speed are given in Fig.A.41. Three text boxes in the figure give the information for each response time (1 s, 6 s, 11 s). From these values, PI with pole compensation method can get the 95% of the reference values during the mechanical response time. It spears good performance in the tracking speed.

Some robustness analyses for the moment of inertia and the coefficient of friction are also taken. Compared with the pole placement method, the robustness of the pole compensation method is not as good as the other. It takes some more time to get the speed reference with parameters variation.

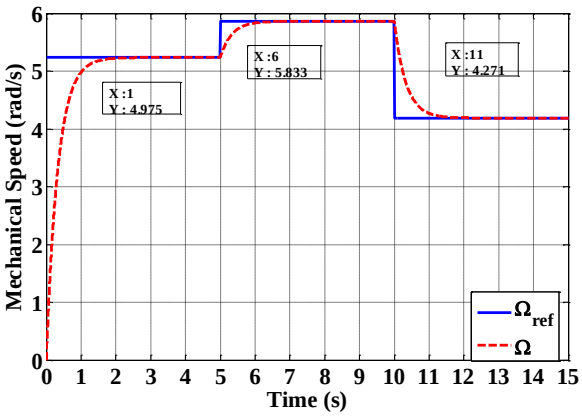

Fig.A.41 Mechanical performace for PI control (Pole Compensation)

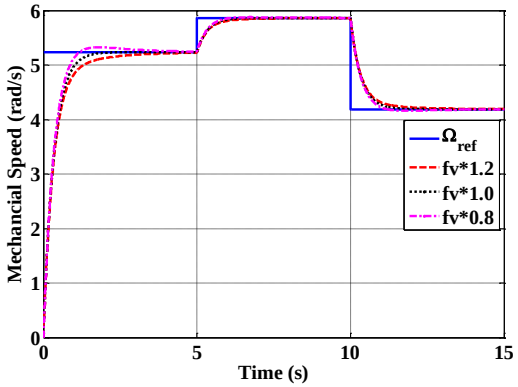

Fig.A.42 Influence of the friction coefficient

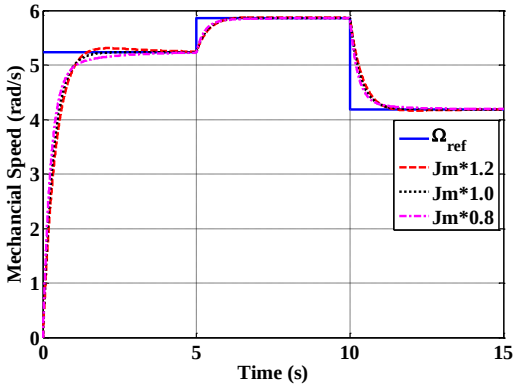

Fig.A.43 Influence of moment of inertia

Appendix XI *Global simulation of MCECS taking into account both converters*

In this section, the system simulation results with converter for marine current speed varying from 2.5 m/s to 2.6 m/s are presented.

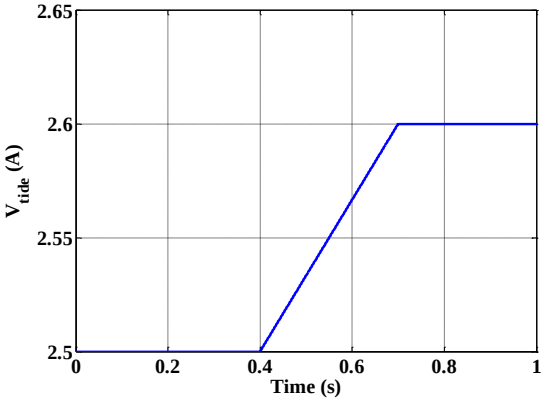

Fig.A.44 Marine current speed

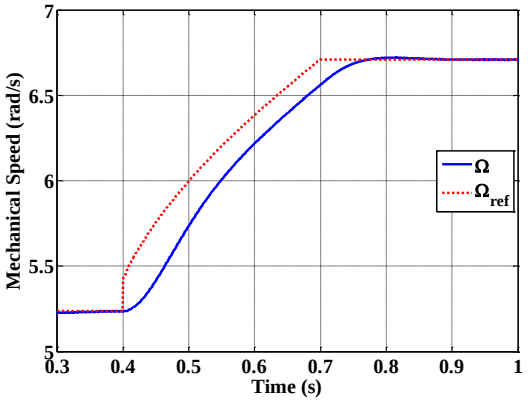

Fig.A.45 Mechanical speed

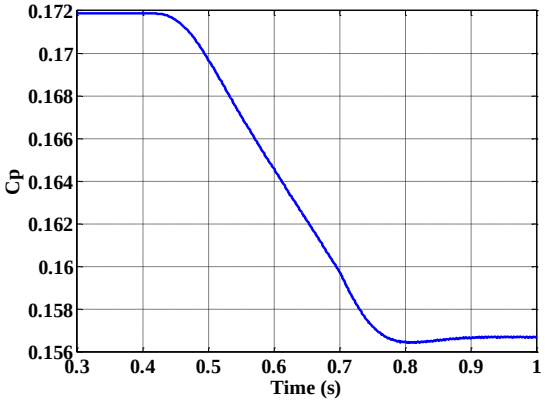

Fig.A.46 Power coefficient

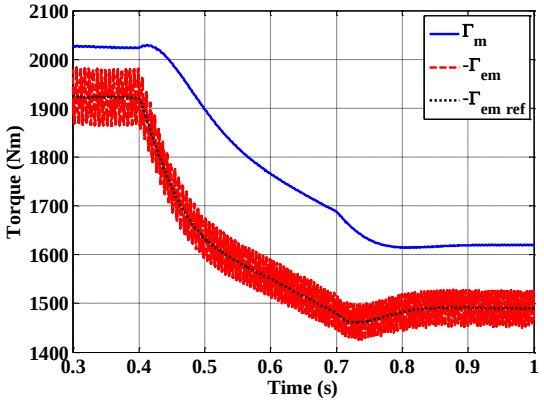

Fig.A.47 Torque

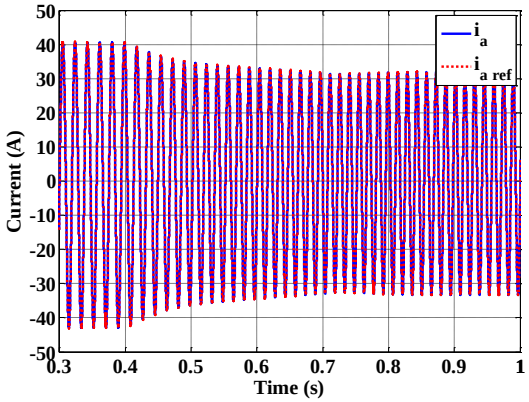

a) for all the marine current speed

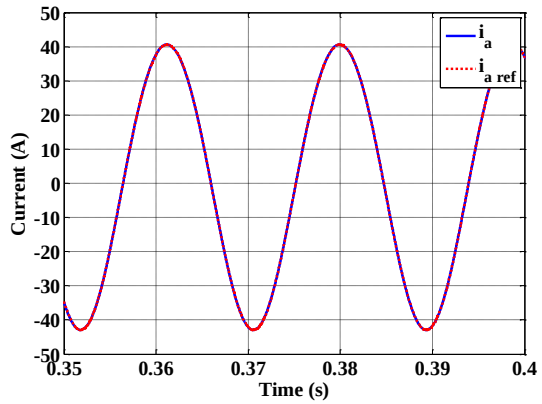

b) for 2.5 m/s marine current speed

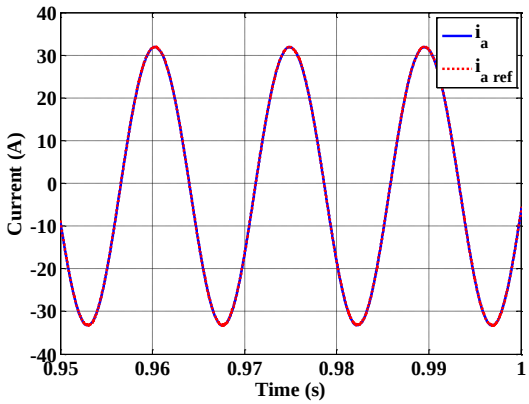

c) for 2.6 m/s marine current speed

Fig.A.48 Machine side current

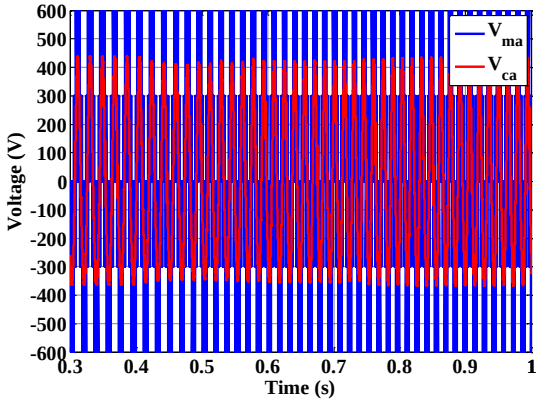

a) for all the marine current speed

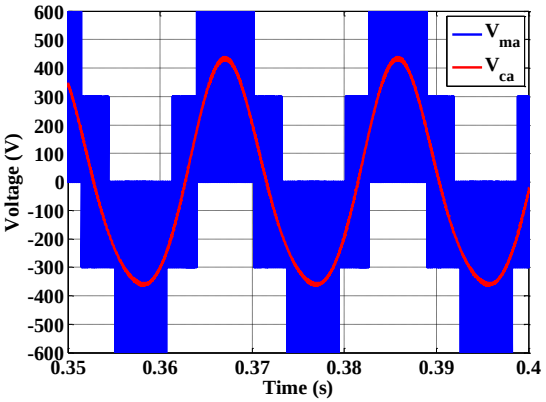

b) for 2.5 m/s marine current speed

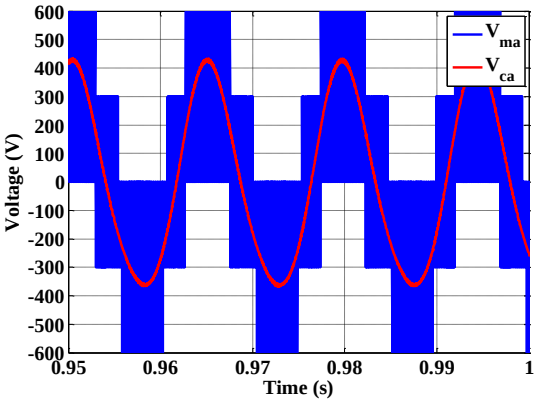

c) for 2.6 m/s marine current speed

Fig.A.49 Machine side voltage

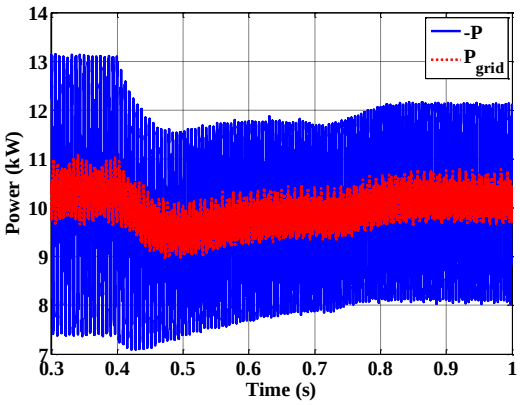

a) for all the marine current speed

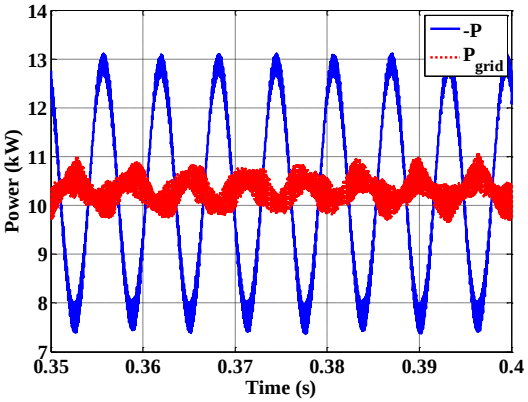

b) for 2.5 m/s marine current speed

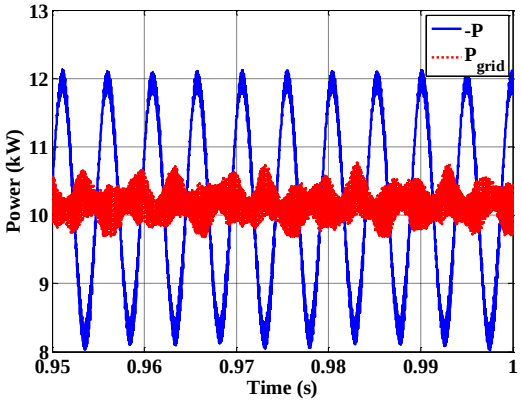

c) for 2.6 m/s marine current speed

Fig.A.50 Machine side and grid side power

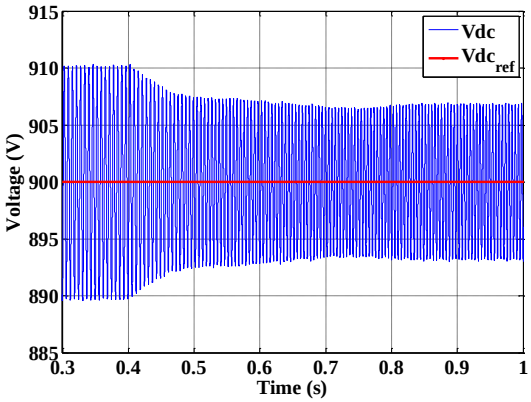

Fig.A.51 DC-bus voltage

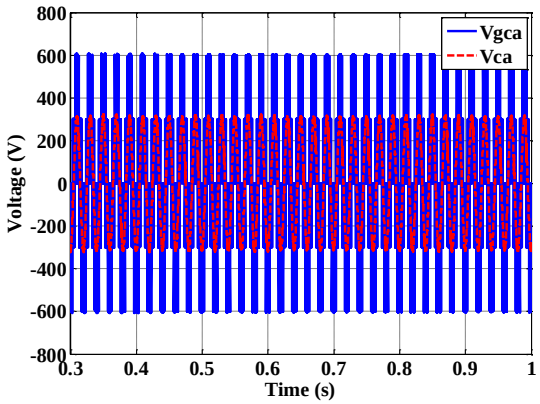

a) for all the marine current speed

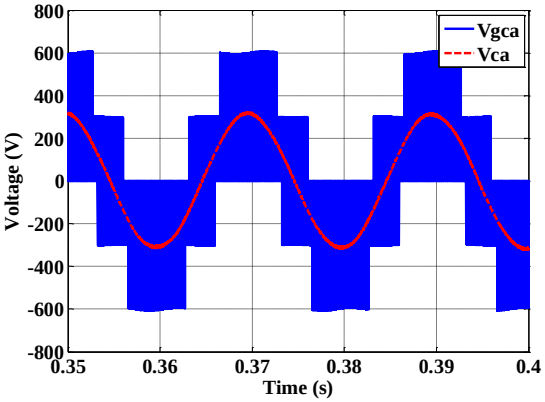

b) for 2.5 m/s marine current speed

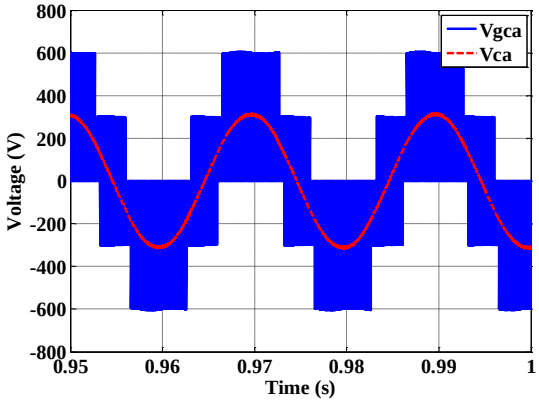

c) for 2.6 m/s marine current speed

Fig.A.52 Grid side voltage

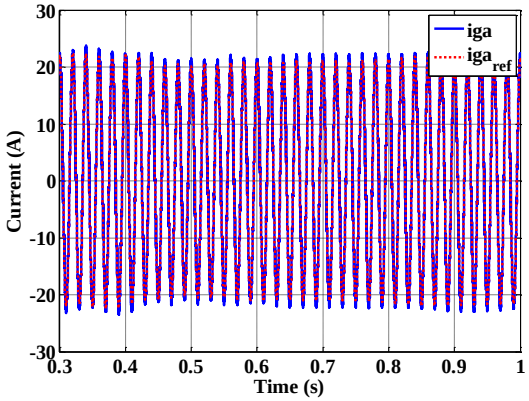

a) for all the marine current speed

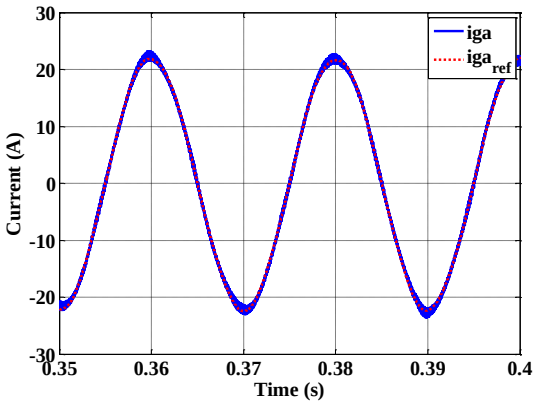

b) for 2.5 m/s marine current speed

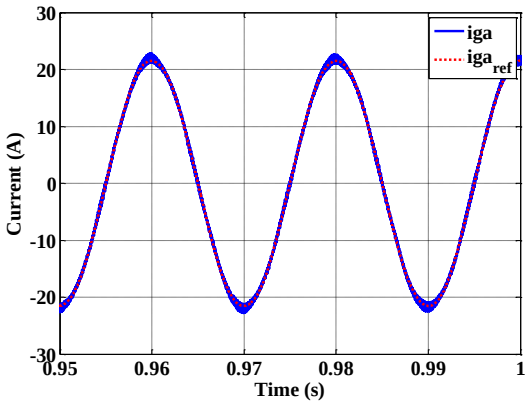

c) for 2.6 m/s marine current speed

Fig.A.53 Grid side current

l'université nantes angers le mans
PÔLE DE RECHERCHE ET D'ENSEIGNEMENT SUPÉRIEUR

UNIVERSITÉ DE NANTES

Thèse de Doctorat

Hao CHEN

Modeling and Control of a Marine Current Energy Conversion System using a Doubly Salient Permanent Magnet Generator

Résumé

Parmi les énergies marines renouvelables hors éolien posé, toutes naissantes, l'énergie des courants marins (énergie hydrolienne) est susceptible de déboucher sur une exploitation commerciale et industrielle à moyen terme. C'est une énergie intermittente, mais très prévisible, ce qui facilite son intégration au réseau.
Les travaux réalisés dans cette thèse rentrent dans ce contexte et ont pour objectif la modélisation et la commande d'une chaîne de conversion d'énergie hydrolienne. Cela nécessite une modélisation multi-physique allant de la ressource jusqu'à l'intégration au réseau électrique, la conception et la commande d'une génératrice innovante à attaque directe et des interfaces d'électronique de puissance associés.
Les concepts de turbines hydroliennes, les projets existants ou en cours ainsi que les structures usuelles de chaînes de conversion sont présentés. Les modèles de la ressource et de la turbine sont dressés. Un modèle dynamique d'une génératrice synchrone à aimants permanents doublement saillante basé sur la méthode des éléments finis et la transformation de Park est ensuite développé. Les résultats obtenus sont comparés à ceux d'une génératrice synchrone à aimants permanents classique montrant ainsi l'originalité, la complexité et les principales caractéristiques de la structure proposée. L'impact de la mutuelle inductance entre les phases statoriques sur les performances de la machine est détaillé.
Des formes particulières de courants d'alimentation sont recherchés et testés par simulation en vue de délivrer un couple quasi constant et de minimiser les pertes Joule.
Différentes stratégies de contrôle sont ensuite élaborées et appliquées à l'ensemble génératrice – convertisseurs bidirectionnels à MLI. Les résultats obtenus en mode de fonctionnement MPPT ou défluxé à l'aide de l'outil de simulation développé sont présentés et discutés pour des cas tests réalistes réalisés sous l'environnement Matlab/Simulink.

Mots clés
Energie hydrolienne, modélisation, commande, machine synchrone à aimants permanents, couple, mode de glissement.

Abstract

Several techniques to extract and exploit ocean energy have been recently suggested. The most studied ones are: marine current energy, wave energy and ocean thermal energy.
This Ph.D. thesis fits in this context and its main objective is to contribute on control and modelling of a Marine Current Energy Conversion System (MCECS). This requires multi-physics modelling from the hydrokinetic resource to the electricity grid, design and control of an innovative low speed non-conventional generator and its associated power electronic interfaces.
At first, turbine concepts, relative projects and usual chain of tidal energy conversion are presented.
Tidal current and turbine modelling are secondly addressed. The dynamic modelling of a low speed Double Salient Permanent Magnet Generator (DSPMG) based on finite element method and Park transformations is developed. Results are compared to classical Permanent Magnet Synchronous Generator (PMSG) to highlight advantages, originality, complexity and principal characteristics of the proposed structure.
Suitable currents are then determined and tested by simulation in order to deliver a quasi-constant torque and minimise Joule losses. The mutual effect on the generator performances is detailed.
Finally, several control strategies are applied to DSPMG associated to a bidirectional back-to-back converter and are analysed. The main results, based on the developed marine current turbine simulation tool, are presented and discussed with illustration by several realistic studies and Matlab/Simulink assessment.

Key Words
Marine Current Turbine, tidal energy, modeling, control, permanent magnet synchronous generator, torque, sliding mode.

L'Université Nantes Angers Le Mans